ZEKE-PFI Photoelectron Spectroscopy of Halogens and Iodine van der Waals Complexes

David A. Beattie

Doctor of Philosophy

The University of Edinburgh

1997

How I admire the eider duck that dives
with a neat loop and no splash and the gannet that suddenly
harpoons the sea. - I'm a guillemot
that still dives
in the first way it thought of: poke your head under
and fly down.

from "Ineducable me"
by Norman MacCaig

Acknowledgments

There are a number of people to whom I am indebted for their help and encouragement throughout the course of my doctoral studies. My supervisors, Professor Robert Donovan and Dr. Kenneth Lawley, are at the top of this list. I would like to thank them for guiding me through my formative years as a physical chemistry researcher. Dr. Martin Cockett (now at the University of York) deserves a special thank you for teaching me how to be an electron spectroscopist and giving me my first insights into ZEKE-PFI spectroscopy.

The benefits of being a member of a large research group have been apparent from day one of my studies. The largest benefit has been the friendships developed with the other PhD. students in the group. I would like to thank Andy Cormack and Neil MacCleod for the discussions (scientific and non-scientific) and for their help in the lab. I would also like to thank the other students in the spectroscopy and dynamics group (a list of names too numerous to mention) for making this an enjoyable three years. Other members of the group who merit a mention are Dr. Trevor Ridley for scientific discussions and Robert Maier for technical assistance.

On a more personal note, there are a number of people outside the Department of Chemistry who have been important to me during the last few years. Dave, Kevin and Steve have been great friends and have kept me on an even keel for longer than I can remember. The Irish girls deserve a mention for making this a memorable summer and making the write-up seem less of a chore. On the family side of things I would like to thank my brother for being a great role model and my father for always being proud of me. Finally, I would like to thank my mother for just about everything.

Abstract

The ground ionic state of a number of halogens and iodine-rare gas van der Waals complexes has been investigated using zero kinetic energy pulsed field ionisation (ZEKE-PFI) photoelectron spectroscopy. The study is divided into two sections; the first deals with the halogens and the factors that influence the vibrational intensity distribution in the ZEKE-PFI spectra, the second deals with the iodine-rare gas van der Waals complexes and the changes that occur in the van der Waals interaction upon ionisation.

The (2+1′) ZEKE-PFI spectra of the X $^2\Pi_{3/2,g}$ and X $^2\Pi_{1/2,g}$ states of I_2^+, recorded *via* the $[^2\Pi_{3/2}]_c$ 5d;2_g and $[^2\Pi_{1/2}]_c$ 5d;2_g Rydberg states respectively, have been reanalysed and the contribution of autoionisation processes to the vibrational intensity distribution has been investigated. Spectra of autoionising Rydberg states in the threshold region of the X $^2\Pi_{3/2,g}$ and X $^2\Pi_{1/2,g}$ states have revealed that forced vibrational autoionisation is responsible for the appearance of the ZEKE-PFI spectra of the X $^2\Pi_{3/2,g}$ state. A similar ZEKE-PFI study of the X $^2\Pi_{3/2,g}$ and X $^2\Pi_{1/2,g}$ states of Br_2^+ has been performed using the $[^2\Pi_{3/2}]_c$ 4d;1_g and $[^2\Pi_{1/2}]_c$ 4d;1_g Rydberg states as intermediates. Accurate values for the adiabatic ionisation energy and spin-orbit splitting of the ground ionic state have been detemined. Forced vibrational autoionisation has been shown to influence the ZEKE-PFI spectrum of the X $^2\Pi_{3/2,g}$ state of Br_2^+.

A coherent two-photon (C2P) ZEKE-PFI study of the ground ionic state of Br_2 and IBr has been performed and the results compared to similar work on I_2. This is the first ZEKE-PFI study of IBr, from which accurate values have been determined for the adiabatic ionisation energy and spin-orbit splitting of the ground ionic state. The C2P ZEKE-PFI spectra of I_2 and IBr exhibit extended vibrational progressions that cannot be explained using Franck-Condon factors. In contrast, the C2P ZEKE-PFI spectrum of Br_2 has only a very short vibrational progression. The differences between the spectra have been attributed to the involvement of a repulsive intermediate state at the one-photon level, leading to extended vibrational progressions in the final state for I_2 and IBr. The X $^2\Pi_{3/2}$ state of IBr^+ has also been

investigated using (2+1′) and (1+2′) excitation routes *via* the b$[^2\Pi_{1/2}]_c$ 6s Rydberg state and the $B\ ^3\Pi_0^+$ valence state respectively.

The I_2-Ar and I_2-Kr van der Waals complexes have been investigated using (2+1) resonance enhanced multiphoton ionisation (REMPI) spectroscopy and (2+1′) ZEKE-PFI spectroscopy. The $[^2\Pi_{3/2}]_c$ 5d;2_g and $[^2\Pi_{3/2}]_c$ 5;0_g Rydberg states of the I_2-Ar complex have been reinvestigated using (2+1) REMPI spectroscopy. Evidence has been found for the existence of two structural isomers; T-shaped and linear. The ZEKE-PFI spectrum of the $\tilde{X}\ ^2\Pi_{3/2,g}$ state of I_2^+-Ar has been recorded *via* the $[^2\Pi_{3/2}]_c$ 5d;2_g Rydberg state and structure due to both isomers has been observed. A similar study was carried out for I_2-Kr in which only one isomer was observed. The (2+1) REMPI spectra of the $[^2\Pi_{3/2}]_c$ 5d;2_g and $[^2\Pi_{3/2}]_c$ 5d;0_g Rydberg states of I_2-Kr have been recorded and the $[^2\Pi_{3/2}]_c$ 5d;2_g Rydberg state used as an intermediate to record the (2+1′) ZEKE-PFI spectrum of the $\tilde{X}\ ^2\Pi_{3/2,g}$ state of I_2^+-Kr. This was the first observation of the I_2-Kr complex in a Rydberg or ionic state. The (2+1) REMPI spectrum of the $[^2\Pi_{1/2}]_c$ 6s;1_g Rydberg state of the I_2-N_2 van der Waals complex has been recorded. Evidence was observed for the existence of two isomers of I_2-N_2 in the Rydberg state. The geometry of the I_2-N_2 complex in the ground neutral state has been investigated using an empirical potential surface.

Contents

1. Introduction

The purpose of this chapter is to introduce the study of molecular ions from an historical perspective. The spectroscopic technique that revolutionised the field of ion spectroscopy was photoelectron spectroscopy (PES). **ZE**ro **K**inetic **E**nergy **P**ulsed **F**ield **I**onisation (ZEKE-PFI) photoelectron spectroscopy is a variant of the technique that allows molecular ions to be studied with unprecedented resolution (< 1 cm^{-1}).[1] Various steps leading to the development of the ZEKE-PFI technique will be discussed in this chapter starting with a short section on the origins of ion spectroscopy and the determination of ionisation energies. The successful technique of photoelectron spectroscopy is the subject of section 1.2 followed in section 1.3 by a discussion on threshold photoelectron spectroscopy (TPES). The importance of lasers to the development of photoelectron spectroscopy through the use of resonance enhanced multiphoton ionisation (REMPI) will be discussed in section 1.4. ZEKE-PFI spectroscopy will be introduced in section 1.5 with a discussion of the development of the technique from its beginnings as an application of REMPI to threshold photoelectron spectroscopy. Finally, an outline of the research presented in the following chapters will be given in section 1.6.

1.1 Ions and Ionisation Energies

The spectroscopy of molecular ions dates back to the 1920's when it was first realised that spectral lines observed in the gas discharge emission spectra of N_2 were coming from a positively charged particle, the N_2^+ molecule.[2] Just as with neutral state emission spectroscopy, the transitions that were observed for cations allowed their electronic states to be characterised. The only piece of information that could not be obtained in this way was the minimum energy needed to produce an ion from a neutral species, the adiabatic ionisation energy.

The adiabatic ionisation energy of molecules, and the ionisation energies for excited electronic states, became important in the following years with the development of molecular orbital theory. The focus on ionisation energies reached a

peak with the proposal by Koopman [3] that the ionisation energy of an electron in a particular molecular orbital is equal to the binding energy of that orbital as calculated by the self-consistant field (SCF)[4] method:

$$IE_i = -\varepsilon_i^{SCF} \qquad (1.1)$$

where IE_i is the ionisation energy of orbital i and ε_i^{SCF} is the SCF calculated energy of orbital i. Koopman's theorem gave the perfect opportunity for experimental observations to be used as a test of the current theory of molecular orbitals.

The first attempts to determine the adiabatic ionisation energies of molecules came from vacuum ultra-violet (VUV) absorption spectra.[5] The VUV wavelength range is roughly between 50 and 200 nm and is defined by the wavelengths absorbed strongly by oxygen. Most molecules are anticipated to have their first ionisation energies in this wavelength region and the observation of continuum absorption in the VUV is indicative of either an ionisation or a dissociation process for the species being studied. The ambiguity of this approach soon led to the development of other techniques for the determination of ionisation energies.

Watanabe introduced the technique of photoionisation efficiency (PIE) spectroscopy [6] which circumvented this problem by detecting the production of charged particles (ion current) with increasing photon energy, rather than detecting the absorption of incident light. The onset of charged particle production was identified with the adiabatic ionisation potential. Subsequent ionisation energies (for excited ionic states) could also be observed as step functions in the ion current; as ionisation is not state selective the ion current generated above the first excited ionic state is a sum of the ion current for ground state production and the ion current for the excited state production. By measuring the energy of the ionisation onsets along the PIE spectrum the ionisation energies of atoms and molecules could be determined. Good examples of step-like PIE spectra are those recorded for NH_3 [7] and NO.[8] However, good examples were rare due to a limitation of the technique; the steps in the ion current could be obscured by autoionising resonances.[9] Autoionising resonances are caused by absorption to high lying neutral Rydberg states lying above the first ionisation energy. These states can decay by ionising to produce an ion and an electron. The ion current observed in PIE can be severely disrupted from the

simple step function as the incident light is scanned across the excited Rydberg states, making it difficult to determine ionisation energies accurately.

Although limiting in PIE spectroscopy, the observation of Rydberg states through autoionising resonances and by neutral state absorption provided another means by which ionisation energies could be determined. Rydberg states form series which converge on the various states of an ion. The series are quite often regular and can be fitted by the general Rydberg equation:

$$E(nl) = IE - \frac{R_y}{(n-\delta)^2} \qquad (1.2)$$

where IE is the ionisation energy of the ionic state to which the series converges, R_y is the Rydberg constant, n is the principal quantum number of the Rydberg state and δ is quantum defect of the Rydberg orbital. The quantum defect of a Rydberg orbital for an atom or molecule represents how different the orbital is from the corresponding orbital in atomic hydrogen. By measuring the energies of Rydberg states converging to an ionic state the ionisation energy can be determined by extrapolation, relying on some knowledge of the quantum defect for the Rydberg series and assuming that the quantum defect remains constant with increasing n (i.e. with increasing energy). Examples of sharp Rydberg spectra which have allowed accurate ionisation energies to be determined include those for H_2 [9] and N_2.[10]

Sharp autoionising resonances are not ubiquitous as they require the Rydberg states to have a reasonably long lifetime. In cases where the Rydberg states are particularly short-lived the autoionising resonances can be quite broad with the result that PIE spectra can have a simple step-like appearance. As a result the detection of ionisation onsets by PIE spectroscopy is complementary to Rydberg extrapolations, one technique being used in situations where the other is not so effective. However, Rydberg extrapolations have limiting factors; an accurate extrapolation of Rydberg state energies to the ionisation energy requires the observation of high n members of the series which is not always possible due to spectral congestion and poor resolution.

The technique which revolutionised the field of valence ionic state spectroscopy and provided the perfect test for the emerging ideas of molecular orbital theory was photoelectron spectroscopy (PES). UV photoelectron spectroscopy was

developed in tandem by two research groups, one in England led by Dr. D. W. Turner,[11] and the other in Russia led by Professor A. N. Terenin.[12] There now follows a discussion of main ideas behind UV-PES and the limitations of the technique.

1.2 Photoelectron Spectroscopy

The principle behind photoelectron spectroscopy is very simple. Irradiation of a sample using monochromatic light of sufficiently high energy will result in the production of photoelectrons. The kinetic energy of these photoelectrons will be directly related to the energy of the ion produced in the photoionisation process through the following relationship:

$$E_e = h\nu - IE - E_{vib} - E_{rot} \qquad (1.3)$$

where E_e is the electron kinetic energy, $h\nu$ is the photon energy, IE is the ionisation energy of the electronic state of the ion and E_{vib} and E_{rot} is the internal energy of the ion. The equation is simply a statement of conservation of energy. For a given excitation energy there will be a distribution of electron energies corresponding to the various levels of excitation (electronic, vibrational and rotational) of the ion. By measuring the energies of the electron distribution a spectrum of the internal energy levels of the ion can be obtained.

The application of this idea was carried out by Turner [11] and Terenin [12] as mentioned in the previous section. The ionising light source most commonly used was a helium discharge lamp. The main output of this lamp are photons of energy 21.22 eV (58.4 nm or 171151 cm^{-1}) corresponding to the $1s^1 2p^1 \rightarrow 1s^2$ transition in atomic helium. The choice of the light source was made on the basis that the valence shell ionisation energies for most molecules is well below this energy allowing for a full examination of all the molecular orbitals.

The analysers used for measuring the kinetic energy of electrons were of two types; electron retardation and electron deflection analysers, both of which use electric fields. Retardation analysers work on the principle that an electron with a certain amount of kinetic energy will be prevented from reaching a detector (eg.an

electron multiplier tube) if subject to a retarding electric field. By varying the strength of the electric field the energy required by the electron to reach the detector can also be varied. By scanning the voltage from high fields (detection of the most energetic electrons) to low fields (detection of low energy electrons) an integral spectrum of electron kinetic energy distribution can be obtained. The electron signal will increase stepwise as the energy thresholds corresponding to the production of an ion in increasingly excited states are reached. The observation of a step function is a result of photoionisation being non state-selective; by lowering the energy required for an electron to be detected (production of an internally excited ion) means that all the more energetic electrons (corresponding to production of ions with less internal excitation) will still be detected. The step-like nature of the spectra obtained through the use of retardation analysers made UV-PES very similar to PIE spectroscopy.[6] The big advantage of PES over PIE was that by using a constant energy photon for ionisation the possibility of autoionising resonances interfering with the signal was greatly reduced.

Deflection analysers exploit the fact that when charged particles are directed into a region of an homogeneous electric field they will be deflected through a certain angle depending upon their initial velocity and mass. For a beam of electrons the deflection angle will be different for the different electron energies. In the analysers commonly used in PES the electron detector was at a constant deflection angle and the electron energies detected were determined by the applied field. By varying the applied field a spectrum of electron peaks could be obtained. Electron deflection analysers thus give a differential signal which is related to the integral signal obtained with PIE spectroscopy.

The study of UV-PES spectra allowed detailed information to be obtained on molecular ions. Not only were ionisation energies determined but the nature of the orbitals from which the electrons were removed was easily determined through analysis of the accompanying vibrational structure. In this way the energy ordering of bonding, anti-bonding and non-bonding orbitals of the neutral molecule could be experimentally determined. The results of UV-PES consolidated the main ideas of

molecular orbital theory and gave values of ionisation energies to compare with calculations of the orbital energies using SCF techniques.

Although UV-PES produced many important results there were two factors which limited what could be achieved with the technique and these were calibration and resolution. These two problems arose from the same source, the measurement of electron kinetic energy through the use of electric fields. Calibration in PES is achieved by using the known ionisation energies of specific gases such as argon. This enables the retarding or deflection voltages applied in each experiment to be equated with the electron kinetic energy. Unfortunately this calibration is susceptible to drift throughout an experiment due to changes in the potentials on the voltage grids caused by the sample gas itself. These difficulties could lead to substantial errors in the determined ionisation energies. Energy resolution in UV-PES was also susceptible to electric field effects. In principle, high resolution can be obtained by ensuring that the electrons entering the analyser were travelling with no off-axis components to their velocity. However, this is often impossible to achieve due to surface potentials in the spectrometer.

The problems with resolution and calibration led researchers to develop other techniques in an attempt to achieve better accuracy and more detailed spectra. Better resolution was desirable because the low frequency vibrations of large polyatomics and the weakly bound states of smaller molecules could not be observed with the resolution available to UV-PES. As well as obtaining more detailed vibrational structure there was a desire to obtain rotationally resolved photoelectron spectra. Rotational structure in photoelectron spectra can give information on the absolute structure of the ion and the angular momentum changes that take place in photoionisation processes thus providing information necessary for the development of theories of photoionisation.

One approach, initiated by Villarejo *et al.*[13] and developed by others [14,15] was a technique which returned to the use of tunable radiation as the excitation source. The difference this time was that the particles detected were electrons produced with zero or near-zero energy; threshold electrons. The technique was called threshold photoelectron spectroscopy (TPES) and is described in detail in the next section.

1.3 Threshold Photoelectron Spectroscopy

As with conventional PES the idea behind threshold photoelecton spectroscopy is very simple. Using tunable radiation molecules are excited through the ionisation thresholds of the ionic states. At each threshold there will be the production of very low energy electrons which can be preferentially detected and the positions of the thresholds marked out as the incident wavelength is scanned. This approach has the benefit of the calibration being provided by a monochromator and not from measurement of the spectra of known atoms with all the associtiated contact potential problems. The light source most commonly used for TPES experiments is that from synchrotron storage rings. Synchrotrons provide high intensity, continuously tunable radiation over a large energy range making them an ideal choice for molecular photoelectron spectroscopy.

The most important aspect of threshold electron spectroscopy is the discrimination against electrons with kinetic energy so that only threshold electrons are detected. A number of methods were developed to achieve this discrimination, the most simple being the "line-of-sight" or steradiancy method,[16] in which photoelectrons are accelerated from the excitation region down a long tube with a small exit aperture at the end. Fast electrons with a significant off-axis velocity component are unlikely to pass through the small aperture at the end to the detector thus allowing for the preferential detection of low energy electrons. However, the "line-of-sight" method does not discriminate against fast electrons whose velocity vector is along the direction of the flight tube. As a result "line-of-sight" analysers often included a deflection type analyser to discriminate against these fast electrons.[17]

One of the most successful analysers in use for the discrimination of fast electrons is the penetrating field spectrometer.[15,18,19] In this case an electric field penetrates into the excitation region and pulls out low energy electrons through a small aperture. The magnitude of the electric field is such that electrons with too much energy will not pass through the aperture. The collection efficiency of this type of spectrometer is very high as threshold electrons distributed over 4π steradians are collected. As with "line-of-sight" analysers, deflection analysers are often used in conjunction with a penetrating field spectrometer to discriminate against fast electrons

with a velocity vector directed towards the aperture.[19] Using this type of analyser, the best resolution that has been achieved to date has been between 16 and 20 cm^{-1}).[20]

The interest in TPES lay not only in the stable calibration and improved resolution but also in the features observed in the spectra that were due to autoionisation processes. Autoionisation effects had been observed in conventional PES in cases where the excitation wavelength coincided with an autoionising resonance. The observed spectra were made up of contributions from direct photoelectron production and from indirect electron production due to autoionisation. A good example of this is the Ne(I) photoelectron spectrum of O_2 in which vibrational structure appears where none would be expected basd on Franck-Condon factors for a transition from the ground state of the neutral molecule.[21] The factors governing the band structure in photoelectron spectra of this type were modelled by Bardsley [22] and Smith.[23] Franck-Condon factors between the initial autoionising state and the final ionic state must be included in order to predict the features caused by indirect electron production.

The contribution of autoionisation to threshold photoelectron spectra is, by the nature of the technique, different to that observed in conventional PES. No single autoionising state is responsible for the intensity effects observed in TPES as the excitation wavelength is not kept constant. Some of the best examples of the effects of autoionisation in TPES are the spectra of I_2, Br_2 and Cl_2.[24] In all of these cases highly excited vibrational levels are observed which have zero Franck-Condon factors for direct excitation from the ground state of the neutral molecule. The mechanism of resonant autoionisation as seen in conventional PES is unlikely to hold in this case as there would need to be exact resonances between the Rydberg states and the vibrationally excited ionic states for the production of detectable threshold electrons. The mechanism which is believed to account for the observed spectra in these and other cases was proposed by Guyon *et al.*[25] and refined by Chupka *et al.*[26] The mechanism involves either direct excitation into a neutral dissociative continuum or to a Rydberg state coupled to a neutral dissociative continuum. The molecule in the continuum state can then autoionise or couple to Rydberg states converging to highly

vibrationally excited states of the ion which can vibrationally autoionise Both of these processes produce threshold electrons and a vibrationally excited ion.

Threshold photoelectron spectroscopy represented a large improvement in terms of calibration and resolution from conventional photoelectrons spectroscopy. However, the increased resolution was still not good enough to obtain rotational structure for the vast majority of molecules as the resolution was limited by the monochromators used. In an effort to get around the monochromator limited resolution pulsed lasers were considered as a possible light source.

1.4 REMPI Spectroscopy and REMPI-PES

One of the most important developments in photoelectron spectroscopy was the use of lasers and multiphoton processes as the route to ionisation. Multiphoton ionisation was first carried out with gas phase atoms in 1965 by Voronov and Delone[27] and was made possible by the use of a high powered ruby laser. Resonance enhanced multiphoton ionisation (REMPI) spectroscopy exploited the ability of lasers to ionise an atom or molecule using more than one photon as a means to investigate excited electronic states. The technique uses the principle that the ionisation signal obtained from a laser multiphoton ionisation process is greatly enhanced if the energy at 1, 2 or 3 times the single photon energy is resonant with an excited state of an atom or molecule. If the ionisation signal is monitored as a function of photon energy then it is possible to map out the excited states. Figure 1-1 shows a schematic of this process with what is termed a (2+1) REMPI scheme. In the example shown in figure 1-1 two photons are needed to reach the excited state and then one further photon (of the same energy) is absorbed, ionising the electronically excited molecule.

The simplest way a REMPI experiment can be performed is to direct a laser into a gas cell containing the molecule of interest. Within the cell, electrodes can monitor the ion current and a spectrum can be obtained by monitoring the signal as the laser wavelength is scanned. Although this approach has the merit of simplicity, it has a few disadvantages. The first is that in a gas cell the molecules are at room temperature and have a Boltzmann distribution of states in the rotational

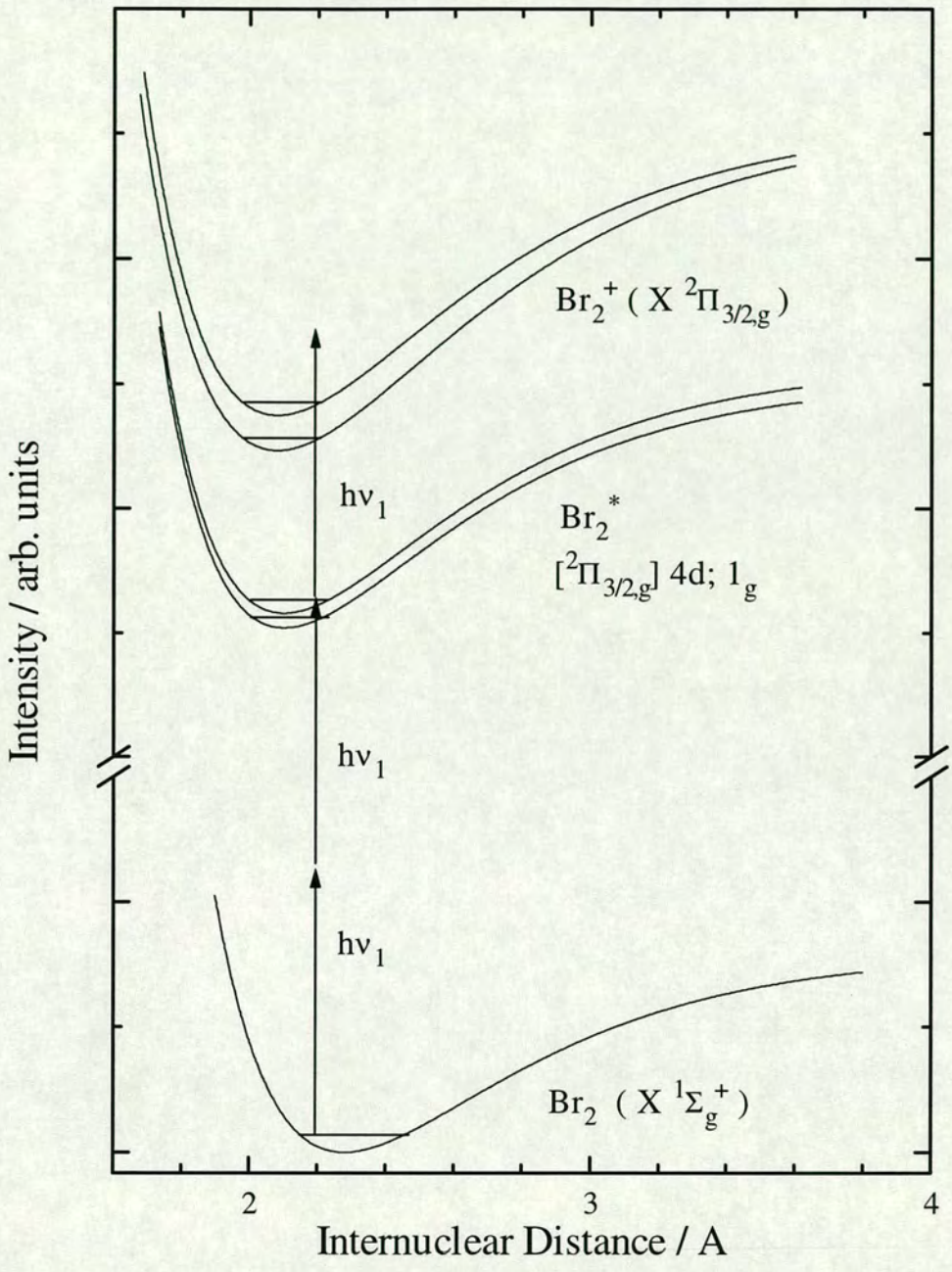

Figure 1-1 - Schematic diagram illustrating a (2+1) REMPI excitation scheme probing the excited Rydberg states of Br_2.

and vibrational degrees of freedom. As a result any REMPI spectra obtained will be complicated by transitions from many initial states. The second disadvantage is that the spectrum is not mass resolved with the result that the ionisation of any species in the gas cell will be detected and may obscure the signal of interest. The solution to these two problems came with the use of supersonic expansions [28] and time-of-flight mass spectrometry [29] in conjunction with REMPI spectroscopy. [30,31]

Supersonic expansions solve the problem of spectral congestion by reducing the number of initially populated states. A supersonic expansion is created when a gas at high pressure (0.5 - 100 atm.) is forced through a small aperture (<0.5 mm) into a region of very low pressure (10^{-5}-10^{-7} mbar). The sample can be pure or seeded in a carrier gas such as helium or argon. The pressure differential between either side of the aperture results in the gas exiting the high pressure region with supersonic speeds (that is, the ratio between the speed of the gas and the local speed of sound is greater than 1). This results in the translational degress of freedom of the sample being cooled to very low temperatures (typically < 1K). The very cold translational temperatures then produce cooling of the rotational and vibrational degrees of freedom, following bimolecular collisions The cooling of the internal degrees of freedom for molecules is a great benefit in spectroscopy where the reduction of initially populated levels reduces the complexity of any spectra recorded.

The degree of internal cooling obtained for any gas expansion is dependent on the expansion conditions such as the pressure of the gas behind the aperture and the diameter of the aperture. The number of binary collisions (and hence the degree of internal cooling) is proportional to the pressure of the gas and the diameter of the aperture. Increasing the pressure of the gas or increasing the diameter of the aperture will therefore increase the amount of rotational and vibrational cooling. However, increasing the aperture diameter will eventually result in the expansion dropping below supersonic speeds and at this point no internal cooling can be achieved. Also, arbitrarily increasing the pressure of the sample is prohibited by the ability of the vacuum pumps to handle the gas flow through the aperture. Pulsed jet expansions were developed to get past the limitation imposed by the capacity of vacuum pumps and to better match the duty cycle of the pulsed lasers that are typically used. The use

of a fast pulsing valve means that the gas only flows for a small fraction of the total time. This drastically reduces the load placed on the vacuum pump and allows far greater backing pressures of the gas to be used, resulting in a greater degree of cooling.

Mass resolved REMPI spectra are obtained by combining REMPI with time-of-flight ion detection. This allows either mass resolved laser excitation spectra or species resolved mass spectra to be obtained.[32] The principle of time-of-flight mass spectrometry is very simple. It relies on the fact that two ions, if accelerated by the same electrostatic field, will have relative flight times that depend solely on the difference in mass between the two ions. This is simply a consequence of Newton's second law. In laser time-of-flight mass spectrometry the ions are produced by either single or multiphoton excitation. An electric field is applied across the ionisation region and the ions are accelerated towards a detector. The ions then pass through a field free drift region where molecules of different mass are separated due to their different velocities on leaving the electric field.

REMPI combined with pulsed jet expansions and time-of-flight detection not only allowed excited states of molecules to be characterised but also provided states through which photoelectron spectra can be obtained. REMPI was developed as the basis of a photoelectron spectroscopy technique by Kimura,[33] Reilly [34] and Compton [35] independantly. The benefits of using resonant intermediate states as the route to ionisation were quite profound. As the excited states of atoms and molecules are unique, using the excited state of a certain molecule as an intermediate produces a photoelectron spectrum solely of that molecule without contributions from any other molecule in the sample. The difficulties that arose from the congestion of photelectron spectra through the prescence of other molecules were circumvented by using this ionisation method. As well as providing species selectivity, the use of intermediate states allowed for studies into photoionisation dynamics from the intermediate state rather than from the ground electronic state.

REMPI-PES uses constant energy photons and energy analysis of the emitted photoelectrons to obtain ionic state spectra in the same manner as conventional PES and has become quite a powerful spectroscopic tool.[36] Rotational resolution has been

achieved for a number of diatomic molecules through the use of intermediate state selection of high rotational levels.[37] However, the development of REMPI-TPES, in which REMPI was applied to threshold photoelectron spectroscopy, overshadowed REMPI-PES as a photoelectron technique. REMPI-TPES became better known as ZEKE photoelectron spectroscopy which in the form of its variant, ZEKE-PFI, has become the dominant high resolution photoelectron technique for the last ten years.

1.5 ZEKE-PFI Spectroscopy

As mentioned, ZEKE spectroscopy started out as a variant of threshold photoelectron spectroscopy. Whereas most TPES experiments had involved either synchrotron or continuum VUV lamps, ZEKE took advantage of the development of pulsed lasers and the use of pulsed molecular beams. With the use of lasers came the possibility of obtaining near optical resolution (<0.1 cm^{-1}) in a photoelectron spectroscopy experiment. Using lasers as a light source was facilitated by the rise of multiphoton excitation routes as a means to ionise a molecule. Multiphoton ionisation had, by the mid-eighties become an established method of producing ions for mass spectrometry and excited state spectroscopy.[38] As well as a new light source with the associated radiation bandwidth benefits, the use of pulsed radiation and sample handling allowed for a simple discrimination against kinetic electrons which was not available with continuous light sources, ie. the use of a time delay before the extraction of the threshold electrons.

The concept of ZEKE photoelectron spectroscopy can be described as follows (a schematic diagram of the process can be seen in figure 1-2). Excitation of a molecule with exactly the right amount of energy to reach an ionic state will produce ions of that state and any ionic states lower in energy. Also produced will be electrons with zero kinetic energy and fast electrons from the production of lower lying ionic states. To preferentially detect the zero kinetic energy electrons (ZEKE electrons), and not the fast electrons, a time delay (approximately 1 μs) is applied during which time the fast electrons should become spatially separated from the ZEKE electrons. By applying a pulsed electric field to collect the electrons and using

the principles of time-of-flight spectroscopy, it can be seen that fast and ZEKE electrons should be separated temporally. By monitoring the correct time-gated signal from the detector it should be possible to record a spectrum of the ionic thresholds by detecting when ZEKE electrons are produced and ignoring electrons with kinetic energy. The removal of the need to measure electron energies opened up the possibility of improving the resolution of photoelectron spectra to a level approaching optical resolution (<0.1 cm^{-1})

The combination of laser excitation and time delay discrimination was first put forward by Müller-Dethlefs *et al.*[39] In this paper they reported the ZEKE photoelectron spectrum of NO recorded *via* a specific rotational level of the $C\,^2\Pi$ Rydberg state in a (3+1′) resonance enhanced multiphoton ionisation (REMPI) scheme. The exact experimental setup involved a time-of-flight stage *and* a steradiancy analsyer to discriminate against fast electrons. Using time delays of around 1 μs they were able to record a fully rotationally resolved photoelectron spectrum of the ground state of NO^+ with a resolution of around 1.2 cm^{-1}. A value for the adiabatic ionisation energy was also obtained of 74717.2 cm^{-1} which differed from the previous ionisation energy as determined from Rydberg extrapolations by 4.3 cm^{-1}.[40] The Müller-Dethlefs group followed this work with another ZEKE study of NO, this time using the $A\,^2\Sigma^+$ state as a resonant intermediate.[41] Further work on benzene [42] and the benzene-Ar van der Waals complex [43] showed that the technique was generally applicable to other molecules and to the study of ionic van der Waals complexes.

Perhaps the most important of all the early developments was the discovery that the majority of the electron signal detected in ZEKE experiments did not actually arise from zero kinetic energy electrons.[44] As mentioned above, there was a discrepancy between the ionisation energy of NO determined by ZEKE with that determined by Rydberg extrapolation. The discrepancy was initially put down to inaccuracies in the Rydberg extrapolations due to the inability to observe the highest members of the Rydberg series. A more accurate Rydberg extrapolation was carried

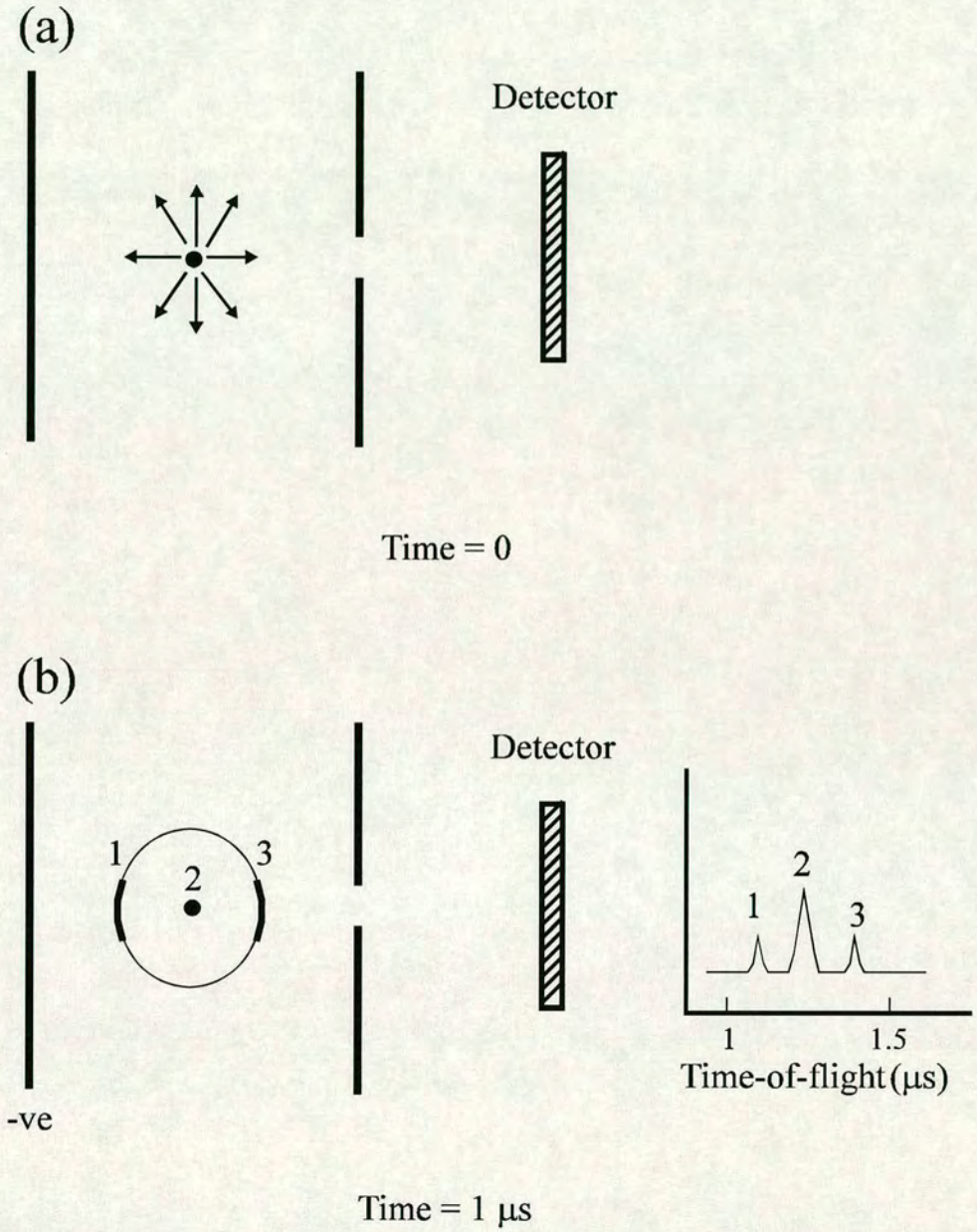

Figure 1-2 - Schematic diagram of ZEKE detection. (a) Time = 0, excitation of the sample with the production of fast and ZEKE electrons. (b) Time = 1 μs, fast electrons have dispersed and the ZEKE electrons remain in the ionisation volume. A negative voltage is applied to one of the voltage grids pushing the electrons to the detector.

out by Biernacki *et al.*[45] after the first ZEKE spectra of NO had been recorded and the ionisation energy was still found to differ from the ZEKE value.

The origin of the discrepancy was found to lie not in the extrapolation but rather in the ZEKE spectrum. The pulsed electric field used to collect the ZEKE electrons was found to also field ionise high lying Rydberg states below the ionisation threshold of NO. These high *n* Rydberg states of NO were thought to have a very short lifetime such that they would not survive the long time delays used in the ZEKE experiments (of the order of microseconds). The field ionisation of these long live high *n* Rydberg states resulted in an apparent lowering of the ionisation energy by an amount proportional to the square root of the extraction field. With the application of an appropriate field correction to account for the field ionisation signal it was seen that the value for the adiabatic ionisation energy determined from the ZEKE spectrum of NO was in fact almost identical to that obtained from accurate Rydberg extrapolations.[44]

The high resolution and general applicability of ZEKE-PFI spectroscopy (as the variant become known) soon led to an explosion of interest in the technique. The resolution of rotational states of the ion offered the first chance for an in depth study of photoionisation dynamics which had only really been investigated in H_2 [46,47,48] and NO.[49,50,51] The realisation that the majority of the signal came from long lived high *n* Rydberg states led to two things. Firstly, the understanding of the field ionisation mechanism allowed the determination of very accurate ionisation energies leading to a general interest in the technique and causing many groups to start using ZEKE-PFI. Secondly, the existence of the high *n* Rydberg states up to tens of microseconds after excitation stimulated the biggest renaissance in Rydberg state spectroscopy that has been seen in recent years.

The molecules studied using the technique in the years following the determination of the field ionisation mechanism ranged from diatomics such as O_2,[52] N_2 and H_2[53] to polyatomics,[54] radicals[55] and molecular complexes.[56,57] However, in the couple of years after 1988 there was also an emphasis on applying the technique in a number of different ways. ZEKE-PFI spectroscopy was applied to monitor

processes such as IVR on the picosecond timescale.[58] Another area which benefitted from the development of ZEKE was anion photoelectron spectroscopy.[59] Anion photoelectron spectroscopy involves the photodetachment of an electron from a negative ion to gain information on the ground and excited states of neutral molecules. As negative ions do not posess Rydberg states the process of anion ZEKE involves the collection of genuine zero kinetic energy electrons and does not involve pulsed field ionisation.[60] This requires careful attention to stray electric and magnetic fields which can have an adverse effect on the true ZEKE signal. Anion ZEKE has also been used to study transition states for reactions.[61]

As was mentioned above, the original ZEKE-PFI experiments used REMPI excitation schemes to reach the high *n* Rydberg states. The intermediate states used in the experiments were characteristically low *n* Rydberg states which have good Franck-Condon overlap with the ionic states of a molecule. This also meant that the photoionisation dynamics were characterised by the nature of the intermediate state rather than by the ground state of the neutral. In an attempt to investigate photoionisation dynamics for transitions from the ground neutral state two different excitation routes were used. The first of these was the use of single photon excitation with VUV and XUV laser systems[53,62] which allowed direct comparisons between the photoionisation dynamics observed in conventional PES with the photoionisation dynamics observed in ZEKE-PFI spectroscopy. Coherent two-photon (C2P) excitation routes also provided the opportunity to compare and contrast the observed photoionisation dynamics.[63]

As well as established techniques being given a boost by ZEKE-PFI spectroscopy a new technique was developed which added another desirable quality to the spectra obtained; mass resolution. As with all photoelectron techniques the information obtained does not have mass resolution, although REMPI excitation can give a certain degree of selectivity. The long lived high *n* Rydberg states populated in ZEKE-PFI gave a possible source of mass resolution in photoelectron spectroscopy. Mass analysed threshold ionisation spectroscopy, devised by P. Johnson at the University of Stoneybrook in 1991,[64] exploited the longevity of the high *n* Rydberg

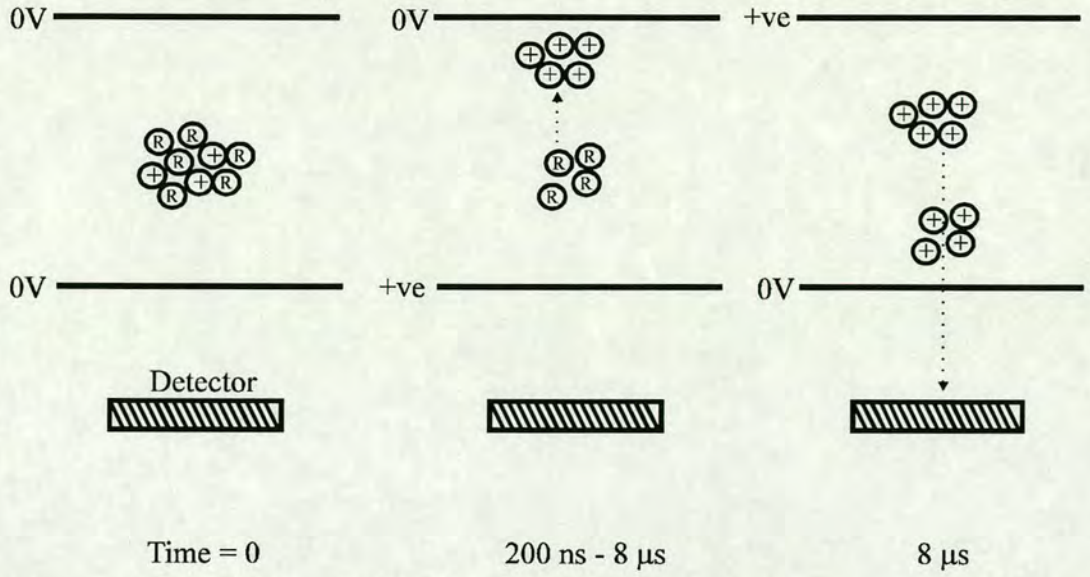

Figure 1-3 - Schematic diagram of the MATI process.

states to achieve mass resolution. The idea behind the technique is shown schematically in figure 1-3. Immediately after the sample interacts with the laser pulse the excitation region will contain prompt ions and a number of molecules in high-*n* Rydberg states. The application of a small discrimination pulse over a few microseconds will separate the prompt ions from the high-*n* Rydberg states. The discrimination pulse will also ionise the highest lying high-*n* Rydberg states. The remaining high-*n* Rydberg states will stay at the point of excitation and after the discrimination pulse a high voltage extraction pulse is used to field ionise the molecules and send them to the detector. The time-of-flight of the prompt and the initially field ionised high-*n* Rydberg states will be different from the second group of high-*n* Rydberg states, allowing a spectrum to be recorded in the same way as a ZEKE-PFI experiment but with the difference that the ions are collected rather than the electrons. The MATI technique tends not to have as high a resolution as ZEKE-PFI spectroscopy although it is still around a few wavenumbers. The technique was applied and further refined by a number of groups.[65]

The success of the MATI technique in the observation of molecular ions from pulsed field ionisation of high-*n* Rydberg states also stimulated efforts towards the production of ions in specific rovibronic states for use in studies of state-specific ion-molecule reactions.[66,67]

The extremely long lifetimes of the high n Rydberg states populated in ZEKE-PFI spectroscopy stimulated interest in Rydberg state spectroscopy. The high n Rydberg states of molecules were expected to have much shorter lifetimes and this led to many studies, both experimental and theoretical, designed to understand the properties of the high n Rydberg states and explain their longevity. There were two mechanisms put forward to explain the unexpected stability of the high n Rydberg states and these were the core-induced stabilization model proposed by R. Levine,[68] and the l and m_l mixing model proposed by W. A. Chupka.[69] The two models are almost diametrically opposed as one relies on intramolecular interactions between the Rydberg electron and the rotating molecular core for stabilisation (Levine's model) and the other requires a complete isolation of the Rydberg state from the molecular core and external interactions for stabilisation (Chupka's model). A large number of experimental studies were carried out to measure the lifetimes of high n Rydberg states [70,71] as well as a number of theoretical studies using the proposed models (core rotation[72,73] and l mixing[74,75,76,77]) to predict the lifetimes and behaviour of the high n Rydberg states.

One of the greatest problems of the rotating core stabilisation approach was that the observed longevity was ubiquitous for atomic [71] and molecular [70] Rydberg states. Gradually results and calculations began to point towards the validity of the l and m_l mixing model. Other experimental results showed just how isolated the high n Rydberg states were from the molecular core, such as the ZEKE-PFI spectrum of the predissociating $A\ ^2\Sigma^+$ state of HBr,[78] which seemed to point towards an external source for stabilisation. The theoretical input of Bixon and Jortner [76,77] to the problem produced some of the most insightful arguments to the debate and provided a framework with which to calculate the lifetimes of Rydberg states undergoing l and m_l mixing. The work which all but decided the matter was an experimental study of the lifetimes of Rydberg states of NO and Xe by Vrakking and Lee.[79] The external mechanism of lifetime lengthening, whereby Rydberg states are subject to l and m_l mixing, was confirmed in this study. The work was followed up by theoretical calculations by Bixon and Jortner,[80] and then by Vrakking [81] in which the lifetime

behaviour of the Rydberg states of NO was calculated and shown to be exactly as observed.

1.6 Outline of Thesis

The research presented in the following chapters focuses on the ZEKE-PFI spectroscopy of halogens and their van der Waals complexes. There are two distinct sections within the overall study. The first section is an investigation into the factors affecting the vibrational intensity distribution in the ZEKE-PFI spectra of I_2, Br_2 and IBr. A number of excitation routes have been used to obtain these ZEKE-PFI spectra including resonant excitation schemes with Rydberg states and valence states as intermediates, and two-photon non-resonant excitation schemes. The second section is a study of I_2-X van der Waals complexes (where X is Ar, Kr and N_2) using REMPI and ZEKE-PFI spectroscopy. This section is concerned mainly with the changes in the van der Waals interaction upon excitation to Rydberg and ionic states.

The structure of the thesis is as follows. Chapter 2 gives a general discussion on background theory concerning electronic transitions and Rydberg states. The discussion in chapter 3 is directed towards the experimental details involved in recording REMPI and ZEKE-PFI spectra. Also included in this chapter is a description of the laser system and spectrometer used to carry out the research discussed in the later chapters. In chapter 4 the ZEKE-PFI spectra of I_2, Br_2 and IBr are presented. This is the first ZEKE-PFI study of Br_2 and IBr. The contribution of autoionisation, accidental resonances and intermediate absorption *via* repulsive states to the observed vibrational intensity distribution in the ZEKE-PFI spectra of these molecules will be discussed. In chapter 5 the REMPI spectra of a number of Rydberg states of I_2-Kr and I_2-N_2 will be presented, as will a reanalysis of certain Rydberg states of I_2-Ar in which there is evidence for the existence of two geometric isomers. The REMPI spectrum of I_2-N_2 has also been shown to provide evidence for the existence of two isomers. The ZEKE-PFI spectra of I_2-Ar and I_2-Kr recorded using Rydberg states as intermediates are also presented in chapter 5. Due to the distinct nature of the areas studied, the conclusions and implications of the work will be given at the end of each chapter.

1.7 References

[1] G. Reiser, W. Habenicht, K. Müller-Dethlefs, E. W. Schlag, *Chem.Phys.Lett.* 1988, **152**, 119.

[2] W. Wein, *Ann.de Phys.* 1922, **69**, 325; *ibid.* 1926, **81**, 994.

[3] T. Koopman, *Physica* 1934, **1**, 104.

[4] D. R. Hartree, *Proc. Cambridge Phil.Soc.* 1928, **24**, 111; V. Fock, *Z.Physik* 1930, **54**, 347.

[5] G. L. Weissler, 'Handbuch der Physik' Ed. Flugge, Springer-Verlag, Berlin, 1956, **21**, 3044.

[6] K. Watanabe, *J.Chem.Phys.* 1959, **26**, 542.

[7] W. A. Chupka, M. E. Russel, *J.Chem.Phys.* 1968, **48**, 1527.

[8] Y. Ono, S. H. Linn, H. F. Prest, C. Y. Ng, E. Miescher, *J.Chem.Phys.* 1980, **73**, 4855.

[9] W. A. Chupka, J. Berkowitz, *J.Chem.Phys.* 1969, **51**, 4244.

[10] W. B. Peatman, B. Gotchev, P. Guertler, V. Seile, E. E. Koch, *J.Chem.Phys.* 1978, **69**, 2089.

[11] D. W. Turner, M. I. Al-Joubery, *J.Chem.Phys.* 1962, **37**, 3007.

[12] F. I. Vilesov, B. L. Kurbatov, A. N. Terenin, *Sov.Phys.Dokl.* 1961, **6**, 883.

[13] D. Villarejo, R. R. Herm, M. G. Inghram, *J.Chem.Phys.* 1967, **46**, 4995; D. Villarejo, R. Stockbauer, M. G. Inghram, *J.Chem.Phys.* **48**, 3342.

[14] T. Baer, B. P. Tsai, *J.Electron Spectrosc.Relat.Phenom.* 1973, **2**, 25.

[15] G. C. King, M. Zubek, P. M. Rutter, F. H. Read, *J.Phys.E.* 1987, **20**, 441.

[16] T. Baer, W. B. Peatman, E. W. Schlag, *Chem.Phys.Lett.* 1969, **4**, 243; W. B. Peatman, T. B. Borne, E. W. Schlag, *Chem.Phys.Lett.* 1969, **3**, 492.

[17] R. Stockbauer, *J.Chem.Phys.* 1973, **58**, 3800.

[18] S. Cvejanovic, F. H. Read, *J.Phys.B.* 1974, **7**, 1180.

[19] R. I. Hall, A. G. McConkey, K. Ellis, G. Dawber, L. Avaldi, M. A. MacDonald, G. C. King, *Meas.Sci.Tech.* 1992, **3**, 316.

[20] A. J. Cormack, *private communication.*

[21] J. A. Kinsinger, J. W. Taylor, *Int.J.Mass Spectrom.Ion.Proc.* 1973, **11**, 461.

[22] J. N. Bardsley, *Chem.Phys.Lett.* 1968, **2**, 329.

[23] A. L. Smith, *Phil.Trans.R. Soc.Lond.* A, 1970, **268**, 169.

[24] A. J. Yencha, M. C. R. Cockett, J. G. Goode, R. J. Donovan, A. Hopkirk, G. C. King, *Chem.Phys.Lett.* 1994, **229**, 347; A. J. Yencha, A. Hopkirk, A. Hiraya, R. J. Donovan, J. G. Goode, R. R. Maier, G. C. King, A. Kvaran, *J.Phys.Chem.* 1995, **99**, 7231.

[25] P. M. Guyon, T. Baer, I. Nenner, *J.Chem.Phys.* 1983, **78**, 3665.

[26] W. A. Chupka, P. J. Miller, E. E. Eyler, *J.Chem.Phys.* 1988, **88**, 3032.

[27] G. S. Veronov, N. B. Delone, *JETP Lett.* 1965, **1**, 66.

[28] R. E. Smalley, L. Wharton, D. H. Levy, *J.Chem.Phys.* 1975, **63**, 4977.

[29] W. C. Wiley, I. H. McLaren, *Rev.Sci.Instrum.* 1955, **26**, 1150.

[30] R. B. Bernstein, *J.Chem.Phys.* 1982, **86**, 1178.

[31] E. W. Schlag, H. J. Neusser, *Acc.Chem.Res.* 1983, **16**, 355.

[32] U. Boesl, R. Weinkauf, C. Weickhardt, E. W. Schlag, *Int.J.Mass.Spectrom.Ion.Proc.* 1994, **131**, 87.

[33] Y. Achiba, K. Shobatake, K. Kimura, Annual Review, Institute for Molecular Science, Okazaki, 1980, 100; K. Kimura, *Adv.Chem.Phys.* 1985, **60**, 161.

[34] J. T. Meek, R. K. Jones, J. P. Reilly, *J.Chem.Phys.* 1980, **73**, 3503.

[35] R. N. Compton, J. C. Miller, A. E. Carter, P. Kruit, *Chem.Phys.Lett.* 1980, **71**, 87.

[36] C. A. de Lange, 'High Resolution Laser Photoionisation and Photoelectron Studies' Eds. I. Powis *et al.* 1995, Wiley, Chichester, 195.

[37] E. de Beer, M. Born, C. A. de Lange, N. P. C. Westwood, *Chem.Phys.Lett.* 1991, **186**, 40; E. de Beer, M. P. Koopmans, C. A. de Lange, Y. Wang, W. A. Chupka, *J.Chem.Phys.* 1991, **94**, 7634.

[38] S. H. Lin, Y. Fujimura, H. J. Neusser, E. W. Schlag, 'Multiphoton Spectroscopy of Molecules', Academic Press, Orlando, 1984.

[39] K. Müller-Dethlefs, M. Sander, E. W. Schlag, *Z.Naturforsch.* Teil A, 1984, **39**, 1089.

[40] E. Miescher, *Can.J.Phys.* 1976, **54**, 2074.

[41] M. Sander, L. A. Chewter, K. Müller-Dethlefs, E. W. Schlag, *Phys.Rev.A.* 1987, **36**, 4543.

[42] L. A. Chewter, M. Sander, K. Müller-Dethlefs, E. W. Schlag, *J.Chem.Phys.* 1987, **86**, 4737.

[43] L. A. Chewter, K. Müller-Dethlefs, E. W. Schlag, *Chem.Phys.Lett.* 1987, **135**, 219.

[44] G. Reiser, W. Habenicht, R. Baumann, K. Müller-Dethlefs, E. W. Schlag, *Chem.Phys.Lett.* 1988, **92**, 414.

[45] D. Th. Biernacki, S. D. Colson, E. E. Eyler, *J.Chem.Phys.* 1988, **88**, 2099.

[46] L. Åsbrink, *Chem.Phys.Lett.* 1970, **7**, 549.

[47] J. E. Pollard, D. J. Trevor, J. E. Reutt, Y. T. Lee, D. A. Shirley, *J.Chem.Phys.* 1982, **77**, 34.

[48] S. T. Pratt, P. M. Dehmer, J. L. Dehmer, *J.Chem.Phys.* 1983, **78**, 4315.

[49] W. G. Wilson, K. S. Viswanathan, E. Sekreta, J. P. Reilly, *J.Phys.Chem.* 1984, **88**, 672.

[50] K. S. Viswanathan, E. Sekreta, E. R. Davidson, J. P. Reilly, *J.Chem.Phys.* 1986, **90**, 5078.

[51] S.W. Allendorf, D. J. Leahy, D. C. Jacobs, R. N. Zare, *J.Chem.Phys.* 1989, **91**, 2216.

[52] R. G. Tonkyn, J. W. Winniczek, M. G. White, *Chem.Phys.Lett.* 1989, **164**, 137; M. Braunstein, V. McKoy, S. N. Dixit, R. G. Tonkyn, M. G. White, *J.Chem.Phys.* 1990, **93**, 5345.

[53] H. H. Fielding, T. P. Softley, F. Merkt, *Chem.Phys.* 1991, **155**, 257.

[54] R. T. Weidmann, E. R. Grant, R. G. Tonkyn, M. G. White, *J.Chem.Phys.* 1991, **95**, 746; *ibid.* 1991, **95**, 7033.

[55] G. C. Eiden, J. C. Weisshar, *J.Phys.Chem.* 1991, **95**, 6194; G. C. Eiden, F. Weinhold, J. C. Weisshar, *J.Chem.Phys.* 1991, **95**, 8665.

[56] G. Reiser, O. Dopfer, R. Lindner, G. Henri, K. Müller-Dethlefs, E. W. Schlag, S. D. Colson, *Chem.Phys.Lett.* 1991, **181**, 1.

[57] M. Takahashi, *J.Chem.Phys.* 1992, **96**, 2594.

[58] J. M. Smith, C. Lakshminarayan, J. L. Knee, *J.Chem.Phys.* 1990, **93**, 4475.

[59] M. W. Siegel, R. J. Celotta, J. L. Hall, J. Levine, R. A. Bennett, *Phys.Rev.A* 1972, **6**, 607; H. B. Ellis,Jnr, G. B. Ellison, *J.Chem.Phys.* 1983, **78**, 6541.

[60] T. N. Kitsopoulos, I. M. Waller, J. G. Loeser, D. M. Neumark, *Chem.Phys.Lett.* 1989, **159**, 300.

[61] I. M. Waller, T. N. Kitsopoulos, D. M. Neumark, *J.Phys.Chem.* 1990, **94**, 2240.

[62] R. G. Tonkyn, M. G. White, *Rev.Sci.Instrum.* 1989, **60**, 125.

[63] A. Strobel, I. Fischer, J. Staecker, G. Niedner-Schatteburg, K. Müller-Dethlefs, V. E. Bondybey, *J.Chem.Phys.* 1992, **97**, 2332; I. Fischer, A. Loeschmidt, A. Strobel, G. Niedner-Schatteburg, K. Müller-Dethlefs, V. E. Bondybey, *J.Chem.Phys.* 1993, **98**, 3592; G. Reiser, W. Habenicht, K. Müller-Dethlefs, *J.Chem.Phys.* 1993, **98**, 8462.

[64] L. Zhu, P. Johnson, *J.Chem.Phys.* 1991, **94**, 5769; P. M. Johnson, L. Zhu, *Int.J.Mass Spectrom.Ion Proc.* 1994, **131**, 193

[65] H.-J. Dietrich, R. Lindner, K. Müller-Dethlefs, *J.Chem.Phys.* 1994, **101**, 3399

[66] Y. Wang, W. A. Chupka, *Chem.Phys.Lett.* 1992, **200**, 192.

[67] F. Merkt, S. R. MacKenzie, T. P. Softley, *J.Chem.Phys.* 1993, **99**, 3400.

[68] D. Bahatt, U. Even, R. D. Levine, *J.Chem.Phys.* 1993, **98**, 1744.

[69] W. A. Chupka, *J.Chem.Phys.* 1993, **98**, 4520; *ibid.* 1993, **99**, 5800.

[70] U. Even, R. D. Levine, R. Bersohn, *J.Phys.Chem.* 1994, **98**, 3472.

[71] A. Muhlpfordt, U. Even, *J.Chem.Phys.* 1995, **103**, 4427.

[72] E. Rabani, L. Ya. Baranov, R. D. Levine, U. Even, *Chem.Phys.Lett.* 1994, **221**, 473.

[73] E. Rabani, R. D. Levine, U. Even, *J.Phys.Chem.* 1994, **98**, 8834.

[74] C. Bordas, P. F. Brevet, M. Broyer, J. Chevaleyre, P. Labastie, J. P. Perrot, *Phys.Rev.Lett.* 1988, **60**, 917.

[75] F. Merkt, R. N. Zare, *J. Chem.Phys.* 1994, **101**, 3495.

[76] J. Jortner, M. Bixon, *J.Chem.Phys.* 1995, **102**, 5636.

[77] M. Bixon, J. Jortner, *J.Chem.Phys.* 1995, **103**, 4431.

[78] A. Mank, T. Nguyen, J. D. D. Martin, J. W. Hepburn, *Phys.Rev.A.* 1995, **51**, R1.

[79] M. J. J. Vrakking, Y. T. Lee, *Phys.Rev.A.* 1995, **51**, R894; M. J. J. Vrakking, Y. T. Lee, *J.Chem.Phys.* 1995, **102**, 8818; *ibid.* 1995, **102**, 8833.

[80] M. Bixon, J. Jortner, *J.Chem.Phys.* 1996, **105**, 1363.

[81] M. J. J. Vrakking, *J.Chem.Phys.* 1996, **105**, 7336.

2. Background Theory

2.1 Electronic Transitions

2.1.1 Diatomic molecular term symbols

The term symbols for diatomic molecules are derived from considerations of the angular momentum of the molecule and the symmetry properties of the electronic wavefunction. In diatomic molecules there are four sources of angular momentum, the orbital and spin angular momentum of the electrons and the nuclear spin and nuclear framework rotational angular momentum. The angular momenta couple in a variety of ways depending on the molecule and electronic state in question. The limiting cases that describe the coupling observed in most diatomics were defined by Hund and labelled Hund's coupling cases, of which there are five; (a) through to (e). A brief description of each coupling case will now be given followed by a discussion of the labelling of states due to the symmetry of the electronic wavefunction. Details of the term symbols for the electronic states investigated using REMPI and ZEKE-PFI spectroscopy in the following chapters will also be given.

A diagram of the vector addition of the angular momenta in each of the coupling cases can be seen in figure 2-1. The most common coupling case is Hund's case (a). The orbital angular momentum ($\boldsymbol{L}$) of the electrons is coupled to the internuclear axis by the Coulomb force caused by the diatomic nuclear framework. The fast precession of $\boldsymbol{L}$ around the internuclear axis results in $\boldsymbol{L}$ no longer being a good quantum number although the projection of $\boldsymbol{L}$ onto the axis, Λ, (in units of $h/2\pi$) which is a good quantum number. Due to spin-orbit coupling the spin angular momentum of the electrons ($\boldsymbol{S}$) is also coupled to the internuclear axis through its coupling to $\boldsymbol{L}$. The spin also has a projection along the axis of magnitude Σ (in units of $h/2\pi$). The resultant of the electronic angular momentum along the axis ($\Omega = |\Lambda + \Sigma|$) can couple to $\boldsymbol{R}$, the nuclear framework rotation angular momentum, to give a

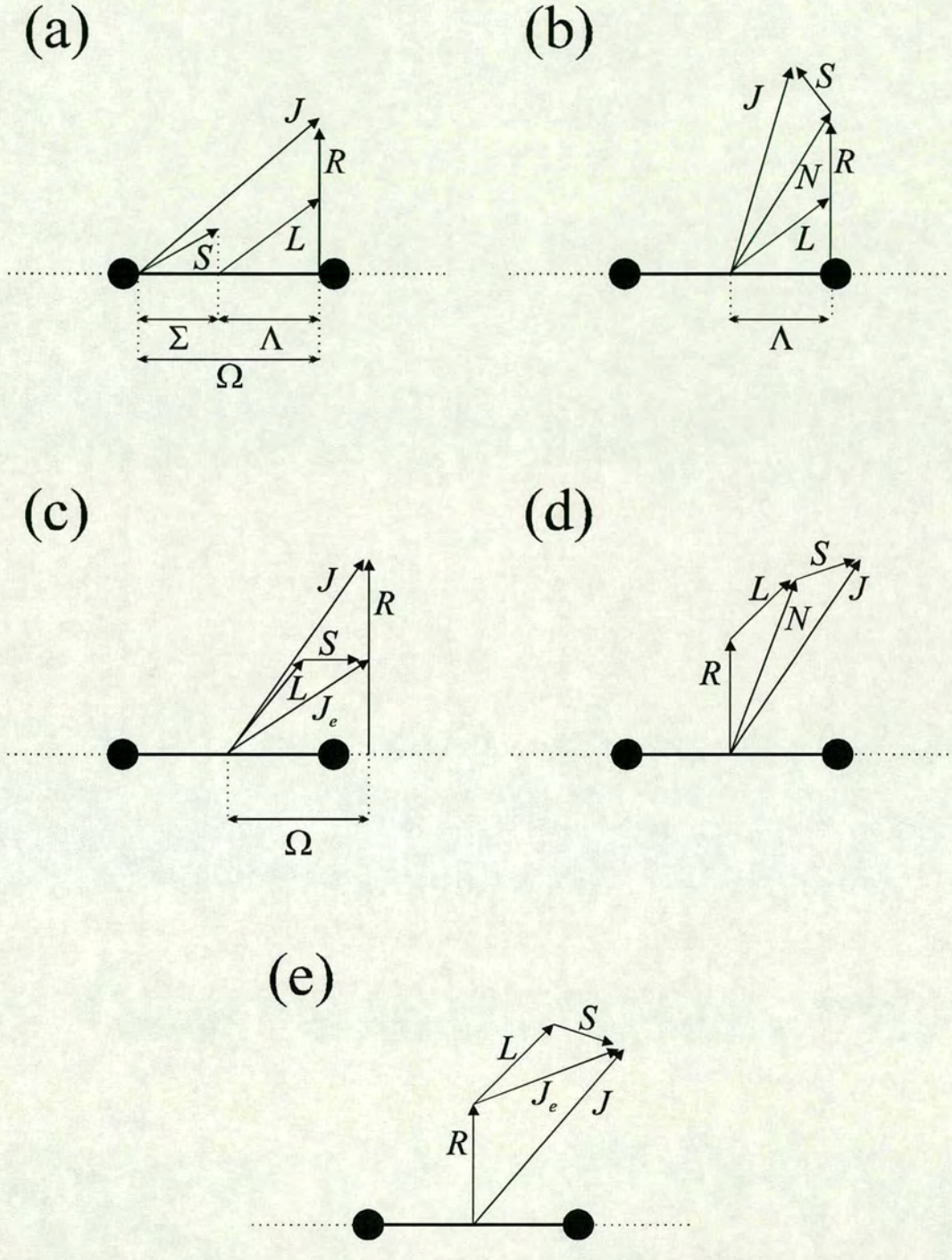

Figure 2-1 - Hund's coupling cases (a) through to (e)

resultant $\boldsymbol{J}$, the total angular momentum. Term symbols for electronic states arising from this coupling case normally only express the values of Λ, $\boldsymbol{S}$ and Ω which are set down in the following way, ${}^{(2S+1)}\Lambda_{\Omega}$, with values of Λ being denoted using the upper case greek letters used in the labelling of atomic electronic states (ie. Σ, Π, Δ etc.)

In the situation where the spin-orbit coupling is very weak the spin angular momentum will not be coupled to the internuclear axis along with the orbital angular momentum. This is the coupling case that is labelled Hund's case (b). In this case $\boldsymbol{L}$ is still coupled to the internuclear axis with the resultant projection along the axis, Λ. The projection of the orbital angular momentum is coupled to the nuclear framework rotation ($\boldsymbol{R}$) to give a resultant , $\boldsymbol{N}$. The spin can then couple to this resultant to give the total angular momentum, $\boldsymbol{J}$. In this case Ω is no longer a good quantum number whereas Λ is. Electronic states that are subject to this coupling are therefore labelled ${}^{(2S+1)}\Lambda$. Hund's case (b) also occurs when $\Lambda = 0$ and $\boldsymbol{S} \neq 0$ with the result that $\boldsymbol{R} = \boldsymbol{N}$ and $\boldsymbol{N}$ couples to $\boldsymbol{S}$ to give the total angular momentum $\boldsymbol{J}$.

The opposite situation to Hund's case (b) where the spin-orbit coupling is very strong results in another coupling case; Hund's case (c). The spin and orbital angular momentum ($\boldsymbol{L}$ and $\boldsymbol{S}$) couple independantly of the internuclear axis to give a resultant electronic angular momentum, $\boldsymbol{J}_e$. The total electronic angular momentum then couples to the axis which results in a projection, $\Omega(h/2\pi)$, along the axis. The projection, Ω, then couples with $\boldsymbol{R}$ to give the total angular momentum $\boldsymbol{J}$. In this case only Ω, rather than Λ, is a good quantum number and states are labelled with the value of Ω. However, in most cases states are also labelled with the value of Λ in order to indicate the magnitude of the orbital angular momentum.

The three coupling cases described so far have all involved some form of coupling of the electronic angular momentum to the nuclear framework. Hund's case (d) represents the situation where this is not the case and the electronic angular momentum does not precess around the internuclear axis. The result of this is that $\boldsymbol{L}$ is still a good quantum number which can then couple with $\boldsymbol{R}$, the molecular rotational angular momentum, to give a resultant $\boldsymbol{N}$. The spin angular momentum, $\boldsymbol{S}$, couples to $\boldsymbol{N}$ to give the total angular momentum, $\boldsymbol{J}$. Examples of this coupling case are

Rydberg states where the electron is remote from the molecular core and as a result does not feel the effect of the Coulombic force along the molecular axis.

The final example of coupling is Hund's case (e). This coupling case was very rarely used to describe electronic states as there were, until recently, very few examples of states of scientific interest which coupled in this way. In recent years the interest in high n Rydberg states, which can best be described using Hund's case (e), has provided a great number of cases which couple in this way. In essence Hund's case (e) is a hybrid between Hund's cases (c) and (d). As in case (c) the spin-orbit interaction is strong enough to couple $\boldsymbol{L}$ and $\boldsymbol{S}$ to give the total electronic angular momentum, $\boldsymbol{J}_e$. However, at this point the coupling becomes more like that of case (d) where the electronic angular momentum does not couple at all to the nuclear framework but does couple to the rotational angular momentum, $\boldsymbol{R}$, to give a total angular momentum, $\boldsymbol{J}$.

The end result of considering the coupling cases is to produce an electronic term symbol using the quantum numbers that can be considered as good within the appropriate coupling case for that state. As mentioned above, the term symbol of the electronic state also involves the symmetry of the electronic wavefunction. The symmetry elements used for diatomic molecule electronic wavefunctions are planes of symmetry (through the nuclear axis) and a point of inversion (eg. if the molecule is a homonuclear diatomic).

If an electronic wavefunction is unchanged (i.e. symmetric) when reflected in a plane of symmetry passing through the internuclear axis, the state is labelled with a '+'. If it is changed (i.e. antisymmetric) it is labelled with a '−'. It is in non-degenerate states that this labelling is used most often (i.e. Σ states) as the state will be either one or the other (i.e. + or −) whereas in degenerate states (Π and Δ states) there are both '+' and '−' states that have the same energy and thus the labelling is redundant. The symmetry symbol for an electronic state whose electronic wavefunction is symmetric (antisymmetric) with respect to inversion through the middle of the bond axis is 'g' ('u') meaning *gerade* (*ungerade).* This operation only applies to homonuclear diatomics.

The notation used for the Rydberg states of I_2, Br_2, IBr and the I_2-X van der Waals complexes can be described as follows: $[^{2S+1}\Lambda_\Omega]_c\ nl\ ;\ \Omega$, where the term within the square brackets describes the spin, orbital and total angular momentum of the core according to Hund's case (a) and the term outside the square brackets indicates the principle quantum number (n) and angular momentum (l) of the Rydberg electron as well as the Hund's case (c) description of the molecule (Ω). The same notation is used for the diatomic halogens and the I_2-X complexes, as formation of a van der Waals complex is generally considered to have little effect on the electronic character of the halogen molecule.

A brief word of explanation is due at this point regarding the assignment of the *gerade* Rydberg states of I_2 and Br_2 used as intermediates in the ZEKE-PFI studies. Previously, all such states reached by two-photon excitation in I_2 and Br_2 had been assigned to Ω - components of the s-series.[1,2] In the case of the lowest member of this series, the 6s in I_2 and the 5s in Br_2, the assignment remains valid. However, polarisation studies on Br_2, coupled with band contour analysis have revealed that all the higher lying states should be reassigned to nd ($\Omega = 0,2$) states. The detailed evidence for this reassignment will be published in a forthcoming paper.[3] These observations have direct relevance to I_2 as exactly the same pattern of Rydberg states and polarisation behaviour is seen in Br_2 and I_2. We have therefore reassigned levels previously labelled ns ($n > 6$) in I_2 to (n - 2)d states with $\Omega = 0,2$ for each spin orbit core state. The energy ordering of the two Ω components is also taken from the work on Br_2,[3] where the $\Omega = 2$ component always lies lower in energy. The reassignment also applies to our work on the I_2-Ar van der Waals complex.[4]

2.1.2 Electric dipole transition selection rules

The term symbols derived for electronic states allow us to express selection rules for electronic transitions caused by absorption or emission of photons. These are termed electric dipole selection rules as the transitions involve the electric vector of the emitted or absorbed radiation. The selection rules that hold for single photon

processes will now be listed followed by a description of the selection rules for two-photon processes.

In single photon processes there are selection rules that hold generally and those that only apply to certain coupling cases. The general selection rules are as follows:

$\Delta J = 0, \pm 1$ (except $J = 0 \leftrightarrow J = 0$ transitions are not allowed)

$+ \leftrightarrow -$ and $- \leftrightarrow +$ (but not $+ \leftrightarrow +$ or $- \leftrightarrow -$)

$g \leftrightarrow u$ and $u \leftrightarrow g$ (but not $g \leftrightarrow g$ or $u \leftrightarrow u$).

Within the individual coupling cases only the quantum numbers which remain defined obey selection rules and these are as follows:

$\Delta\Lambda = 0, \pm 1$ (i.e. $\Sigma \leftrightarrow \Sigma$ and $\Pi \leftrightarrow \Sigma$ but not $\Sigma \leftrightarrow \Delta$) which applies for Hund's case (a) and (b)

$\Delta S = 0$ (i.e. singlet $\leftrightarrow$ triplet transitions are forbidden) which applies for Hund's case (a) and (b)

$\Delta\Sigma = 0$ (both states case (a)) and

$\Delta\Omega = 0, \pm 1$ (both states case (c)).

The selection rules governing changes in angular momentum and the symmetry of the electronic wavefunction for two-photon transitions are also well known and they are:

$\Delta J = 0, \pm 1, \pm 2$ ($J = 0 \leftrightarrow J = 0$ transitions *are* allowed)

$+ \leftrightarrow +$ and $- \leftrightarrow -$, $+ \leftrightarrow -$ and $- \leftrightarrow +$

$g \leftrightarrow g$ and $u \leftrightarrow u$ (but not $g \leftrightarrow u$ or $u \leftrightarrow g$)

with the following rules holding within specific coupling cases (for the coupling cases that correspond to each selection rule see above),

$$\Delta\Lambda = 0, \pm1, \pm2 \text{ (i.e. } \Sigma \leftrightarrow \Sigma, \Sigma \leftrightarrow \Delta \text{ and } \Pi \leftrightarrow \Sigma)$$

$$\Delta S = 0 \text{ (i.e. singlet} \leftrightarrow \text{triplet transitions are forbidden)}$$

$$\Delta\Sigma = 0 \text{ and } \Delta\Omega = 0, \pm1, \pm2.$$

Selection rules give an indication of how strong a transition will be, or to put it another way, how large the cross section for photon absorption will be for a given transition. As well as having different selection rules from one-photon transitions (and therefore different cross sections for photon absorption) two-photon processes are strongly influenced by the polarisation of the absorbed or emitted light.[5] Bray and Hochstrasser [6] determined that for rotating diatomic molecules the cross section for two-photon absorption increases when using circularly polarised light as opposed to linearly polarised light. The exact ratio is around 3/2 for circular/linear. The enhancement with the use of circularly polarised light is dependent on the actual transition involved. In transitions where $\Delta\Omega = 0, \pm1, \pm2$ all rotational branches of the transition between two electronic states are enhanced except the Q branch of a $\Delta\Omega = 0$ transition. In this case the transition is suppressed by using circularly polaised light with a ratio between 0 and 1/4 for circular/linear.

Polarisation studies can prove useful in the assignment of electronic states in two-photon absorption experiments. A good example of this is the recent reassignment of the *gerade* Rydberg states of molecular bromine.[3]

2.1.3 Photoionisation

The photoionisation process is not subject to as many strict selection rules as electronic transitions between neutral states. Due to the nature of the process (the emission of an electron) any electronic state that lies lower in energy than the excitation energy can be excited with the balance of energy being carried away by the photoelectron. The electronic angular momentum change in the molecule, accompanying any photoionisation, can also be accomodated by the emission of a photoelectron with a corresponding amount of angular momentum. As with all electronic transitions, the vibrational transitions that occur in photionisation are

governed in the main by Franck-Condon factors which are discussed in the following section.

2.1.4 Franck-Condon principle

In electronic transitions there is no strict selection rule governing the change of vibrational quantum number (c.f. the $\Delta v = \pm 1$ selection rule for transitions within the same electronic state). The result is that a distribution of vibrational levels is populated in the final state. The relative intensities of peaks in a distribution are determined by the Franck-Condon factors for the transitions between the initial vibrational level, v″, and the final vibrational levels, v′.

Franck-Condon factors arise from the Franck-Condon principle which was developed by J. Franck on a classical basis and further developed on a wave-mechanical basis by E. U. Condon. The Franck-Condon principle states that an electronic transition occurs on such a fast timescale relative to the motion of the nuclei that the nuclei remain effectively stationary during the process. This is also a statement of the Born-Oppenheimer separation of the molecular wavefunction, where the internuclear separation is fixed for the electronic wavefunction. The transition dipole moment (μ_{if}) for an electronic transition between two vibronic levels can be calculated from the following expression:

$$\mu_{if} = M_e \int \psi_{vib'}^* \psi_{vib''} \, dR \qquad (2.1)$$

where M_e is the electronic transition moment (outside the integral if it is assumed to be independant of R, the internuclear separation) and $\psi_{vib'}$ and $\psi_{vib''}$ are the vibrational wavefunctions of the initial and final states. As the intensity of a transition is proportional to the square of the transition moment it can be seen that the relative intensity for transitions from an initial v″ to some final vibrational levels will be proportional to the square of the second term in the above equation (given that M_e is non-zero), i.e.

$$\left| \int \psi_{vib'}^* \psi_{vib''} \, dR \right|^2 = \left| \langle v' | v'' \rangle \right|^2. \qquad (2.2)$$

This square of the vibrational overlap integral is called the Franck-Condon factor for the transition.

The influence of the Franck-Condon factors on the vibrational intensity distribution observed in an electronic transition is illustrated in figure 2-2. The figure is split into three sections (a), (b) and (c). In each section there are two diatomic potential curves representing the initial and final electronic states. The initial state wavefunction is also shown on each initial state potential. Due to the Franck-Condon principle the initial state wavefunction defines a 'window' for the transitions to the final state with the result that the most intense transitions will be those that have the greatest overlap between the initial state wavefunction. In this case the initial state is $v'' = 0$ and the single lobe of the wavefunction defines the 'window' of maximum overlap with the vibrational levels of the final state.

In figure 2-2 (a) the potential curves have very similar equilibrium separations. The vibrational wavefunction that has the greatest overlap with the initial state wavefunction is $v' = 0$ which represents a change in vibrational state of $\Delta v = 0$. The distribution of populated vibrational levels in the final state is dominated by this transition. The same behaviour would be observed were the initial state to be $v'' = 2$, with the most intense transition being to $v' = 2$. The $\Delta v = 0$ transition is sometimes referred to as the diagonal transition using the terminology of matrix mechanics. In Figure 2-2 (b) the final state potential is less strongly bound than the initial state resulting in the 'window' of greatest overlap from the initial state wavefunction projecting onto the inner lobes of some excited vibrational states. As a result we see a wide distribution of populated vibrational levels in the final state with the maximum of the distribution being an excited vibrational level. In part (c) of figure 2-2 we see the opposite situation to part (b). In this case the final electronic state is more strongly bonding than the initial state. The 'window' of greatest overlap from the initial state wavefunction projects onto the outer lobes of more highly excited vibrational wavefunctions than the $\Delta v = 0$ transition. In this case the intensity distribution of populated vibrational states is narrower than in (b).

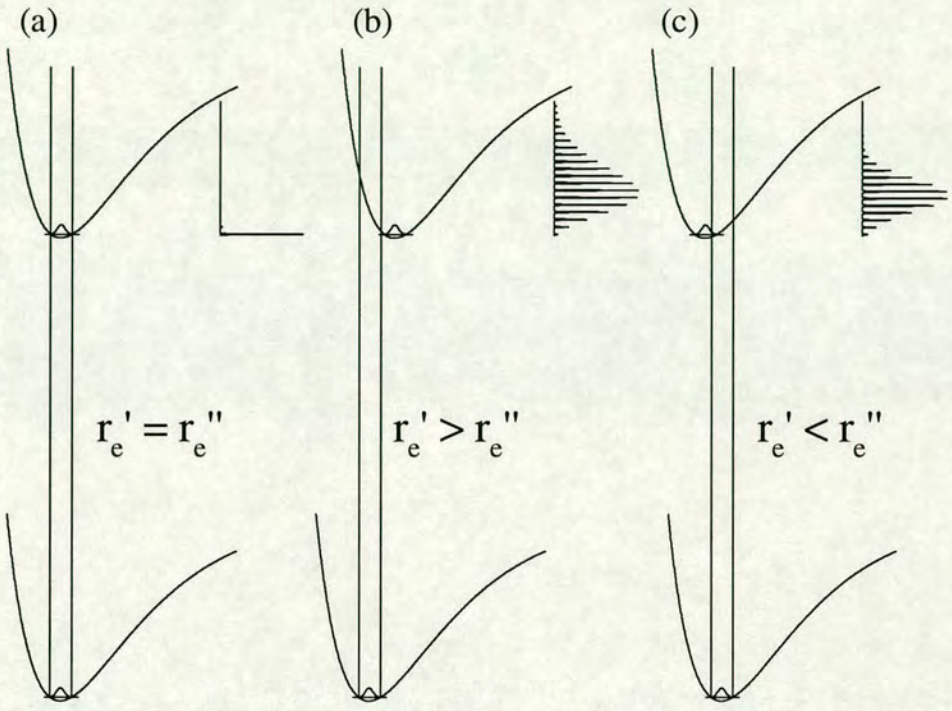

Figure 2-2 - Schematic diagram of the influence of Franck-Condon factors on the observed vibrational intensity distribution seen in an electronic transition. The black lines at each side of the initial state wavefunction define the Franck-Condon windows for excitation. The spectra at the side of each final state potential represent the vibrational intensity distribution for each electronic transition.

A smaller number of vibrational state wavefunctions of the final state have good overlap with the initial state wavefunction due to the 'window' of overlap projecting onto the more shallow gradient of the outer limb of the final state potential.

Perhaps one of the most important uses of Franck-Condon factors is in the simulation of observed vibrational intensity distributions. Assuming appropriate functional forms for the initial and final state potentials, the intensity distribution can be simulated by varying parameters such as the change in equilibrium separation between the initial and final states. This allows bond length changes to be deduced from vibrationally resolved electronic spectra.

2.2 Rydberg States

2.2.1 Nature of a Rydberg state

Rydberg states have been at the heart of spectroscopy and quantum theory since the observation of the Balmer series of spectral lines of atomic hydrogen. They are defined as electronically excited states of atoms or molecules that have an electron in an orbital with a value of n, the principal quantum number, greater than the value of n in the valence shell. Unless otherwise stated, the discussion in this section will be concerned with molecular Rydberg states.

Rydberg states form series of constant l (angular momentum quantum number) but increasing n. With increasing n the Rydberg electron gains more energy and increases its orbital radius. The expectation value for the radius of a Rydberg orbital scales as n^2 with the result that with just a small increase in n the orbital radius can become very large. The large orbital radius of a Rydberg state results in it having very different properties to a valence state. They are much more polarisable and are far more sensitive to external fields and the presence of other atoms and molecules.

The Rydberg series converge to the ionisation limits of a molecule as n continues to increase. Also, as the core can be excited independantly of the Rydberg electron, there is a Rydberg series that converges onto every ionic state of a molecule be it rotational, vibrational or electronic. The general formula which can predict the energy of states in a Rydberg series (as stated in Chapter 1, equation 1.2):

$$E(nl) = IE - \frac{R_y}{(n-\delta_{nl})^2}$$

where IE is the ionisation limit to which the series converges, R_y is the Rydberg constant and δ_{nl} is the n and l dependant quantum defect. The quantum defect of a Rydberg orbital is a measure of how different the orbital is from the corresponding hydrogenic orbital.

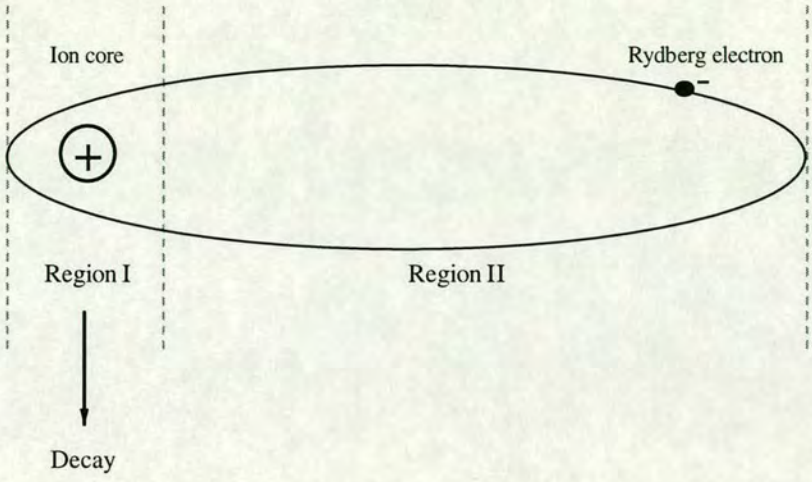

Figure 2-3 - A Rydberg electron in a Bohr orbit around the ionic core. Region I defines the area around the ionic core and region II defines the area in which the Rydberg electron is isolated from the ionic core. It is in region I that the Rydberg electron can interact with the core electronic, vibrational and rotational degrees of freedom which can result in Rydberg state decay.

In figure 2-3 we see a schematic diagram of a Rydberg state in a semiclassical orbit around the ionic core. There are two regions through which the electron travels. Region II is where the electron spends the majority of its time, quite some distance from the core of the molecule. In this region the electron views the core as a simple point charge as it is too far away to be influenced by interactions with the valence electrons or with the internal degrees of freedom of the molecule (vibrational and rotational motion). Region I is the area closest to the core. It is in this region that the Rydberg electron does interact with the core of the molecule and it is this interaction that can cause the Rydberg state to decay.

2.2.2 Rydberg state decay

The decay routes open to Rydberg states are the same as those open to valence states, namely radiative decay and predissociation. In radiative decay the energy of the Rydberg electron is converted into light with the emission of a photon. Predissociation involves the break up of the molecule using the energy of the Rydberg electron. The electronic energy couples to the internal vibrational coordinates which results in dissociation of the molecule.

As well as radiative decay and predissociation Rydberg states have a decay route that is not open to valence states; autoionisation. Autoionisation can occur when a molecule is in an excited neutral state lying above the ground ionic state. The molecule can ionise by transferring energy from the core of the molecule to the Rydberg electron. A more detailed discussion of autoionisation and the effects of autoionisation in ZEKE-PFI spectroscopy is given in section 2.3

All of the decay processes mentioned involve a coupling of the Rydberg electron to the core of the molecule. The rate of these processes is therefore linked to the amount of time that a Rydberg electron spends in the region of the molecular core. This can be quantified in a semi-classical way by considering the Bohr collision frequency. The Bohr collision frequency is the number of times the Rydberg electron collides with the core of the molecule per unit time and can be expressed as follows:

$$\nu = \frac{2\ R_y}{n^3 h} \qquad (2.3)$$

where R_y is the Rydberg constant, h is Plancks constant and n is the principle quantum number of the Rydberg orbital. The frequency of collision (ν) of the Rydberg electron with the core of the molecule decreases with n, or more specifically with n^3. The n^3 dependance of the Bohr collision frequency indicates that the rate of decay of a Rydberg orbital should decrease with increasing n, i.e. the lifetime will increase as n^3. The n dependence of the Bohr collision frequency provides a scaling law that allows predictions of the decay rates and lifetimes of higher n Rydberg states based on measured decay rates of lower n Rydberg states.

2.2.3 Field ionisation

Field ionisation of high n Rydberg states is the main source of electron signal in ZEKE-PFI spectroscopy. The effects of electric fields on Rydberg states need to be understood if the mechanism of ZEKE-PFI is to be understood. There follows a discussion on these effects which will focus on three areas; (1) the effect of an electric field on the potential experienced by a Rydberg electron, (2) the effect of an electric field on the Rydberg states themselves and (3) field ionisation of Rydberg states using a pulsed electric field.

The potential experienced by a Rydberg electron in an isolated atom can be described to a first approximation by the Coulomb potential:

$$V = -\frac{e}{(4\pi\varepsilon_0)r} \qquad (2.4)$$

where e is the charge of the electron and r is the separation of the electron from the core. When a dc electric field is applied to the system the potential experienced by the electron is altered to include the potential caused by the electric field:

$$V = -\frac{e}{(4\pi\varepsilon_0)r} + Fz \qquad (2.5)$$

where F is the electric field strength and z is the direction of the field.

A schematic diagram of the two potentials along the direction of the applied field can be seen in figure 2-4. The solid line represents the Coulomb potential and the dashed line represents the Coulomb potential with the addition of the potential due to the electric field. The distortion of the potential by the electric field results in a saddle point on one of the limbs of the potential. This represents the lowering of the ionisation energy by an amount proportional to the strength of the electric field. The electronic states above the saddle point are no longer bound and those below the saddle point are susceptible to ionisation by tunnelling from the distorted potential through what is called static field ionisation. Using a semi-classical model [7,8] the shift of the ionisation potential can be calculated using the following relationship:

$$\Delta E = 6.1\sqrt{F} \qquad (2.6)$$

where ΔE is the ionisation shift and F is the electric field strength in units of V/cm. In this simple picture exciting an atom to an energy anywhere above the lowered

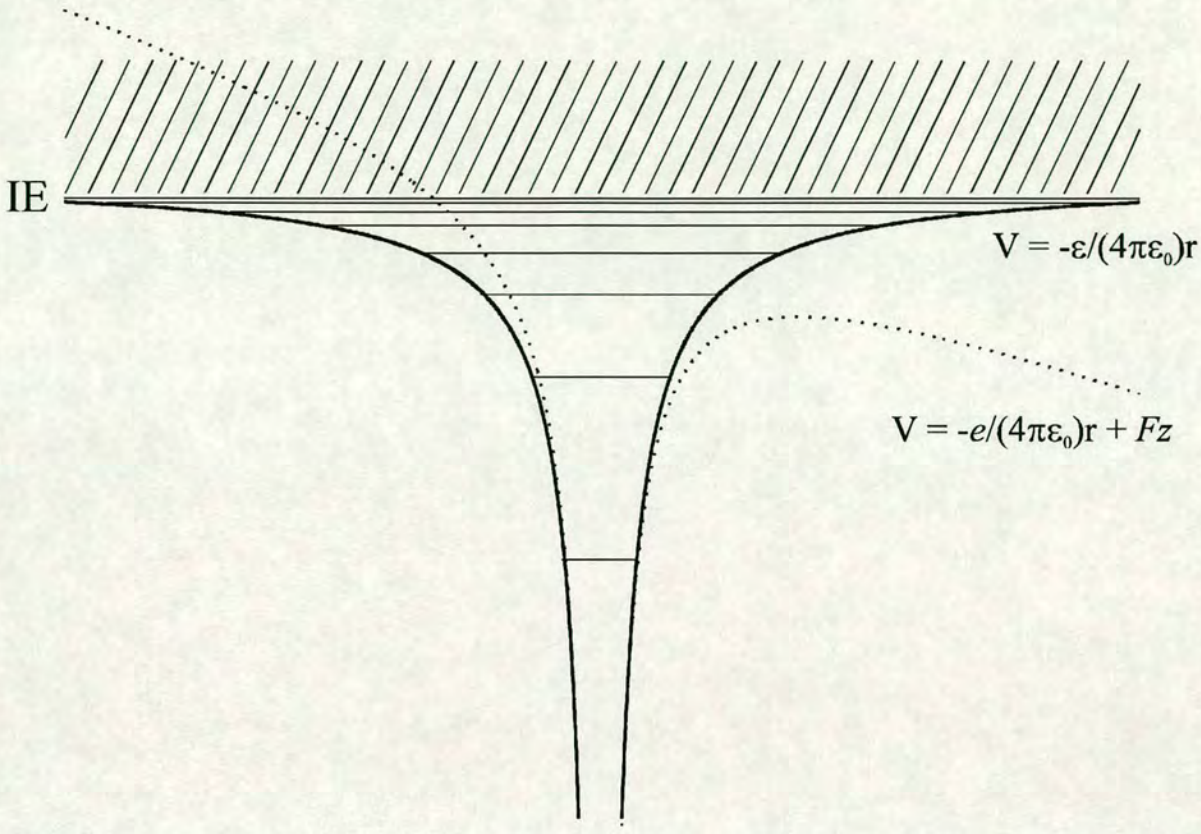

Figure 2-4 - The potential experienced by a Rydberg electron due to the ionic core of a molecule (thick line - Coulomb potential) and the potential experienced by a Rydberg electron with the application of an electric field (dashed line). The hashed area above the limits of the Coulomb potential represents the ionisation continuum.

ionisation energy will result in ionisation. This is true in the situation where a constant d.c. field is applied to the atom. However, the situation is more complex when a pulsed electric field is used to lower the ionisation energy and field ionise the atom. The minimum field required to field ionise an atomic Rydberg state can vary depending on the characteristics of the pulsed electric field. To understand why the minimum field can change the effect of the electric field on the initially populated state needs to be understood.

An applied field not only distorts the potential experienced by a Rydberg state, it also separates degenerate Rydberg states through the Stark effect. The different *l* levels of reasonably high *n* Rydberg states lie so close in energy that they can be

considered to behave like those of a hydrogen atom in the prescence of an electric field (i.e. the l levels for a given n are degenerate and are susceptible to the linear Stark effect). The splitting of the degenerate Rydberg states results in a dense Stark manifold of states whose energy depends on the strength of the applied field. The Stark states cannot be described in terms of the quantum numbers used to describe the initial Rydberg states as l is no longer a good quantum number. The quantum numbers used to define the Stark states arise from solving the schrodinger equation using parabolic coordinates [9] and they are n, n_1, n_2 and m. Figure 2-5 shows an example of a Stark manifold of states for a H atom. The splitting between the states of different k (where $k = n_1 - n_2$) for a given value of m can be seen to increase with the applied field. The number of Stark states for a given value of n is determined from the following sum rule:[9]

$$n_1 + n_2 + |m| + 1 = n \qquad (2.7)$$

which, for a given value of n and m, leads to $n - |m|$ Stark states. The passage of a Stark state to ionisation can be seen in figure 2-5 as the field strength increases and the classical limit for ionisation is lowered.

Another point to be taken from figure 2-5 is that the Stark states of different n do eventually cross when the field is of sufficient magnitude. In the region of the high n Rydberg states accessed in ZEKE-PFI spectroscopy the different n Rydberg states are very close together. When the levels undergo Stark splitting due to the pulsed electric field (1 - 3 V/cm) the individual Stark manifolds for each n overlap almost immediately. In the case where the adjacent n levels cross it has been shown that there are two mechanisms through which an atom or molecule in a Rydberg state can ionise due to a pulsed electric field; adiabatic and diabatic.[10] The type of ionisation depends on the passage of the initially prepared Rydberg state through the Stark manifold of states to ionisation as the pulsed field is applied. For atomic hydrogen the different n,$|m|$ Stark manifolds overlap and the individual Stark states cross. The passage of the initially prepared state through the overlapping region to ionisation is diabatic, that is, it remains in the same Stark state. The result of this is that the field required to ionise a Rydberg state deviates from the classical value resulting in a field ionisation shift of around $3.1 - 4\sqrt{F}$.[10,11]

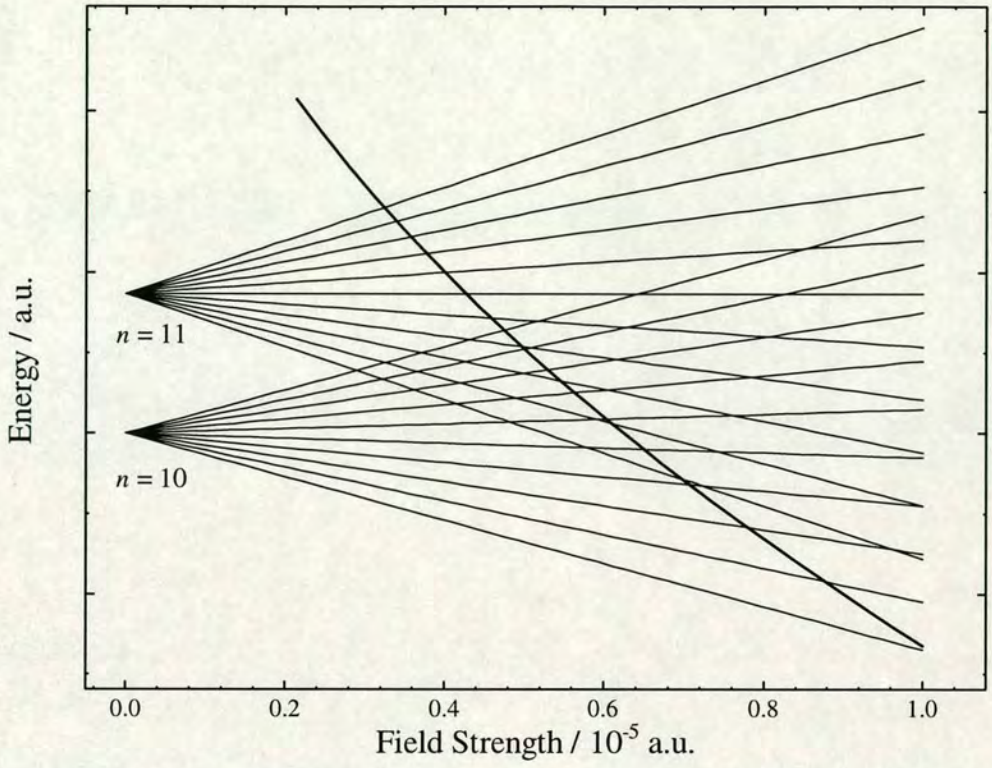

Figure 2-5 - Stark manifold for the hydrogen atom $n = 10$ and 11 Rydberg states. The curved line represents the classical limit for field ionisation.

In the case of non-hydrogenic systems the Stark manifolds are full of avoided crossings. This is due to a lack of symmetry in the potential experienced by the Rydberg electron in multi-electron atoms or molecules. Depending on the characteristics of the pulsed electric field the passage of the initial Rydberg state through the Stark manifold will be diabatic or adiabatic.[12] If the pulsed electric field is fast rising then the passage through the Stark manifold to ionisaton will be relatively fast and the atom or molecule will be ionised diabatically (i.e. by staying on the same diabatic Stark state and passing through the avoided crossings). If the pulsed electric field is slow rising then the passage will be adiabatic (i.e. never changing states at an avoided crossing). The adiabatic mechanism results in a field ionisation shift of $6.1 \sqrt{F}$ and the diabatic mechanism results in a field ionisation shift of roughly $4.0 \sqrt{F}$.

The size of the shift is a quantity that needs to be known to enable the correction of ZEKE-PFI spectra to give the true ionisation energies of a molecule. If the classical picture held then this would be a simple matter but, as has been discussed, the real picture is more complicated. It is almost impossible to predict exactly how a molecule will field ionise with the result that the only reliable way to measure field ionisation shifts in ZEKE-PFI spectroscopy is to perform a series of experiments using different field strengths and extrapolating the ionisation energy to zero-field. An example of this will be given in Chapter 3. Another way to determine field free ionisation energies was developed by Müller-Dethlefs *et al.* [13] in which they used a stepped field ionisation pulse that allowed them to measure the ionisation energy at different field strengths simultaneously.

2.2.4 Lifetimes of high *n* Rydberg states

For the purposes of this discussion the term high-*n* Rydberg states refers to those with a value of *n* greater than 100. It is these states that are harvested in ZEKE-PFI spectroscopy to pinpoint the positions of the ionic thresholds. As has been mentioned in Chapter 1, the most interesting thing about these states is their extremely long lifetimes. The decay of low-*n* Ryderg states scales as n^{-3} due to the Bohr collision frequency. However, this scaling law was shown to be completely inadequate in the prediction of the lifetimes of the *p* Rydberg states of NO observed in the ZEKE-PFI spectra recorded by Reiser *et al.*[14] Chupka showed that these Rydberg states should only survive for 200 ns based on simple the n^3 scaling law.[15] This is in complete disagreement with the pulsed field ionisation signal from the high-*n* states that is observed for up to 12 μs after excitation. Lifetimes of this length would require a scaling law of around n^5 rather than n^3.[15]

The reason behind the longevity of the high-*n* Rydberg states was a subject of intense debate and experimental investigation. As mentioned in chapter 1. there were initially two possible explanations for the increased lifetime of the Rydberg states, stabilization of the Rydberg electrons by interactions with the rotating molecular core[16] and stabilization of the electrons by interactions with stray electric fields and

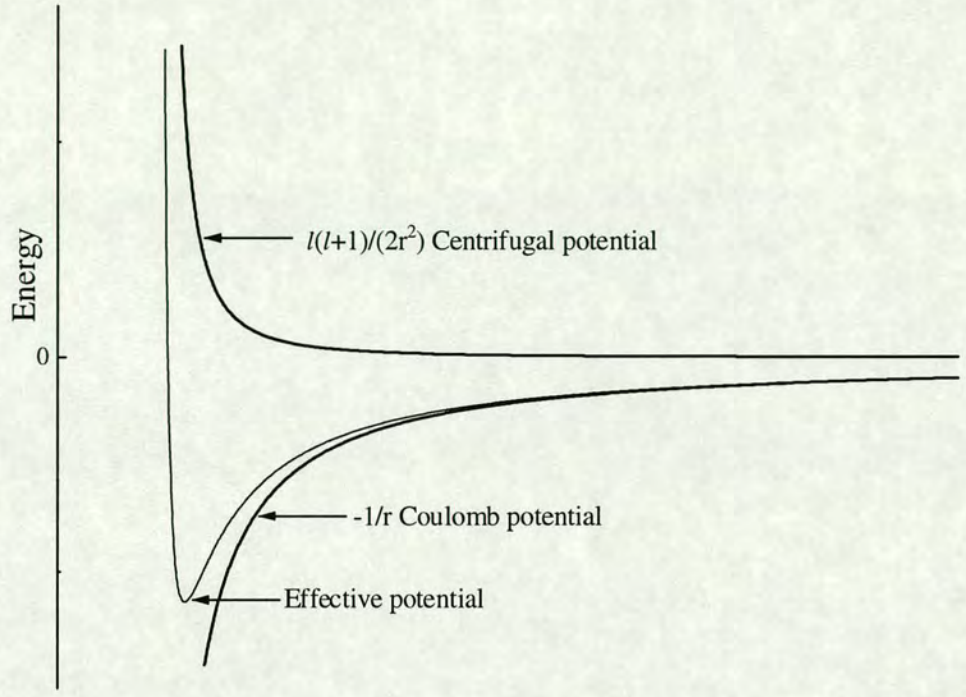

Figure 2-6 - Schematic diagram of the effective potential experienced by a Rydberg electron in orbital with large orbital angular momentum. The two components to the potential (the coulomb and centrifugal potential) are also shown.

collisions with ions.[15] The stray electric field/ion collision mechanism has now been recognised as the mechanism responsible for the lifetime lengthening.

There now follows a brief description of the external conditions model for lifetime lengthening of high *n* Rydberg states as proposed by Chupka, [15] developed by Bixon and Jortner [17] and confirmed experimentally and theoretically by Vrakking and Lee.[18] As mentioned earlier in this chapter, Rydberg state decay depends on an interaction with the ionic core of the molecule. Rydberg states interact less with the core with increasing *n* but they also interact less with the core with increasing *l*. This can be understood by considering the effective potential that Rydberg electrons experience. Figure 2-6 shows the potential that a high *l* Rydberg state will experience which is a sum of the Coulomb interaction and a centrifugal term. With increasing *l* a potential barrier is created that prevents the Rydberg electron from interacting with

the core. A Rydberg electron in a high n, high l orbital is said to be non-penetrating and is considered in semiclassical terms as moving in a circular orbit. Non-penetrating orbitals are therefore very stable with respect to the decay processes open to Rydberg states.

However, in the case of ZEKE-PFI spectroscopy the high-n Rydberg states populated by photoexcitation are low-l states due to the strict dipole allowed selection rule of $\Delta l = \pm 1$. The low-l states are relatively penetrating compared to the high-l states and the lifetimes should follow the n^3 scaling law. As intimated earlier, the mechanism whereby these short lived, high-n, low-l Rydberg states are converted to long lived, high-n, high-l Rydberg states is through the interactions with stray electric fields and collisions with other charged particles in the interaction region.

The mechanism whereby stray electric fields can produce Rydberg states with high-l character is through the Stark effect. A brief description of the Stark effect in atomic hydrogen follows which will illustrate the main qualitative ideas behind the production of Rydberg states with high-l character. In hydrogen the Stark effect mixes the degenerate l states of a given n shell to produce mixed orbitals. This is because in the prescence of an axially symmetric electric field l is no longer a good quantum number and any states have to be expressed as a superposition of l states. This effect can be seen schematically in figure 2-7. The states involved in the stark effect are the $2s$ and $2p$ states of atomic hydrogen. With the application of an electric field the two states are mixed to produce states which cannot be described as either $l = 1$ or $l = 0$. The states have character from both the $2s$ and $2p$ orbitals.

In the case of the high-n Rydberg states of molecules roughly the same thing happens. Although the different l states for a given n are not exactly degenerate to begin with it only takes a small field for these states to begin to mix in the same way as the hydrogenic Rydberg states. The mixing of the states results in the quickly decaying, low-l character of the initially prepared Rydberg states to be diluted across the $(n - |m|)$ Stark states. The decay of the mixed states thus becomes proportional to n^4 with the extra power of n coming from the dilution of the decay probability of the low-l states through the n (or rather, $n - |m|$) Stark states. This goes half way to explaining the observed longevity of the high-n Rydberg states.

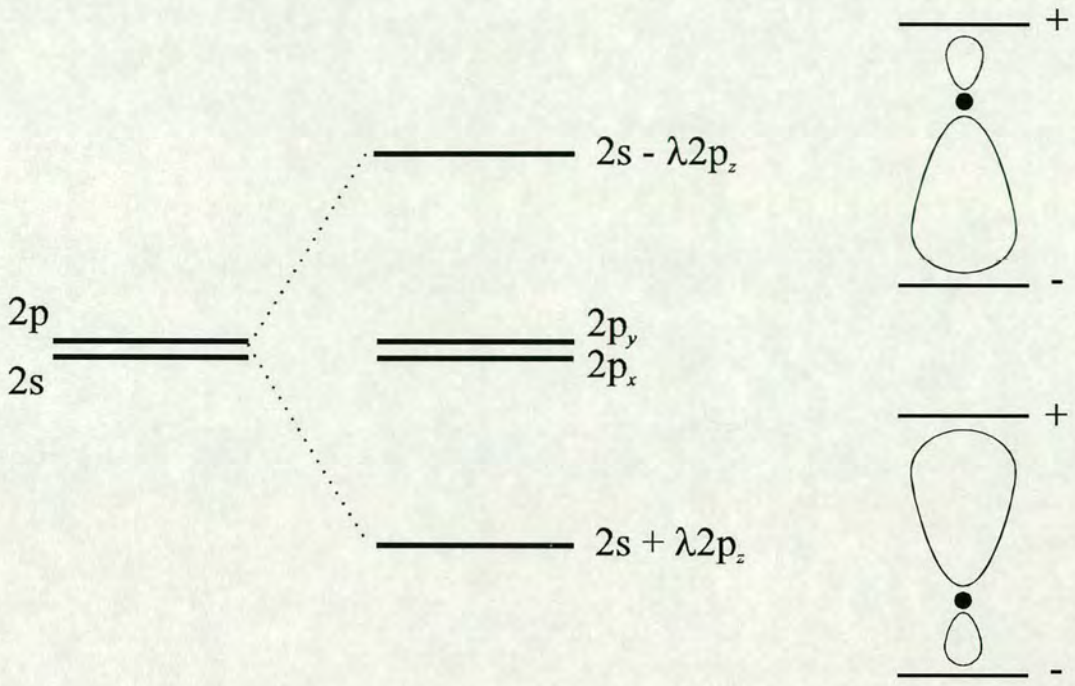

Figure 2-7 - The splitting of the degenerate 2s and 2p orbitals of atomic hydrogen due to the Stark effect. The 2s and $2p_z$ orbitals are mixed by the electric field resulting in orbitals which cannot be described using the angular momentum quantum number,*l*.

The other power of *n* that is required by the observed lifetime signals from ZEKE-PFI spectroscopy and direct measurements comes from the influence of charged particles in the ionisation region of any spectrometer. The *l* and m_l (azimuthal quantum number) mixing properties of ionic collisions is a well known phenomenon in atomic physics.[19,20] In the case of ZEKE-PFI spectroscopy it is not really a collisional process but rather a perturbation of the electric field experienced by the Rydberg electrons. Just as the stray fields mix the *l* quantum number of the Rydberg states due to symmetry breaking (i.e. *l* no longer being a good quantum nunber due to the axially symmetric electric field), the prescence of charged particles removes the axial symmetry of the system resulting in m_l no longer being a good quantum number. The result is the same as with the *l* mixing in that the quickly decaying character of the

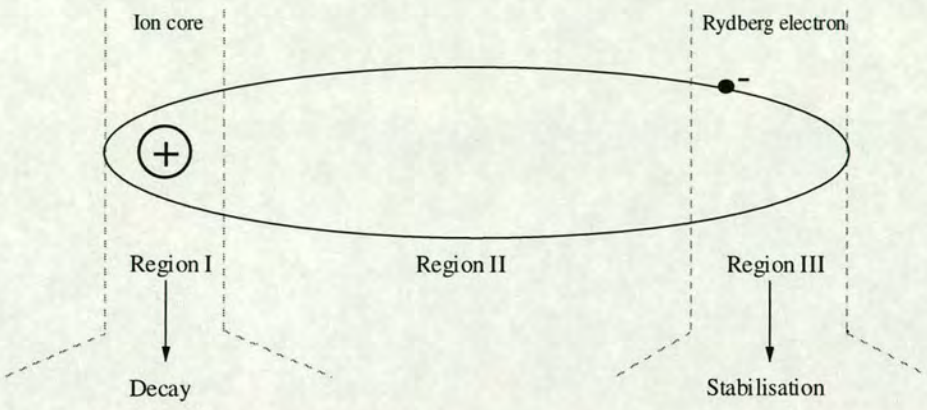

Figure 2-8 - Schematic diagram of the Bohr orbit of a high n Rydberg electron. The orbit passes through three regions which determine the dynamics of the Rydberg state. Region I and region II are the same as in figure 2-3. Region III defines the area in which the Rydberg electron is susceptible to external perturbations which increase the longevity of the Rydberg state.

optically prepared high-n, low-l, low-m_l Rydberg states is diluted through the n sublevels produced by the mixing of the m_l states.

The mechanism was verified by Vrakking and Lee [18(a)] through variations in electric field and charged particle concentration for lifetime measurements of Rydberg states of NO and Xe respectively. The scaling of the high-n Rydberg states was found to vary as approximately $n^{4.6}$ rather than n^5 and this discrepancy was put down to incomplete m_l mixing. The theoretical verification came in the form of calculations that predicted the onset of increased longevity in certain experimental conditions with increasing n. Bixon and Jortner [17] established a theoretical framework for these calculations. Vrakking[18(b)] also calculated the onset using a different method A schematic diagram of a high-n Rydberg state in a semi-classical orbit can be seen in figure 2-8 which illustrates the main features of the theoretical approach to the to two

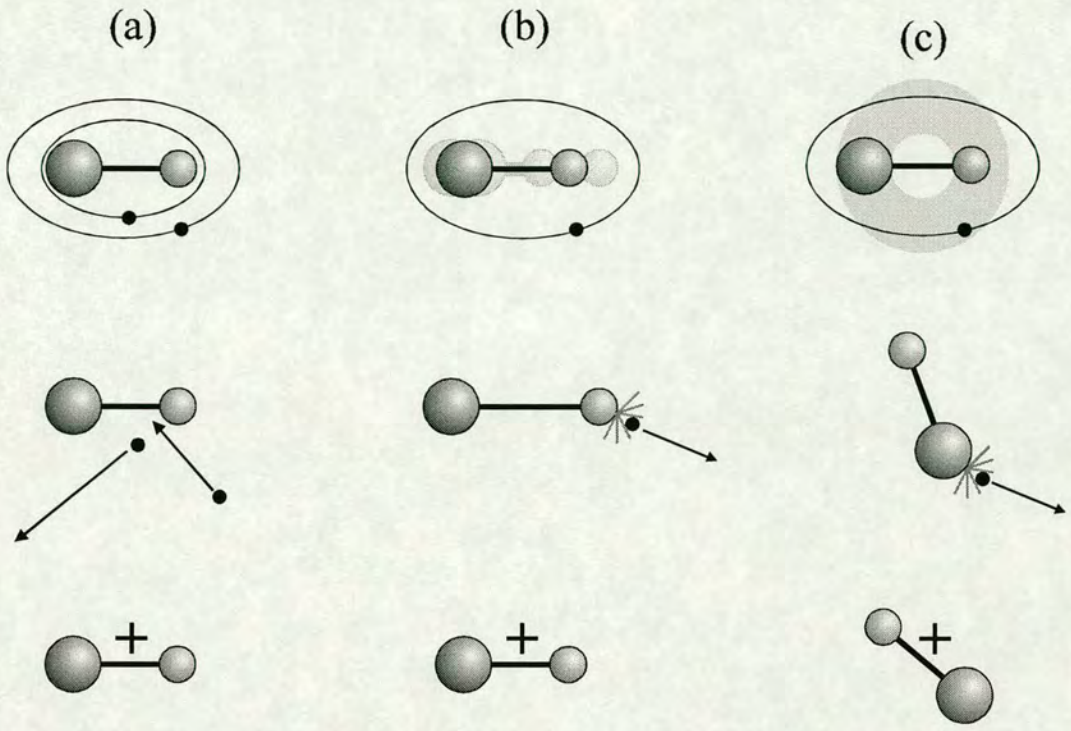

Figure 2-9 - Schematic diagram illustrating the three types of autoionisation; (a) electronic, (b)vibrational and (c) rotational.

lifetime calculations. The motion of the electron is split into three regions as opposed regions in the generic Rydberg diagram in figure 2-5. The extra region (region III) in this diagram is the area where the Rydberg electron is far from the core and comes under the influence of external electric fields and surrounding ions.

2.2.5 Autoionisation

As mentioned earlier, one of the major decay routes for Rydberg states is autoionisation. Autoionisation occurs when a Rydberg state of the molecule lies energetically above the ground ionic state. The Rydberg state in this case will be one that is converging on some excited state of the molecular ion. The state is doubly excited, possessing energy in the Rydberg electron and in excitation of the core. The energy of the core can be transfered to the Rydberg electron causing ionisation and

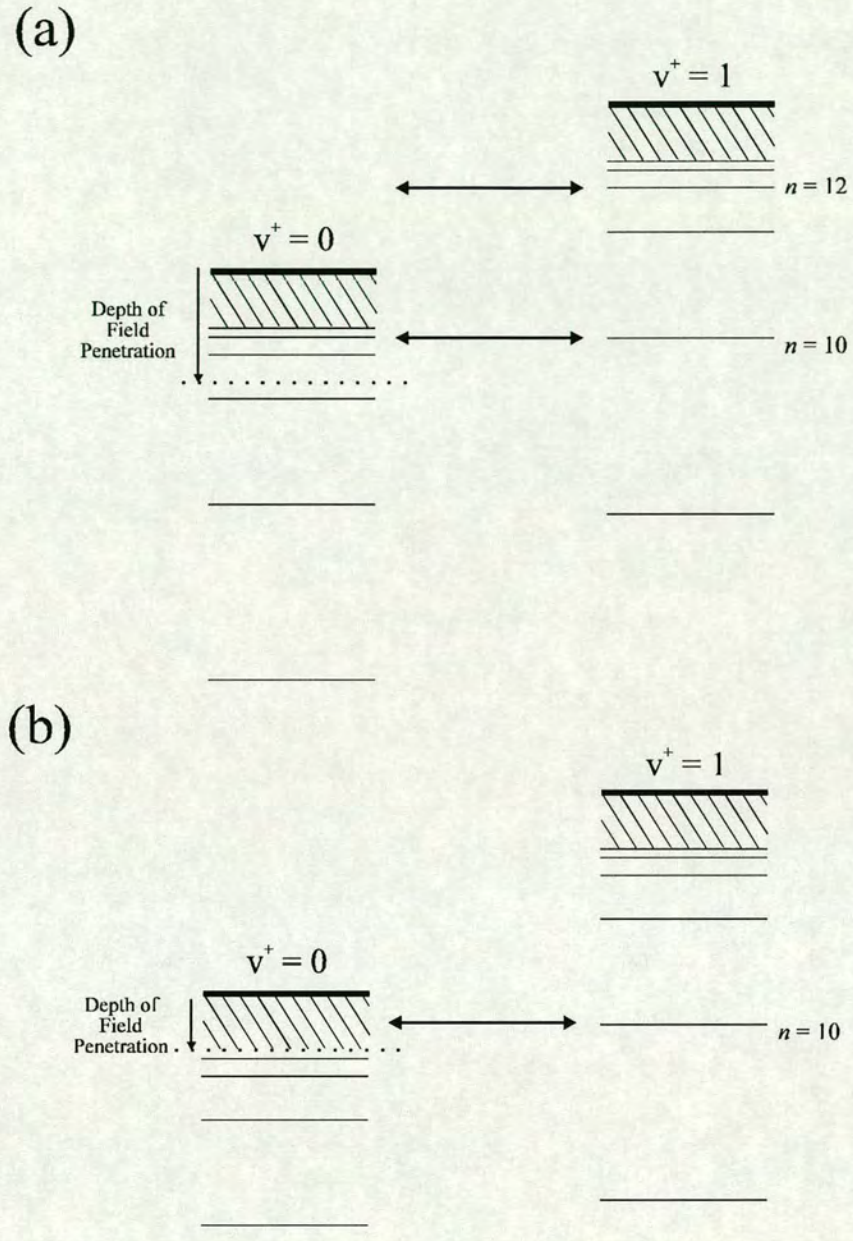

Figure 2-10 - An example of (a) forced autoionisation and (b) forced autoionisation contributing to the intensity of a ZEKE- PFI signal. The hashed area represents the high *n* Rydberg manifold.

subsequent relaxation of the core. A schematic diagram illustrating the three autoionisation mechanisms (electronic, vibrational and rotational) is shown in figure 2-9. In each example there is relaxation of the core and ejection of the Rydberg electron.

The effects of autoionisation in PES and TPES were discussed in chapter 1. Autoionisation can also have an effect in ZEKE-PFI spectra through the mechanism of 'forced' autoionisation. The lowering of the ionisation energy for a given state caused by the application of an electric field can result in the autoionisation of a Rydberg state. Figure 2-10 (a) illustrates this point where on the left we see a Rydberg series converging on the ground ionic state and on the right we see a series converging on an excited state of the ion ($v^+ = 1$). If we were to populate the $n = 12$ Rydberg state converging on the $v^+ = 1$ limit it would be able to autoionise straightforwardly as described above with the molecular core relaxing to the ground state of the ion. If however we were to populate the $n = 10$ level converging on the excited state the molecule would not be able to autoionise. With the application of an electric field we lower the the ionisation energy of the ground state to below the $n = 10$ Rydberg state (converging to the excited ionic state) and now it can autoionise to produce a deexcited molecular core and a free electron.

If the $n = 10$ Rydberg state was at the same energy as the high n Rydberg states converging on the ground ionic state then when the pulsed electric field ionises the high n Rydberg states the $n = 10$ Rydberg state can autoionise and produce an electron which will be detected along with the PFI electron signal. This is illustrated in figure 2-10 (b) Enhancements caused by this process have been seen in the ZEKE-PFI spectra of N_2 [21] and H_2.[22] The coupling mechanism between the low n Rydberg states and the high n Rydberg pseudo-continuum is similar to that for 'complex resonances' as seen in the autoionisation spectrum of H_2 recorded by Jungen and Raoult.[23] In this case transitions to the $n = 27$-33 Rydberg states of H_2 converging on $v^+ = 4$, $N^+ = 2$ of the ground ionic state are seen only as structure superimposed on the autoionisation peak for the $6p$ Rydberg state converging to $v^+ = 6$.

2.3 References

[1] R. J. Donovan, R. V. Flood, K. P. Lawley, A. J. Yencha and T. Ridley, *Chem.Phys.* 1992, **164**, 439.

[2] T. Ridley, K. P. Lawley, R. J. Donovan and A. J. Yencha, *Chem.Phys.* 1990, **148**, 315.

[3] R. J. Donovan, A. C. Flexen, K. P. Lawley, T. Ridley, *Chem.Phys.* (submitted for publication).

[4] (a) M. C. R. Cockett, J. G. Goode, K. P. Lawley, R. J. Donovan, *Chem.Phys.Lett.* 1993, **214**, 27; (b) M. C. R. Cockett, J. G. Goode, R. R. Maier, K. P. Lawley, R. J. Donovan, *J.Chem.Phys.* 1994, **101**, 126; (c) J. G. Goode, M. C. R. Cockett, K. P. Lawley, R. J. Donovan, *Chem.Phys.Lett.* 1994, **231**, 521; (d) M. C. R. Cockett, D. A. Beattie, K. P. Lawley, R. J. Donovan, *Chem.Phys.Lett.* 1996, **259**, 554.

[5] P. R. Monson, W. M. McClain, *J.Chem.Phys.* 1970, **53**, 29; W. M. McClain, *J.Chem.Phys.* 1971, **55**, 2789.

[6] R. G. Bray, R. M. Hochstrasser, *Mol.Phys.* 1975, **31**, 1199.

[7] T. F. Gallagher, L. M. Humphrey, W. E. Cooke, R. M. Hill, S. A. Edelstein, *Phys.Rev.A.* 1977, **16**, 1098; W. E. Cooke, T. F. Gallagher, *Phys.Rev.A.* 1978, **17**, 1226.

[8] M. A. Duncan, T. G. Dietz, R. E. Smalley, *J.Chem.Phys.* 1981, **75**, 2118.

[9] H. A. Bethe, E. E. Salpeter, 'Quantum Mechanics of One- and Two-Electron Atoms', 1957, Springer-Verlag, Berlin.

[10] D. Kleppner, M. G. Littman, M. L. Zimmerman, 'Rydberg States of Atoms and Molecules', Eds. R. F. Stebbing, F. B. Dunning, Cambridge University Press, Cambridge, 1983, Chapt. 6, 73.

[11] P. Pillet, H. B. van Linden van den Heuvell, W. W. Smith, R. Kachru, N. H. Tran, T. F. Gallagher, *Phys.Rev.A.* 1984, **30**, 280.

[12] T. F. Gallagher, 'Rydberg Atoms' Cambridge University Press, Cambridge, 1994, Chapter 7, 103.

[13] R. Lindner, H.-J. Dietrich, K. Müller-Dethlefs, *Chem.Phys.Lett.* 1994, **228**, 417.

[14] G. Reiser, W. Habenicht, K. Müller-Dethlefs, E. W. Schlag, *Chem.Phys.Lett.* 1988, **152**, 119.

[15] W. A. Chupka, *J.Chem.Phys.* 1993, **98**, 4520; *ibid.* 1993, **99**, 5800

[16] D. Bahatt, U. Even, R. D. Levine, *J.Chem.Phys.* 1993, **98**, 1744.

[17] J. Jortner, M. Bixon, *J.Chem.Phys.* 1995, **102**, 5636.

[18] (a)M. J. J. Vrakking, Y. T. Lee, *J.Chem.Phys.* 1995, **102**, 8818; *ibid,* 1995, **102**, 8833;(b) M. J. J. Vrakking, *J.Chem.Phys.* 1996, **105**, 7336.

[19] T. F. Gallagher, S. A. Edelstein, R. M. Hill, *Phys.Rev.A.* 1977, **15**, 1945.

[20] K. B. MacAdam, R. Rolfes, D. A. Crosby, *Phys.Rev.A.* 1981, **24**, 1286; K. B. MacAdam, R. G. Rolfes, X. Sun, J. Singh, W. L. Fuqua III, D. B. Smith, *Phys.Rev.A.* 1987, **36**, 4254.

[21] F. Merkt, P. M. Guyon, *J.Chem.Phys.* 1993, **99**, 3400.

[22] F. Merkt, T. P. Softley, *J.Chem.Phys.* 1992, **96**, 4149.

[23] Ch. Jungen, M. Raoult, *Farad.Discuss.Chem.Soc.* 1981, **71**, 253.

3. Experimental Details

3.1 Introduction

This chapter focuses on the experimental aspects of the work presented in the rest of the thesis. The development of ZEKE-PFI spectroscopy has been discussed in Chapter 1 and the theoretical aspects of field ionisation and lifetime lengthening of high n Rydberg states have been covered in Chapter 2. In this chapter only the details relevant to carrying out REMPI and ZEKE-PFI experiments will be discussed.

In section 3.2 a description of the laser system will be given, followed in section 3.3 by a description of the REMPI/ZEKE-PFI spectrometer. Section 3.4 will discuss the various routes that can be used to excite a molecule from the ground state to the high n Rydberg manifold. The details of performing a ZEKE-PFI experiment are described in section 3.5. Also included in section 3.5 is a description of threshold electron spectroscopy, a technique which detects autoionising Rydberg states using electron detection and pulsed electric fields. The chapter is rounded off in section 3.6 with a discussion on the various aspects of data handling involved in REMPI and ZEKE-PFI spectroscopy.

3.2 Laser System

The use of lasers as the light source in ZEKE-PFI spectroscopy is almost universal. The only other light source that has been used to perform ZEKE-PFI experiments is a synchrotron storage ring. Synchrotron sources produce very bright and broad band radiation (from 6 eV to 12 keV) which, when used with a monochromator, can be tuned and scanned across the ionisation thresholds of a molecule. The main problem with the use of synchrotrons is that the available monochromators do not have sufficient resoloution to give ZEKE-PFI any benefits over other techniques such as threshold photoelectron spectroscopy (TPES). Despite this some ZEKE-PFI studies have been carried out using synchrotron radiation [1] and

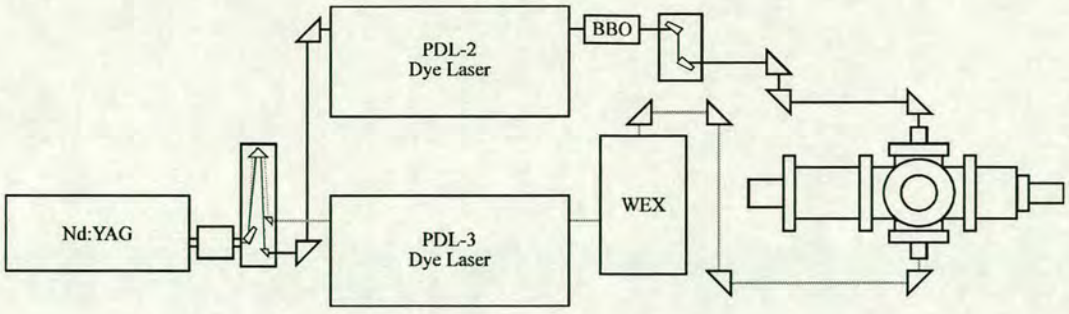

Figure 3-1 - Schematic diagram of the laser system used for the work presented in this thesis.

more may be done in the future with the development of higher resolution monochromators together with third generation synchrotron sources.[2]

A schematic diagram of the laser system used for the work presented in this thesis is shown in figure 3-1. A Q-switched Nd:YAG laser and frequency mixing module (DCR-2A Quanta Ray), which can produce wavelengths of 1064 nm (fundamental), 532 nm (second harmonic) and 355 nm (third harmonic), is used to pump two dye lasers (Quanta Ray PDL-2A and PDL-3). The Nd:YAG laser operates at a frequency of 10 Hz. The dye lasers have a tuning range of 420 to 850 nm using Exciton laser dyes (C440 to LDS 821). For wavelengths above 540 nm the second harmonic of the Nd:YAG laser is used to pump the dye lasers. Wavelengths below that value require the use of the third harmonic. The different harmonics of the Nd:YAG laser are separated using a prismatic separator which allows the use of all three output wavelengths simultaneously (if needed).

The output from the dye lasers can be doubled using KD*P (KH_2PO_4) and BBO (β-barium borate) crystals. The KD*P crystals are mounted within a wavelength extender module (Quanta-Ray WEX) which allows automatic tracking of the crystal that produces the dye second harmonic while the dye laser scans over its wavelength range. The dye lasers are scanned using a home built stepper module which is triggered by the data collection software on a PC. The BBO crystal is in a home built crystal mount and the dye second harmonic is manually tracked using a photodiode and oscilloscope. Colour filters are used to separate the dye fundamental

output from the second harmonic for the red and green wavelength dyes whereas a pelin broca prismatic separator is used to separate the fundamental and second harmonic of the blue and near ultraviolet dyes. The dye fundamental can also be frequency mixed with the Nd:YAG fundamental using the KD*P crystals in the WEX module. The output beams from the dye lasers are counter propagated through the spectrometer through adjustable 7.6 cm focal length lenses.

3.3 Spectrometer

A schematic of the spectrometer used for the work presented in this thesis is shown in figure 3-2. The spectrometer can be divided into three main components: (1) the pulsed molecular beam, (2) the laser time-of flight mass spectrometer, and (3) the vacuum system. The pulsed molecular beam, time-of-flight stage and the direction of laser propagation are arranged orthogonal to one another (the lasers are directed into and out of the plane of the paper in figure 3-2).

The spectrometer consists of two differentially pumped vacuum chambers. The main (excitation) chamber is pumped by a Balzers TPU 510S turbomolecular pump (500 ls^{-1}) backed by a Maruyama CP-80 rotary pump. The pulsed jet expansion chamber is pumped independantly using an Edwards 160-700 diffusion pump (700 ls^{-1}) with a liquid nitrogen trap. The diffusion pump is backed by an Edwards ED200 rotary pump. Under operating conditions the pressure in the expansion chamber can reach 5×10^{-6} mbar whereas the pressure in the main chamber will only reach 4×10^{-7} mbar (from a pressure of 2×10^{-7} mbar without the pulsed expansion being switched on). The pressure in both chambers is monitored using Edwards AIM-S-NW25 penning gauges and active gauge controller. The backing line to the diffusion pump is also monitored using an Edwards APG-M-NW16AL pirani gauge.

The pulsed supersonic expansion is produced by using a General Valve (Iota 1) pulsed nozzle assembly with an aperture of 300 μm. The repetition rate of the valve is 10 Hz with a pulse duration of 300 μs. The expansion jet is skimmed to produce a narrow collimated molecular beam.

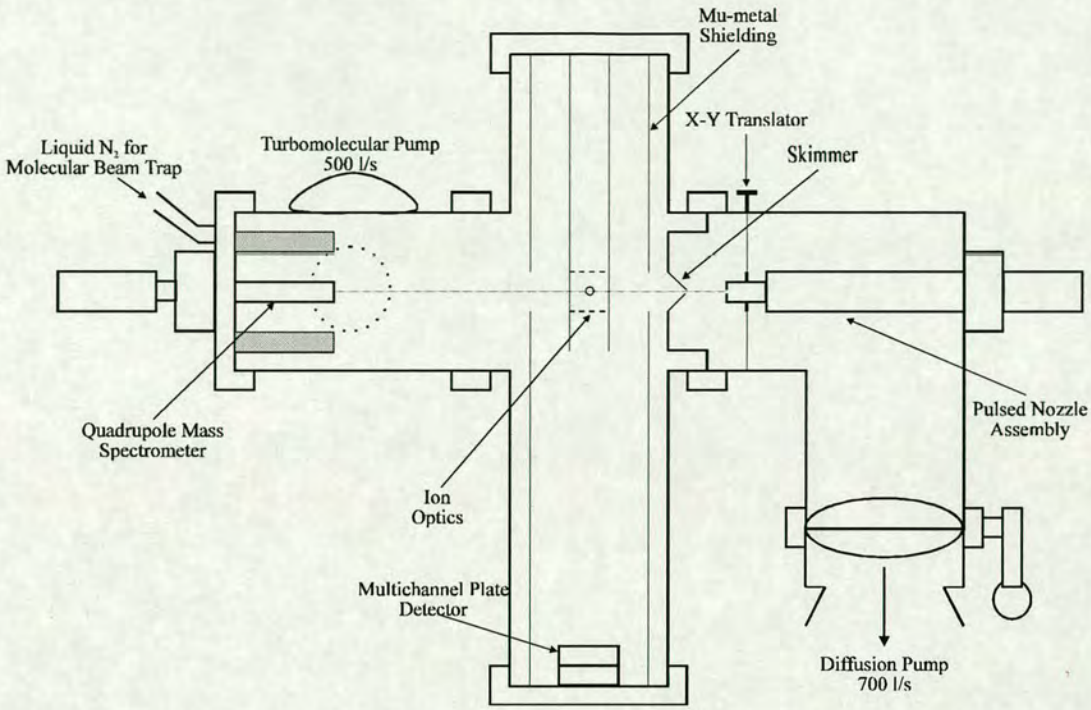

Figure 3-2 - Schematic diagram of the REMPI/ZEKE-PFI spectrometer.

Beam Dynamics skimmer (aperture 0.49 mm) which is positioned four centimetres from the pulsed nozzle. The beam direction is adjusted using an X-Y translator which holds the front end of the pulsed nozzle assembly A VG quadrupole mass spectrometer (SX200), positioned at the far end of the spectrometer is used to align the molecular beam through the middle of the interaction region.

The ion optics for the time-of-flight stage consist of two copper mesh grids. The bottom grid is held at earth and this defines the start of the field free region for the time-of-flight spectrometer. When used for REMPI spectroscopy d.c. fields are applied to the top and middle grids. The voltage applied to the top grid is supplied by a Stanford Research Systems high voltage power supply (PS325) and was typically between 2.0 and 2.5 kV. The voltage to the bottom grid was supplied by a Brandenburg power supply and was typically between -50 and -300 V. In the ZEKE-PFI experiments pulsed electric fields are applied to the top and bottom grids and are used to ionise the high-*n* Rydberg states and send the electrons to the detector. The

pulsed field applied to the top grid is supplied by a home built, variable output, pulsed voltage unit with an output range of 0.6 V to 21 V. The field applied to the bottom plate is supplied by a Farnell PG102 pulse generator with a range of 30 mV to 10 V. The electron detector is a dual multichannel plate (MCP) electron multiplier with matched anode. The voltage applied to the MCP is typically between 4.0 and 4.2 kV. The time-of-flight signal from the MCP is monitored using a digital oscilloscope (LeCroy 9310). The electron signal from any given time-of-flight spectrum is processed unamplified using a Stanford Research Systems SRS250 boxcar integrator and recorded on a PC.

The timing of the experiment is controlled by the Q-switch output of the Nd:YAG laser which is used to trigger all of the collection electronics (oscilloscope, boxcar, PC). The timing of the pulsed jet and the pulsed electric fields is also determined by the Q-switch output but can be varied relative to the Q-switch using an EG&G 9650 digital delay generator. The timing of the pulsed molecular beam relative to the Q-switch enables maximum overlap to be achieved between the laser pulse and each molecular beam pulse. Exact details of the laser configuration and the pulsed electric fields are given at the start of every results section in Chapters 4 and 5.

3.4 Excitation Routes

3.4.1 Single Photon Excitation

The first ionisation energies of most molecules lie in the vacuum ultra-violet (VUV) region of the electromagnetic spectrum. This region covers the wavelengths between 100 and 200 nm. The definition of electromagnetic radiation as VUV is that it is absorbed by air (or more specifically oxygen) therefore any experiments using VUV radiation need to be carried out in high vacuum. The use of lasers to produce tunable VUV radiation is far from straightforward. Commercially available dye lasers can only produce wavelengths between 320 and 1000 nm. This light can be frequency doubled using birefringent crystals to reach wavelengths of around 200 nm but this is still too long to excite most molecules to the ionisation threshold with one photon.

The most common way of generating VUV light for use in single photon ZEKE-PFI studies is to use non-linear optical processes in rare gases and metal vapours. As atoms have a centre of inversion the first non-zero non-linear term in the power series expansion for the interaction with light and matter is the third order term. Third order processes require three input photons from a dye laser to produce one VUV output photon. The fact that four photons are involved gives the process the name of four-wave mixing. There are two ways that four-wave mixing can generate VUV radiation. The first involves straightforward third harmonic generation where three photons of the same energy are used to produce one photon with three times the energy of the initial (fundamental) photons. The second way is to use two lasers of different wavelengths in a resonant excitation scheme by tuning one laser (ν_1) to a resonance with the non-linear medium (the rare gas or metal vapour) at the two-photon level and then using a third photon from the second laser (ν_2) to either produce the sum frequency photon ($\nu_3 = 2\nu_1 + \nu_2$) or the difference frequency photon ($\nu_3 = 2\nu_1 - \nu_2$). Of the two methods, sum and difference frequency mixing is the more efficient (i.e. has a better conversion efficiency) and has a broader tuning range of 200 - 60 nm (50000 - 150000 cm^{-1}).

3.4.2 Multiple Photon Excitation

As mentioned above, commercially available dye lasers provide constantly tunable radiation between 200 and 1000 nm (using doubling crystals to produce the shorter wavelengths). Although not energetic enough to excite most molecules directly from the ground state to the ionisation threshold, photons of this energy can be used in multi-photon excitation routes to reach the ionisation thresholds *via* excited electronic states of the neutral molecule. As well as being easier to perform compared to single photon excitation, resonant multiphoton excitation has a number of other benefits among which molecular specificity is probably the most important. Electronic states are specific to an individual molecule and using them as intermediate states means that only that molecule will be excited to the high-*n* Rydberg manifold and field

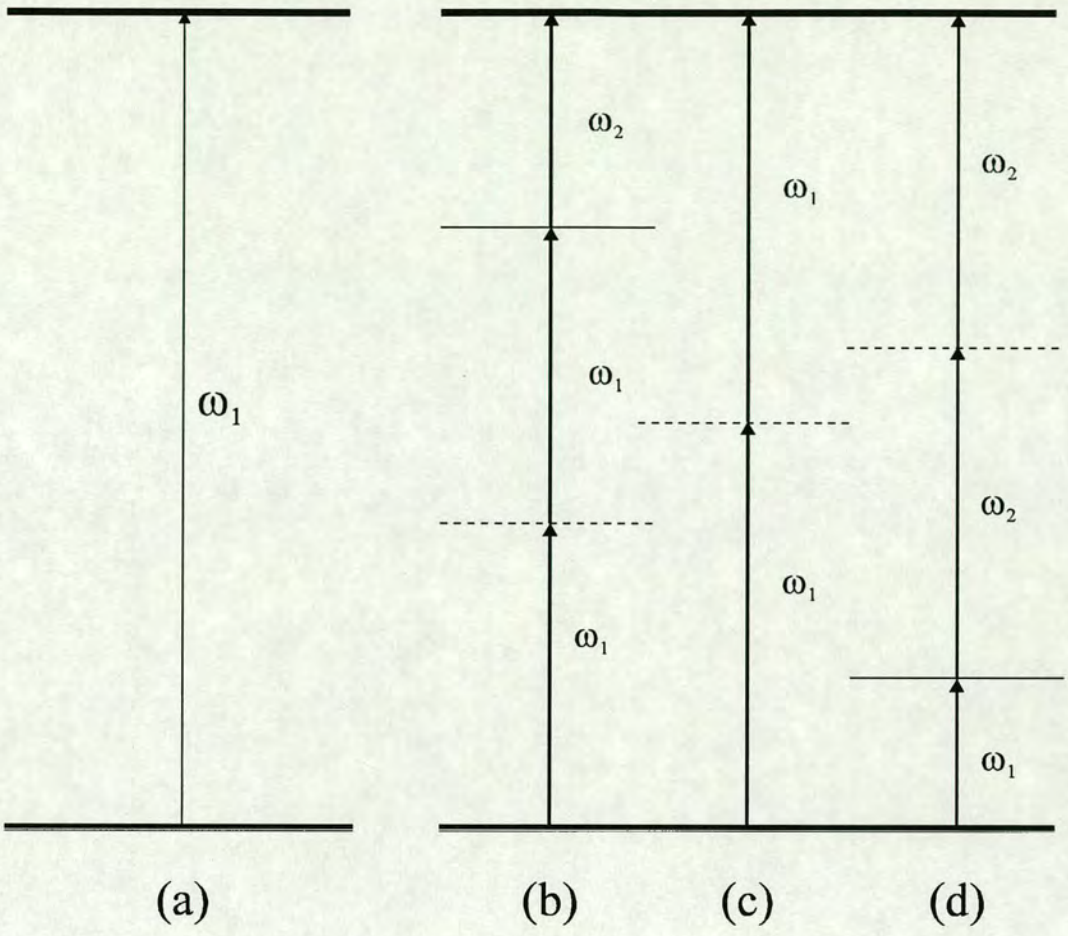

Figure 3-3 -Excitation routes that can be used to reach the high *n* Rydberg manifold; (a) single photon, (b) multiphoton *via* a Rydberg state, (c) coherent two-photon and (d) multiphoton *via* a valence state. Solid horizontal lines represent real intermediate states whereas dashed horizontal lines represent virtual intermediate states.

ionised. The specificity allows for the simplification of spectra by removing ZEKE-PFI signals due to other molecules from the spectrum. The study of van der Waals complexes using ZEKE-PFI spectroscopy benefits greatly from the use of resonant excitation. Another important advantage is that spectra are often much simpler to interpret as the use of an intermediate state means that the final step in the excitation can be from a single rovibronic state, or a narrow range of rotational states.

There are a number of ways in which a resonant excitation can be performed. Figure 3-3 shows a schematic diagram of the different multi-photon excitation routes that can be used. The notation used to describe resonant excitation can be described as follows: $(m + n')$ where m is the number of photons used to reach the resonant

excited state and n is the number of photons used to reach the high-n Rydberg manifold of the molecule from the excited intermediate state. The prime beside n is used to denote that a second laser (colour) is providing the photons for the final excitation. The examples in the diagram are those for (2+1′) and (1+2′) excitation (figure 3-3 (b) and (d)). Also shown is the coherent two-photon excitation route (figure 3-3 (d)) which is very similar to single photon ionisation (figure 3-3 (a)) but has a much lower cross section.

Resonant multi-photon excitation allows a great deal of flexibility in the choice of the intermediate state. Valence states can be used in (1+2′) excitation routes as in previous work by the Edinburgh ZEKE group on I_2.[3] However, by far the most common intermediate states are Rydberg states accessed using (m+1′) excitation routes. The value of m is normally 2 or 3 and the excited states used are low-n Rydberg states. The energies required normally fall into the range 50000 - 80000 cm^{-1} right up to around 12000 cm^{-1} below the ionisation thresholds.

3.5 ZEKE-PFI Spectroscopy

3.5.1 Pulsed Field Ionisation: Application

As described in Chapter 2, the application of a pulsed electric field to a molecule in a high-n Rydberg state will result in ionisation of the molecule, provided the electric field is of sufficient magnitude. In practise, the use of pulsed electric fields in ZEKE-PFI spectroscopy is more involved than using just a single pulsed field. The main motivation behind using more than one pulse lies in the search for better resolution. Although the limiting resolution in ZEKE-PFI is determined by the bandwidth of the laser used, the actual resolution depends more on the arrangement of the pulsed electric fields.

It has been shown that the long lived manifold of high-n Rydberg states (i.e. those that survive for more than 1 μs) extend some 5 cm^{-1} below the ionisation threshold that they are converging upon.[4] The result of this is that even if one excites these states with a laser with a bandwidth of 0.5 cm^{-1} the use of a voltage pulse of

greater than around 2 V/cm will result in an experimental resolution of 5 cm^{-1}. This effect is shown schematically in figure 3-4(a). Here we have two ionic states that are 3 cm^{-1} apart with the high-*n* manifold extending 5 cm^{-1} below them. Scanning the excitation laser through this region and field ionising the Rydberg states with a 2 V/cm pulse will result in heavily overlapped pair of peaks. Only states separated by more than 5 cm^{-1} will be fully resolved using the above mentioned experimental conditions. The positive side of this is that a resolution of 5 cm^{-1} can be achieved using any size of voltage pulse provided that it is delayed by around 1 μs.

Higher resolution can be achieved in a variety of ways. One way is to use a smaller voltage pulse and thus reduce the depth that the field penetrates into the high *n* Rydberg manifold. This approach has the disadvantage of smaller signal as the number of Rydberg states being field ionised is decreased. This is due to the smaller penetration and the fact that the highest Rydberg states will have been depleted due to ionisation by stray electric fields that are present in the spectrometer.

Another way to achieve higher resolution is to use not one but two pulsed electric fields. A schematic of the effect of using two electric fields is shown in figure 3-4(b). The first pulse, of smaller magnitude field ionises the highest lying Rydbergs whereas the second pulse, at a later time and of larger magnitude, field ionises the small segment of Rydberg states between the limits reached by the two pulses. This increases the resolution of the spectra obtained as the resolution is determined by the energy difference between the two limits of penetration of the electric fields. An extra benefit of this configuration for the pulsed electric fields is that the first pulse can act as a discrimitation pulse against the detection of fast electrons. Varying the voltages of the two fields allows very high resolution spectra to be obtained and also allows for the maximisation of signal as there will be a section in the middle of the high-*n* Rydberg manifold that will be most populated (the highest will be depleted by stray field ionisation and the lowest will be depleted by decay processes).

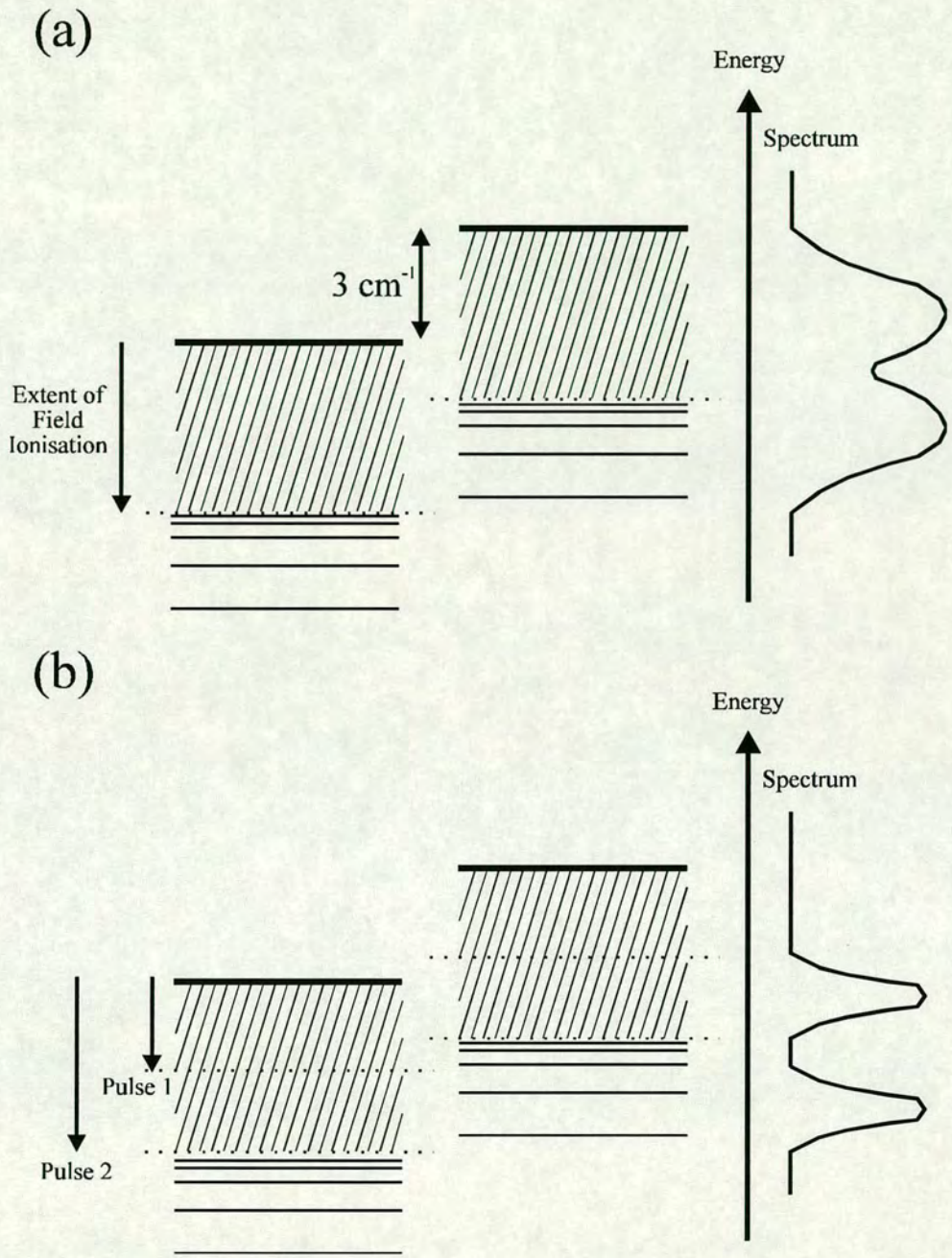

Figure 3-4 - (a) Field limited resolution in ZEKE-PFI spectroscopy with the use of a single pulsed field. (b) The double pulse technique which results in better resolution of spectra.

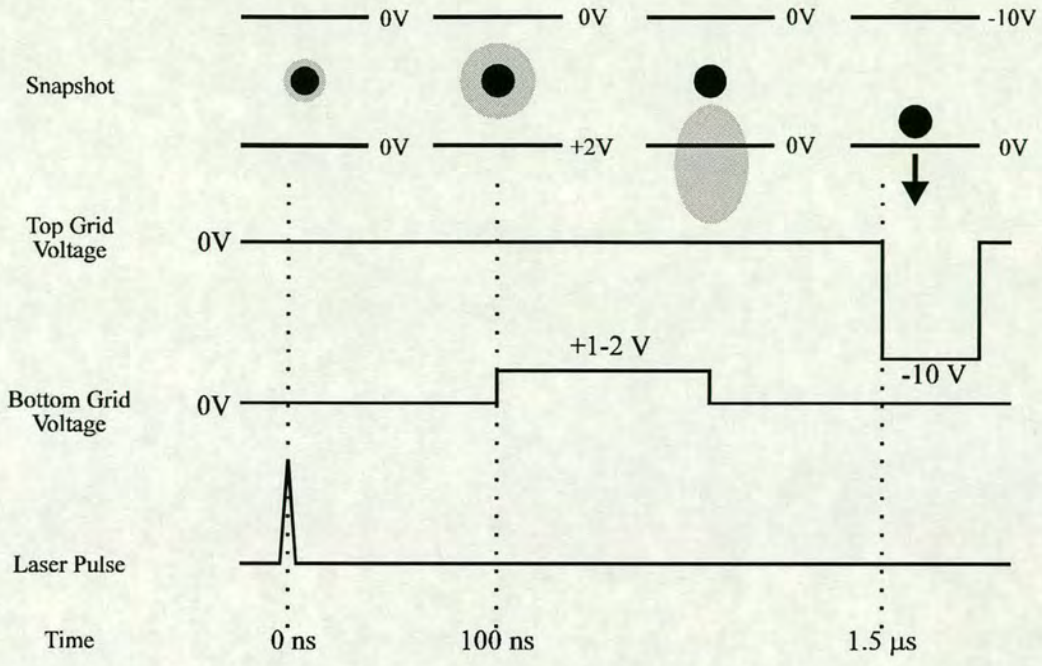

Figure 3-5 - Timeline for a ZEKE-PFI experiment. The top section gives a view of the interaction region during one repetition cycle. The next two sections illustrate the voltage pulse applied to the two copper grids. The gray area in the snapshot represents the kinetic electrons produced from direct photoionisation.

3.5.2 Experimental Timeline

The timeline of a single cycle in a ZEKE-PFI experiment gives the opportunity to decribe the exact details of the ZEKE process and to describe the parameters related to pulsed field ionisation. Figure 3-5 is a schematic diagram of the timing of an experiment. The diagram is split into four sections: a snapshot of the excitation region, the voltage on the top grid, the voltage on the bottom grid and the laser pulse. The time axis runs from left to right.

The laser pulse defines the zero of time. At time zero in the excitation region we have a certain number of high-n Rydberg excited molecules and a certain number of prompt electrons (electrons produced from direct photoionisation). After around 100 ns the prompt electrons have begun to disperse from the centre of the excitation region. At 100 ns the discrimination pulse is applied (roughly 0.3-0.6 V/cm). This

voltage pulse pulls down the prompt electrons and field ionises a small number of the high *n* Rydberg states. After the first pulse has been switched off all that remains in the interaction region is a small number of high *n* Rydberg states. At around 1 to 1.5 μs the second field ionisation (and collection) pulse is applied which field ionises the remaining Rydberg states and sends them to the detector.

3.5.3 Non-ZEKE Peaks

The use of resonant excitation schemes brings a great deal of flexibility and specificity to the technique of ZEKE-PFI spectroscopy. However, the use of multiple photons of different wavelengths (especially tunable wavelengths) opens up the possibility of accidental resanances with neutral excited electronic states. This in itself presents no problem as, unless the accidental resonance still results in the excitation of the molecule to the high-*n* Rydberg manifold, these accidental resonances will not be detected in a ZEKE-PFI spectrum. The situation where this can present a problem is when the accidental resonance results in a large ionisation signal. In this case the large concentration of ions in the excitation region can form a plasma which holds all of the charged particles (ions and electrons) in the interaction region. The result of this is that the discrimination against electrons with kinetic energy does not work. The plasma holds the fast electrons in the ionisation region during the time delay normally used to allow the kinetic electrons to disperse and when the pulsed electric field is applied all the electrons are detected.

This kind of behaviour results in non-ZEKE peaks appearing in the ZEKE-PFI spectrum. Examples of non-ZEKE peaks appearing in ZEKE-PFI spectra can be seen in the (2+1) ZEKE-PFI spectrum of I_2 [5] or the (1+2′) ZEKE-PFI spectrum of I_2.[3] Non-ZEKE peaks have also been seen in a femtosecond multiphoton ZEKE study of xenon.[6,7] Non-ZEKE peaks can be diminished by using neutral density filters to reduce the laser power or by using larger discrimination pulsed fields. However, both of these methods reduce the intensity of the real ZEKE peaks and as a result these measures are only used when the non-ZEKE peaks obscure the ZEKE-PFI spectrum.

3.5.4 Threshold electron spectroscopy

Threshold electron spectroscopy is a technique which allows autoionising Rydberg resonances to be mapped out. Autoionising Rydberg resonances are a well known phenomenon in photoionisation spectra,[8] where the resonances normally appear as very sharp lines against a background of ion production and can be used to extrapolate to higher ionisation thresholds of a molecule. Autoionising resonances have been shown to have an effect on the intensities of peaks in ZEKE-PFI spectra through forced autoionisation [9] and window resonances [10] and as such it is of interest to determine which Rydberg states are responsible for the intensity effects.

In the case of threshold electron spectroscopy the electrons produced by the autoionising Rydberg states are detected as opposed to the ions. As a result no mass resolution is possible although with the use of resonant multi-photon excitation schemes species selectivity is easily obtained. Detection of electrons allows for discrimination against prompt electrons through the use of a time delay before the application of a collection pulse. The result is that electrons produced from direct photoionisation will have a 'head start' to make their way from the ionisation region before any electrons are produced by autoionisation, resulting in a much smaller background signal in the threshold electron spectrum. In the same way, electrons produced by autoionisation processes which release a substantial amont of energy will also be discriminated against.

In terms of experimental details the threshold electron experiments are similar to the ZEKE-PFI experiments. The only difference is that no effort is made to discriminate against fast electrons or, more specifically, threshold electrons (very fast electrons are discriminated against by the time delay applied approximatley 300 ns to 1 μs before the pulsed field extraction.

Figure 3-6 shows a typical threshold electron spectrum, which in this case is the threshold region of the band origin of the $\tilde{X}\,^2\Pi_{3/2,g}$ state of Br_2. This spectrum is recorded using a (2+1′) excitation scheme *via* the $[^2\Pi_{3/2}]_c$ 4d;1_g Rydberg state. The exact details of the spectrum are discussed in chapter 4 but for the purposes of this introductory section on the technique the important thing to notice is that a clear

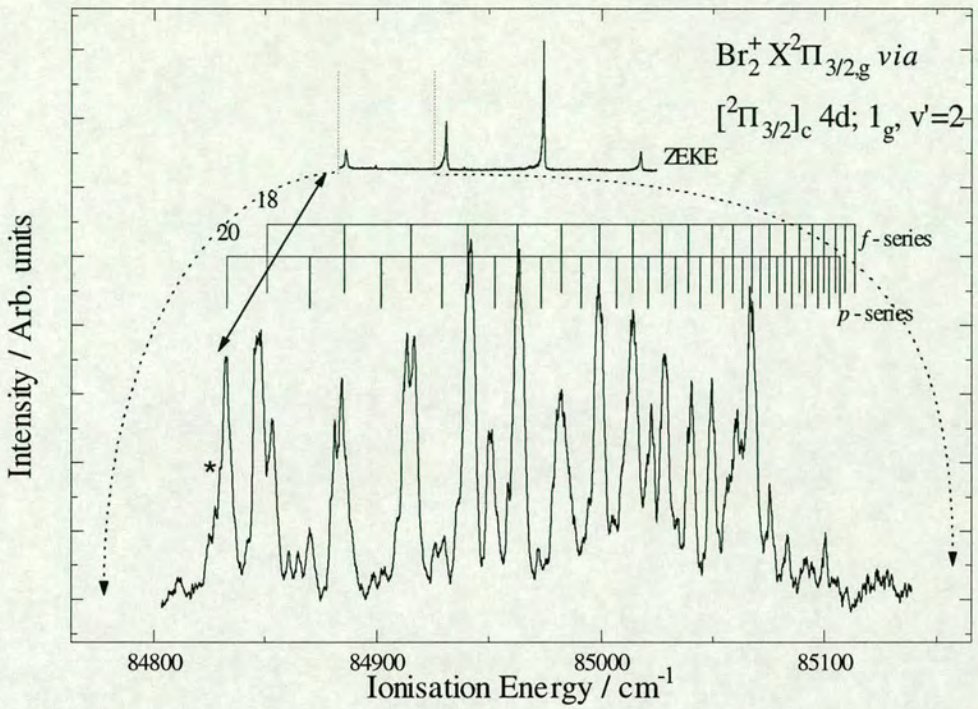

Figure 3-6 - An example of a threshold electron spectrum. The top trace is a ZEKE-PFI spectrum of Br_2 indicating the energy region probed in the threshold electron spectrum (lower trace). The asterisk marks the position of the adiabatic ionisation energy of Br_2.

autoionising Rydberg series progression is observed. The spectrum was recorded using a delay of 300 ns for the 3.8 V/cm extraction pulse.

3.6 Data Handling

3.6.1 Calibration

Energy calibration is perhaps the most important aspect of data handling in any form of spectroscopy. The energy counter reading scale of the dye lasers used in the work presented in this thesis are calibrated using the optogalvanic spectrum of neon. The optogalvanic effect is the result of the change in the electrical properties of a gas discharge when light of a certain wavelength is shone into it. The electrical current that flows through a gas discharge (caused by ionisation of the gas by an applied voltage) is a sensitive function of the energy already possessed by the atoms in the discharge. As a result, if a laser is shone onto the discharge and excites the gas to an excited state the current through the discharge changes. If the optogalvanic spectrum of a gas is known then it can be used to calibrate the output of a dye laser. In this case we use a neon discharge in a hollow cathode lamp. The optogalvanic spectrum of neon has been published,[11] giving a ready source of the information for the calibration of the dye lasers.

The counter reading from the dye laser for each neon transition is plotted against the true counter reading (calculated from the known transition energy) and a linear regression calculation provides an equation which can be used to correct the counter reading of the dye laser. The correction data is only valid for the energy range for which it was recorded and as a result the dye laser counter reading needs to be calibrated for all the dyes that are used. An example of an optogalvanic spectrum is shown in figure 3-7 (a). This spectrum was recorded using a mix of DCM and R640 laser dyes and an example of the plot of counter reading against true counter reading is given in figure 3-7 (b).

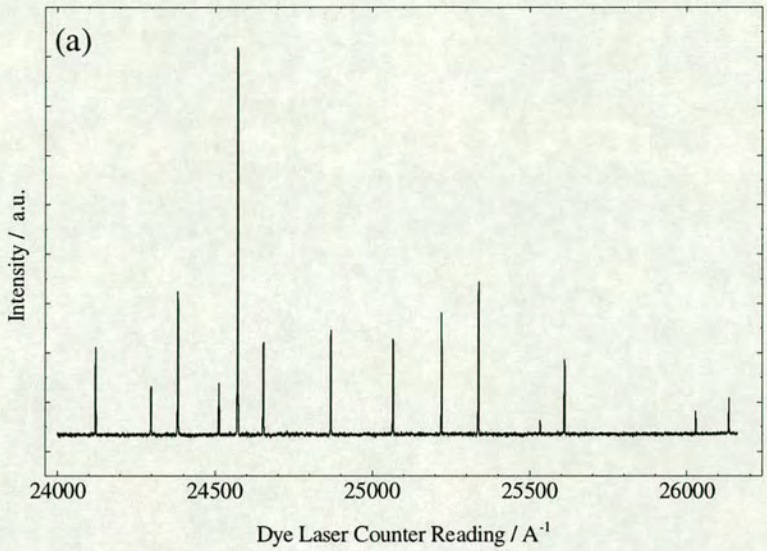

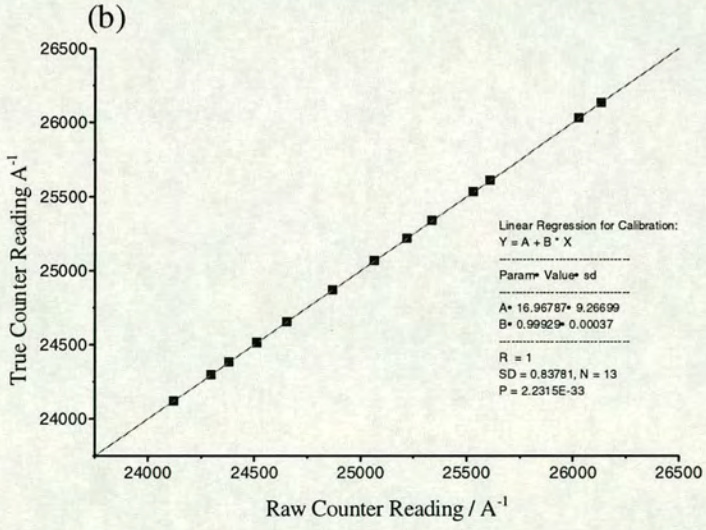

Figure 3-7 - (a) Optogalvanic spectrum of neon recorded with DCM dye in the PDL-2A dye laser (b) Linear regression calculation to allow calibration of the dye laser counter reading.

3.6.2 Field Correction

As a consequence of the mechanism by which ZEKE-PFI signals are obtained (i.e. by the pulsed field ionisation of high-*n* Rydberg states) the peaks in a ZEKE-PFI spectrum are subject to a field ionisation shift. The lowering of the ionisation energy by the application of a pulsed electric field has been discussed in chapter 2 so a description of the mechanism will not be given here.

The field ionisation shift has been shown to be proportional to $c\sqrt{F}$, where c is some constant that depends upon the ionisation mechanism (diabatic or adiabatic) and F is the strength of the electric field in units of V/cm. One way in which the positions of the peaks in a spectrum can be corrected for the field ionisation shift is to record a ZEKE-PFI spectrum using a variety of field strengths and plot the energy of the ZEKE-PFI peak against the square root of the applied field. The points should follow a straight line with gradient c which can be extrapolated back to zero field to give a value for the field-free ionisation energy.

An example of a set of scans of a ZEKE-PFI peak with varying electric field can be seen in figure 3-8 (a). The peak is the origin band of the $\tilde{X}\,^2\Pi_{3/2,g}$ state of Br_2^+ and the dotted line represents the position of the field free ionisation energy. The plot of line position against the square root of the field is shown in figure 3-8 (b). In this case the constant c has the value of 5.4 which is close to the limit for adiabatic ionisation of the high-*n* Rydberg states.

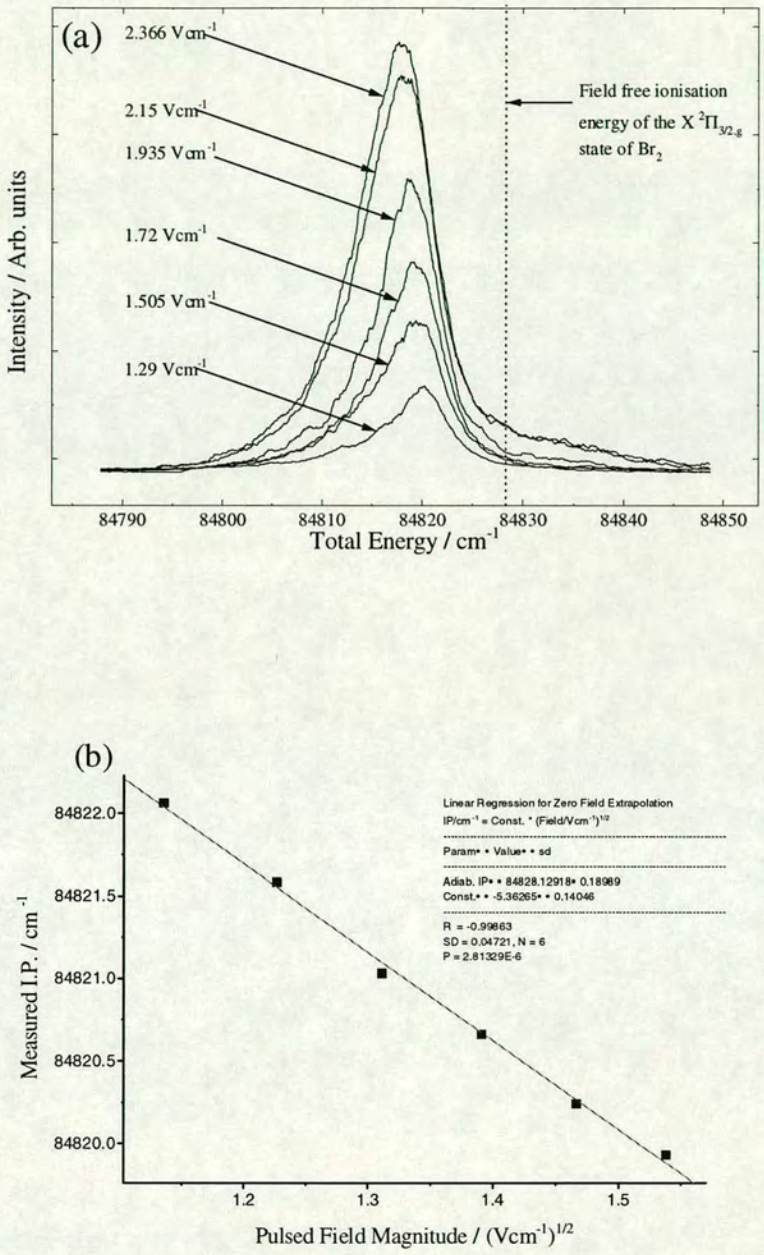

Figure 3-8 - An example of pulsed field correction. In (a) we see a number of spectra recorded at different field strengths. In (b) the peak positions form each spectra are plotted against the square root of the applied field and the field free energy is obtained by extrapolation

3.6.3 Power Normalisation

In spectra where the vibrational intensity distribution is sought there can be problems when the laser power changes dramatically from one end of a scan to the other. This is quite common when covering large energy regions which can only be achieved by using more than one laser dye. If any information on the vibrational intensity distribution is needed for a progression that continues from one dye range to another then the spectra need to be normalised to the laser power. This can be achieved quite simply by recording the laser power throughout a scan using a photodiode, an oscilloscope and a channel of a boxcar integrator. Spectra are divided by the laser power curve to yield a power independant intensity distribution. In the case of a two-photon process the square of the laser power is used to divide the intensity.

3.7 References

[1] F. Merkt, P. M. Guyon, *J.Chem.Phys.* 1993, **99**, 3400; C.-W. Hsu, P. Heimann, M. Evans, S. Stimson, P. T. Fenn, C. Y. Ng, *J.Chem.Phys.* 1997, **106**, 8931.

[2] C. W. Ksu, M. Evans, C. Y. Ng, P. Heimann, *Rev.Sci.Instrum.* 1997, **68**, 1694; C. W. Hsu, P. Heimann, M. Evans, S. Stimson, P. T. Fenn, C. Y. Ng, *J.Chem.Phys.* 1997, **106**, 8931.

[3] M. C. R. Cockett, *J.Phys.Chem.* 1995, **99**, 16228.

[4] G. Reiser, W. Habenicht, K. Müller-Dethlefs, *J.Chem.Phys.* 1993, **98**, 8462.

[5] M. C. R. Cockett, J. G. Goode, K. P. Lawley, R.J. Donovan, *J.Chem.Phys.* 1995, **102**, 5226.

[6] A. Zavriyev, I. Fischer, D. M. Villeneuve, A.Stolow, *Chem.Phys.Lett.* 1995, **234**, 281.

[7] D. M. Villeneuve, I. Fischer, A. Zavriyev, A. Stolow, *J.Chem.Phys.* 1997, **107**, 5310.

[8] W. A. Chupka, J. Berkowitz, *J.Chem.Phys.* 1969, **51**, 4244.

[9] F. Merkt, P. M. Guyon, *J.Chem.Phys.*, 1993, **99**, 3400; F. Merkt, T. P. Softley, *J.Chem.Phys.* 1992, **96**, 4149.

[10] F. Merkt, T. P. Softley, *Int.Rev.Phys.Chem.* 1993, **12**, 205.

[11] S. H. Ashworth, J. M. Brown, 'An Atlas of Optogalvanic Transitions in Neon', Report RAL-91-069 of the Rutherford Appleton Laboratory, UK.

4. The ZEKE-PFI Photoelectron Spectra of I_2, Br_2 and IBr: Factors Affecting Vibrational Intensity Distributions

4.1 Introduction

The work presented in this chapter focuses on the ZEKE-PFI spectroscopy of I_2, Br_2 and IBr. The halogens and interhalogens have been the subject of a great deal of spectroscopic investigation as they represent a good example of related homonuclear and heteronuclear diatomics. The spectroscopy of the ionic states of the halogens and interhalogens has been studied in detail using conventional photoelectron spectroscopy, [1,2,3,4,5] laser induced fluorescence [6,7] and threshold photoelectron spectroscopy.[8,9] However, the determined ionisation energies for the halogens from these studies are only accurate to approximately 30 cm^{-1}. Molecular iodine has been the subject of recent work by this research group using ZEKE-PFI spectroscopy, [10,11,12] in which various excitation routes were explored (coherent two-photon, two-colour (2+1′) and two-colour (1+2′)) and accurate spectroscopic constants were determined for the X $^2\Pi_{3/2,g}$, X $^2\Pi_{1/2,g}$, A $^2\Pi_{3/2,u}$ and a $^4\Sigma_u^-$ states of I_2^+. The work in this chapter follows up on the I_2 study and investigates the ground ionic states of Br_2 and IBr using ZEKE-PFI spectroscopy. As well as determing accurate spectroscopic constants for Br_2^+ and IBr^+, we have investigated the contribution of final state and intermediate state interactions to the observed vibrational intensity distributions in the ZEKE-PFI spectra of I_2, Br_2 and IBr.

The intensities of vibrational peaks in any form of electronic spectroscopy are, to a first approximation, governed by Franck-Condon factors. A good prediction or simulation of peak intensities can be obtained by calculating the overlap of the vibrational wavefunctions between the initial vibronic state and the possible final vibronic states. As discussed in Chapter 2, the simulation of vibrational intensity

distributions using Franck-Condon factors is the standard way of determining bond length changes upon excitation between electronic states.

However, the simple Franck-Condon picture of vibronic transition intensities can be upset quite dramatically. Deviations from the expected vibrational intensity distribution (Franck-Condon controlled) are mainly due to final state interactions or intermediate state interactions. Final state interactions occur when the final state in an electronic transition is perturbed or mixed with another electronic state leading to unexpected intensities for the vibronic transitions. Intermediate state interactions can occur when multiple photon excitation schemes are used in electronic transitions. Accidental resonances with states at the intermediate photon level can have a pronounced effect on the observed vibrational intensity distribution.

In ZEKE-PFI photoelectron spectroscopy both of these type of interactions can and do occur. The nature of the ZEKE-PFI technique means that excitation is to pseudo-continua of high *n* Rydberg states that converge on the ionisation thresholds of a molecule. The density of other Rydberg states around the ionisation thresholds of a molecule (converging to higher ionisation thresholds) can be substantial leading to the possibility of final state interactions and perturbations to the intensity of vibrational peaks in ZEKE-PFI spectra. Also, due to the dominance of multiple photon excitation schemes used in ZEKE-PFI spectroscopy, there is the possibility that intermediate state interactions could alter the vibrational intensity distributions observed.

Simple final state interactions involving the high *n* Rydberg manifold and a single low *n* Rydberg level can manifest themselves in two ways; the ZEKE-PFI peaks can have their intensity enhanced or depleted. Enhancement of ZEKE-PFI peaks is caused through the mechanism of forced autoionisation, as discussed in section 2.5. This type of interaction has been observed in the single photon ZEKE-PFI spectra of N_2 [13] and H_2 [14] with forced *vibrational* autoionisation being the cause of the intensity enhancement in H_2. Depletion of ZEKE-PFI peak intensities is termed a 'window resonance' and is the result of a shortening of the lifetime of the high *n* Rydberg states by the interaction with a resonant low *n* Rydberg state. The effect of window resonances in ZEKE-PFI spectra was discussed in depth in a review article by Merkt

and Softley.[15] The review focuses mainly on rotational autoionisation processes as they are the most common cause of 'window resonances'.

Other types of final state interaction are those involving more than two states. Three state coupling processes are quite common in threshold electron spectroscopy (TPES)[16] where interactions between low *n* Rydberg states, neutral repulsive continua and highly vibrationally excited high *n* Rydberg states can cause extended vibrational progressions to be observed. Examples of extended vibrational progressions can be seen in the TPES spectra of I_2, Br_2 and Cl_2 recorded by Yencha *et al.*[8,9] The three state mechanism can also have an influence on the vibrational intensity distribution in a ZEKE-PFI spectrum as seen in the work of Kong and Hepburn on O_2^+, excited by single photon VUV radiation.[17] In this study, vibrational levels up to $v^+ = 24$ were observed in the ZEKE-PFI spectrum. In the conventional He(I) photoelectron spectrum of O_2, which reflects the Franck-Condon factors for the transition, only vibrational levels up to $v^+ = 5$ are observed.[18] Kong and Hepburn invoke a similar mechanism to that used to explain the observation of highly vibrationally excited states in TPES spectra. However, the mechanism invoked by Kong and Hepburn differs in one respect. The extension of the observed vibrational intensity distributions in TPES relied upon indirect excitation of the vibrationally excited ion states. In the work of Kong and Hepburn it was seen that the excitation is directly to the high *n* Rydberg states below the vibrationally excited ionic states. It was also shown that an exact resonance with a low *n* Rydberg state is not required to allow the observation of the highly vibrationally excited peaks in the ZEKE-PFI spectrum.

Intermediate state interactions can also have a large effect on the observed vibrational intensity distributions in ZEKE-PFI spectroscopy. The most dramatic example of an intermediate state interaction is the coherent two-photon (C2P) ZEKE-PFI spectra of the alkyl iodides, CH_3-I and C_2H_5-I.[19] C2P ZEKE-PFI spectroscopy uses two photons of the same energy to excite a molecule directly from the ground state of the neutral to the ion. In the C2P ZEKE-PFI spectra of the two molecules mentioned above, extended vibrational progressions are seen in the R-I stretching mode (where R = CH_3 and C_2H_5) where, on the basis of Franck-Condon factors, only

an origin band should be observed. The reason given as the cause of the extended progression is absorption to a repulsive intermediate state at the one-photon level, resulting in bond extension and a widening of the Franck-Condon window for excitation to the high *n* Rydberg states. This explanation has been conclusively proven in a comparison of the single photon and C2P ZEKE-PFI spectra of CH_3-I by Zhu and Grant [20] where no progression is seen in the CH_3-I stretch in the single photon ZEKE-PFI spectrum.

Interactions involving bound intermediate states can also influence vibrational intensity distributions in ZEKE-PFI spectroscopy. An example of this is the (1+2′) ZEKE-PFI spectrum of I_2,[10] in which accidental resonances with the ion-pair states of I_2 at the (1+1′) two-photon energy have been shown to enhance certain vibrational levels in the ZEKE-PFI spectrum.

The structure of the chapter is as follows. In section 4.2 and 4.3 the (2+1′) ZEKE-PFI spectra of the X $^2\Pi_{3/2,g}$ and X $^2\Pi_{1/2,g}$ states of I_2^+ and Br_2^+ are presented. The vibrational intensity distributions observed are shown to be influenced by forced vibrational autoionisation. In section 4.4 and 4.5 the C2P ZEKE-PFI spectra of the X $^2\Pi_{3/2,g}$ and X $^2\Pi_{1/2,g}$ states of Br_2^+ and IBr^+ are presented. The influence of intermediate state interactions in these spectra and the C2P ZEKE-PFI spectra of the analogous states in I_2 is discussed. Finally, in section 4.6, the (2+1′) and (1+2′) ZEKE-PFI spectra of the X $^2\Pi_{3/2,g}$ state of IBr^+ are presented. The contributions of final state ((2+1′) ZEKE-PFI spectrum) and intermediate state interactions ((1+2′) ZEKE-PFI spectrum) to the spectra are discussed.

4.2 Vibrational Autoionisation in the (2+1′) ZEKE-PFI Spectrum of I_2

4.2.1 Introduction

The ZEKE-PFI photoelectron spectrum of I_2 has been recorded *via* a number of excitation routes by the Edinburgh ZEKE group.[10,11,12] The first route used was a two-colour (2+1′) excitation *via* the $[^2\Pi_{3/2}]_c$ 5d; 2_g and $[^2\Pi_{1/2}]_c$ 5d; 2_g Rydberg states.[11] In this work the ZEKE-PFI spectra of the two spin-orbit components of the ground ionic state ($X\ ^2\Pi_{3/2,g}$ and $X\ ^2\Pi_{1/2,g}$) were recorded by exciting through the corresponding 5d; 2_g spin-orbit Rydberg state. One of the most interesting features of this work was the vibrational intensity distributions of the ZEKE spectra of the $X\ ^2\Pi_{3/2,g}$ and $X\ ^2\Pi_{1/2,g}$ states. It was observed that the vibrational intensity distribution of the $X\ ^2\Pi_{1/2,g}$ state agreed with predictions based on Franck-Condon factors whereas the distribution of the $X\ ^2\Pi_{3/2,g}$ state did not.

The explanation given at the time was that low *n* Rydberg states, converging on the upper spin orbit state, were undergoing forced autoionisation and contributing to the intensity of the ZEKE peaks. For low *n* Rydberg states to contribute in this way there needs to be a close resonance between a low *n* Rydberg state and the manifold of high *n* Rydberg states below the ionisation threshold. If there is no resonance then the low *n* Rydberg state will not be able to influence the intensity of the ZEKE peak. As mentioned, the upper spin orbit component is seemingly unaffected by any autoionisation processes whereas the lower spin orbit component is greatly affected. Spin-orbit autoionising Rydberg states appeared to be the obvious choice to explain the differences between the two spectra as there are no Rydberg states that can spin-orbit autoionise into the upper spin-orbit component.

In an effort to observe and identify any autoionising Rydberg states around the threshold region of I_2 a threshold electron spectrum has been recorded around the band origins of both spin-orbit states. In a threshold electron experiment electrons produced by autoionisation are detected as the wavelength of the laser is scanned across the ionisation thresholds of a molecule. A small time delay is used before the

collection pulse is applied to discriminate against very fast electrons (produced from multiple photon absorption) by allowing them to escape the ionisation region. This ensures that only electrons from autoionising Rydberg states near the ionisation threshold are observed.

It has emerged from this work that the Rydberg states responsible for the anomalous intensity distribution in the ZEKE-PFI spectra of the X $^2\Pi_{3/2,g}$ state of I_2 are not Rydberg states converging on the upper spin-orbit component. From the threshold electron spectra it will be seen that forced *vibrational* autoionisation, rather than spin-orbit autoionisation, is the cause of the observed distributions. This is only the second observation of forced vibrational autoionisation affecting the intensity of a peak in a ZEKE-PFI spectrum, the first being observed in the single-photon ZEKE-PFI spectrum of H_2.[14]

4.2.2 Results

4.2.2.1 Experimental Details

The details of the (2+1′) ZEKE-PFI experiments of I_2 have been described in a previous publication and will not be mentioned here.[11] For the (2+1′) threshold electron experiments the pump laser used DCM and a mixture of R610 and R590 dyes to produce light of between 635 and 590 nm which was frequency doubled using a KD*P crystal to produce the UV wavelengths necessary to excite the $[^2\Pi_{3/2}]_c$ 5d; 2_g and $[^2\Pi_{1/2}]_c$ 5d; 2_g Rydberg states respectively. The probe laser used LD821 dye to produce visible/near infra-red light which was used (undoubled) to excite I_2 from the Rydberg states to the thresholds of the X $^2\Pi_{3/2,g}$ and X $^2\Pi_{1/2,g}$ states of I_2^+. Voltage pulses of between 3 and 3.8 V/cm^{-1} were applied to the top plate of the spectrometer to detect the threshold electrons after a delay of approximately 1.15μs. The iodine sample was placed within a heated nozzle assembly which was held at approximately 70 °C. The resultant iodine vapour was seeded in the argon carrier gas at 1.2 atm. pressure and introduced to the chamber through a General Valve pulsed nozzle.

4.2.2.2 The (2+1′) ZEKE-PFI spectrum of I_2

The ZEKE spectra of the X $^2\Pi_{3/2,g}$ and the X $^2\Pi_{1/2,g}$ states of I_2 recorded *via* the $[^2\Pi_{3/2}]_c$ 5d;2_g and $[^2\Pi_{1/2}]_c$ 5d;2_g are shown in figures 4-1 and 4-2 respectively. As these spectra have been presented in a previous publication,[11] a detailed discussion of the assignment will not be given. Only the details relevant to the discussion of final state interactions will be mentioned. The $[^2\Pi_{3/2}]_c$ 5d;2_g and $[^2\Pi_{1/2}]_c$ 5d;2_g Rydberg states of I_2 have previously been characterised in a (2+1) resonance enhanced multiphoton ionisation (REMPI) study [21] although the assignment of the states are taken from more recent work on the REMPI spectroscopy of analogous Rydberg states of Br_2.[22]

Given the similarity of the intermediate state potentials with those of the ion it was expected that any transitions would be reasonably diagonal in nature (i.e. $\Delta v = 0$). ZEKE spectra were recorded *via* a number of vibrational levels of the $[^2\Pi_{3/2}]_c$ and $[^2\Pi_{1/2}]_c$ 5d; 2_g Rydberg states in order to cover a reasonable portion of the ionic state potentials. As can be seen in Figure 4-2, the ZEKE spectra of the upper spin orbit component (X $^2\Pi_{1/2,g}$) exhibit classic Franck-Condon behaviour for the vibrational intensity distributions, with most of the intensity in the diagonal transtion ($\Delta v = 0$) and a small amount of intensity in the off-diagonal transitions ($\Delta v = \pm 1$). However, the vibrational intensity distributions in the ZEKE spectra of the lower spin orbit component (X $^2\Pi_{3/2,g}$) do not follow the expected Franck-Condon pattern. Although the diagonal transitions in the spectra in Figure 4-1 do still dominate, the off-diagonal transitions to lower energy ($\Delta v = -1$ and -2) have a substantial amount of intensity.

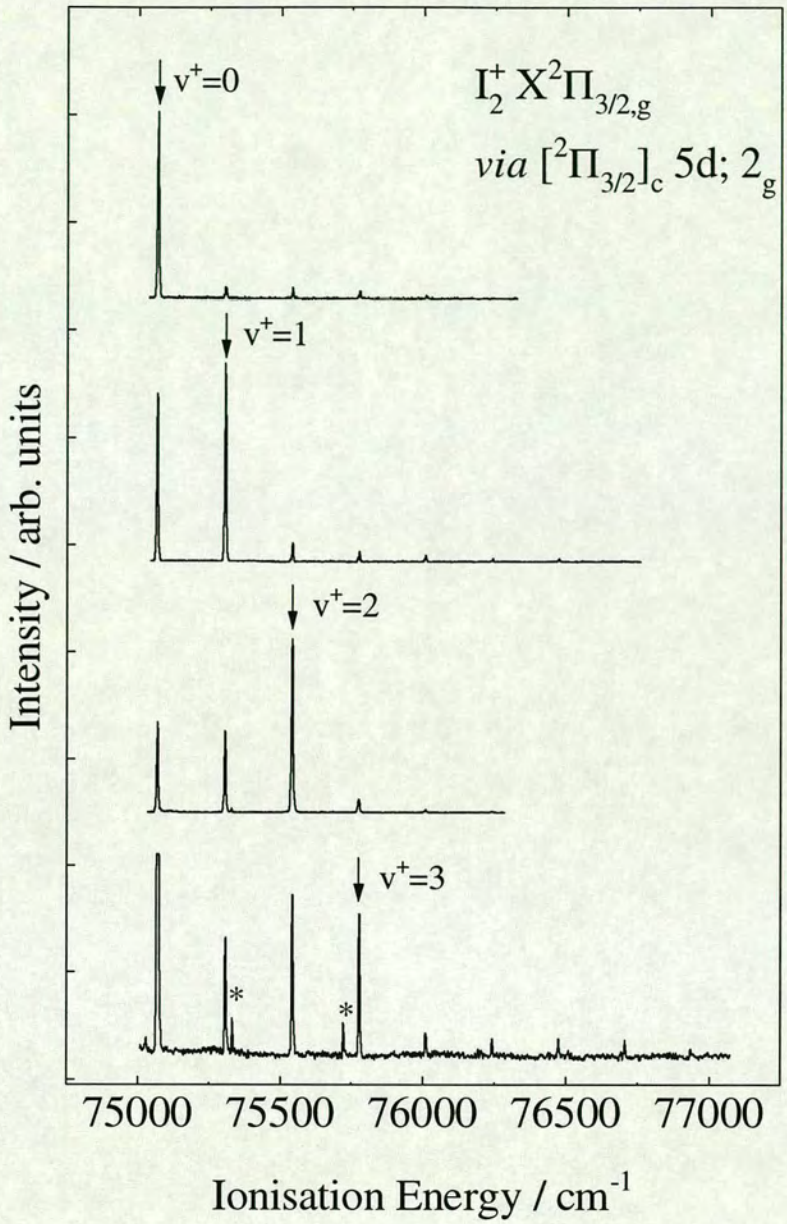

Figure 4-1 - The (2+1′) ZEKE-PFI spectrum of I_2 recorded *via* the $[^2\Pi_{3/2}]_c$ 5d;2_g Rydberg state. The vertical arrows indicate the $\Delta v = 0$ transition and the small peaks marked with an asterisk indicate accidental $A \leftarrow X$ neutral state resonances (see text for details).

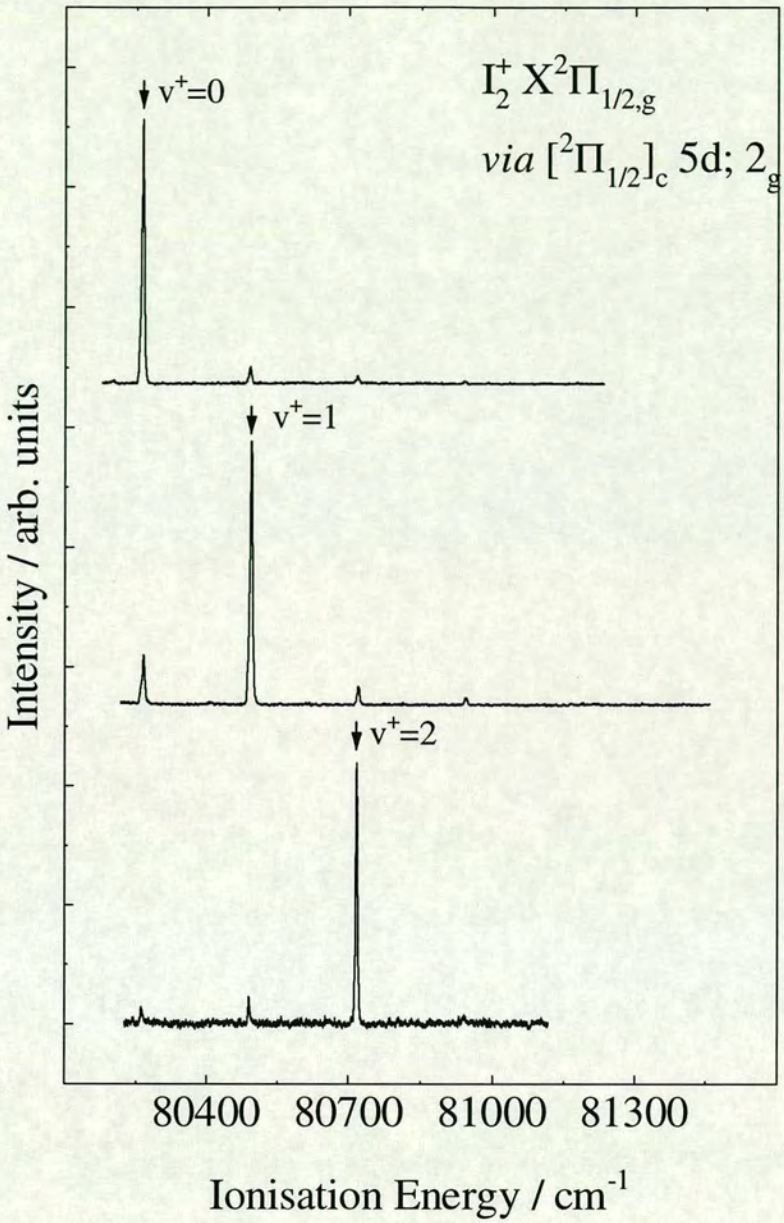

Figure 4-2 - The (2+1′) ZEKE-PFI spectrum of I_2 recorded *via* the $[^2\Pi_{1/2}]_c$ 5d;2_g Rydberg state. The vertical arrows indicate the $\Delta v = 0$ transition.

4.2.2.3 The (2+1′) threshold electron spectrum of I_2 in the region of the X $^2\Pi_{3/2,g}$ state

The (2+1′) threshold electron spectrum of I_2 in the region of the band origin of the X $^2\Pi_{3/2,g}$ state of I_2^+ is shown in Figure 4-3. The intermediate state used was v′ = 1 of the $[^2\Pi_{3/2}]_c$ 5d; 2_g Rydberg state. The corresponding ZEKE-PFI spectrum is also shown at the top of Figure 4-3. The double headed arrow indicates the position of the band origin of the X $^2\Pi_{3/2,g}$ state in both spectra.

The threshold spectrum is dominated by two autoionising Rydberg state progressions which converge on $v^+ = 1$ of the X $^2\Pi_{3/2,g}$ state of I_2^+. These progressions have been assigned to *p* Rydberg series (a $p\sigma$ and $p\pi$ series) on the basis of the Laporte selection rule, atomic quantum defects,[23] and molecular quantum defects from the single photon VUV work of Venkateswarlu.[24] The intermediate state in this case is a *d* Rydberg state. In a one-photon transition from this state we would expect to populate either *p* or *f* Rydberg states based on considerations of the parity of the final state. The quantum defects of the Rydberg states observed in the spectra were calculated using the Rydberg equation:

$$T([\Omega_c]nl) = IP(\Omega_c) - \frac{R}{[n-\delta(l)]^2} \qquad (4.1),$$

$T([\Omega_c]nl)$ is the observed energy of the Rydberg state, R is the Rydberg constant, $IP(\Omega_c)$ is the energy of the ionic state that the Rydberg series converges to and $\delta(l)$ is the angular momentum dependent quantum defect. Using the energy of $v^+ = 1$ as $IP(\Omega_c)$ the Rydberg states separated into two series with quantum defects of 3.45 and 3.65. These values are very close to the range of atomic iodine quantum defects for *p* Rydberg states of 3.35-3.55. The Rydberg series to lower energy ($\delta = 3.65$) has been assigned to be a $p\sigma$ series and the series to higher energy ($\delta = 3.45$) has been assigned to be a $p\pi$ series based on the quantum defects of the $p\sigma$ and $p\pi$ series observed by Venkateswarlu.[24] The peak energies and the assignment of the autoionising Rydberg states are given in table 4-1. The ladders in figure 4-3 are simulations of the positions of Rydberg states that most closely match the observed Rydberg state positions.

The important feature in the threshold electron spectrum is the exact resonance of the $n = 25$ $p\sigma$ Rydberg state (75065±2 cm^{-1}) with the position of the ZEKE peak for the band origin of the X $^2\Pi_{3/2,g}$ state of I_2^+ (75066 ±2 cm^{-1}). This would seem to give support to the interpretation that forced autoionisation is the reason behind the anomalous intensity distributions in the ZEKE-PFI spectrum of I_2. However, the Rydberg state that is resonant with the band origin is undergoing forced vibrational, rather than spin-orbit, autoionisation. Also of interest is the fact that no autoionising Rydberg progressions converging to higher vibrational levels are observed. This observation is consistent with the proposed $\Delta v = -1$ propensity rule for vibrational autoionisation.[25]

4.2.2.4 The (2+1′) threshold electron spectrum of I_2 in the region of the X $^2\Pi_{1/2,g}$ state

The (2+1′) threshold electron spectrum of I_2 in the region of the band origin of the X $^2\Pi_{1/2,g}$ state of I_2^+ is shown in figure 4-4. The intermediate state used was $v' = 1$ of the $[^2\Pi_{1/2}]_c$ 5d; 2_g Rydberg state. The corresponding ZEKE-PFI spectrum for this region is also shown at the top of figure 4-4. The double headed arrow indicates the position of the band origin of the X $^2\Pi_{1/2,g}$ state in both spectra.

The threshold spectrum is dominated by an autoionising Rydberg state progression which converges on $v^+ = 1$ of the X $^2\Pi_{1/2,g}$ state of I_2^+. The progression has been assigned to $p\pi$ Rydberg series on the basis of quantum defects, the Laporte selection rule and the quantum defect of the $p\pi$ series in the threshold electron spectrum of the X $^2\Pi_{3/2,g}$ state (see figure 4-3). The peak energies and assignments of the autoionising Rydberg states are given in table 4-2. The ladder in figure 4-4 represents a simulation of the Rydberg state line positions that most closely matches the observed line positions.

It can be seen from figure 4-4 that no autoionising Rydberg level is resonant or near-resonant with the band origin of the X $^2\Pi_{1/2,g}$ state of I_2^+. This observation points to a possible explanation of the differences between the ZEKE-PFI spectra of the X $^2\Pi_{3/2,g}$ and X $^2\Pi_{1/2,g}$ states of I_2^+. Without a resonance a low n Rydberg state

will not be able to influence the intensity of a ZEKE peak if a simple two state coupling is responsible.

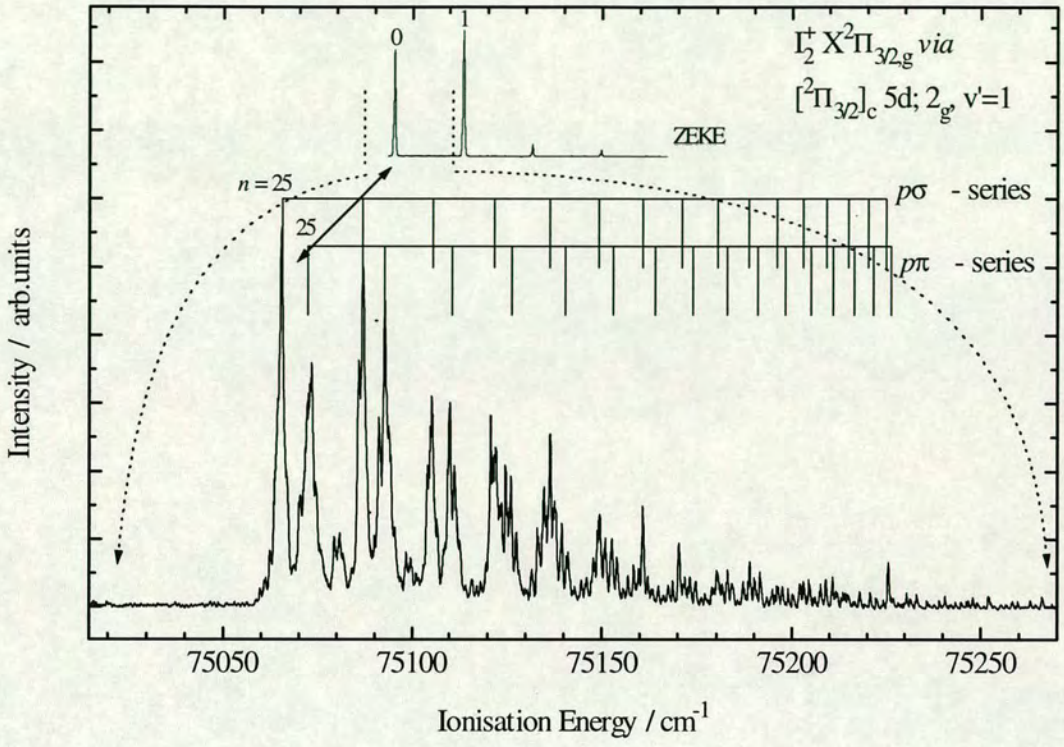

Figure 4-3 - The (2+1′) threshold electron spectrum of I_2 in the region of the $X\ ^2\Pi_{3/2,g}$, $v^+ = 0$ ionisation threshold, recorded *via* $v' = 1$ of the $[^2\Pi_{3/2}]_c$ 5d;2_g Rydberg state. The top trace is the ZEKE-PFI spectrum recorded with the same excitation scheme. The double headed arrow indicates the position of $v^+ = 0$ in both spectra. The area of the ZEKE-PFI spectrum enclosed by the dotted lines represents the energy range of the threshold electron spectrum

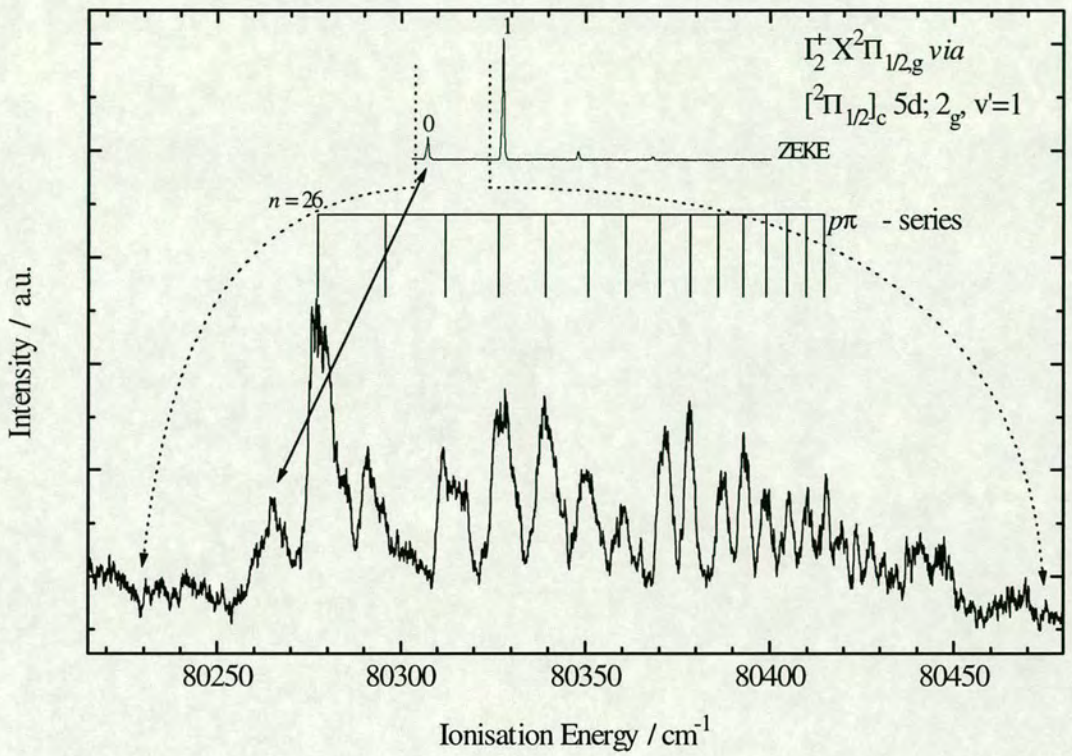

Figure 4-4 - The (2+1′) threshold electron spectrum of I_2 in the region of the X $^2\Pi_{1/2,g}$, $v^+ = 0$ ionisation threshold, recorded *via* $v' = 1$ of the $[^2\Pi_{1/2}]_c$ 5d;2_g Rydberg state. The top trace is the ZEKE-PFI spectrum recorded with the same excitation scheme. The black arrow indicates the position of $v^+ = 0$ in both spectra. The area of the ZEKE-PFI spectrum enclosed by the dotted lines represents the energy range of the threshold electron spectrum.

Table 4-1 - Peak positions and assignments of the autoionising Rydberg states converging on $v^+ = 1$ of the X $^2\Pi_{3/2,g}$ state of I_2^+.

Peak Energy (cm^{-1})	Assignment	Peak Energy (cm^{-1})	Assignment
75065	$n = 25, p\sigma$	75073	$n = 25, p\pi$
75087	$n = 26, p\sigma$	75093	$n = 26, p\pi$
75105	$n = 27, p\sigma$	75110	$n = 27, p\pi$
75121	$n = 28, p\sigma$	75125	$n = 28, p\pi$
75136	$n = 29, p\sigma$	75139	$n = 29, p\pi$
75149	$n = 30, p\sigma$	75153	$n = 30, p\pi$
75161	$n = 31, p\sigma$		
75170	$n = 32, p\sigma$		
75180	$n = 33, p\sigma$		
75189	$n = 34, p\sigma$		

Table 4-2 - Peak positions and assignments of the autoionising Rydberg states converging on $v^+ = 1$ of the X $^2\Pi_{1/2,g}$ state of I_2^+.

Peak Energy (cm^{-1})	Assignment	Peak Energy (cm^{-1})	Assignment
80278	$n = 26, p\pi$	80393	$n = 36, p\pi$
80295	$n = 27, p\pi$	80399	$n = 37, p\pi$
80312	$n = 28, p\pi$	80405	$n = 38, p\pi$
80328	$n = 29, p\pi$	80410	$n = 39, p\pi$
80339	$n = 30, p\pi$	80415	$n = 40, p\pi$
80350	$n = 31, p\pi$	80419	$n = 41, p\pi$
80360	$n = 32, p\pi$	80423	$n = 42, p\pi$
80371	$n = 33, p\pi$	80427	$n = 43, p\pi$
80378	$n = 34, p\pi$	80431	$n = 44, p\pi$
80387	$n = 35, p\pi$		

4.2.3 Discussion

The observation of a low *n* autoionising Rydberg state having an exact resonance with the ZEKE-PFI peak of the band origin of the X $^2\Pi_{3/2,g}$ state of I_2^+ would seem to explain the observation of a non Franck-Condon intensity distribution in the ZEKE-PFI spectrum shown in figure 4-1. Forced vibrational autoionisation of this Rydberg state ($n = 25\ p\sigma$) would seem to be the source of the enhanced intensity of the $v^+ = 0$ peak in the ZEKE-PFI spectrum *via* $v' = 1$ of the $[^2\Pi_{3/2}]_c$ 5d; 2_g Rydberg state in figure 4-1.

The intensity anomalies in the other ZEKE-PFI spectra recorded *via* different vibrational levels of the same Rydberg state can also be explained by invoking the mechanism of forced vibrational autoionisation. It would be expected that the resonance will be less exact around the $v^+ = 1$ and 2 ZEKE-PFI peaks as the vibrational spacing will change, eventually tuning off the resonance with the Rydberg state with increased vibrational excitation. However, for the first few vibrational levels the $n = 25\ p\pi$ Rydberg state converging on $v^+ = x + 1$ will be resonant with the ZEKE-PFI peak for $v^+ = x$, resulting in an enhancement of the ZEKE-PFI signal, as observed in the ZEKE-PFI spectra shown in figure 4-1.

The fact that only the X $^2\Pi_{3/2,g}$ state has an exact resonance with a Rydberg state converging on a higher ionic threshold, and the X $^2\Pi_{1/2,g}$ state does not, provides an explanation for the observed differences between the ZEKE-PFI spectra of the two spin-orbit components. For forced autoionisation to influence the intensity of a ZEKE-PFI peak there needs to be a near or exact resonance. The threshold electron spectrum of the X $^2\Pi_{1/2,g}$ state shows us that there is no resonance between a low *n* Rydberg state and the position of the ZEKE-PFI peak for $v^+ = 0$ and therefore there can be no enhancement of the ZEKE-PFI signal.

Another contributing factor to the differences between the ZEKE-PFI spectra of the two spin-orbit components is spin-orbit autoionisation. Spin-orbit autoionisation may well reduce the possibility of forced vibrational autoionisation intensity effects by shortening the lifetime of possible resonant Rydberg states. A very short lived Rydberg state resonant with a ZEKE-PFI peak can sometimes result in a

decrease in intensity of the peak producing a 'window resonance'.[15] However, in this case, it is more likely that there is simply no resonance with which to cause any intensity effect.

.Spin-orbit autoionisation may be responsible for only one Rydberg series being observed in the threshold electron spectrum of I_2 in the region of the $X\ ^2\Pi_{1/2,g}$ state (figure 4-4). Only the $p\pi$ Rydberg series is observed which contrasts with the observation of two Rydberg series ($p\pi$ *and* $p\sigma$) in the threshold electron spectrum around the lower spin-orbit component of the X state (figure 4.3). The reason for the absence of the $p\sigma$ series could be due to preferential spin-orbit autoionisation. If a Rydberg state were to spin orbit ionise the energy given to the electron will most likely be far greater than if the Rydberg state were to vibrationally autoionise. Electrons produced from spin-orbit autoionisation may not be observed in the threshold electron experiments as they will have enough energy to escape from the ionisation region in the 1μs or so between excitation of the Rydberg state and collection of any electrons from autoionisation processes.

The reason why a $p\sigma$ Rydberg state would peferentially spin-orbit autoionise over a $p\pi$ Rydberg state is not clear. Electronic autoionsation, of which spin-orbit autoionisation is a sub-class, involves an electron exchange interaction where the Rydberg electron relaxes into a valence orbital and the excess energy of the molecule is used to kick out an electron from a valence orbital of higher energy. In this way, electronic autoionisation is very much like an Auger process. In I_2 spin-orbit autoionisation requires that one of the valence electrons from the outer π_g shell is exchanged for the Rydberg electron. Intuitively, it would be expected that any electron exchange will be far more likely in a process that does not require a change in the value of the Rydberg electron orbital angular momentum around the internuclear axis (λ_{Ryd}). This would seem to indicate that the $p\pi$ series ($\lambda_{Ryd} = 1$) should be more susceptible to exchange with a π_g valence electron ($\lambda = 1$) than the $p\sigma$ series ($\lambda_{Ryd} = 0$). However, this does not agree with the observations from the threshold electron spectra of I_2.

In summary, we have presented the (2+1′) threshold electron spectra of the energy regions around the band origins of both spin-orbit components of the ground state of I_2^+ ($\tilde{X}\,^2\Pi_{3/2,g}$ and $\tilde{X}\,^2\Pi_{1/2,g}$). The autoionising Rydberg series observed provide an explanation of the observed intensity perturbations in the (2+1′) ZEKE-PFI spectra of I_2.[11] The mechanism through which the intensity of the vibrational peaks is altered has been determined to be forced vibrational autoionisation.

4.3 The (2+1′) ZEKE-PFI Spectrum of Br_2

4.3.1 Introduction

The cation states of molecular bromine have been reasonably well studied using photoelectron spectroscopy, [1,2,3,5] laser induced fluorescence (LIF),[6,7] and velocity modulation spectroscopy.[26] More recently, Br_2 has been studied by threshold photoelectron spectroscopy (TPES).[9] Accurate (sub-wavenumber) spectroscopic constants for the X $^2\Pi_{3/2,g}$, *A* $^2\Pi_{3/2,u}$ and *A* $^2\Pi_{1/2,u}$ states of Br_2 have been determined from the LIF [6,7] and velocity modulation spectroscopy.[26] However, the most accurate values obtained for the ionisation energies of the two spin-orbit components of the ground state, X $^2\Pi_{3/2,g}$ and X $^2\Pi_{1/2,g}$, are 84833±24 cm^{-1} and 87648±24 cm^{-1} respectively.[9]

In this section we present the (2+1′) ZEKE-PFI photoelectron spectrum of the X $^2\Pi_{3/2,g}$ and X $^2\Pi_{1/2,g}$ states of Br_2^+. The intermediate states used in the study were the $[^2\Pi_{3/2}]_c$ 4d; 1_g and $[^2\Pi_{1/2}]_c$ 4d; 1_g Rydberg states. The choice of Rydberg states was one of convenience in terms of the laser wavelengths needed for the excitation. The two Rydberg states have already been characterised by mass-resolved (2+1) REMPI spectroscopy.[27,28] A schematic potential diagram of the two Rydberg states and the spin-orbit components of the ground ionic state of Br_2 is shown in figure 4-5.

In this section we report accurate ionisation energies for the X $^2\Pi_{3/2,g}$ and X $^2\Pi_{1/2,g}$ spin-orbit components of the ground state of Br_2^+ from which we have determined an accurate value for the spin-orbit splitting of the X $^2\Pi_g$ state. We also compare the (2+1′) ZEKE-PFI spectra obtained for Br_2 with those of I_2. Some evidence is seen of non Franck-Condon behaviour in the ZEKE-PFI spectrum of the X $^2\Pi_{3/2,g}$ state of Br_2^+ and this has been investigated using threshold electron spectroscopy. Threshold electron spectra of the region around the first two vibrational levels of the X $^2\Pi_{3/2,g}$ state of Br_2^+ have been recorded. These spectra provide evidence for the contribution of forced vibrational autoionisation to the (2+1′) ZEKE-PFI spectra of the X $^2\Pi_{3/2,g}$ state of Br_2^+. The conditions necessary for

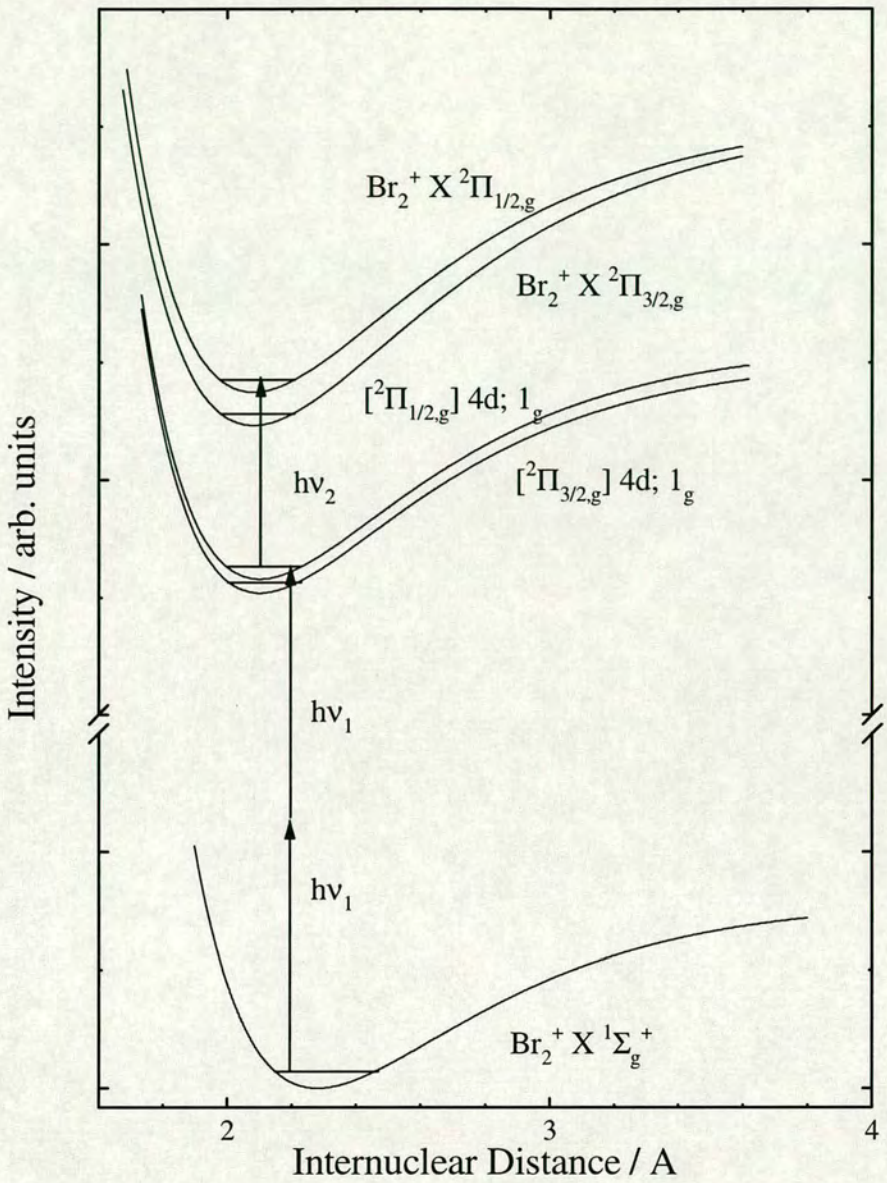

Figure 4-5 - Schematic potential energy diagram showing the neutral and ionic states of bromine involved in the (2+1′) multiphoton ionisation process.

forced vibrational autoionisation to contribute to the intensity of vibrational peaks seen in ZEKE-PFI spectra are discussed.

4.3.2 Results

4.3.2.1 Experimental Details

The ZEKE-PFI and threshold electron experiments presented in this section used the same laser configuration. The pump laser in the two-colour excitation used R590 and R575 dyes to produce light of wavelengths 567 and 557 nm respectively. This light was then doubled using a KD*P crystal to allow two-photon excitation to the intermediate Rydberg states at approximately 70500 and 71700 cm^{-1}. The probe laser used LDS 698 dye to reach the high *n* Rydberg states converging to the $X\ ^2\Pi_{3/2,g}$ state and a DCM/R640 mixture to reach the high *n* Rydberg states converging to the $X\ ^2\Pi_{1/2,g}$ state.

In the ZEKE-PFI experiments the pulsed electric fields were arranged as follows. The voltage pulse on the top plate was between 3.1 and 3.4 V/cm^{-1}, applied at approximately 1.1 μs after the laser excitation. The pulse on the bottom plate was between 1 and 1.2 V/cm^{-1} applied between 300 ns and 1.3 μs after the laser excitation. The sample of Br_2 was prepared in a bulb of helium with an approximate ratio of 10% Br_2 / 90% He. The sample was introduced into the chamber through the General Valve pulsed nozzle with a stagnation pressure of between 350 and 500 Torr.

In the threshold electron experiments the pulsed electric fields were arranged as follows: the voltage pulse on the top plate was between 2.4 and 3.1 V/cm^{-1} applied at approximately 300 ns after laser excitation, the pulse on the bottom plate was $1V/cm^{-1}$, again applied approximately 300 ns after the laser excitation. The Br_2 was of the same concentration used in the ZEKE-PFI experiments and the stagnation pressure was between 400 and 750 Torr.

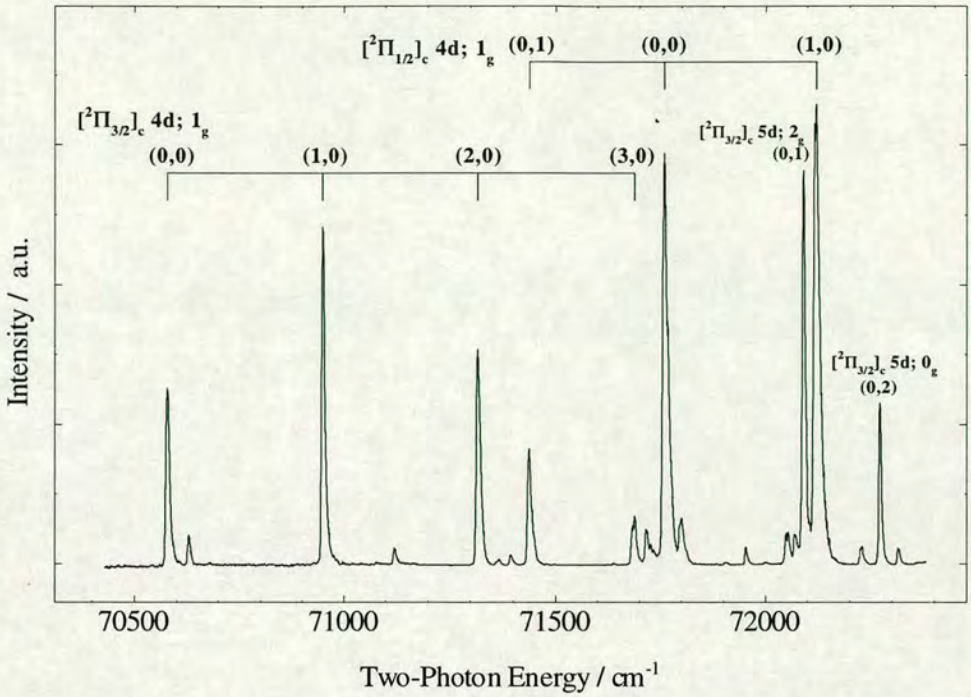

Figure 4-6 - The (2+1) REMPI spectrum of Br_2 in the 70500-72500 cm^{-1} two-photon energy range. The spectrum was recorded by monitoring the $^{79\text{-}81}Br_2^+$ mass channel.

4.3.2.2 The (2+1′) ZEKE-PFI spectrum of the X $^2\Pi_{3/2,g}$ state of $^{79\text{-}81}Br_2$

Figure 4-6 shows the mass resolved (2+1) REMPI spectrum of Br_2 in the range 70400-71900 cm^{-1} recorded using the $^{79\text{-}81}Br_2^+$ mass channel. The spectrum shows the $[^2\Pi_{3/2}]_c$ 4d; 1_g Rydberg state and the first few vibrational levels of the $[^2\Pi_{1/2}]_c$ 4d; 1_g Rydberg state. The spectrum compares well with that obtained in the room temperature total ion REMPI work of Ridley *et al.*[27] and the assignment of the spectrum is taken from that and more recent work.[28]

The two-colour (2+1′) ZEKE-PFI spectra of $^{79\text{-}81}Br_2$ ionised *via* the band origin of the $[^2\Pi_{3/2}]_c$ 4d; 1_g Rydberg state as well as *via* the first two vibrationally excited states are presented in figure 4-7 (a), (b) and (c). The ZEKE-PFI spectra are isotpomer specific due to selection of the $^{79\text{-}81}Br_2$ isotopomer at the intermediate Rydberg state level. In the spectrum *via* the band origin of the intermediate state the most intense peak is assigned to the band origin of the X $^2\Pi_{3/2,g}$ state giving a value of 84828±2 cm^{-1} for the adiabatic ionisation energy (corrected for the field ionisation shift). This assignment is made on the basis that transitions between the Rydberg

state and the X $^2\Pi_{3/2,g}$ state are expected to be dominated by the diagonal transition ($\Delta v = 0$). Although this was shown not to be the case generally in the (2+1′) ZEKE-PFI spectrum of the X $^2\Pi_{3/2,g}$ state of I_2,[11] it did apply to the transition from the band origin of the intermediate Rydberg state. The value of the ionisation energy for the X $^2\Pi_{3/2,g}$ state compares with the value of 84832±24 cm^{-1} obtained from the TPES study of Yencha *et al.*[9]

The (2+1′) ZEKE-PFI spectrum *via* v′ = 1 in the $[^2\Pi_{3/2}]_c$ 4d; 1_g Rydberg state is shown in figure 4-7 (b). As in figure 4-7 (a), the spectrum is dominated by the diagonal transition. However, given the expected small bond length change upon excitation from the Rydberg state, there seems to be an unusually large transition for the $v^+ = 0$ band (almost half the size of the diagonal transition). Figure 4-7 (c), which shows the (2+1′) ZEKE-PFI spectrum *via* v′ = 2 in the $[^2\Pi_{3/2}]_c$ 4d; 1_g Rydberg state, shows some enhancement of the $\Delta v = -1$ ($v^+ = 1$) transition relative to the $\Delta v = +1$ ($v^+ = 3$) transition. Enhancement of this kind was also seen in I_2 [11] and was found to be caused by forced vibrational autoionisation (see section 4.1).

The peaks in the ZEKE-PFI spectrum *via* v′ = 2 were fitted to the general expression for vibrational peak spacings ($G_v = T_e + \tilde{\omega}_e(v+{}^1/_2) - \tilde{\omega}_e x_e(v+{}^1/_2)^2$) to yield values for the vibrational constants for the X $^2\Pi_{3/2,g}$ state of $^{79\text{-}81}Br_2$; the constants are as follows, $\tilde{\omega}_e$=369±2 cm^{-1} and $\tilde{\omega}_e x_e$=1.8±0.5 cm^{-1}. These values are not expected to be very accurate as only three data points can be taken from the peak separations. The constants determined in the velocity modulation spectroscopy study of the *A* -*X* transition in $^{79\text{-}81}Br_2$ by Zackrisson [26] were $\tilde{\omega}_e$=365.27063±0.00082 cm^{-1} and $\tilde{\omega}_e x_e$=1.13155±0.00014 cm^{-1}.

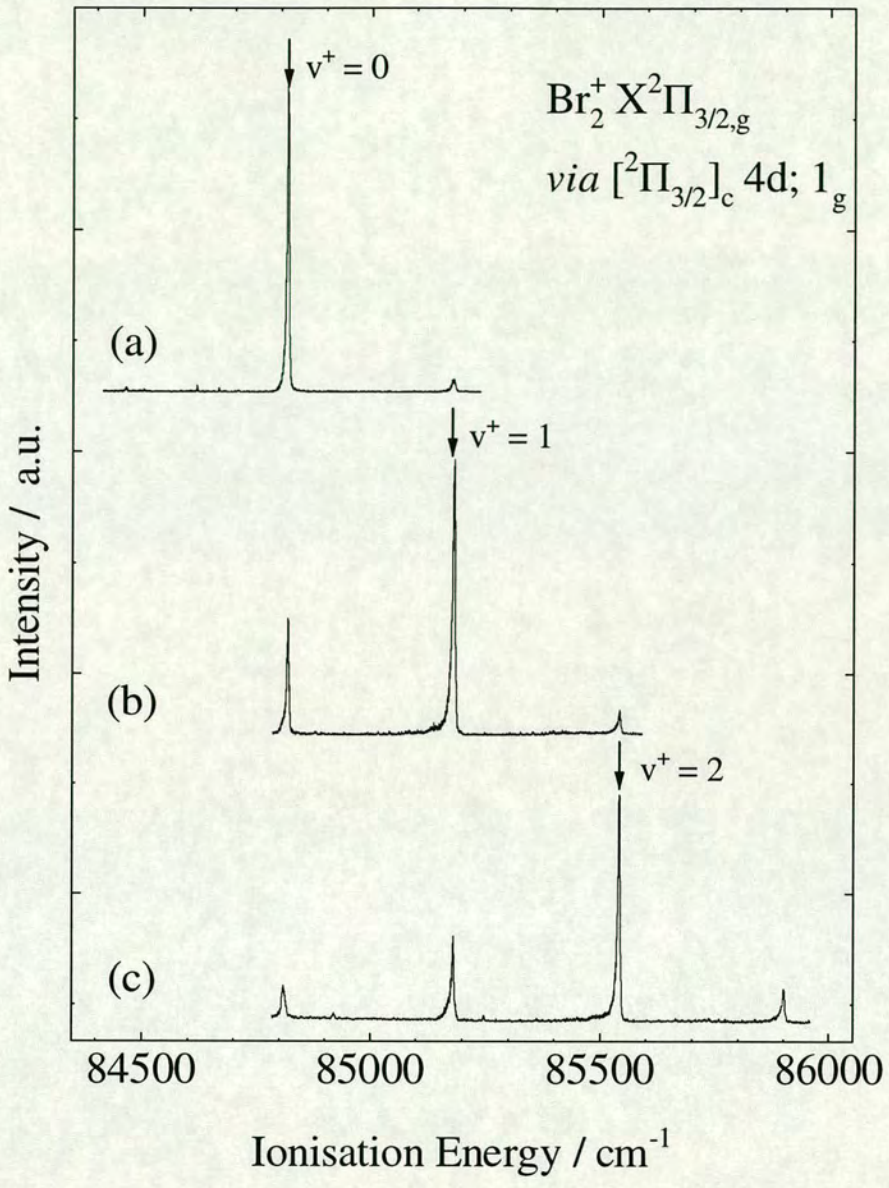

Figure 4-7 - The (2+1′) ZEKE-PFI spectrum of Br_2 recorded *via* the $[^2\Pi_{3/2}]_c$ 4d;1_g Rydberg state. The vertical arrows indicate the $\Delta v = 0$ transition.

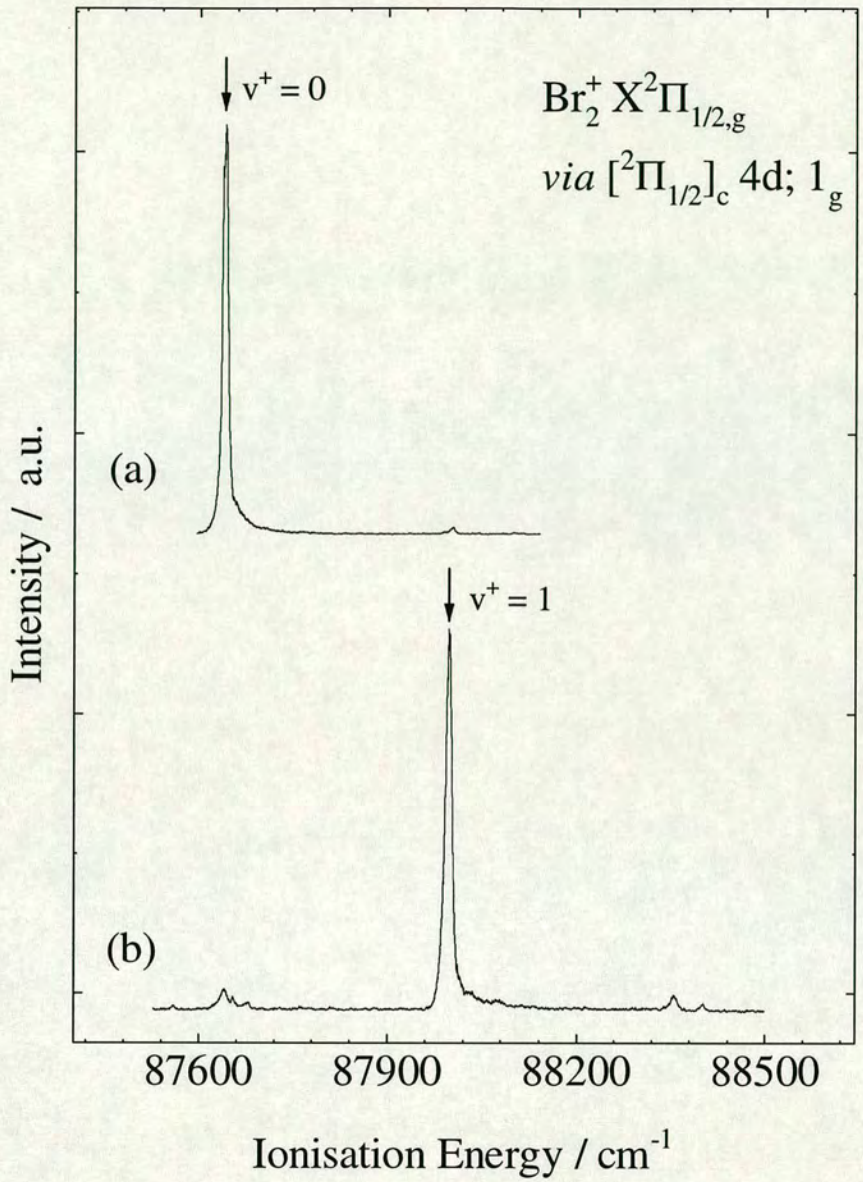

Figure 4-8 - The The (2+1′) ZEKE-PFI spectrum of Br_2 recorded *via* the $[^2\Pi_{1/2}]_c$ 4d;1_g Rydberg state. The vertical arrows indicate the $\Delta v = 0$ transition

4.3.2.3 The (2+1′) ZEKE-PFI spectrum of the X $^2\Pi_{1/2,g}$ state of $^{79}Br_2$

The two-colour (2+1′) ZEKE-PFI spectra of $^{79\text{-}81}Br_2$ ionised *via* the band origin of the $[^2\Pi_{1/2}]_c$ 4d; 1_g Rydberg state as well as *via* the first vibrationally excited state are presented in figure 4.8 (a) and (b). In the spectrum *via* the band origin of the intermediate state the most intense peak is assigned to the band origin of the X $^2\Pi_{1/2,g}$ state giving a value of 87648±2 cm^{-1} for the adiabatic ionisation energy (corrected for the field ionisation shift). This assignment is made on the basis that transitions between the Rydberg state and the X $^2\Pi_{1/2,g}$ state are expected to be dominated by the diagonal transition ($\Delta v = 0$). This was shown to be the case in the (2+1′) ZEKE-PFI spectrum of the X $^2\Pi_{1/2,g}$ state of I_2^+.[11] The value of the ionisation energy for the X $^2\Pi_{1/2,g}$ state compares with the value of 87647±24 cm^{-1} obtained from the TPES study of Yencha *et al.*[9] The ionisation energy of the upper spin-orbit component allows us to report a value of 2820±4 cm^{-1} for the spin-orbit splitting of X $^2\Pi_g$ state of Br_2^+.

The (2+1′) ZEKE-PFI spectrum *via* v′ = 1 in the $[^2\Pi_{1/2}]_c$ 4d; 1_g Rydberg state is shown in figure 4-8 (b). As in figure 4-8 (a), the spectrum is dominated by the diagonal transition. The two spectra in Figure 4-8 exhibit classic Franck-Condon behaviour for transitions from a Rydberg state with a very similar potential to the final ionic state, X $^2\Pi_{1/2,g}$.

4.3.2.4 The (2+1′) threshold electron spectrum of Br_2.

As a result of the similarity of the ZEKE-PFI spectra of Br_2 with those of I_2 it was decided that threshold electron spectra of the regions around the first two vibrational thresholds of the X $^2\Pi_{3/2,g}$ state of Br_2 should be recorded to probe for evidence of low *n* Rydberg states resonant with ZEKE-PFI vibrational peaks. If resonant, these Rydberg states could explain the observed vibrational intensity distribution of the X $^2\Pi_{3/2,g}$ state of Br_2^+ through enhancement by forced vibrational autoionisation. Figure 4-9 shows the (2+1′) threshold electron spectrum of Br_2

recorded *via* $v' = 1$ of the $[^2\Pi_{1/2}]_c$ 4d; 1_g Rydberg state. The same energy region of the (2+1′) ZEKE-PFI spectrum of Br_2 is shown at the top of Figure 4-9.

The threshold spectrum is dominated by three autoionising Rydberg state progressions which converge on $v^+ = 1$ of the $X\ ^2\Pi_{3/2,g}$ state of Br_2^+. These progressions have been assigned to two *p* (a $p\sigma$ and a $p\pi$) and one *f* Rydberg series on the basis of atomic[23] and molecular quantum defects[29] and the Laporte selection rule. The quantum defects of the Rydberg states observed in the spectra were calculated using the Rydberg equation as described in section 4.2.2.3. Using the energy of $v^+ = 1$ as $IP(\Omega_c)$ the Rydberg states separated into three series with quantum defects of 2.2, 2.7 and 0.05. These values are very close to the range of atomic bromine quantum defects of 2.35-2.71 for *p* Rydberg states and < 0.05 for *f* Rydberg states. The *p* Rydberg series to lower energy has been assigned to be a $p\sigma$ series and the Rydberg series to higher energy has been assigned to be a $p\pi$ series. This assignment is based on the one photon VUV work of Venkateswarlu.[29] The assignment to *p* and *f* Rydberg series agrees with the fact that the intermediate state in this case is a *d* Rydberg state. In a one-photon transition from this state we would expect to populate either *p* or *f* Rydberg states. It should be noted that the $n = 20$ $p\sigma$ Rydberg state is almost resonant with the $v^+ = 0$ ZEKE-PFI peak. The peak energies and the assignment of the autoionising Rydberg states is given in table 4-4. The ladders in figure 4-9 represent a simulation of the positions of Rydberg states that most closely matches the observed Rydberg state positions

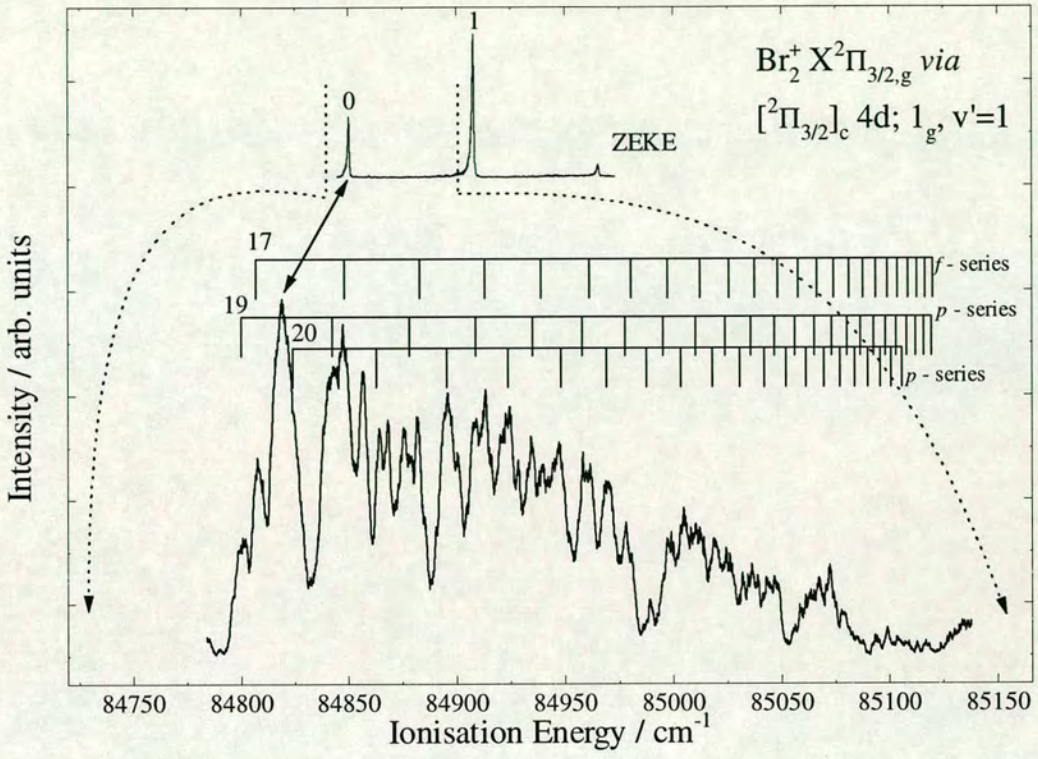

Figure 4-9 - The (2+1′) threshold electron spectrum of Br_2 in the region of the $X\ ^2\Pi_{3/2,g}$, $v^+ = 0$ ionisation threshold, recorded *via* $v' = 1$ of the $[^2\Pi_{3/2}]_c$ 4d;1_g Rydberg state. The top trace is the ZEKE-PFI spectrum recorded with the same excitation scheme. The double headed arrow indicates the position of $v^+ = 0$ in both spectra. The area of the ZEKE-PFI spectrum enclosed by the dotted lines represents the energy range of the threshold electron spectrum

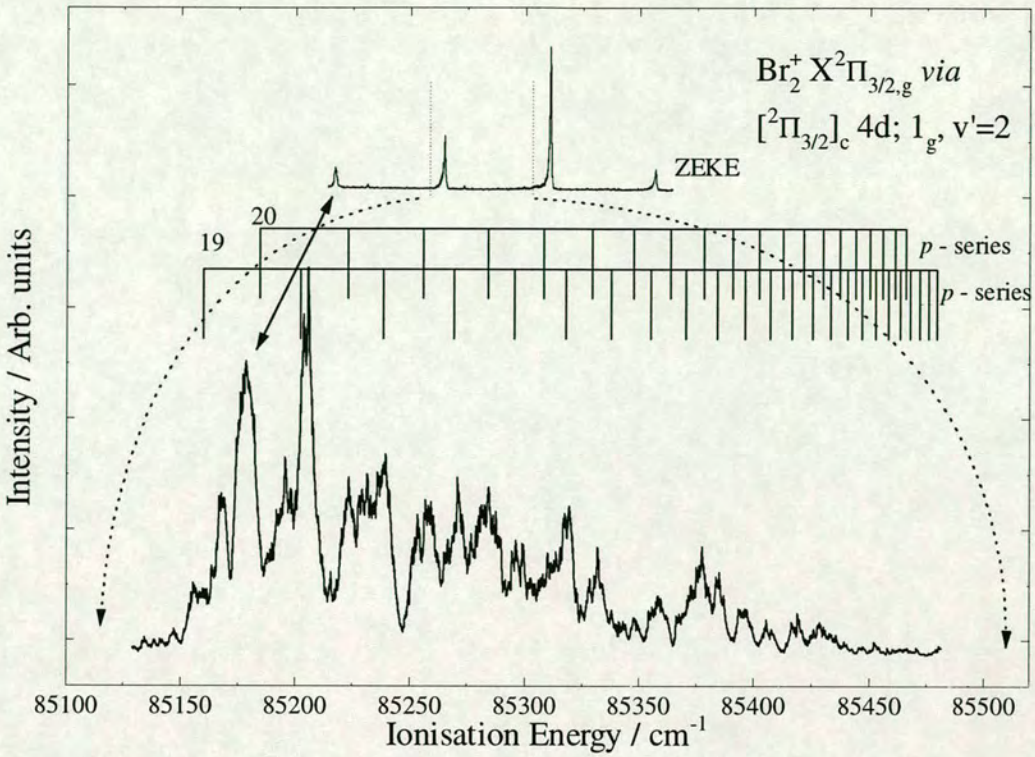

Figure 4-10 - The (2+1′) threshold electron spectrum of Br_2 in the region of the $X\ ^2\Pi_{3/2,g}$, $v^+ = 1$ ionisation threshold, recorded *via* $v' = 2$ of the $[^2\Pi_{3/2}]_c$ 4d;1_g Rydberg state. The top trace is the ZEKE-PFI spectrum recorded with the same excitation scheme. The double headed arrow indicates the position of $v^+ = 1$ in both spectra. The area of the ZEKE-PFI spectrum enclosed by the dotted lines represents the energy range of the threshold electron spectrum.

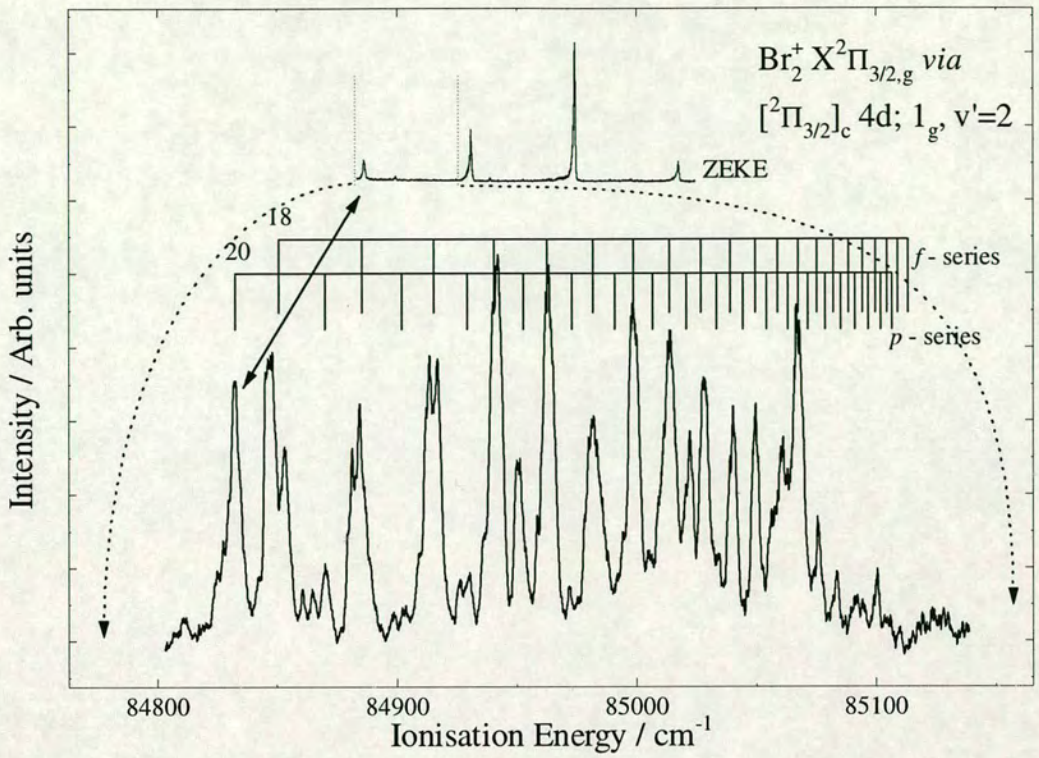

Figure 4-11 - The (2+1′) threshold electron spectrum of Br_2 in the region of the X $^2\Pi_{3/2,g}$, $v^+ = 0$ ionisation threshold, recorded *via* $v' = 2$ of the $[^2\Pi_{3/2}]_c$ 4d;1_g Rydberg state. The top trace is the ZEKE-PFI spectrum recorded with the same excitation scheme. The double headed arrow indicates the position of $v^+ = 0$ in both spectra. The area of the ZEKE-PFI spectrum enclosed by the dotted lines represents the energy range of the threshold electron spectrum.

No autoionising Rydberg progressions converging to higher vibrational levels are observed which is consistent with the proposed $\Delta v = -1$ propensity rule for vibrational autoionisation.[25]

Figure 4-10 shows the (2+1′) threshold electron spectrum of Br_2 recorded *via* $v' = 2$ of the $[^2\Pi_{1/2}]_c$ 4d; 1_g Rydberg state. In this case the energy region that has been covered is the threshold for the $v^+ = 1$ level of the X $^2\Pi_{3/2,g}$ state of Br_2. The same energy region of the (2+1′) ZEKE-PFI spectrum of Br_2 is also shown in Figure 4-10.

The threshold spectrum has a number of peaks that can be assigned to two Rydberg series converging on $v^+ = 2$; a $p\pi$ and a $p\sigma$ series. Again, these assignments have been made on the basis of atomic and molecular quantum defects and the Laporte selection rule. The assignments of the Rydberg peaks are given in table 4-5. The ladders in figure 4-10 are simulations of the positions of the Rydberg peaks that fit the observed Rydberg peak positions using the calculated quantum defects.

The first thing to note from the spectrum in figure 4-10 is that there is not a noticeable Rydberg peak at the position of the $v^+ = 1$ peak in the spectrum. There is the possibility that the $n = 20$ $p\sigma$ Rydberg peak is just underneath the ZEKE peak and is adding some intensity to it (see top of figure 4-10) although in the ZEKE-PFI spectrum *via* $v' = 2$ the intensity of the $v^+ = 1$ peak does not seem to be greatly enhanced. Another difference between the threshold spectrum in figure 4-10 compared with that in figure 4-9 is that the structure is not as extensive as the Rydberg progressions in figure 4-9. This could be due to the fact that their is another vibrational autoionisation channel open to these Rydberg states ($\Delta v = -2$). The electrons produced from the $\Delta v = -2$ channel would not be observed in the threshold spectrum as they will have enough kinetic energy to escape the ionisation region in the time before the collection pulse is applied. However, on the basis of the $\Delta v = -1$ propensity rule [25] it would be expected that the fraction of Rydberg states autoionising to the $\Delta v = -2$ channel would be quite small. It should also be noted that no *f* series Rydberg peaks are observed.

Figure 4-11 shows another (2+1′) threshold electron spectrum of Br_2 recorded *via* $v' = 2$ of the $[^2\Pi_{1/2}]_c$ 4d; 1_g Rydberg state. In this case the energy region covered

is the region around the band origin of the X $^2\Pi_{3/2,g}$ state of Br_2. The same energy region of the (2+1′) ZEKE-PFI spectrum of Br_2 is shown at the top of figure 4-11. The peaks in the threshold spectrum have been assigned to two Rydberg series converging on $v^+ = 1$ of the X $^2\Pi_{3/2,g}$ state of Br_2; one $p\sigma$ series and one *f* series. The *f* series is by far the dominant series in the spectrum whereas there are only a few strong peaks in the $p\sigma$ series progression. The assignment of the Rydberg series is based on the assignment of the Rydberg series in Figure 4-9. The peak positions are listed in Table 4-6.

The position of the origin band of the X $^2\Pi_{3/2,g}$ state of Br_2 is shown on the threshold spectrum. It can be seen that although the $n = 20$ $p\sigma$ Rydberg peak is still on the shoulder of the origin band, there does not seem to be any significant enhancement of the peak in the ZEKE-PFI spectrum *via* $v^+ = 2$.

Table 4-3 - Peak positions and assignments of the autoionising Rydberg states converging on $v^+ = 1$ of the X $^2\Pi_{3/2,g}$ state of I_2^+ *via* $v' = 1$ of the $[^2\Pi_{3/2}]_c$ Rydberg state.

Peak Energy (cm^{-1})	Assignment	Peak Energy (cm^{-1})	Assignment
84801	$n = 19, p\pi$	84989	$n = 26, p\sigma$
84843	$n = 20, p\pi$	85005	$n = 27, p\sigma$
84878	$n = 21, p\pi$	85019	$n = 28, p\sigma$
84908	$n = 22, p\pi$	85032	$n = 29, p\sigma$
84934	$n = 23, p\pi$	85043	$n = 30, p\sigma$
84958	$n = 24, p\pi$		
84978	$n = 25, p\pi$	84808	$n = 17, f$
85010	$n = 26, p\pi$	84847	$n = 18, f$
		84882	$n = 19, f$
84824	$n = 20, p\sigma$	84913	$n = 20, f$
84864	$n = 21, p\sigma$	84939	$n = 21, f$
84896	$n = 22, p\sigma$	84962	$n = 22, f$
84924	$n = 23, p\sigma$	84980	$n = 23, f$
84947	$n = 24, p\sigma$	84998	$n = 24, f$
84969	$n = 25, p\sigma$	85012	$n = 25, f$

Table 4-4 - Peak positions and assignments of the autoionising Rydberg states converging on $v^+ = 2$ of the $X\ ^2\Pi_{3/2,g}$ state of I_2^+ *via* $v' = 2$ of the $[^2\Pi_{3/2}]_c$ Rydberg state.

Peak Energy (cm^{-1})	Assignment	Peak Energy (cm^{-1})	Assignment
85155	$n = 19, p\pi$	85406	$n = 30, p\pi$
85205	$n = 20, p\pi$	85417	$n = 31, p\pi$
85239	$n = 21, p\pi$		
85271	$n = 22, p\pi$	85184	$n = 20, p\sigma$
85296	$n = 23, p\pi$	85223	$n = 21, p\sigma$
85318	$n = 24, p\pi$	85257	$n = 22, p\sigma$
85338	$n = 25, p\pi$	85284	$n = 23, p\sigma$
85358	$n = 26, p\pi$	85310	$n = 24, p\sigma$
85373	$n = 27, p\pi$	85332	$n = 25, p\sigma$
85384	$n = 28, p\pi$	85348	$n = 26, p\sigma$
85396	$n = 29, p\pi$	85377	$n = 28, p\sigma$

Table 4-5 - Peak positions and assignments of the autoionising Rydberg states converging on $v^+ = 1$ of the X $^2\Pi_{3/2,g}$ state of I_2^+ *via* $v' = 2$ of the $[^2\Pi_{3/2}]_c$ Rydberg state.

Peak Energy (cm^{-1})	Assignment	Peak Energy (cm^{-1})	Assignment
84847	$n = 18, f$	85083	$n = 32, f$
84884	$n = 19, f$	85094	$n = 33, f$
84914	$n = 20, f$	85100	$n = 34, f$
84942	$n = 21, f$		
84963	$n = 22, f$	84832	$n = 20, p\sigma$
84981	$n = 23, f$	84870	$n = 21, p\sigma$
84999	$n = 24, f$	84899	$n = 22, p\sigma$
85014	$n = 25, f$	84926	$n = 23, p\sigma$
85028	$n = 26, f$	84950	$n = 24, p\sigma$
85040	$n = 27, f$	84972	$n = 25, p\sigma$
85050	$n = 28, f$	85005	$n = 27, p\sigma$
85061	$n = 29, f$	85022	$n = 28, p\sigma$
85067	$n = 30, f$	85034	$n = 29, p\sigma$
85075	$n = 31, f$		

4.3.3 Discussion

The (2+1′) ZEKE-PFI spectra of the X $^2\Pi_{3/2,g}$ and X $^2\Pi_{1/2,g}$ states of Br_2^+ show similarities with the analogous spectra of I_2^+ (see section 4.2, figure 4-1). In both cases the ZEKE-PFI spectra recorded for the X $^2\Pi_{3/2,g}$ state show a vibrational intensity distribution that deviates from the expected distribution based on Franck-Condon factors. Section 4.1 included an investigation into this effect in I_2 using threshold electron spectroscopy. In the threshold electron spectrum of I_2 an exact resonance of the $n = 25$ $p\sigma$ Rydberg state with the position of the ZEKE peak for the band origin of the X $^2\Pi_{3/2,g}$ state of I_2^+ was seen. In the threshold electron spectrum of the analogous energy range for Br_2 we see that there is only a near resonance of the $n = 20$ $p\sigma$ Rydberg state with the ZEKE peak for the band origin of the X $^2\Pi_{3/2,g}$ state of Br_2^+. It should be noted that the intensity of the $\Delta v = -1$ peak in the ZEKE-PFI spectrum of Br_2 is around half the intensity of the diagonal transition, which contrasts with the observation that the two peaks in the ZEKE-PFI spectrum of I_2 have very nearly the same intensity. This observation is consistent with the requirement of a fairly close resonance of a low n Rydberg state with the manifold of high n Rydberg states for any forced vibrational autoionisation to affect the intensity pattern of a ZEKE-PFI spectrum. In I_2 the resonance is almost exact and the resulting forced vibrational autoionisation has a large effect on the vibrational intensity distribution of the ZEKE spectrum. In Br_2 the resonance is not quite as close and as a result the effect of forced vibrational autoionisation is not as marked.

In the ZEKE-PFI spectrum of the X $^2\Pi_{1/2,g}$ state of Br_2^+, as in the analogous spectrum for I_2^+, the vibrational intensity distributions observed exhibit classic Franck-Condon behaviour. It is expected that the reason behind this is that there are no resonances involving low n Rydberg states converging on higher ionisation thresholds and the high n Rydberg states that constitute the ZEKE-PFI signal. Spin-orbit autoionisation may also play a role by shortening the lifetime of any Rydberg states in the region of the X $^2\Pi_{1/2,g}$ state thresholds. The shortening of the lifetime of Rydberg states resonant with the high n Rydberg states could cancel out any possible

enhancement by creating a 'window resonance' whereby intensity is taken from the ZEKE-PFI peak.

One curious observation should be noted concerning the threshold electron spectra recorded by pumping $v' = 2$ in the $[^2\Pi_{3/2}]_c$ 4d; 1_g Rydberg state. In the spectrum *via* $v' = 1$ (see Figure 4-9) we see three Rydberg series; a $p\sigma$, $p\pi$ and an f series. In the threshold electron spectrum shown in Figure 4-10 (*via* $v' = 2$, around the $v^+ = 1$ threshold) we only observe the two p series in any detail. However in the threshold spectrum shown in Figure 4-11 (around the $v^+ = 0$ threshold) only the f Rydberg series is seen to any great extent. The reason behind this observation is not clear as we would expect to observe the same Rydberg series and relative intensities as seen in the threshold spectrum *via* $v' = 1$.

In summary, we have presented the (2+1′) ZEKE-PFI photoelectron spectra of both spin-orbit components of the ground ionic state of Br_2. We have determined accurate values for the ionisation energies of these states; 84828±2 cm^{-1} for the $X\ ^2\Pi_{3/2,g}$ state and 87648±2 cm^{-1} for the $X\ ^2\Pi_{1/2,g}$ state, giving a value of 2820±2 cm^{-1} for the spin-orbit splitting for the $X\ ^2\Pi$ state. The contribution of forced vibrational autoionisation to the vibrational intensity distribution of the $X\ ^2\Pi_{3/2,g}$ state of Br_2 has been investigated using (2+1′) threshold electron spectroscopy applied to the energy regions around the vibrational thresholds of the $X\ ^2\Pi_{3/2,g}$ state. The comparison of the work presented in this section compared to the ZEKE-PFI and threshold electron spectra of I_2 presented in section 4.2 supports the strong resonance condition for forced vibrational autoionisation to have an effect in ZEKE-PFI spectra.

4.4 The C2P ZEKE-PFI Spectrum of Br_2

4.4.1 Introduction

One of the most straightforward ways to perform a ZEKE-PFI experiment is to use coherent two-photon (C2P) excitation. In C2P ZEKE-PFI the molecule is excited directly from the ground electronic state to the high *n* Rydberg states using two photons. Unlike resonant excitation schemes used in ZEKE-PFI, the C2P excitation route allows spectra to be recorded without the need to characterise a suitable intermediate state.

Although straightforward, the C2P excitation route has not been used on too many systems. This is probably due to the fact that REMPI excitation schemes have their own advantages such as species and state selectivity which can greatly simplify the resultant ZEKE-PFI spectra. However, in cases where it is desirable to compare angular momentum transfer for transitions from the ground neutral states with one or two photons, C2P excitation can yield important information.[30] Other instances when C2P excitation can be useful are when large energy ranges need to be scanned (facilitated by the broad tunability of commercially available dye lasers in the 400-200 nm range),[12,31] or when little is known about the excited neutral states of a molecule i.e. radical species.[32]

The Edinburgh ZEKE group has used the C2P excitation route in the past with molecular iodine.[10] In this study the motivation was to cover a very large energy range and record the C2P ZEKE-PFI spectrum of the ground and excited $A\ ^2\Pi_{3/2,u}$ state of I_2. As well as acheiving this aim there was an unexpected bonus that came from the C2P work on I_2. This bonus came in the form of an extended progression in the I_2 stretch for both spin-orbit components of the $X\ ^2\Pi_g$ state. The main vibrational progression extended to $v^+ = 30$ for the lower spin-orbit component ($X\ ^2\Pi_{3/2,g}$) and up to $v^+ = 6$ for the upper spin-orbit component ($X\ ^2\Pi_{1/2,g}$). This was unexpected given the distribution observed in previous Ne(I) photoelectron work [4] in which the progressions for the two components only extended as far as $v^+ = 4$, reflecting the Franck-Condon factors for the transition. Also, in a higher energy scan around the *A*

$^2\Pi_{3/2,u}$ state, peaks were observed that were assigned to $v^+ = 60$-90 in the X $^2\Pi_{3/2,g}$ state and $v^+ = 30$-40 in the X $^2\Pi_{1/2,g}$ state, although these peaks were very weak. The extended nature of the progressions was attributed to autoionisation processes similar to those used to explain the extended vibrational progression seen in the single-photon ZEKE-PFI spectrum of O_2 recorded by Kong and Hepburn.[17] Further evidence for this interpretation came from the TPES work on I_2 which showed a similarly extended progression for the X $^2\Pi_{3/2,g}$ state of I_2^+.[8]

In this section we present the C2P ZEKE-PFI spectrum of both spin-orbit components of the ground state of Br_2^+. The motivation behind this study was to obtain a similarly extended progression in the ZEKE-PFI spectra of the two spin-orbit components of the ground state of Br_2. The expectation that an extended progression would be seen was based on the fact that Br_2 shows similar forced autoionisation behaviour to I_2 in the (2+1′) ZEKE-PFI spectra. Also, the TPES work on Br_2 shows an extended progression for the X $^2\Pi_{3/2,g}$ and X $^2\Pi_{1/2,g}$ states of Br_2^+ [9] similar to the extended progression in the X $^2\Pi_{3/2,g}$ state of I_2^+.[8] No attempt has been made to record ZEKE-PFI spectra of the *A* $^2\Pi_{3/2,u}$ state of Br_2 as it lies outwith the energy range of the dye laser system. It will be shown that Br_2 does not exhibit an extended, non Franck-Condon progression like that observed in the C2P ZEKE-PFI spectrum of I_2. The possibility that an intermediate state interaction is responsible for the observed differences in the C2P spectra of Br_2 and I_2 is discussed.

4.4.2 Results

4.4.2.1 Experimental Details

This study involved just one dye laser (PDL-2A, bandwidth of fundamental output ≈ 1 cm^{-1}) to excite bromine from its ground state to the ion. The laser used C480, C460 and C440 dyes to produce wavelengths between 474 and 449 nm. The output of the dye laser was frequency doubled using a BBO crystal and the doubled output was separated from the dye fundamental using a home-built Pelin-Broca prismatic separator.

The pulsed electric fields were arranged as follows: the top plate voltage pulse was between 3.3 and 3.8 V/cm^{-1} applied at approximately 2.6 μs after laser excitation, the voltage pulse on the bottom plate was between 0.5 and 0.8 V/cm^{-1} applied at 130ns and switched off at 2.4 μs. The voltage pulse on the bottom plate was used solely as a discrimination pulse to reduce any trapped/fast electron signal. Neutral density filters were also used to attenuate the laser power in an effort to remove trapped electron signals from intruding into the ZEKE-PFI electron channel on the time-of-flight profile. Bromine was introduced into the chamber as part of a 5:1 mixture of He:Br_2 at stagnation pressures between 550 and 700 Torr.

4.4.2.2 The C2P ZEKE-PFI spectrum of the X $^2\Pi_{3/2,g}$ and X $^2\Pi_{1/2,g}$ states of Br_2

The coherent two photon (C2P) ZEKE-PFI spectrum of bromine in the energy range 84500-86500 is presented in figure 4-12. The spectrum has been power normalised to the square of the laser power. The spectrum shows a vibrational progression that has been assigned to the X $^2\Pi_{3/2,g}$ state of Br_2^+. The origin of the progression has been assigned to the peak at 84831±4 cm^{-1} (field corrected) on the basis of the (2+1′) ZEKE-PFI spectrum of Br_2 (see section 4.3). The value of the adiabatic ionisation energy compares well with the value from the (2+1′) ZEKE study (84828±2 cm^{-1}). The vibrational progression extends for a further 3 vibrational levels. As well as the main progression there are three other peaks in the ZEKE-PFI spectrum. Two of the peaks are assigned to hot bands originating from v″ = 1 in the ground state. The separations between these two peaks and the peaks in the main progression are 322 cm^{-1} which compares with the separation between v″ = 0 and v″ = 1 in the ground state of 320 cm^{-1}.[33] The third peak is assigned as a sequence band from v″ = 2 to v$^+$ = 2. However, the intensity of this peak is surprisingly large given the intensity of the v″ = 1 to v$^+$ = 1 sequence band. The cause of this intensity mismatch is not known.

The first thing to note about the appearance of the spectrum is that the vibrational progression is extremely short. It is even shorter than the He(I) spectrum of Cornford *et al.*[3] which was observed to extend to v$^+$ = 4.

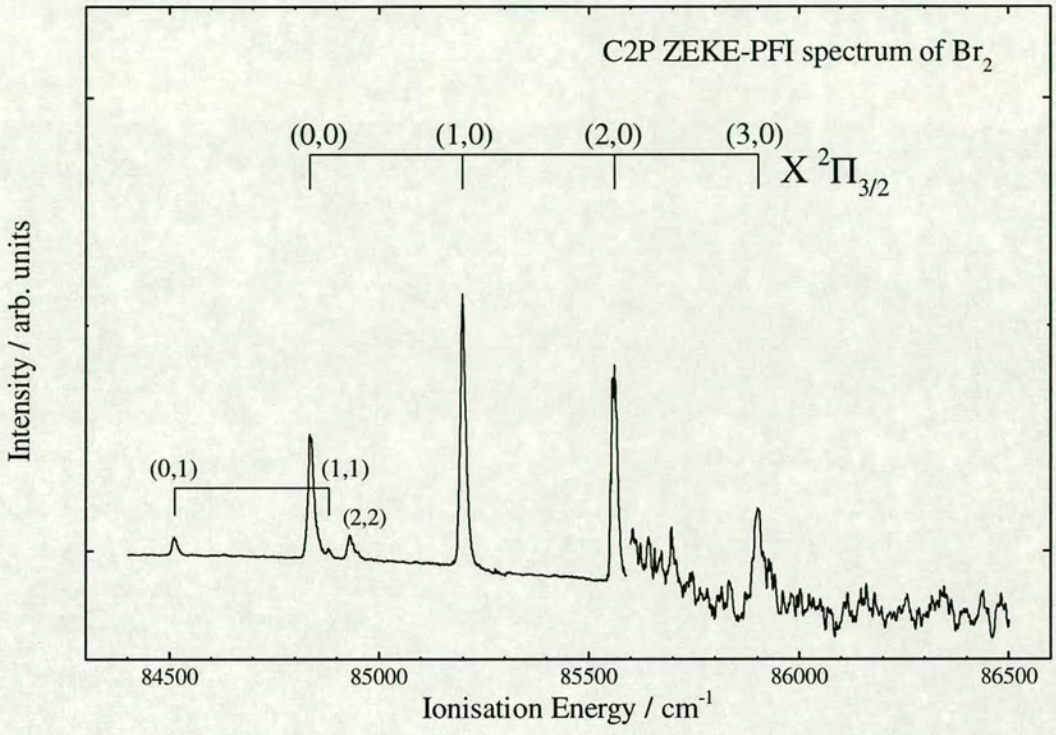

Figure 4-12 - The C2P ZEKE-PFI spectrum of the X $^2\Pi_{3/2}$ state of Br_2^+ in the 84400-86500 cm^{-1} two-photon energy range. The assignments are given using the (v^+, v'') notation where v^+ is the vibrational state of the ion and v'' is the initial vibrational state. The decrease in the signal to noise ratio for the latter part of the spectrum was caused by the change to a lower power laser dye.

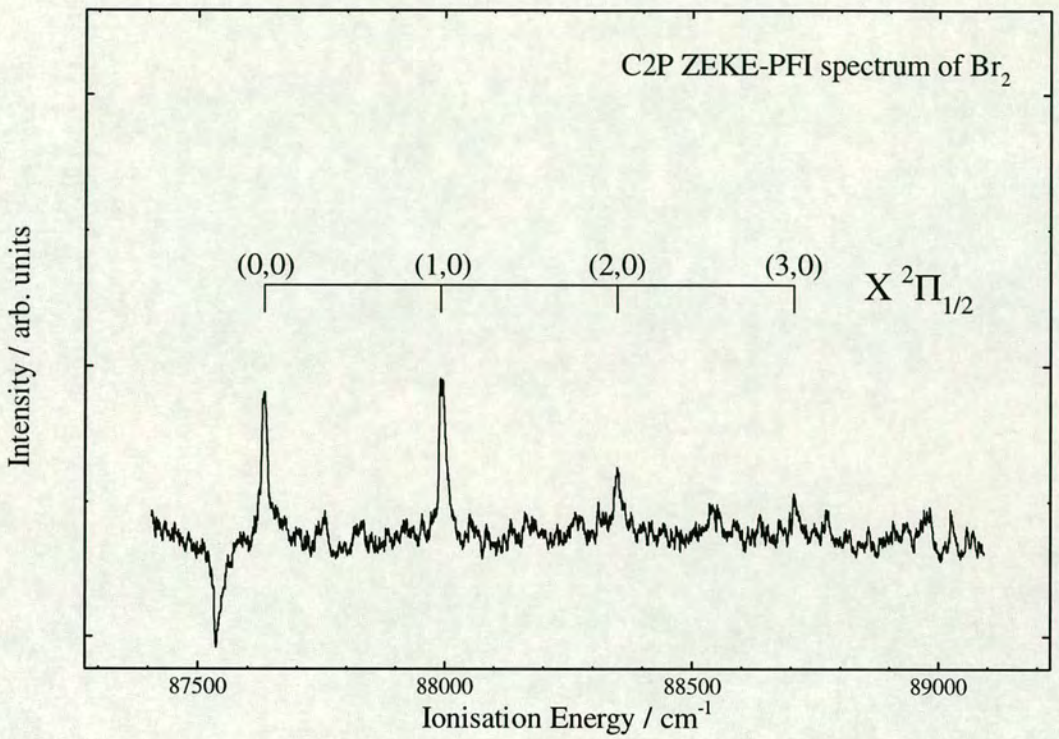

Figure 4-13 - The C2P ZEKE-PFI spectrum of the $X\ ^2\Pi_{1/2}$ state of Br_2^+ in the 87400-89100 cm^{-1} two-photon energy range. The assignments are given using the (v^+, v'') notation where v^+ is the vibrational state of the ion and v'' is the initial vibrational state.

This result was unexpected given that the same experiment with I_2 yielded a very extended vibrational progression and Br_2 has similar forced autoionisation and resonant autoionisation characteristics to I_2 (see section 4.2 and the TPES work on I_2 and Br_2 [8,9]).

The peaks in the spectrum were fitted to the general expression for vibrational energy level spacings ($G_v = T_e + \tilde{\omega}_e(v+^1/_2) - \tilde{\omega}_e x_e(v+^1/_2)^2$) to yield values for the vibrational constants for the X $^2\Pi_{3/2,g}$ state of Br_2; the constants are as follows, $\tilde{\omega}_e$=370±5 cm^{-1} and $\tilde{\omega}_e x_e$=2.2±1.0 cm^{-1}. These values compare with the constants determined in the velocity modulation spectroscopy study of the *A -X* transition in $^{79-81}Br_2$ by Zackrisson [26] of $\tilde{\omega}_e$=365.27063±0.00082 cm^{-1} and $\tilde{\omega}_e x_e$=1.13155±0.00014 cm^{-1} and also with our previously determined values of 369±3 cm^{-1} and 1.8±0.5 cm^{-1} from the (2+1′) ZEKE-PFI spectrum of $^{79-81}Br_2$.

The coherent two photon (C2P) ZEKE-PFI spectrum of bromine in the energy range 87400-89100 is presented in Figure 4-13. The spectrum has not been power normalised as the laser power remained reasonably constant throughout the scan. The spectrum shows a vibrational progression that has been assigned to the X $^2\Pi_{1/2,g}$ state of Br_2^+. The origin of the progression has been assigned to the peak at 87647±4 cm^{-1} (field corrected) on the basis of the (2+1′) ZEKE-PFI spectrum of Br_2 (see section 4.3). The value of the adiabatic ionisation energy compares well with the value from the (2+1′) ZEKE study. The vibrational progression extends for a further 3 vibrational levels. The dip that is marked with an asterisk is an instrument artefact that arises from ringing in the time-of-flight profile due to an exceptionally large fast electron signal.

Once again we see that the vibrational progression observed is shorter than would be expected based on the Franck-Condon factors.[3] In the TPES spectrum of Br_2 [9] the X $^2\Pi_{1/2,g}$ state has a progression that extends as far as $v^+ = 40$ and in the C2P ZEKE-PFI spectrum of I_2 the progression of the X $^2\Pi_{1/2,g}$ state extends past $v^+ = 6$. The contrast between these observations indicates that autoionisation processes play little, if any, part in influencing the vibrational progression for the X $^2\Pi_{3/2,g}$ state of Br_2^+.

The peaks in the spectrum were fitted to the general expression for vibrational energy level spacings ($G_v = T_e + \tilde{\omega}_e(v+^1/_2) - \tilde{\omega}_e x_e(v+^1/_2)^2$) to yield values for the vibrational constants for the $\tilde{X}\,^2\Pi_{3/2,g}$ state of Br_2; the constants are as follows, $\tilde{\omega}_e$=360±5 cm^{-1} and $\tilde{\omega}_e x_e$=1.0±0.5 cm^{-1}.

4.4.3 Discussion

The most important feature of this work is that the C2P ZEKE-PFI spectrum of Br_2 does not behave in the same way as that of I_2. The extended nature of the I_2 progressions was initially attributed to autoionisation processes similar to those seen in O_2.[17] However, that explanation is beginning to look less likely as Br_2, a molecule that has been shown to share similar forced vibrational and resonant autoionisation characteristics with I_2, gives a very different C2P ZEKE-PFI spectrum.

As discussed in the introduction to this chapter the deviation of vibrational intensity distributions from the expected distribution is quite common in ZEKE-PFI spectroscopy. In this case we have to explain why, against all expectations based on the intensity distribution of a similar ZEKE-PFI study on I_2 and the TPES work on Br_2, we see a vibrational intensity distribution that extends no further than would be expected based on Franck-Condon factors. It is indisputable that final state interactions are the cause of the extended vibrational progressions seen in the TPES work on I_2 and Br_2. However, it is disputable that final state interactions are the cause of the extended progression in the C2P ZEKE-PFI spectrum of I_2. The C2P excitation route opens up the possibility for intermediate state interactions to disrupt the vibrational intensity distribution observed. A clear example of this is the C2P ZEKE studies of CH_3-I and C_2H_5-I,[19,20] where it was shown that the extended vibrational progression observed in the R-I stretch (where R is CH_3 or C_2H_5) is due to absorption to a repulsive state at the intermediate one-photon level.[20]

The relevance of the work on CH_3-I and C_2H_5-I is that I_2 has a reasonably strong UV absorption in the one-photon energy range used to reach the X $^2\Pi_{3/2}$ and X $^2\Pi_{1/2}$ states.[34] The state responsible for this absorption was assigned as the $C\,^3\Sigma_u^+$ repulsive state.[34] Absorption *via* this repulsive state could be the cause of the extended vibrational progression in the C2P ZEKE spectrum of I_2. Another point that

absorption *via* a repulsive state could explain is the difference between the main sections of the progressions of the X $^2\Pi_{3/2}$ state ($v^+ = 0..30$) and the X $^2\Pi_{1/2}$ state ($v^+ = 0..6$) of I_2. The two vibrational intensity distributions should be very similar given that they are for spin-orbit components of the same electronic state and will have similar potential surfaces. However, in a (1+1) excitation *via* a repulsive state the transition to the ionic states will depend on the strength of absorption at the intermediate level which will change as the energy of the laser is scanned. At the one-photon energy used to reach the X $^2\Pi_{3/2}$ state of I_2 the absorption is close to the maximum.[34] At the analogous energy for reaching the X $^2\Pi_{1/2}$ state of I_2 the absorption is much smaller.[34] On the basis of this information it would be expected that any absorption *via* a repulsive intermediate state will not be as great for excitation to the X $^2\Pi_{1/2}$ state and that the vibrational progression will not be as extended as that of the X $^2\Pi_{3/2}$ state.

In Br_2 the UV absorption at the one-photon level for the energies used to access the X $^2\Pi_{3/2,g}$ and X $^2\Pi_{1/2,g}$ states is very small.[35] If we assume that the reason behind the extended progression in I_2 is bond stretching due to continuum absorption at the one-photon level then we begin to see an explanation for the differences between the C2P ZEKE-PFI spectra of I_2 and Br_2; I_2 has an extended vibrational progression because of a strong intermediate absorption to a repulsive state and Br_2 has a short vibrational progression because there is no significant intermediate absorption. However, the arguments presented here to explain the extended nature of the I_2 vibrational progressions rely on circumstantial evidence and a single photon ZEKE-PFI study of I_2 would be needed to confirm the explanation.

In summary, we have presented the C2P ZEKE-PFI spectrum of the two spin-orbit components of the ground state of Br_2. The adiabatic ionisation energies of these states are as follows: 84831±4 cm^{-1} for the X $^2\Pi_{3/2}$ state and 87647±4 cm^{-1} for the X $^2\Pi_{1/2}$ state. This yields a value of 2816±6 cm^{-1} for the spin-orbit splitting constant for the X $^2\Pi$ state of Br_2^+ which agrees well with the value of 2820±3 cm^{-1} determined in the (2+1′) ZEKE-PFI study of Br_2.

4.5 The C2P ZEKE-PFI Spectrum of IBr

4.5.1 Introduction

In this section we present the C2P ZEKE-PFI photoelectron spectrum of both spin orbit components of the ground ionic state of IBr ($X\ ^2\Pi_{3/2,1/2}$). Iodine bromide has been the subject of many spectroscopic studies with the main focus being on the spectroscopy of the ion pair and Rydberg states[36,37] and on the valence $B\ ^3\Pi_{0+}$ state which is predissociated by the 0^+ repulsive state.[38] The depth with which neutral IBr has been studied contrasts strongly with the lack of work on the IBr cation. Two photoelectron studies have been carried out prior to this work,[2,4] only one of which gives vibrational resolution of the ground electronic state of IBr^+.[4]

As has been mentioned in section 4.4, the C2P excitation route is one of the most straightforward ways in which to carry out a ZEKE-PFI study of a molecule. The use of the C2P excitation route in ZEKE-PFI photoelectron spectroscopy can lead to the observation of an extended vibrational progression, as seen in the C2P ZEKE-PFI spectra of I_2,[12] CH_3-I and C_2H_5-I [19,20], allowing detailed information on the potential of the vibrational coordinate to be determined. However, this was shown not to be the case in the C2P ZEKE-PFI study of Br_2 (see section 4.4) in which it was seen that the vibrational progressions in the two spin orbit components of the ground state extend no further than would be expected based on Franck-Condon factors.

The differences between the C2P ZEKE-PFI spectra of I_2 and Br_2 were discussed in section 4.4, leading to the conclusion that absorption *via* a repulsive state could be the cause of the extended progression in I_2. This explanation seems to account for the appearance of the C2P ZEKE-PFI spectrum of Br_2 as there is only a weak absorption at the intermediate one-photon level in Br_2 and in the C2P ZEKE-PFI spectrum we only see a short vibrational progression.

One of the main aims of this study, other than to abtain accurate spectroscopic constants for the spin-orbit components of the ground state of the IBr^+, was to investigate the form of the vibrational intensity distribution in the C2P ZEKE-PFI spectrum. Similar to I_2,[34] iodine bromide has a strong UV absorption in the one-

photon energy range needed to reach the X $^2\Pi_{3/2}$ and X $^2\Pi_{1/2}$ states.[39] The state responsible for this absorption was assigned, along with the analogous continuum absorption in the other interhalogens (ICl and BrCl), to the 0^+ repulsive state.[40] If intermediate absorption to a repulsive state is the cause of the extended progression seen in the C2P ZEKE-PFI spectrum of I_2 then there is the possibility that the vibrational progression in the C2P ZEKE-PFI spectrum of IBr may be similarly extended.

In this work we report accurate values for the adiabatic ionisation energies of the X $^2\Pi_{3/2}$ and X $^2\Pi_{1/2}$ spin-orbit components of the ground state of IBr^+. We also report accurate vibrational constants for both spin-orbit states. An extended vibrational progression is observed for the X $^2\Pi_{3/2,g}$ spin-orbit component of the ground state of IBr^+ which lends weight to the interpretation that the extended progression in the C2P ZEKE-PFI spectrum of I_2 is caused by intermediate state interaction.

4.5.2 Results

4.5.2.1 Experimental Details

The dye laser used to perform these experiments (PDL-3, bandwidth of fundamental output ≈ 0.1 cm^{-1}) used LD489 and C480 dyes to produce light with wavelengths between 509 and 465 nm. The dye fundamental output was frequency doubled using a BBO crystal to produce light with the required two-photon energy to reach both spin-orbit components of the ground state of IBr (79000-85000 cm^{-1}). The dye fundamental output was separated from the doubled light using a home made Pelin-Broca prismatic separator.

The arrangement of the pulsed electric fields was as follows: the voltage applied to the top plate was 3.5 V/cm^{-1} at 500 ns after laser excitation, the voltage on the bottom plate was 0.33 V/cm^{-1} between 170 ns and 410 ns after laser excitation. The voltage pulse on the bottom plate was used solely as a discrimination against fast electrons and to reduce the intrusion of plasma peaks in the ZEKE-PFI electron channel in the time-of-flight profile. Solid IBr (Fisons) was placed in a bulb which

was then evacuated and filled with helium. The bulb was heated using a heat gun to enrich the gas mixture with IBr. The sample was introduced into the chamber through the General Valve pulsed nozzle with a stagnation pressure of 500-600 Torr.

4.5.2.2 The C2P ZEKE-PFI spectrum of the X $^2\Pi_{3/2,g}$ state of IBr

Figure 4-14 shows the C2P ZEKE-PFI spectrum of the lower spin orbit component (X $^2\Pi_{3/2}$) of the ground ionic state of IBr^+. The assignment of the vibrational structure is given in figure 4-14 and is discussed below.

As we are exciting directly from the ground state, nominally without using a resonant intermediate state, we simultaneously excite both isotopomers of IBr ($I^{79}Br$ and $I^{81}Br$). The vibrational structure reflects this, with the isotope shift being resolved with increasing vibrational excitation. The resolution of the isotope shift allows absolute vibrational numbering to be determined for the peaks in the spectrum leading us to assign the peak at 79018±1 cm^{-1} to the band origin of the X $^2\Pi_{3/2}$ state. The peak positions of both isotopomers were combined and fitted to the expression for vibrational energy levels ($G_v = T_e + \tilde{\omega}_e((v+^1/_2)/\mu) - \tilde{\omega}_e x_e((v+^1/_2)/\mu)^2$,where μ is the reduced mass of the isotopomer) to yield values of $\tilde{\omega}_e$ and $\tilde{\omega}_e x_e$ for $I^{79}Br$ and $I^{81}Br$; $\tilde{\omega}_e$ = 303±1 cm^{-1} and $\tilde{\omega}_e x_e$ = 1.0±0.1 cm^{-1} for $I^{79}Br^+$ and $\tilde{\omega}_e$ = 300±1 cm^{-1} and $\tilde{\omega}_e x_e$ = 0.9±0.1 cm^{-1} for $I^{81}Br^+$. The value for $\tilde{\omega}_e$ compares with the value of 310±10 cm^{-1} determined from the vibrationally resolved photoelectron spectrum of Higginson *et al.*[4]

A weaker progression can also be seen in the Figure 4-14, starting approximately 266 cm^{-1} to the red of the band origin of the main progression. The peak spacing is identical to that of the main progression and the separation between the two band origins is equal to the separation between v = 0 and v = 1 in the ground state of neutral IBr (268 cm^{-1}).[33] This leads us to assign the weak progression as a hot band originating from v = 1 in the ground state of the neutral.

The peaks marked with ampersands (&) and asterisks are assigned as iodine atomic Rydberg transitions and bromine molecular Rydberg transitions respectively.[41,42] Bromine is present in the molecular beam as IBr exists in equilibrium with I_2 and Br_2. The atomic iodine is either from photodissociation of I_2 or IBr.

These peaks appear in the ZEKE spectrum of IBr as a result of plasma effects caused by the high laser powers used in this study, which were necessary to excite IBr directly from the ground state to the ion with two photons. The ionisation from the atomic iodine and molecular bromine Rydberg states results in such a large concentration of charged particles that a plasma is generated in the excitation region. The plasma is able to trap photoelectrons in the excitation region during the discrimination delay and as a result, when the pulsed electric field is applied, a signal is seen at the energies corresponding to the Rydberg transitions. Peaks of this kind have been seen in the (2+1′) ZEKE-PFI spectra of I_2 in which an accidental resonance of the probe photon with the *A* state of I_2 resulted in a strong ionisation signal and a peak in the ZEKE spectrum of I_2.[11] The reader is referred to Chapter 3 for a fuller discussion of this effect.

4.5.2.3 The C2P ZEKE-PFI spectrum of the X $^2\Pi_{1/2}$ state of IBr

Figure 4-15 shows the C2P ZEKE-PFI spectrum of the upper spin orbit component (X $^2\Pi_{1/2}$) of the ground ionic state of IBr^+. The assignment of the vibrational structure is given in figure 4-15 and is discussed below.

The band origin of the X $^2\Pi_{1/2}$ state is assigned to the peak at 83680±1 cm^{-1}. The assignment of the band origin is made on the basis of the similarity of the progression with the start of the lower spin orbit state progression and the fact that there is no peak to lower energy. The progression for the X $^2\Pi_{1/2}$ state only continues as far as $v^+ = 3$ and as a result no information on the isotope shift was obtained. The assignment of the band origin gives a spin orbit splitting of 4662±2 cm^{-1} for the X $^2\Pi$ state of IBr^+. The peak separations yielded values of $\tilde{\omega}_e$ = 300±1 cm^{-1} and $\tilde{\omega}_e x_e$ = 2.0±0.2 cm^{-1} when fitted to the general expression for vibrational energy levels. The value of the spin-orbit constant compares with the value determined by Potts and Price [2] of 4597±80 cm^{-1} and the value from Higginson *et al.*[4] of 4807±65 cm^{-1}. The value of $\tilde{\omega}_e$ for the X $^2\Pi_{1/2,g}$ state of IBr from Higginson *et al.* [4] of 300±10 cm^{-1} is shown to be quite accurate when compared to the value determined in the present study.

The two peaks marked with asterisks are atomic iodine ZEKE peaks for the I^+ $^3P_1 \leftarrow I\ ^2P_{1/2}$ and $I^+\ ^3P_2 \leftarrow I\ ^2P_{3/2}$ transitions.[41,43] The neutral atomic iodine is most likely produced from the photodissociation of IBr or I_2. An indication that there is a relatively large amount of Br_2 in the molecular beam can be seen from the two peaks to higher energy of the main IBr progression. These are assigned to $v^+ = 0$ and $v^+ = 1$ of the $\tilde{X}\ ^2\Pi_{3/2,g}$ state of Br_2^+ on the basis of previous work (see section 4.2 and 4.3).

A summary of the spectroscopic data obtained from the ZEKE-PFI spectra of IBr^+ is given in Table 4-7.

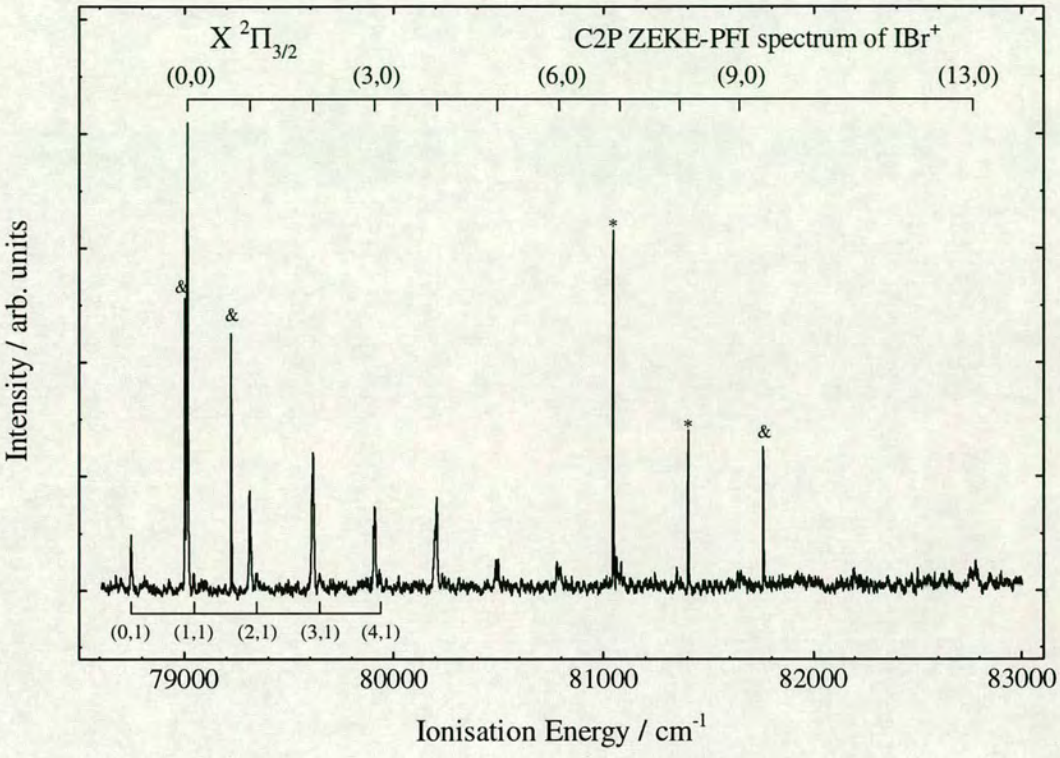

Figure 4-14 - The C2P ZEKE-PFI spectrum of the X $^2\Pi_{3/2}$ state of IBr^+ in the 78600-83000 cm^{-1} two-photon energy range. The assignments are given using the (v^+, v'') notation where v^+ is the vibrational state of the ion and v'' is the initial vibrational state. The sharp peaks marked with ampersands (&) and asterisks are plasma peaks caused by strong ionising transitions from atomic iodine (&) and molecular bromine (*) Rydberg states.

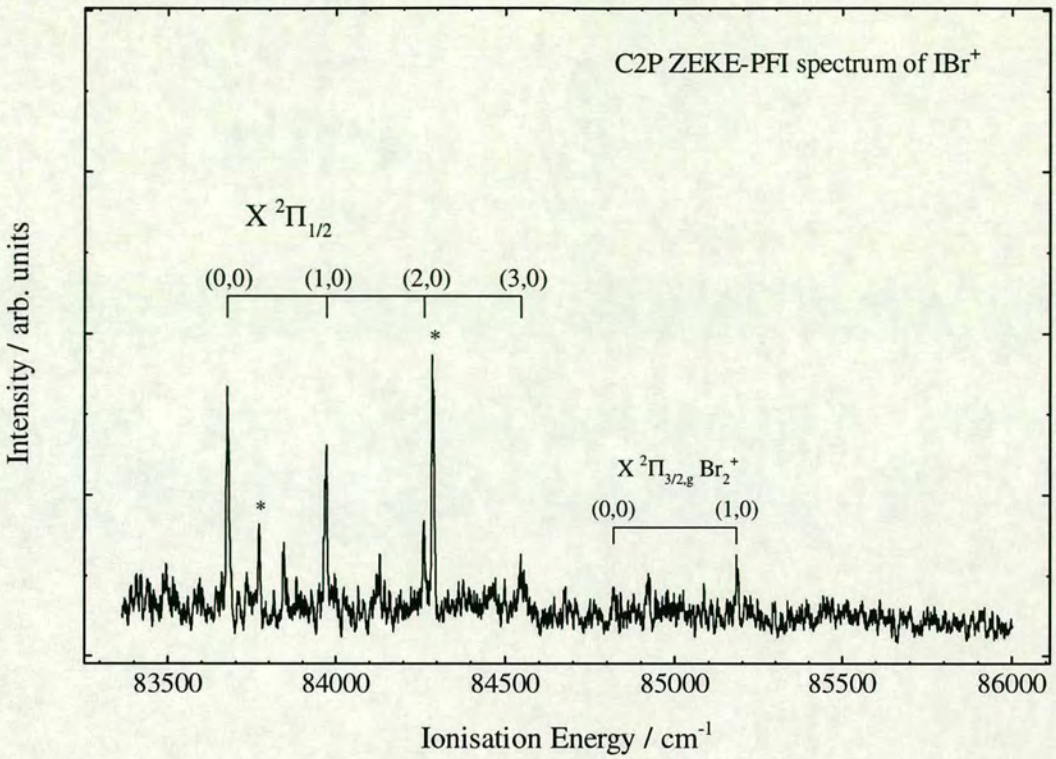

Figure 4-15 - The C2P ZEKE-PFI spectrum of the X $^2\Pi_{1/2}$ state of IBr^+ in the 83400-86000 cm^{-1} two-photon energy range. The notation used for the assignment of the vibrational peaks is the same as used in Figure 1. The peaks marked with an asterisk are atomic iodine ZEKE transitions (see text for details).

Table 4-6 - Spectroscopic data obtained for the X $^2\Pi_{3/2}$ and X $^2\Pi_{1/2}$ states of IBr^+

State	Adiabatic Ionisation Energy (cm^{-1})	ϖ_e (cm^{-1})	$\varpi_e x_e$ (cm^{-1})	D_0[a] (cm^{-1})
$I^{79}Br^+$ X $^2\Pi_{3/2}$	79018±1	303±1	1.0±0.1	19808±2
$I^{81}Br^+$ X $^2\Pi_{3/2}$	79018±1	300±1	0.9±0.1	19808±2
IBr^+ X $^2\Pi_{1/2}$	83680±1	300±1	2.0±0.1	15146±2

[a] Assuming dissociation to Br ($^2P_{3/2}$) + I^+ ($^3P_2$)

4.5.3 Discussion

The main feature to note from this work is the similarity of the C2P ZEKE-PFI spectrum of IBr with that of I_2. As in I_2, we have observed an extended vibrational progression in the C2P ZEKE-PFI spectrum of the X $^2\Pi_{3/2}$ state of IBr^+. The progression extends further than would be expected based on the vibrational intensity distribution of the Ne (I) photoelectron spectrum of IBr^+ in which only four vibrational levels are seen for this state.[4] Although the vibrational progressions of the X $^2\Pi_{3/2,g}$ and X $^2\Pi_{1/2,g}$ states extend further in the C2P ZEKE-PFI spectrum of I_2 than in IBr, the same general trends are observed in both such as the X $^2\Pi_{3/2,g}$ state progression extending further than the progression of the X $^2\Pi_{1/2,g}$ state. In I_2 weaker peaks are seen to continue all the way up to $v^+ = 90$ and $v^+ = 60$ for the X $^2\Pi_{3/2,g}$ and X $^2\Pi_{1/2,g}$ state respectively. The vibrational progressions in IBr could not be observed to extend this far due to the poor signal to noise ratio. In I_2 the signal to noise ratio is very good whereas in IBr it is relatively poor, due to the experimental difficulties of handling the IBr, which exists in equilibrium with I_2 and Br_2. In order to push the equilibrium towards IBr the bulb is normally filled with an excess of Br_2 which can sometimes lead to a substantial amount of Br_2 passing through the pulsed nozzle and into the chamber (this is illustrated by the fact that the C2P ZEKE-PFI spectrum of Br_2 is observed around the X $^2\Pi_{1/2,g}$ state of IBr^+).

The similarities between the C2P ZEKE-PFI spectra of I_2 and IBr, coupled with the known similarities of the UV absorption spectra of the two molecules, lends weight to the interpretation that intermediate state interactions dominate the vibrational intensity distribution observed in both cases. In I_2 and IBr we know that there exists strong UV absorption to repulsive continua at the one-photon energy. Absorption into these repulsive states (the $C\ ^3\Sigma_u^+$ in I_2 and the 0^+ in IBr) could cause the extended progressions observed as a repulsive state will open up the Franck-Condon window to highly vibrationally excited states of the ion. The opening of the Franck-Condon window has not only been observed in ionic state spectroscopy [19,20] but also in neutral state spectroscopy such as the investigation of ion-pair states of I_2 and Cl_2 [44] and the low lying Rydberg states of CH_3-I [45] using two-colour REMPI

spectroscopy. In both of these cases a repulsive state was used to allow the observation of vibrationally excited states that would otherwise not be excited.

Absorption *via* a repulsive intermediate state in IBr can also explain the differences between the progressions of the X $^2\Pi_{3/2}$ state ($v^+ = 0..9,13$) and the X $^2\Pi_{1/2}$ state ($v^+ = 0..3$). The vibrational intensity distribution for the X $^2\Pi_{3/2,g}$ and X $^2\Pi_{1/2,g}$ states should be very similar given that they are spin-orbit components of the same electronic state and as such will have very similar potential surfaces. The strength of the absorption to the intermediate repulsive state varies with energy at the one-photon level so any contribution of the repulsive state to the final vibrational intensity distribution will also vary with one-photon energy. In this case, at the one-photon energy used to reach the X $^2\Pi_{3/2}$ state of IBr the absorption is slightly to the blue of the maximum,[39] and at the analogous energy for reaching the X $^2\Pi_{1/2}$ state the absorption is almost half of the strength of the maximum.[39] On the basis of this information it would be expected that the influence of a repulsive intermediate state will not be as great in the ZEKE-PFI spectrum of the X $^2\Pi_{1/2}$ state and that the vibrational progression may not be as extended as that of the X $^2\Pi_{3/2}$ state.

Another contributing factor to the difference between the progressions for the two spin-orbit components might be the ubiquitous relative decrease in intensity for the upper spin orbit component of states in ZEKE-PFI spectroscopy[46] due to decay of the high *n* Rydberg states by spin-orbit autoionisation, a decay route which is not open to the lower spin-orbit states. This would cause a relative shortening of the vibrational progression as the higher vibrational peaks would not be observed due to a poor signal-to-noise ratio.

As with I_2 it would be desirable to carry out a single-photon ZEKE-PFI experiment on IBr to verify the involvement of a repulsive intermediate state in the spectra presented here. Another possible experiment would be a two-colour (1+1′) ZEKE-PFI experiment in which the first photon is tuned to the maximum of the repulsive state absorption and the second photon is used to scan across the states of the ion. If the repulsive state is the cause of the extended progression in I_2 and IBr then this excitation scheme would maximise the involvement of the repulsive state. Another aspect of this excitation scheme is that the progressions of the two spin-orbit

components of the ground ionic state would be expected to be very similar. The observation of similar, extended progressions would be another indication that the repulsive state is the controlling factor for the vibrational intensity distribution observed.

In summary, we have presented the vibrationally resolved photoelectron spectrum of IBr in both spin orbit components of the ground ionic state using the technique of C2P ZEKE-PFI photoelectron spectroscopy. The adiabatic ionisation energies of these states are as follows: 79018±1 cm^{-1} for the X $^2\Pi_{3/2}$ state and 83680±1 cm^{-1} for the X $^2\Pi_{1/2}$ state. This yields a value of 4662±2 cm^{-1} for the spin-orbit splitting constant of the X $^2\Pi$ state of IBr^+. Extended vibrational structure was observed in the X $^2\Pi_{3/2}$ state of IBr^+ which has been attributed to absorption *via* the 0^+ repulsive state at the intermediate one-photon energy. This observation also throws light on the interpretation of a similar extended progression in the C2P ZEKE-PFI spectrum of I_2.

4.6 The (2+1′) and (1+2′) ZEKE-PFI Spectrum of IBr

4.6.1 Introduction

In section 4.5 we presented the C2P ZEKE-PFI spectrum of IBr. To perform a ZEKE-PFI study that does not involve direct excitation from the ground state bound intermediate states need to be known and characterised. In I_2 and Br_2 this is not a problem as there are many *gerade* Rydberg states that can be used in a (2+1′) excitation scheme to reach the ground state of both I_2^+ and Br_2^+.[11] Also, valence states can be used as intermediates as in the (1+2′) ZEKE-PFI spectrum of I_2.[10] In this case the valence $B\ ^3\Pi_{0u}^+$ state of I_2 was used in an attempt to access different parts of the ionic state potentials as the *B* state has a very different equilibrium separation from the ground ionic state.

With IBr the choice is somewhat limited as most of the Rydberg states are strongly perturbed by ion-pair states.[37] Only two Rydberg states are free of strong ion-pair mixing and these are the weak b′ $[^2\Pi_{1/2}]_c$ 6s;0^+ and the stronger b $[^2\Pi_{1/2}]_c$ 6s;1 Rydberg states. Both of these Rydberg states are based on the X $^2\Pi_{1/2}$ spin-orbit component of the ground state of IBr^+ but lie too low in energy to be used as intermediates to probe the X $^2\Pi_{1/2}$ state due to contraints of the laser system. However, they are high enough in energy to be used as intermediates in a (2+1′) ZEKE-PFI study of the X $^2\Pi_{3/2}$ lower spin-orbit component of the ground state of IBr^+. As excitation from the b_6 and b_6' Rydberg states should preferentially be to the upper spin-orbit component obtaining a signal in the ZEKE-PFI spectrum of the lower spin-orbit component would be of interest.

For excitation through the valence *B* state of IBr we are faced with an interesting system where inter-state coupling plays a major role. The valence $B\ ^3\Pi_0^+$ state of IBr is predissociated by the repulsive 0^+ state (see figure 4-16, which shows a schematic diagram of the ground and excited states of IBr and IBr^+). The system has been the

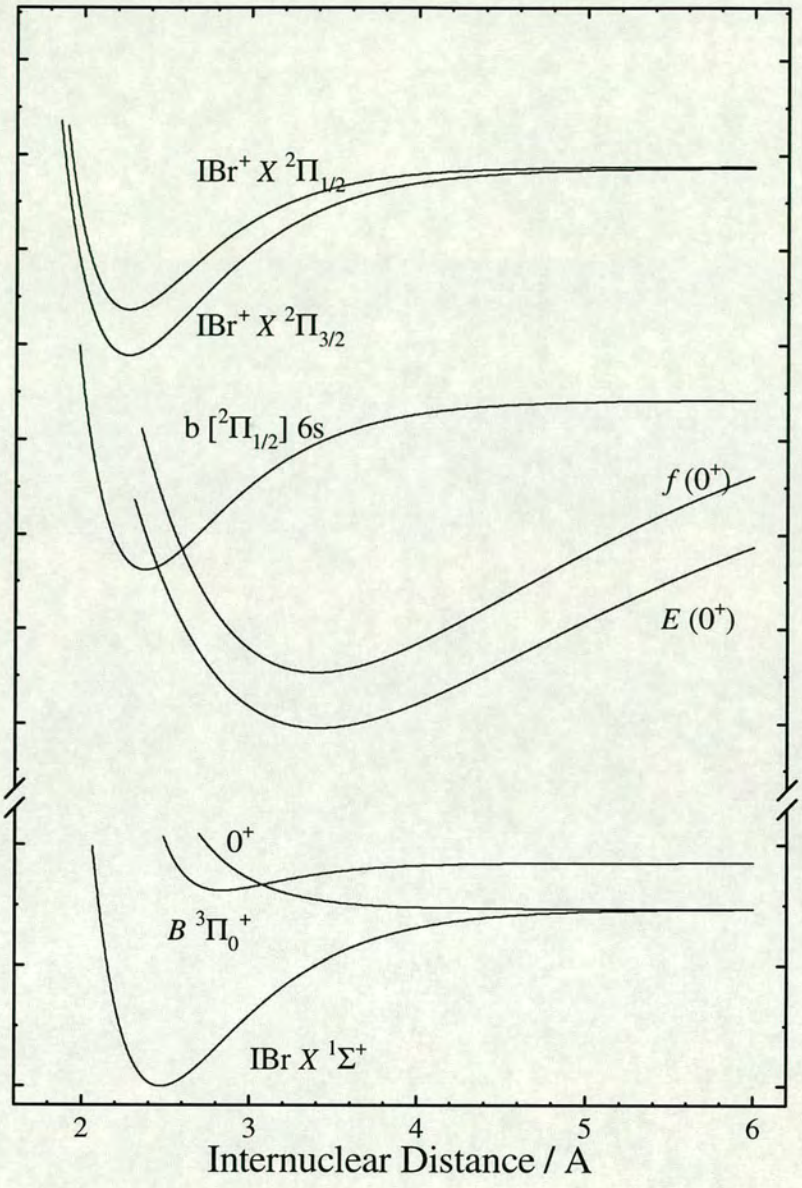

Figure 4-16 - Schematic potential energy diagram showing the neutral and ionic states of iodine bromide used in the (2+1′) and (1+2′) excitation schemes.

subject of a great deal of experimental [47,48,49,50] and theoretical [51] investigation due to the fact that it cannot be described as diabatic or adiabatic. Bound vibrational levels above the crossing point of the two states (somewhere above $v' = 4$) are only observed when there is a coincidence of J values between the unperturbed $B\ ^3\Pi_0^+$ state vibrational levels and the vibrational levels of the adiabatic potential formed from the mixing of the two states (termed the B' (0^+) state). The mixed nature of this system makes it an interesting choice as an intermediate state in a ZEKE-PFI experiment.

In this section we present the (2+1′) ZEKE-PFI spectrum of $I^{79}Br$ *via* the b $[^2\Pi_{1/2}]_c$ 6s;1 Rydberg state and the (1+2′) ZEKE-PFI spectrum of $I^{79}Br$ *via* the valence $B\ ^3\Pi_0^+$ state. The role of forced vibrational autoionisation and the influence of accidental resonances in the ZEKE-PFI spectra of IBr are discussed in the light of the spectra presented here.

4.6.2 Results

4.6.2.1 Experimental Details

The pump dye laser in the in the (2+1′) ZEKE-PFI work presented here used LDS 698 dye to produce light with a wavelength between 714 and 692 nm. This light was frequency doubled using a KD*P crystal with the dye fundamental being separated from the doubled output using a colour filter. This produced light with the required two-photon energy to excite into the $b[^2\Pi_{1/2}]_c$ 6s; 1 Rydberg state of $I^{79}Br$ (56000-57800 cm^{-1}) . The probe laser was pumped using the frequency tripled output of the Nd:YAG laser (355 nm). The dyes used for the probe laser were C460 and C440. The pulsed fields used in the (2+1′) ZEKE-PFI work were arranged as follows. The voltage pulse to the top plate was 3.8 V/cm^{-1} applied 1.12 μs after laser excitation. The voltage pulse on the bottom plate was 0.1 V/cm^{-1} applied between 130-690 ns after laser excitation.

In the (1+2′) ZEKE-PFI work two dyes were used for the pump laser, R590 and a DCM/R640 mixture to produce light of wavelengths 560 and 610 nm respectively. One visible photon was used to pump the $B\ ^3\Pi_0^+$ valence state of $I^{79}Br$.

The probe laser used a mixture of DCM and R640 to produce light of wavelengths 655 to 590 nm. The output from the probe laser was frequency doubled using a KD*P crystal and the dye fundamental was removed using a colour filter. The pulsed fields used in the (1+2′) ZEKE-PFI work were arranged in the same way as the (2+1′) ZEKE-PFI work.

Solid IBr (Fisons) was placed in a bulb which was then evacuated and filled to approximately 750 Torr with helium. The bulb was heated to ensure that the gas mixture was rich in IBr. The sample was introduced into the chamber *via* the General Valve pulsed nozzle with a stagnation pressure of between 420 and 730 Torr.

4.6.2.2 The (2+1′) ZEKE-PFI spectrum of the X $^2\Pi_{3/2,g}$ state of IBr^+

In this section we present the (2+1′) ZEKE-PFI spectrum of the X $^2\Pi_{3/2,g}$ state of $I^{79}Br$ recorded via the b[$^2\Pi_{1/2}$] 6s;1 Rydberg state. In figure 4-17 we present the mass resolved (2+1) REMPI spectrum of IBr recorded using the $I^{79}Br^+$ mass channel. The assignment of the spectra is taken from Yencha *et al.* and Donovan *et al.*[37] The v′ = 0, 1 and 2 vibrational levels were used as intermediates in an effort to cover a reasonable portion of the ground state potential as transitions from the b[$^2\Pi_{1/2}$] 6s;1 Rydberg state are expected to be diagonal in nature (Δv=0).

Figure 4-18 (a), (b) and (c) show the (2+1′) ZEKE-PFI spectra of $I^{79}Br$ recorded *via* three vibrational levels of the b_6 Rydberg state. In the spectrum via v′=0 (Figure 4.17 (a)) the peak at 79019±3 cm^{-1} is assigned as the origin band of the X $^2\Pi_{3/2}$ state. This value is in good agreement with the value obtained for the origin band from the C2P ZEKE-PFI of IBr (79018±1 cm^{-1}). The peak separations in figure 4-18 (c) (*via* v′ = 2) were fitted to the general expression for vibrational peak separations ($G_v = T_e + \tilde{\omega}_e(v+{}^1/_2) - \tilde{\omega}_e x_e(v+{}^1/_2)^2$) to yield values of $\tilde{\omega}_e$ and $\tilde{\omega}_e x_e$ for $I^{79}Br$; $\tilde{\omega}_e$ = 300±5 cm^{-1} and $\tilde{\omega}_e x_e$ = 1.3±0.5 cm^{-1}. These values are in agreement with those determined from the C2P ZEKE-PFI spectrum of IBr presented in section 4.5.

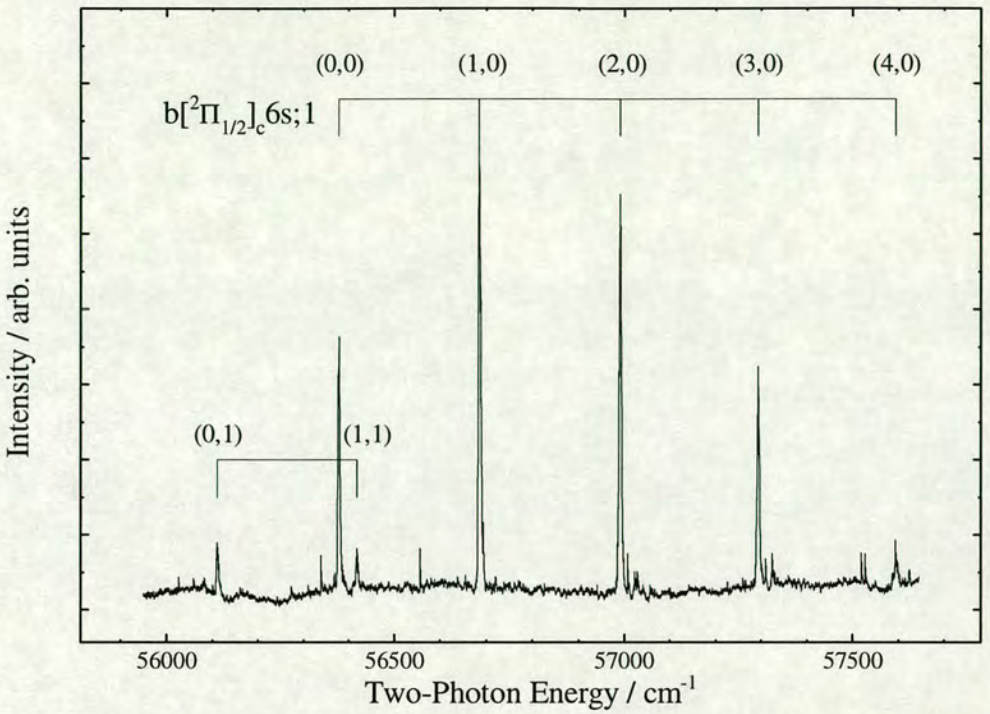

Figure 4-17 - The (2+1) REMPI spectrum of IBr in the 56000-57600 cm^{-1} two-photon energy range, recorded using the $I^{79}Br^+$ mass channel.

In each of the spectra there is a peak marked with an asterisk. This peak appears at constant probe photon energy, that is, the photon used to excite the IBr from the b_6 Rydberg state to the ion. This type of interloper signal has been observed in the (2+1′) ZEKE-PFI spectrum of I_2 [11] and was attributed to a double resonance involving the valence *A* state and an ion-pair state producing a large quantity of ions in the interaction region. The ion density from this accidental double resonance is thought to create a plasma in the interaction region which traps the kinetic electrons and allows them to be detected in the ZEKE electron channel in the time-of-flight spectrum. It is most probable that the marked peaks in figure 4-18 are also due to some accidental resonance resulting in a large ion density leading to a 'plasma' peak. However, the probe photon energy (22470 cm^{-1}) is too large to excite the molecule from the ground state to any of the valence states of IBr. One possibility is that the accidental resonance is a two-photon transition to one of the many

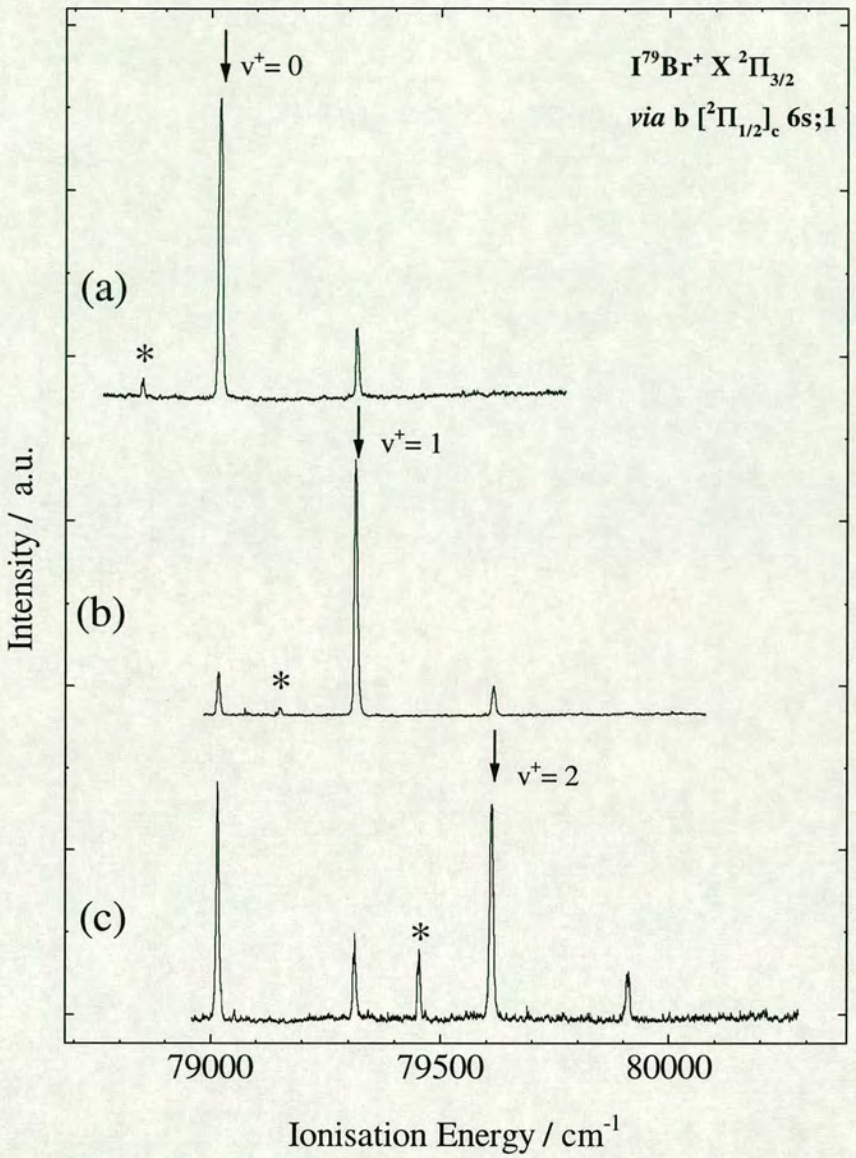

Figure 4-18 - The (2+1′) ZEKE-PFI spectrum of IBr recorded *via* the b_6 $[^2\Pi_{3/2}]_c$ $4d;1_g$ Rydberg state. The vertical arrows indicate the $\Delta v = 0$ transition and the small peaks marked with an asterisk indicate accidental $E(0^+) \leftarrow X$ neutral state resonances (see text for details).

accessible ion-pair states of IBr. The two-photon energy (44940 cm^{-1}) is very close to the energy of the v′ = 48 level of the *E* (0^+) ion-pair state.[36] Ionisation from the ion-pair state could produce the large concentration of ions needed to form a plasma which would result in a peak in the ZEKE electron channel. However, this explanation is only a tentative one as the Franck-Condon factors to the ion-pair states from the ground neutral state should be vanishingly small for this transition.

Another interesting feature of the spectra in figure 4-18 is the anomalous vibrational intensity distribution of the spectrum *via* v′ = 2 (trace (c)). It can be seen that there is substantial intensity in the $v^+ = 0$ peak (Δv = -2) which is not what one would expect given the similarity of the potentials for the b_6 Rydberg state and the ground state of the ion. This non Franck-Condon behaviour has also been observed in the (2+1′) ZEKE-PFI spectrum of the ground X $^2\Pi_{3/2,g}$ state of I_2 [11] and Br_2 (see section 4.3). The explanation in both of these cases has been shown to be forced vibrational autoionisation. It is assumed that a similar mechanism is responsible here although no threshold electron spectra have been recorded to probe for autoionising Rydberg states around the ionisation threshold.

4.6.2.3 The (1+2′) ZEKE-PFI Spectrum of the X $^2\Pi_{3/2,g}$ state of $I^{79}Br$

For the intermediate state vibrational levels to be used in the (1+2′) excitation route we chose one vibrational state that lies below the avoided crossing of the *B* $^3\Pi_0^+$ state and the 0^+ state, v′ = 2, and one that lies above, v′ = 19. The assignment of these vibrational levels is made on the basis of the observations of Selin [47] and the spectroscopic constants derived from the positions of the first five vibrational levels of the *B* $^3\Pi_0^+$ state.[33,49]

In figure 4-19 (a) and (b) we present the (1+2′) ZEKE-PFI spectrum of $I^{79}Br$ recorded by exciting through v′ = 1 and 19 of the valence *B* $^3\Pi_0^+$ state. In figure 4-19 (a), *via* v′ = 2, the peak at 79017±2 cm^{-1} is assigned to the band origin of the X $^2\Pi_{3/2,g}$ state of $I^{79}Br^+$ based on the C2P and (2+1′) ZEKE-PFI spectra of IBr presented in this section and section 4.3. As well as the origin band we see 7 more vibrational levels (v^+ = 1,4,6,9,10,14,16). The assignment of these peaks has been

made on the basis of the vibrational constants determined from the C2P ZEKE-PFI study of IBr. The appearence of the (1+2′) ZEKE-PFI spectrum is very patchy and the vibrational intensity distribution does not seem to follow any discernable pattern. Similarly in the ZEKE-PFI spectrum *via* v′ = 19 (Figure 4-19 (b)) we also have a very patchy vibrational intensity distribution. We observe $v^+ = 0$ through to 3 and also $v^+ =$ 11 and 15. Again there does not seem to be any pattern to the vibrational intensity distribution.

Also seen in the spectra presented in Figure 4-19 are a number of peaks that do not belong to the vibrational progression of the X $^2\Pi_{3/2,g}$ state of IBr (marked with asterisks). It is likely that these peaks are due to plasma effects caused by accidental resonances of the probe photon at the one-photon level (i.e. (1+1′)) around the ion-pair states of IBr. This type of behaviour can be seen in the (1+2′) ZEKE-PFI spectrum of I_2 [11] where accidental resonance of this type have been assigned to specific ion pair resonances at the (1+1′) level of excitation.

In an effort to see if accidental resonances could also explain the observed fragmentary intensity pattern in the (1+2′) ZEKE-PFI spectra of IBr a (1+1′+1′) double resonance REMPI spectrum was recorded *via* v′ = 19 of the *B* $^3\Pi_0^+$ state. Figure 4-20 shows the mass resolved DREMPI spectrum of $I^{79}Br$ recorded *via* v′ = 19 of the *B* $^3\Pi_0^+$ state and gating on the $I^{79}Br^+$ mass channel. The corresponding region of the (1+2′) ZEKE-PFI spectrum *via* v′ = 19 of the *B* $^3\Pi_0^+$ state (covering the first four vibrational levels of the ion) is also shown in Figure 4-20. The two spectra can be overlayed in this way as the probe photon is the same in both cases. In the DREMPI spectrum it is absorption of one probe photon that is being monitored and detected by ionisation with one or more probe photons. In the ZEKE-PFI spectrum it is absorption of two probe photons being monitored. Adding the energy of one probe photon to the DREMPI spectrum places the two spectra in the same energy region and allows for easy identification of possible accidental resonances in the ZEKE-PFI spectrum at the one probe photon level.

A vibrational progression with a spacing of approximately 110 cm^{-1} can be seen in the DREMPI spectrum. The peaks have been assigned to the v′ = 26 - 31

levels of the f (0^+) ion pair state using the spectroscopic constants determined by Brand *et al.*[52] (see figure 4-16 for the position of the f (0^+) ion pair state potential). The band origin and $v^+ = 3$ have exact resonances with these ion pair peaks whereas the $v^+ = 2$ peak has a resonance with an unassigned peak (marked with an asterisk). This unassigned peak also appears in the spectrum when the pump laser (that accesses the $B\ ^3\Pi_0^+$ state) is blocked, indicating that it is a one-colour signal due to excitation by the probe laser only. The two-probe-photon energy for this peak is 61800 cm^{-1} which places it around the c_6 Rydberg state [37] although it cannot be assigned to this Rydberg state or any of the other Rydberg states in this region. Of the four vibrational levels of the X $^2\Pi_{3/2}$ state of IBr in this energy region only one does not have a resonance with a excited neutral state at the intermediate photon energy ($v^+ = 1$). From the above observations it would seem that the vibrational intensity distribution in the (1+2′) ZEKE-PFI spectrum of IBr^+ *via* the $B\ ^3\Pi_0^+$ state is dominated by peaks due to a (1+1′+1′) double resonance excitation scheme *via* the f (0^+) ion-pair state.

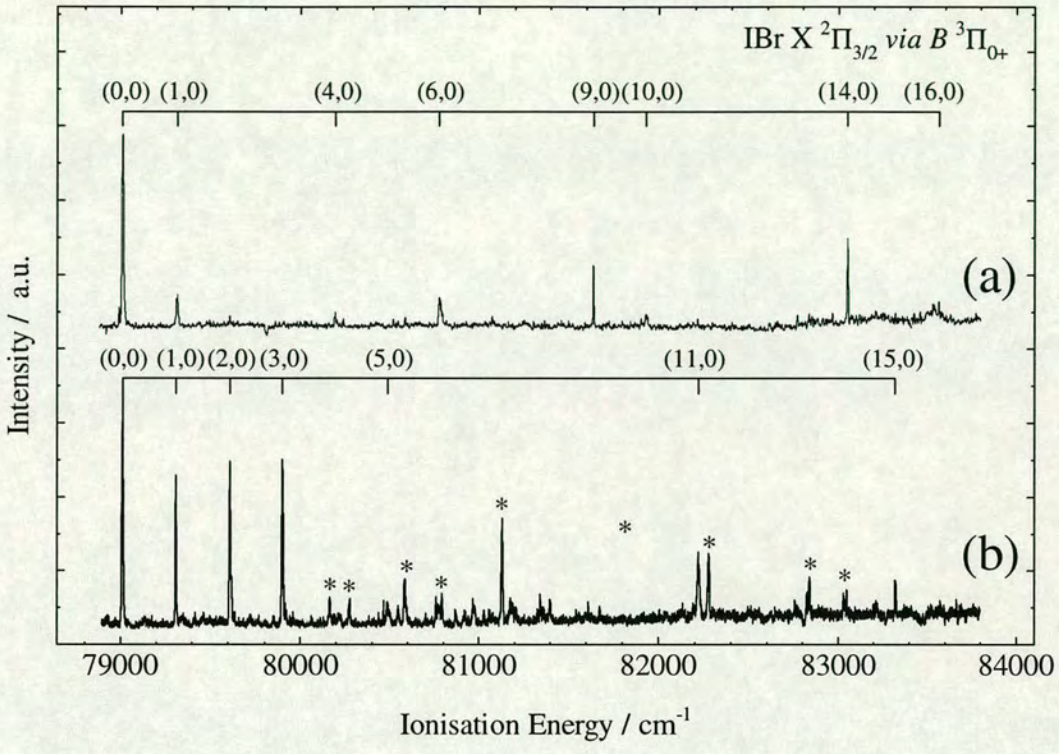

Figure 4-19 - The (1+2′) ZEKE-PFI spectrum of IBr in the range 78900-83900 cm^{-1} recorded *via* (a) v′ = 2 and (b) v′ = 19 of the valence $B\ ^3\Pi_{0+}$ state. The asterisks denote peaks due to possible accidental resonances with neutral states.

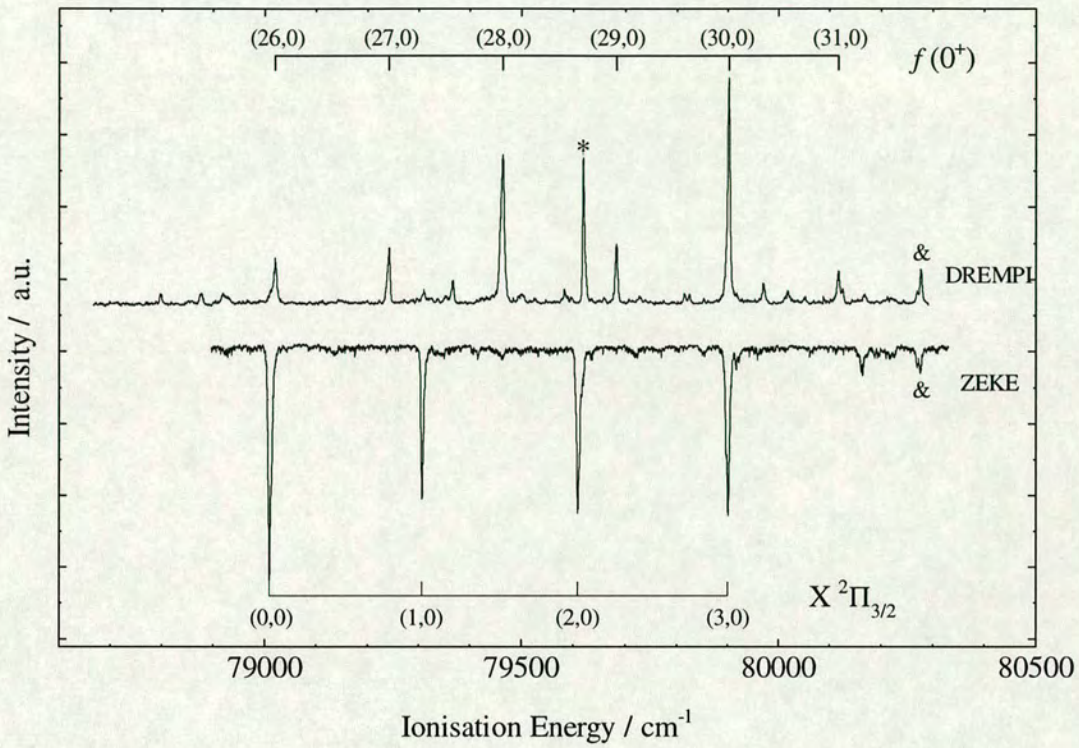

Figure 4-20 - A comparison of the (1+2′) ZEKE-PFI (lower) and the (1+1′+1′) DREMPI spectra (upper) recorded *via* v′ = 19 of the valence $B\ ^3\Pi_{0+}$ state. The energy axis is that corresponding to the ZEKE-PFI spectrum. The ion-pair spectrum was recorded using the $I^{79}Br^+$ mass channel.

4.6.3 Discussion

Of the work presented in this section the most difficult to understand at first glance is the (1+2′) ZEKE-PFI spectra of IBr *via* the $B\ ^3\Pi_0^+$ valence state. The vibrational intensity distributions seen in the two spectra presented in Figure 4-19 do not seem to follow any logical pattern. In the case of the (1+2′) ZEKE-PFI spectrum of I_2 [10] similar behaviour was observed, although certain portions of the vibrational intensity distribution did behave in the way expected based on Franck-Condon factors. The peaks whose intensity did not match the expected intensity were shown to be influenced by accidental resonances at the probe laser one-photon energy with ion-pair states of I_2. The accidental resonances were seen to enhance vibrational peaks in the ZEKE-PFI spectrum.

This has been shown to be the case with the (1+2′) ZEKE-PFI spectrum of IBr. The (1+1′+1′) double resonance REMPI spectrum of $I^{79}Br$ in the energy region that corresponds to the (1+2′) ZEKE-PFI spectrum shows clear evidence of accidental resonances with ion-pair states for certain ionic vibrational levels. The resonances with the ion-pair states will enhance the transition to the high *n* Rydberg states below the ionic vibrational levels and may also be providing the necessary Franck-Condon overlap for the transitions to be observed. This would explain the patchy nature of the (1+2′) ZEKE-PFI spectra as it is unlikely that there will be resonance for every vibrational level of the ion. The strong ZEKE-PFI signals obtained when an accidental resonance is found indicate that the ion-pair states of IBr could be used as intermediates in a (2+1′) ZEKE-PFI experiment.

In the (2+1′) ZEKE-PFI spectrum of IBr *via* $v' = 2$ (figure 4-18 (c)) we see a situation similar to that seen in the (2+1′) ZEKE-PFI spectra of Br_2 and I_2. This time the intensity pattern shows an enhancement in a $\Delta v = -2$ transition without much enhancement in the $\Delta v = -1$ transition. This contrasts the behaviour seen in the spectra of I_2 and Br_2 in which the $\Delta v = -1$ transition is always more enhanced or at least of the same magnitude as the $\Delta v = -2$ transition. The cause of the enhancement in IBr may be due to forced vibrational autoionisation although there is the possibility of forced spin-orbit autoionisation as transitions from the b $[^2\Pi_{1/2}]_c$ 6s;1 Rydberg state

will preferentially populate Rydberg states based on the X $^2\Pi_{1/2}$ ionic state. A Rydberg state based on the X $^2\Pi_{1/2,}$ could be resonant with the $v^+ = 0$ peak of the X $^2\Pi_{3/2}$ state. However, threshold electron spectra would need to be recorded to confirm the cause of the enhancement and identify the Rydberg state responsible.

In summary we have presented the (2+1′) and (1+2′) ZEKE-PFI spectra of the X $^2\Pi_{3/2,g}$ state of $I^{79}Br$ *via* the b $[^2\Pi_{1/2}]_c$ 6s;1 Rydberg state and the *B* $^3\Pi_0^+$ valence state respectively. In the ZEKE-PFI spectra *via* the b_6 Rydberg state forced autoionisation processes may be affecting the observed vibrational intensity distribution of the X $^2\Pi_{3/2,g}$ state. It was also noted that the ZEKE-PFI signal *via* the b_6 Rydberg state was reasonably strong even though we were exciting through a Rydberg state based on the X $^2\Pi_{1/2,g}$ state of IBr. In the ZEKE-PFI spectra *via* the *B* $^3\Pi_0^+$ state it was seen that accidental resonance *via* the *f* (0^+) ion-pair states at the one-probe-photon level were responsible for the observation of vibrational peaks of the $\tilde{X}\,^2\Pi_{3/2,g}$ state and for other peaks due to plasma effects.

4.7 Conclusions

From the work presented here it would seem that Franck-Condon factors have little influence over the observed vibrational intensity distributions in ZEKE-PFI spectroscopy. The reason behind this is the almost ubiquitous prescence of final state interactions in any ZEKE-PFI experiment. The (2+1′) ZEKE-PFI spectra of I_2, Br_2 and IBr all show signs of forced vibrational autoionisation contributing to the intensity of certain vibrational levels. As well as the influence of final state interactions, intermediate state interactions in the form of accidental resonances can seriously affect the observed distributions. This was illustrated by the fragmentary vibrational intensity distributions seen in the (1+2′) ZEKE-PFI of IBr where vibrational levels of the ion were only detected due to accidental resonances with the $f\,(0^+)$ ion-pair state after absorption of two photons.

However, in some examples of intermediate state interactions the observed distributions can be explained perfectly using Franck-Condon arguments. Absorption *via* a repulsive intermediate state and the susequent widening of the Franck-Condon window can give access to highly excited vibrational levels of the final state that would otherwise not be observed. This is proposed to be the cause of the distributions observed in the C2P ZEKE-PFI spectra of I_2 and IBr where the vibrational progressions observed extend far further than would be expected based on non-resonant two photon excitation from the ground electronic state.

There remains some further work that could confirm some of the conclusions reached from the ZEKE-PFI study of I_2, Br_2 and IBr. The most obvious of which would be a single-photon ZEKE-PFI study of these molecules. This would confirm without any doubt whether the extended progressions seen in I_2 and IBr are the result of intermediate state interactions or final state interactions. A related experiment would be a two colour C2P ZEKE-PFI study of I_2, Br_2 and IBr where the first photon is tuned to the maximum of a repulsive continuum absorption. Again, the results of such a study would elucidate the mechanism behind the observation of highly excited vibrational levels in the one colour C2P ZEKE-PFI spectra. This type of experiment would be particularly interesting if carried out on Br_2 as there are regions of the UV

absorption curve that are quite strong absorptions but just not in the energy range used in a one colour C2P excitation scheme.

A (2+1′) ZEKE-PFI study of IBr *via* an ion-pair state would be another possible experiment to perform. Excitation through a specific ion-pair level would open up a very wide Franck-Condon window for excitation to the high *n* Rydberg states. The strong ZEKE-PFI signals obtained when an ion-pair state was accidentally used as an intermediate in the (1+2′) ZEKE-PFI study seems to suggest that the ion-pair states would be very good intermediate states.

The spectroscopic constants determined for IBr and Br_2 are summarised in Table 4-7. The most important data is that obtained for the two spin-orbit states of IBr ($X\ ^2\Pi_{3/2}$ and $X\ ^2\Pi_{1/2}$). Previous to this study the best ionisation energies for IBr were only accurate to $\pm 30\ cm^{-1}$ and the spin-orbit splitting between the two components was subject to an even greater error. The accuracy of the vibrational constants also represents a significant improvement from previous work. The important results from the Br_2^+ data are the accurate ionisation energies and the spin-orbit splitting for the $X\ ^2\Pi_{3/2,g}$ and $X\ ^2\Pi_{1/2,g}$ states. The vibrational constants could not be determined to the same level of accuracy as the dispersed fluorescence work of Zackrisson.[26]

Table 4-7 - Spectroscopic data obtained for the X $^2\Pi_{3/2}$ and X $^2\Pi_{1/2}$ states of IBr^+ and Br_2^+.

State	Adiabatic Ionisation Energy (cm^{-1})	ϖ_e (cm^{-1})	$\varpi_e x_e$ (cm^{-1})	D_0 (cm^{-1})	Spin-Orbit Splitting (cm^{-1})
IBr^+					
X $^2\Pi_{3/2}$	79018±1	303±1 [a] 300±1 [c]	1.0±0.1 [a] 0.9±0.1 [c]	19808±2 [b]	
					4662±2
X $^2\Pi_{1/2}$	83680±1	300±1	2.0±0.1	15146±2 [b]	
Br_2^+					
X $^2\Pi_{3/2}$	84828±2	369±4 [d] 370±6 [f]	1.8±0.5 [d] 2.2±0.5 [f]	26352±3 [e]	
					2820±4
X $^2\Pi_{1/2}$	87648±2 [d]	360±6 [f]	1.0±0.5 [f]	23532±3 [e]	

[a] $I^{79}Br$

[b] Assuming dissociation to Br ($^2P_{3/2}$) + I^+ ($^3P_2$) [33,53]

[c] $I^{81}Br$

[d] Determined from (2+1′) ZEKE-PFI spectum

[e] Assuming dissociation to Br ($^2P_{3/2}$) + Br^+ ($^3P_2$) [33,53]

[f] Determined from C2P ZEKE-PFI spectum

4.8 References

[1] D. C. Frost, C. A. McDowell, D. A. Vroom, *J.Chem.Phys.* 1967, **46**, 4255.

[2] A. W. Potts, W. C. Price, *Trans.Faraday.Soc.* 1971, **67**, 1242

[3] A. B. Cornford, D. C. Frost, C. A. McDowell, J. L. Ragle, I. A. Stenhouse, *J.Chem.Phys.* 1971, **54**, 2651.

[4] B. R. Higginson, D. R. Lloyd, P. J. Roberts, *Chem.Phys.Lett.* 1973, **19**, 480.

[5] H. van Lonkhuyzen, C. A. de Lange, *Chem.Phys.* 1984, **89**, 313.

[6] T. Harris, J. H. D. Eland, R. P. Tuckett, *J.Mol.Spect.* 1983, **98**, 269.

[7] P. Hamilton, *Chem.Phys.Lett.* 1987, **140**, 591.

[8] A. J. Yencha, M. C. R. Cockett, J. G. Goode, R. J. Donovan, A. Hopkirk, G. C. King, *Chem.Phys.Lett.* 1994, **229**, 347.

[9] A. J. Yencha, A. Hopkirk, A. Hiraya, R. J. Donovan, J. G. Goode, R. R. J. Maier, G. C. King, A. Kvaran, *J.Phys.Chem.* 1995, **99**, 7231.

[10] M. C. R. Cockett, *J.Phys.Chem.* 1995, **99**, 16228.

[11] M. C. R. Cockett, J. G. Goode, K. P. Lawley, R. J. Donovan, *J.Chem.Phys.* 1995, **102**, 5226.

[12] M. C. R. Cockett, K. P. Lawley, R. J. Donovan, *J.Chem.Phys.* 1996, **105**, 3347.

[13] F. Merkt, P. M. Guyon, *J.Chem.Phys.* 1993, **99**, 3400.

[14] F. Merkt, T. P. Softley, *J.Phys.Chem.* 1992, **96**, 4149.

[15] F. Merkt, T. P. Softley, *Int. Rev.Phys.Chem.* 1993, **12**, 205.

[16] P. M. Guyon, T. Baer, I. Nenner, *J.Chem.Phys.* 1983, **78**, 3665; W. A. Chupka, P. J. Miller, E. E. Eyler, *J.Chem.Phys.* 1988, **88,** 3032.

[17] W. Kong, J. W. Hepburn, *Can.J.Phys.* 1994, **72**, 1284.

[18] J. H. D. Eland, "Photoelectron Spectroscopy" 2nd. Ed., 1984, London, Butterworth.

[19] A. Strobel, A. Lochschmidt, I. Fischer, G. Niedner-Schatteburg, and V. E. Bondybey, *J.Chem.Phys.* 1993, **99**, 733; A. Strobel, I. Fischer, A. Lochschmidt, K. Müller-Dethlefs, and V. E. Bondybey, *J.Phys.Chem.* 1994, **98**, 2024; N. Knoblauch, A. Strobel, I. Fischer, and V. E. Bondybey, *J.Chem.Phys.* 1995, **103**, 5417.

[20] Y.-F. Zhu and E. R. Grant, *J.Phys.Chem.* 1993, **97**, 9582.

[21] R. J. Donovan, R. V. Flood, K. P. Lawley, A. J. Yencha, T. Ridley, *Chem.Phys.* 1992, **164**, 439.

[22] R. J. Donovan, A. C. Flexen, K. P. Lawley, T. Ridley, *Chem.Phys.* (submitted for publication)

[23] C. E. Moore, "Atomic Energy Levels", Nat.Stan.Ref.Data.Sys.-Nat.Bur.Stan. **35**, 1971.

[24] P Venkateswarlu, *Can.J.Phys.* 1970, **48**, 1055.

[25] G. Herzberg, Ch. Jungen, *J.Mol.Spect.* 1972, **41**, 425.

[26] M. Zackrisson, *J.Mol.Spect.* 1994, **163**, 371.

[27] T. Ridley, K. P. Lawley, R. J. Donovan, *Chem.Phys.* 1990, **148**, 315.

[28] R. J. Donovan, A. C. Flexen, K. P. Lawley, T. Ridley, (submitted for publication).

[29] P. Venkateswarlu, *Can.J.Phys.* 1969, **47**, 2525.

[30] A. Strobel, I. Fischer, J. Staecker, G. Niedner-Schatteburg, K. Müller-Dethlefs, V. E. Bondybey, *J.Chem.Phys.* 1992, **97**, 2332.

[31] G. Reiser, W. Habenicht, K. Müller-Dethlefs, *J.Chem.Phys.* 1993, **98**, 8462.

[32] C.-W. Hsu, D. P. Baldwin, C.-L. Liao, C. Y. Ng, *J.Chem.Phys.* 1994, **100**, 8047; C.-W. Hsu, C. Y. Ng, *J.Chem.Phys.* 1994, **101**, 5596.

[33] K. P. Huber, G. Herzberg, "Constants of Diatomic Molecules", Van-Nostrand Reinhold, New York, 1979.

[34] M. Tamres, W. K. Duerksen, J. M. Goodenow, *J. Phys.Chem.* 1968, **72**, 966.

[35] R. G. Aickin, N. S. Bayliss, *Trans.Farad.Soc.* 1938, **34**, 1371.

[36] J. C. D. Brand, U. D. Deshpande, A. R. Hoy, S. M. Jaywant, E. J. Woods, *J.Mol.Spect.* 1983, **99**, 339; J. C. Brand, D. R. Dhatt, A. R. Hoy, D. C. P. Tse, *J.Mol.Spect.* 1986, **119**, 398; K. P. Lawley, D. Austin, J. Tellinghuisen, R. J. Donovan, *Mol.Phys.* 1987, **62**, 1195.

[37] A. J. Yencha, R. J. Donovan, A. Hopkirk, D. Shaw, *J.Phys.Chem.* 1988, **92**, 5523; R. J. Donovan, R. V. Flood, K. P. Lawley, R. Maier, C. R. Redpath, T. Ridley, and A. J. Yencha, *Arab.J.Sci.Eng.* 1992, **17**, 253; A. J. Yencha, T. Ridley, R. Maier, R. V. Flood, K. P. Lawley, R. J. Donovan, A. Hopkirk, *J.Phys.Chem.* 1993, **97**, 4582.

[38] R. J. Donovan, D. Husain, *Trans.Farad.Soc.* 1968, **64**, 2325; M. S. Child, *Mol.Phys.* 1976, **32**, 1495; M. A. A. Clyne, M. C. Heaven, *J.Chem.Soc.Farad.II.* 1980, **76**, 49

[39] D. J. Seery and D. Britton, *J.Phys.Chem.* 1964, **68**, 2263.

[40] R. S. Mulliken, *Phys.Rev.* 1934, **46**, 549; *ibid*, 1940, **57**, 500.

[41] C. E. Moore, "Atomic Energy Levels", Nat.Stan.Ref.Data.Sys.-Nat.Bur.Stan. **35**, 1971.

[42] T. Ridley, K. P. Lawley, R. J. Donovan, *Chem.Phys.* 1990, **148**, 315.

[43] D. R. Lide (Ed.), "CRC Handbook of Chemistry and Physics", 74th Edition, 1993-1994.

[44] M. S. N. Al-Kahali, R. J. Donovan, K. P. Lawley, T. Ridley, *Chem.Phys.Lett.* 1994, **220**, 225; R. J. Donovan, K. P. Lawley, Z. Min, T. Ridley, A. J. Yarwood, *Chem.Phys.Lett.* 1994, **226**, 525; M. S. N. Al-Kahali, R. J. Donovan, K. P. Lawley, Z. Min, T. Ridley, *J.Chem.Phys.* 1996, **104**, 1825.

[45] Z. Min, T. Ridley, K. P. Lawley, R. J. Donovan, *J.Photochem.Photobio.* A, 1996, **100**, 9.

[46] C. A. de Lange, Chapter 6 in "High Resolution Laser Photoionization and Photoelectron Studies", Wiley, Chichester, 1995.

[47] L. A. Selin, *Ark.Fys.* 1962, **21**, 529.

[48] J. J. Wright, M. D. Harvey, *J.Chem.Phys.* 1978, **68**, 864.

[49] M. A. A. Clyne, M. C. Heaven, *J.Chem.Soc.Farad.II.* 1980, **76**, 49.

[50] H. Knockell, E. Tiemann, D. Zoglowek, *J.Mol.Spect.* 1981, **85**, 225.

[51] M. S. Child, R. B. Bernstein, *J.Chem.Phys.* 1973, **59**, 5916; M. S. Child, *Mol.Phys.* 1976, **32**, 1495.

[52] J. C. Brand, U. D. Deshpande, A. R. Hoy, S. M. Jaywant, E. J. Woods, *J.Mol.Spect.* 1983, **99**, 339.

[53] D. R. Lide (Ed.), "CRC Handbook of Chemistry and Physics", 74th Edition, 1993-1994.

5. REMPI and ZEKE-PFI Studies of I_2-X van der Waals Complexes (X = Ar, Kr, N_2)

5.1 Introduction

The spectroscopy of van der Waals complexes represents one of the main areas in the study of intermolecular interactions. Within this general field the spectroscopy of the electronically excited states of van der Waals complexes is a particularly interesting area. The excited states of van der Waals complexes are, in general, similar to the excited states of the solute molecule in the complex, perturbed slightly by the prescence of the solvent atoms or molecules. However, the different contributions to the intermolecular potential between the solute and solvent molecules (dispersion, induction, electron-electron repulsion) can vary with the electronic states of the solute molecule. As a result the excited electronic states of a van der Waals complex can have very different binding energies, equilibrium separations and geometries relative to the complex in the ground electronic state.

The main techniques used to study the excited states of van der Waals molecules are laser induced fluorescence (LIF)[1] and REMPI spectroscopy. Pulsed molecular beams are normally used to generate the molecules by passing the solute molecule in a carrier gas containing the solvent molecule through a pulsed jet expansion. LIF excitation and dispersed emission spectroscopy allow the determination of vibrational and rotational information for ground and excited states of van der Waals molecules. However, LIF is is not species selective with the result that the fluorescence observed can be from from any emitting species in the molecular beam. This can cause congestion of spectra when more than one van der Waals molecule is present in the expansion. The problem of species selectivity can be solved through the use of REMPI spectroscopy combined with time-of-flight mass spectrometry,[2,3] which provides mass resolution for the excitaton spectra of van der Waals molecules. The first example of REMPI being used to study the excited states

of a van der Waals complex was the work of Sato *et al.*[4] on the $C\,^2\Pi$ Rydberg state of NO-Ar.

In the study of excited state van der Waals molecules a distinction can be made between two groups; large solute and small solute molecules. The division is based on the changes in the van der Waals interaction when the molecule is promoted to an electronically excited state. A large solute molecule is defined in this case as a carbon containing polyatomic, whereas a small solute molecule is defined to be a diatomic or small polyatomic. A few of the basic trends in the changes to the van der Waals interaction for both types of complex will now be discussed. For the sake of brevity the two types of complex will be referred to as LS (large solute van der Waals molecule) and SS (small solute van der Waals molecule)

Excitation of an LS to a valence state normally results in a strengthening of the van der Waals interaction. This is indicated in spectra as a red-shift (movement to lower energy) of the origin band of the LS excited state relative to the bare solute molecule excited state. Examples of this are the $S_1 \leftarrow S_0$ transitions for the complexes of benzene,[5] aniline,[6] and naphthalene[7] with argon. The increase in binding energy is thought to be caused by the increased polarisability of the excited valence state resulting in larger dispersion forces between the solute and solvent molecules. Rydberg states of LS complexes present a more complicated picture than that seen in the majority of valence state studies. The 3*s* Rydberg states of diazobicyclo[2.2.2]octane (DABCO) and azabicyclo[2.2.2]octane (ABCO) have been studied by Shang *et al.*[8] using REMPI spectroscopy. In this study they observed that Rydberg states of solute - rare gas complexes were *blue* shifted relative to the Rydberg state of the bare solute molecule. The blue shift was explained by an increase to the electron-electron repulsion between the solute and solvent caused by the larger Rydberg orbital. Also in this study it was observed that if a polar solvent molecule (as opposed to the non-polar rare gas atoms) was complexed to ABCO and DABCO then the Rydberg state was *red* shifted relative to the bare solute Rydberg state. The increase in binding was attributed to dipole-induced dipole interactions and formation of a charge transfer complex between the solute and solvent molecules.

For SS complexes the behaviour of valence and Rydberg states is almost exactly opposite to the behaviour of LS complexes. Valence states of SS complexes such as the *B* states of the rare gas - iodine complexes[9] tend to be blue shifted relative to the bare solute valence state as a consequence of increased electron-electron repulsion. The REMPI spectra of Rydberg states of SS complexes such as the NO-X complexes (where X is a rare gas atom or CH_4)[10] are all red shifted relative to the bare solute Rydberg states. Another example of red shifted Rydberg states of SS complexes is the $g\ ^3\Sigma^-(0^+)$ Rydberg state of HI-Ar.[11] The increased binding energy can be rationalised by considering the solvent molecule to be within the radius of the Rydberg orbital and subject to charge-induced dipole interactions. The electron in the Rydberg orbital no longer shields the solvent from the ionic core of the solute molecule with the result that the solvent is exposed to a partial positive charge. The exceptions to these Rydberg state red shifts are the lowest lying Rydberg states of NO-Ar [12] and NO-Kr [13] (the $A\ ^2\Sigma^+$ state) where the excitation spectra are blue-shifted due to electron-electron repulsion. In this case the Rydberg orbital is not large enough to enclose the solvent atom and as a result forces it away with the result that the complex is more weakly bound.

The study of van der Waals cations is another area in which changes are seen in the van der Waals interaction. When a van der Waals molecule ionises the solvent atom or molecule is exposed to a full positive charge on the solute molecule. The resultant charge-induced dipole interaction can significantly strengthen the van der Waals bond. The study of van der Waals cations began in earnest with the arrival of ZEKE-PFI photoelectron spectroscopy.[14] Previous photoelectron techniques did not offer the resolution required to investigate the low frequency vibrational modes of van der Waals cations. Mass resolution of the ionic spectra of van der Waals complexes can also be obtained with mass analysed threshold ionisation (MATI),[15,16] the sister technique to ZEKE-PFI. Other techniques can also used to study the ionic van der Waals complexes, these include ion-depletion IR spectroscopy[17] and IR dissociation spectroscopy.[18] However, these techniques give information on the effect of the

solvent atom or molecule on the vibrational modes of the solute molecule, and no direct information on the intermolecular potential.

In this chapter we present the mass resolved (2+1) REMPI spectra of the $[^2\Pi_{3/2}]_c$ 5d;2 and $[^2\Pi_{3/2}]_c$ 5d;0 *gerade* Rydberg states of the I_2-Kr van der Waals complex and the $[^2\Pi_{1/2}]_c$ 6s;1 *gerade* Rydberg state of the I_2-N_2 van der Waals complex. The spectra and the constants determined are compared to those of the analogous Rydberg states of I_2-Ar.[19] This is the first observation of either the I_2-Kr or I_2-N_2 complex in an excited Rydberg state. An empirical potential surface has been constructed for the ground state of the I_2-N_2 complex which has been used to investigate the complex geometry. We also present a reanalysis of the REMPI spectra of the $[^2\Pi_{3/2}]_c$ 5d;2 and $[^2\Pi_{3/2}]_c$ 5d;0 *gerade* Rydberg states of I_2-Ar. The Rydberg spectra provide evidence for the existence of a second, linear isomer of I_2-Ar.

The $[^2\Pi_{3/2}]_c$ 5d;2_g Rydberg states of I_2-Ar and I_2-Kr have been used as intermediates in a (2+1′) ZEKE-PFI study of the ground ionic states ($\tilde{X}\,^2\Pi_{3/2,g}$) of the two complexes. This is the first observation of the $\tilde{X}\,^2\Pi_{3/2,g}$ state of I_2-Kr. The $\tilde{X}\,^2\Pi_{3/2,g}$ state of I_2-Ar has been the subject of a previous ZEKE-PFI study by this group.[20] In this case the ZEKE-PFI spectrum of the $\tilde{X}\,^2\Pi_{3/2,g}$ state of I_2-Ar is used as a probe to provide further evidence of the existence of two isomers of the complex. Isomer specific ZEKE-PFI spectra are obtained and are compared to the previous ZEKE-PFI study.[20]

The layout of the chapter is as follows: section 5.2 is concerned with the REMPI and ZEKE-PFI spectra of I_2-Ar, section 5.3 presents the REMPI and ZEKE-PFI spectra of I_2-Kr and section 5.3 presents the REMPI spectrum of I_2-N_2 and the results of the empirical potential calculation. Conclusions are given in section 5.4.

5.2 Structural Isomerism in I_2-Ar

5.2.1 Introduction

The I_2-Ar van der Waals complex was first observed by Levy *et al.* in the fluorescence excitation and dispersed fluorescence spectra from the valence *B* [$^3\Pi_{0u}^+$] state.[21] This work was one of a set of papers published by Levy *et al.* on the I_2-rare gas van der Waals complexes which determined their binding energies,[22] photodissociation dynamics and predissociation dynamics.[23] The simplicity of the system and the large amount of experimental data on the I_2-rare gas van der Waals complexes gave theoreticians the chance to try to understand the van der Waals interaction and the way it influences dynamical processes.[24]

One of the most interesting dynamical processes that the I_2-Ar van der Waals complex undergoes is the one atom cage effect. The ability of solvent molecules in the condensed phase to prevent dissociation of a molecule (caging) is well documented.[25] It was shown, firstly by Saenger *et al.*[26] and Valentini and Cross,[27] that the dissociation of I_2 can be prevented by solvent atoms in the gas phase. A larger study by Phillipoz *et al.*[28] showed that a single Ar atom is able to prevent the dissociation of I_2 excited up to 900 cm^{-1} above the dissociation limit of the *B* [$^3\Pi_{0u}^+$] state. These observations stimulated much theoretical activity directed at the photodissociation dynamics of I_2-Ar and the role of the Ar atom in the recombination of the I_2 molecule.[27,29,30,31,32] However, it was only recently that theoretical simulations of the cage effect have managed to reproduce the vibrational population distributions observed in the *B* state subsequent to the caging process.[33] In this work kinematic energy transfer is assumed to be the mechanism for the cage effect with the I_2-Ar complex adopting a linear geometry in the ground state.

The geometry of the I_2-Ar complex was the key factor in determining the mechanism of the one-atom cage effect. The complex was initially assumed to be linear in analogy with the determined structures of several heteronuclear diatomic -Ar van der Waals complexes (Ar-ClF, Ar-HF and Ar-HCl[34]). However, a number of homonuclear diatomic - Ar van der Waals complexes were found to have a T-shaped

structure (I_2-He,[35] Br_2-Ne,[36] Cl_2-Ne,[37] and Cl_2-Ar [38]). This left the geometry of the I_2-Ar complex in doubt until Burke and Klemperer[39] obtained a rotationally resolved fluorescence excitation spectrum of the $B\ ^3\Pi_{0u}^+ \leftarrow X\ ^1\Sigma_{0g}^+$ transition. Rotational band contour analysis allowed them to determine that a T-shaped complex is responsible for the observed discrete fluorescence structure. However, in another study by Burke and Klemperer on the same system,[40] continuum fluorescence was observed between the discrete vibrational levels of the *B* state of the complex which was attributed to the possible existence of a linear complex. They argued that due to the increased electron-electron repulsion directed along the I-I bond axis towards the Ar atom, and the lengthening of the I-I bond upon excitation to the *B* state, that any $B \leftarrow X$ transition of the linear isomer would result in a broad, continuum like fluorescence from numerous vibrationally excited states of the van der Waals modes.

The experimental and theoretical work points towards the existence of two isomers of I_2-Ar. However, the only direct structural information that has been obtained (determined from the rotationally resolved fluorescence work of Burke and Klemperer[39]) shows that the I_2-Ar complex is T-shaped in the ground and valence *B* states. Observation of a linear isomer in the ground or excited states of I_2-Ar would confirm the mechanism of the one-atom cage effect and explain the continuum fluorescence observed between discrete levels of the $B \leftarrow X$ fluorescence.

As mentioned in the introduction to this chapter, the I_2-Ar van der Waals complex has been studied by the ZEKE group in Edinburgh. In previous studies a number of *gerade* Rydberg states were characterised (for n = 5 to 7) using mass resolved (2+1) REMPI spectroscopy.[19] In the light of Burke and Klemperer's structural analysis,[39] it was assumed at the time that the complex most probably adopted a T-shaped conformation both in the neutral ground state as well as in all of the Rydberg states characterised in the study. This assumption was further supported by the observation that the complex was able to support as many as five quanta of the I_2 stretching mode (for $[^2\Pi_{1/2}]_c$ 6s;1_g Rydberg state) without dissociating, which suggested very weak coupling between the inter- and intra-molecular modes. More recently, the 5d Rydberg states based on both spin-orbit ionic ground states were used a resonant intermediate states in a two-colour study of the two spin-orbit components

of the ground ionic state of I_2^+-Ar using ZEKE-PFI photoelectron spectroscopy.[20] Accurate values for the ionisation energies and vibrational constants for the complex were determined for both spin-orbit states.

In the earlier REMPI study,[19] we noted that many of the vibrational bands assigned to the $[^2\Pi_{3/2}]_c$ 5d; 2_g Rydberg state were split into apparent doublets. At the time the explanation put forward was that the splitting might be due either to van der Waals bending mode structure or to partially resolved rotational branch heads. However, neither explanation is convincing, and it has subsequently emerged from the work presented here, that the splitting almost certainly arises from two partially overlapping vibrational progressions due to two structural isomers; T-shaped and linear. In the work presented in this section we probe the $[^2\Pi_{3/2}]_c$ 5d; 2_g Rydberg state of the complex using (2+1′) ZEKE-PFI photoelectron spectroscopy in order to record both state specific and isomer specific ZEKE-PFI spectra and provide further spectroscopic evidence for the existence of two structural isomers. This is the first direct spectroscopic evidence that I_2-Ar has a bound linear isomer.

5.2.2 Results

5.2.2.1 Experimental Details

The pump dye laser in both the REMPI and ZEKE-PFI studies used DCM dye. The output from the dye laser was frequency doubled using a KD*P crystal to produce ultraviolet light in the wavelength range 321 to 314 nm. The probe dye laser used to record the ZEKE-PFI spectra used LDS 821 and LDS 867 dyes to produce the near infra-red light which was used to excite the I_2-Ar complexes from the intermediate Rydberg states to the ionisation thresholds. The I_2-Ar complexes were generated by passing argon at various stagnation pressures (550 Torr to 3 atm.) over iodine at 65-75 °C (in a heated sample reservoir) and expanding the mixture through a pulsed jet expansion. The pulsed electric fields were arranged as follows: the top plate voltage pulse was 3.0 V/cm^{-1} applied at approximately 1.15 μs after laser excitation, the voltage pulse on the lower plate was between 0.8 and 0.9 V/cm^{-1} applied at 1.1 μs after excitation.

5.2.2.2 The (2+1) REMPI spectrum of the $[^2\Pi_{3/2}]_c$ 5d:Ω_g (Ω=0,2) Rydberg states of I_2-Ar

The mass resolved (2+1) REMPI spectrum recorded by monitoring the I_2^+-Ar mass channel is shown in figure 5-1. This spectrum has been presented in some detail previously[19] and so we shall discuss only the features that are relevant to the present work. The spectrum is composed of partially overlapping vibrational progressions arising from the $[^2\Pi_{3/2}]_c$ 5d; 2_g (figure 5-1(a); recorded with circularly polarised light) and $[^2\Pi_{3/2}]_c$ 5d; 0_g (figure 5-1(b); recorded with linearly polarised light) Rydberg states of I_2-Ar. The vibrational structure for both states essentially arises from simultaneous excitation of both the I-I stretch (ν_1 mode) and the I_2···Ar stretch (ν_3 mode). For the $[^2\Pi_{3/2}]_c$ 5d;0_g state, the progression terminates suddenly at $3_0^1 1_0^3$ (1 quantum in ν_3 plus 3 quanta in ν_1) which suggests that the complex dissociates at this point . The $3_0^1 1_0^3$ band appears at an internal vibrational energy of 758 cm^{-1} but we

know from the spectral red shift of the band origin that the lower limit to the zero point dissociation energy for this state is 563±5 cm^{-1}. Thus, it would appear that the coupling between the two vibrational modes is sufficiently weak to enable the complex to accomodate a further 195 cm^{-1} of internal energy before it dissociates. This is consistent with the geometry of the complex being T-shaped.

The dips that can be seen in the spectra in figure 5-1 (a) and (b) are artefacts that are due to ringing in the time-of-flight profile. The ringing occurs when a particularly strong transition of bare I_2 is excited. The ion signal on the MCP plates can distort the baseline of the time-of-flight profile and cause an apparent dip in the signal intensity of the I_2^+-Ar mass channel. The transitions in this case are to the bare I_2 $[^2\Pi_{3/2}]_c$ 5d; 2_g and $[^2\Pi_{3/2}]_c$ 5d;0_g Rydberg states.

The intensity variation of the signal from the $[^2\Pi_{3/2}]_c$ 5d; 2_g Rydberg state and the $[^2\Pi_{3/2}]_c$ 5d; 0_g Rydberg states when circularly polarised light is used to excite I_2-Ar is in agreement with the predictions of Bray and Hochstrasser[41] for two-photon transitions in diatomic molecules. The origin of this effect was discussed in Chapter 2. The $[^2\Pi_{3/2}]_c$ 5d; 2_g Rydberg state progression that can be seen in figure 5-1(a) (recorded with circularly polarised light) reveals more complex structure than that seen in the progression for the 5d; 0_g state. For both $\nu_1 = 0$ and $\nu_1 = 1$, each vibrational band appears significantly broader than observed for the 5d; 0_g progression, and on most of the bands, an apparent splitting can be resolved. However, for the $\nu_1 = 2$ progression the doublet structure has almost disappeared and the peaks have adopted a narrower profile similar to the peaks in the 5d; 0_g progression. In fact, the doublet structure arises, not from a splitting of the peaks, but from two overlapping vibrational progressions with near identical band origins. It appears from the spectrum that one of the progressions terminates at 1_0^2 while the other continues at least as far as $3_0^4 1_0^2$. If we assume that the

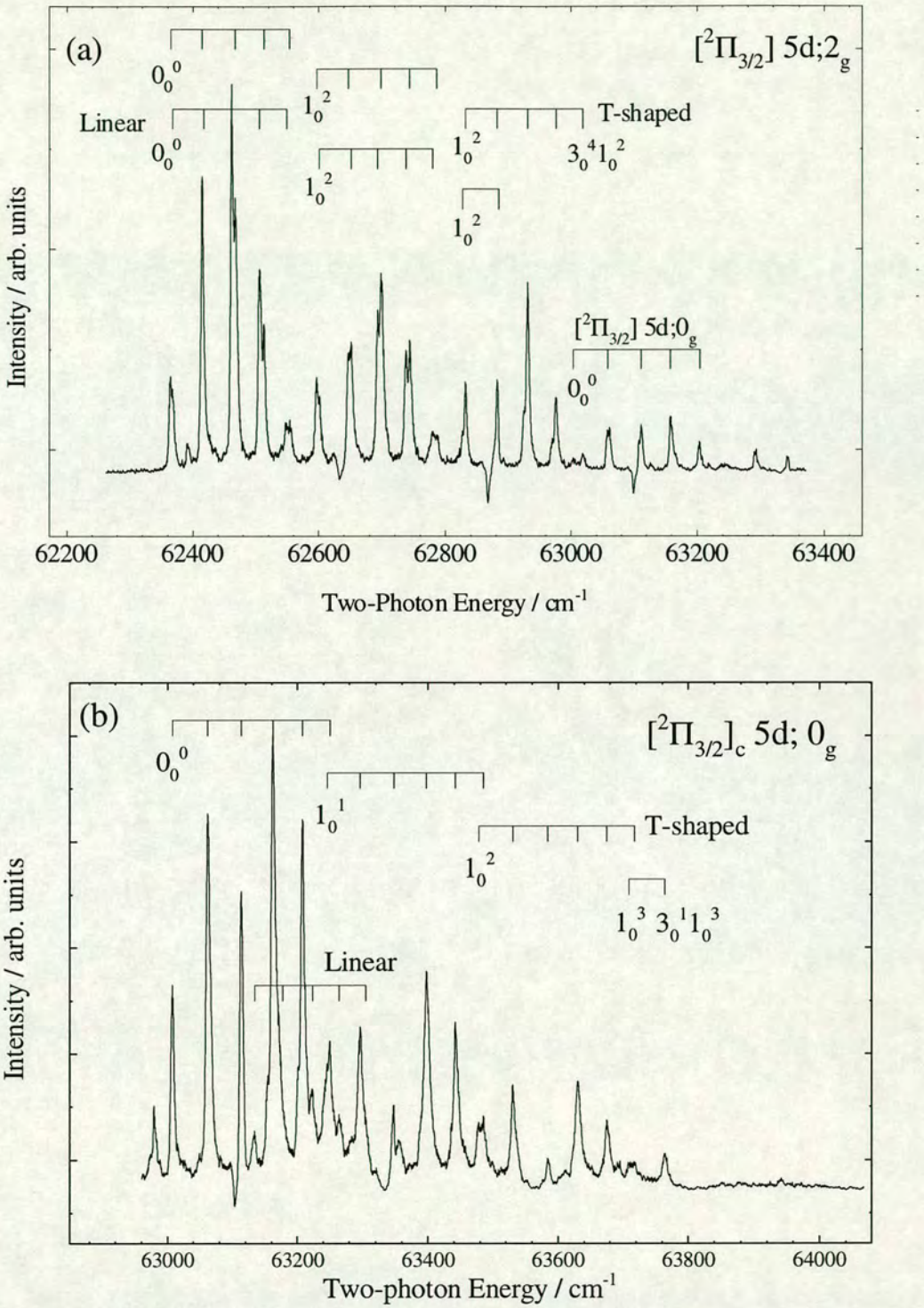

Figure 5-1- (a) The (2+1) mass resolved REMPI spectrum of the $[^2\Pi_{3/2}]_c$ 5d; 2_g state of I_2-Ar recorded with circularly polarised light in the range 62250 to 63250 cm^{-1}. (b) The (2+1) mass resolved REMPI spectrum of the $[^2\Pi_{3/2}]_c$ 5d; 0_g state of I_2-Ar recorded with linearly polarised light in the range 63000 to 64000 cm^{-1}. The dips seen in both spectra are instrumental artefacts (see text)

point at which the progression terminates represents the point at which the complex dissociates, then we can conclude that for the shorter progression the onset of dissociation occurs at 463 cm^{-1} internal vibrational energy (compared with a calculated value for D_0 of about 503 cm^{-1}), while for the longer progression, dissociation occurs at a lower limit of 655 cm^{-1}. On this basis, we can make a provisional assignment of the shorter progression to the linear isomer, for which the van der Waals stretch might be expected to couple more efficiently with the I_2 stretch, and the longer progression to the T-shaped isomer.

Expanded scans of the $v_1 = 0,1$ and 2 bands of the $[^2\Pi_{3/2}]_c$ 5d; 2_g Rydberg state are shown in figure 5-2(a),(b),(c) respectively. The assignment of the structure to the two isomers is based on the peak separations of the $v_1 = 2$ band which is assumed to be due to the T-shaped isomer. For $v_1 = 0$, we note that every band except the 3_0^1 band is split to a greater or lesser extent. The splitting of the vibrational bands increases with vibrational excitation which implies slightly different vibrational constants for the two isomers. The comparatively narrow 3_0^1 band arises from a near perfect overlap of the two 3_0^1 bands for the isomers. This occurs because the vibrational separation between the band origin and the 3_0^1 is smaller than that between the 3_0^1 and 3_0^2 for one of the isomer progressions while the progression due to the second isomer behaves in a typically anharmonic fashion. The onsets of the two progressions appear at 62368 and 62372 cm^{-1} which represent spectral red shifts, with respect to the bare I_2 molecule, of 271 and 267 cm^{-1} respectivley. The fact that we see both isomers requires that they have comparable binding energies on their respective electronic ground states. The overlapping $[^2\Pi_{3/2}]_c$ 5d; 2_g Rydberg state band origins further implies that the binding energies are also nearly equal in this Rydberg state.

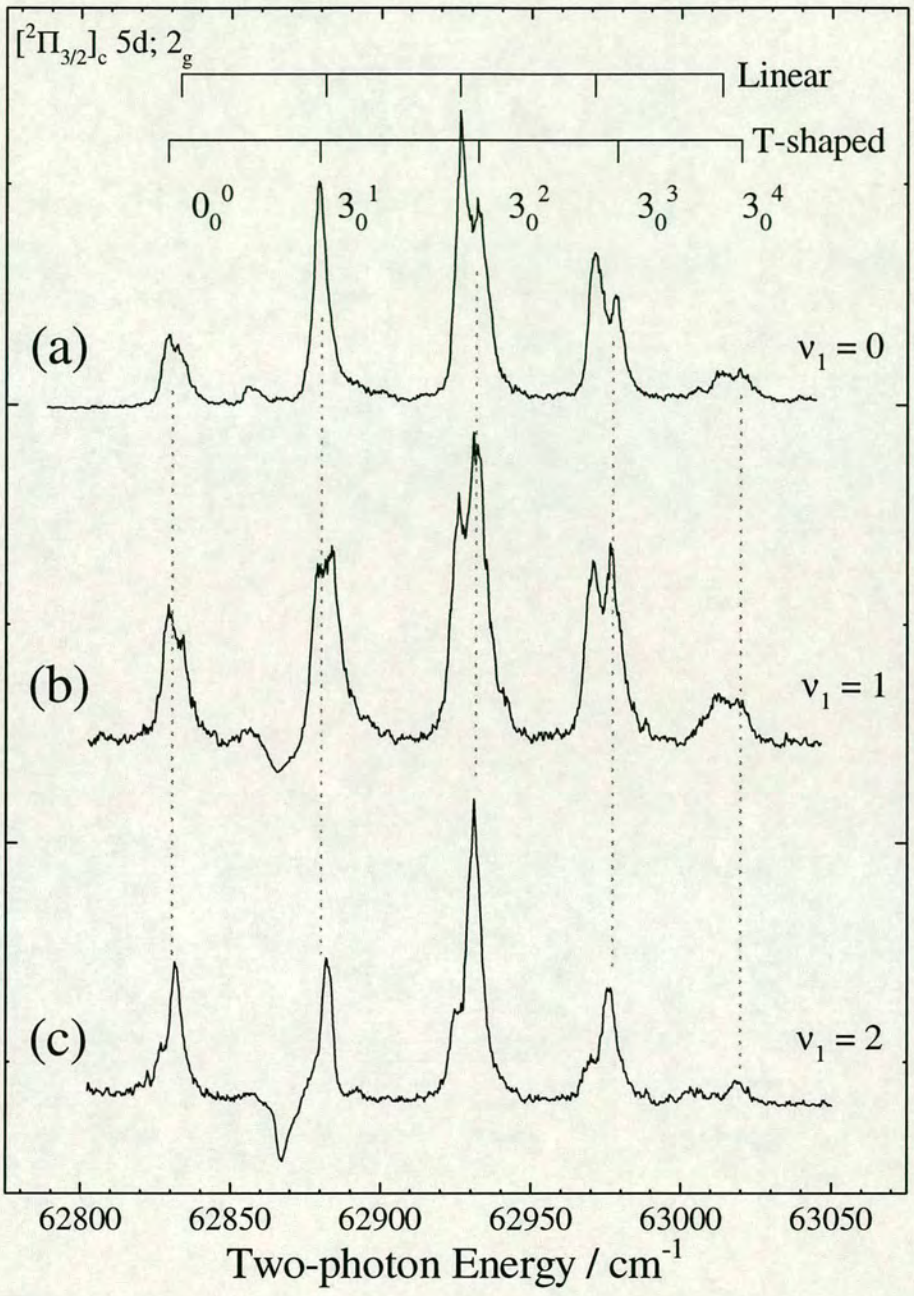

Figure 5-2 - Expanded scans of (a) the $\nu_1 = 0$, (b) $\nu_1 = 1$ and (c) $\nu_1 = 2$ bands of the $[^2\Pi_{3/2}]_c$ 5d; 2_g Rydberg state of I_2-Ar. The energy axis only refers to scan (c).

The appearance of the $\nu_1 = 1$ band in figure 5-2(b) differs from the $\nu_1 = 0$ band, with every vibrational band, including $3_0^1 1_0^1$, exhibiting doublet structure. The more pronounced structure occurs for this band because of a slight difference in the I-I stretching mode frequency between the two isomers. This would be expected to further separate the two isomers in the $\nu_1 = 2$ band, but by this point, the linear isomer has started to dissociate and no longer contributes to the progression (see figure 5-2(c)).

A number of additional features, the most obvious of which appears between the origin band and the 3_0^1 band of the 5d; 2_g state, are assigned as van der Waals sequence bands. This assignment is made on the basis of the decreasing relative intensities of the bands as the stagnation pressure increased (see figure 5-3). We note that the intensity of the higher energy component of the 3_0^2 band also decreases with increasing pressure and attribute this to a sequence band underneath the 3_0^2 band. Of particular significance, from the point of view of identifying the vibrational mode(s) responsible for these features, is the fact that we see no hot band features to the red of the band origin. This would present something of a problem if the sequence band structure was due to van der Waals stretching mode excitation in the ground electronic state but not if we assume that the bending mode (ν_2) is responsible. Bending transitions are restricted to $\Delta\nu$ = even (the transition dipole by symmetry is an even function of the bending angle θ) so transitions involving this mode will be strongly diagonal and we should see sequence bands rather than overtones.

If we now return to the $[^2\Pi_{3/2}]_c$ 5d; 0_g Rydberg state progression (see figure 5-1(b)), we can identify a number of weaker features in addition to the main progression already assigned. In contrast to the hot band structure observed for the $[^2\Pi_{3/2}]_c$ 5d; 2_g Rydberg state, these bands form a progression with an average spacing consistent with excitation of the van der Waals stretching mode. Given the precedent set by the $[^2\Pi_{3/2}]_c$ 5d; 2_g Rydberg state, it seems probable that these bands are due to excitation of the linear isomer. In this case, their displacement further to the blue of the main $[^2\Pi_{3/2}]_c$ 5d; 0_g Rydberg state progression is indicative of a larger difference of the relative stabilities of

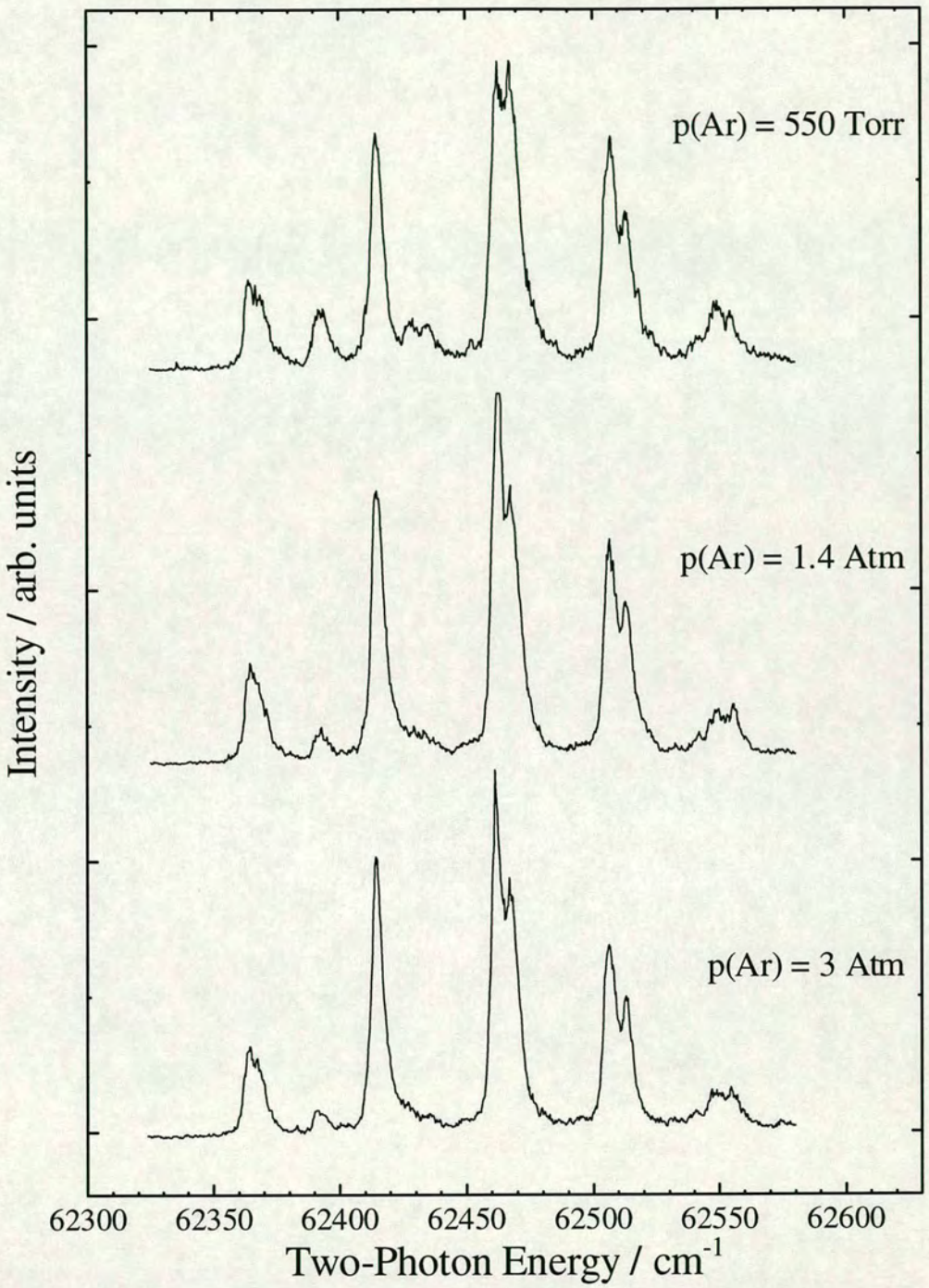

Figure 5-3 - The effect of argon stagnation pressure on the $v_1 = 0$ band of the $[^2\Pi_{3/2}]_c$ 5d; 2_g Rydberg state of I_2-Ar.

the two isomers in this state than in the $[^2\Pi_{3/2}]_c$ 5d; 2_g Rydberg state. The apparent brevity of the I_2 stretching mode progression would seem to provide further support for this conclusion.

Although the REMPI spectrum provides a great deal of circumstantial evidence for the existence of two isomers, we can further strengthen our assignments by extending the scope of this study to the ionic state. We already know the ionisation energy and vibrational constants for the T-shaped isomer from earlier ZEKE-PFI work on the complex, and should also be able to use ZEKE-PFI spectroscopy to probe the $[^2\Pi_{3/2}]_c$ 5d; 2_g Rydberg state of the complex in a two colour pump-probe ionisation scheme, to record isomer specific ZEKE-PFI spectra. Any significant differences in the relative stability of the two isomers in the ionic state will be revealed by measurable differences in their respective ionisation energies.

5.2.2.3 The (2+1′) ZEKE-PFI Photoelectron Spectrum of the $\tilde{X}\,^2\Pi_{3/2,g}$ state of I_2-Ar

The two colour (2+1′) ZEKE-PFI spectra of I_2^+-Ar ionised *via* the overlapping band origins of the $[^2\Pi_{3/2}]_c$ 5d; 2_g Rydberg state, as well as the first two vibrational excited levels of the $I_2\cdots$Ar van der Waals stretch are shown in figure 5-4(a),(b),(c). A consequence of the closely overlapping bands in the REMPI excitation spectrum means that each ZEKE spectrum contains comparable contributions from both isomers. However, assignment of the spectra is straightforward. The spectrum in figure 5-4(a), recorded *via* the two band origins, reveals just two features separated by 43 cm^{-1}. As this does not correspond to any of the vibrational frequencies obtained from the earlier ZEKE-PFI spectra recorded *via* the $[^2\Pi_{3/2}]_c$ 5d;0_g state,[20] we assign the two features to the band origins of the two isomers. The separation is an indication of the relative stabilities of the two isomers in the ionic state. The lack of additional vibrational structure is consistent with the relatively small change in equilibrium geometry expected for ionisation from the 5d Rydberg state. The ionisation energy of 74523±2 cm^{-1} (corrected for the field ionisation shift) measured for the lower energy band corresponds

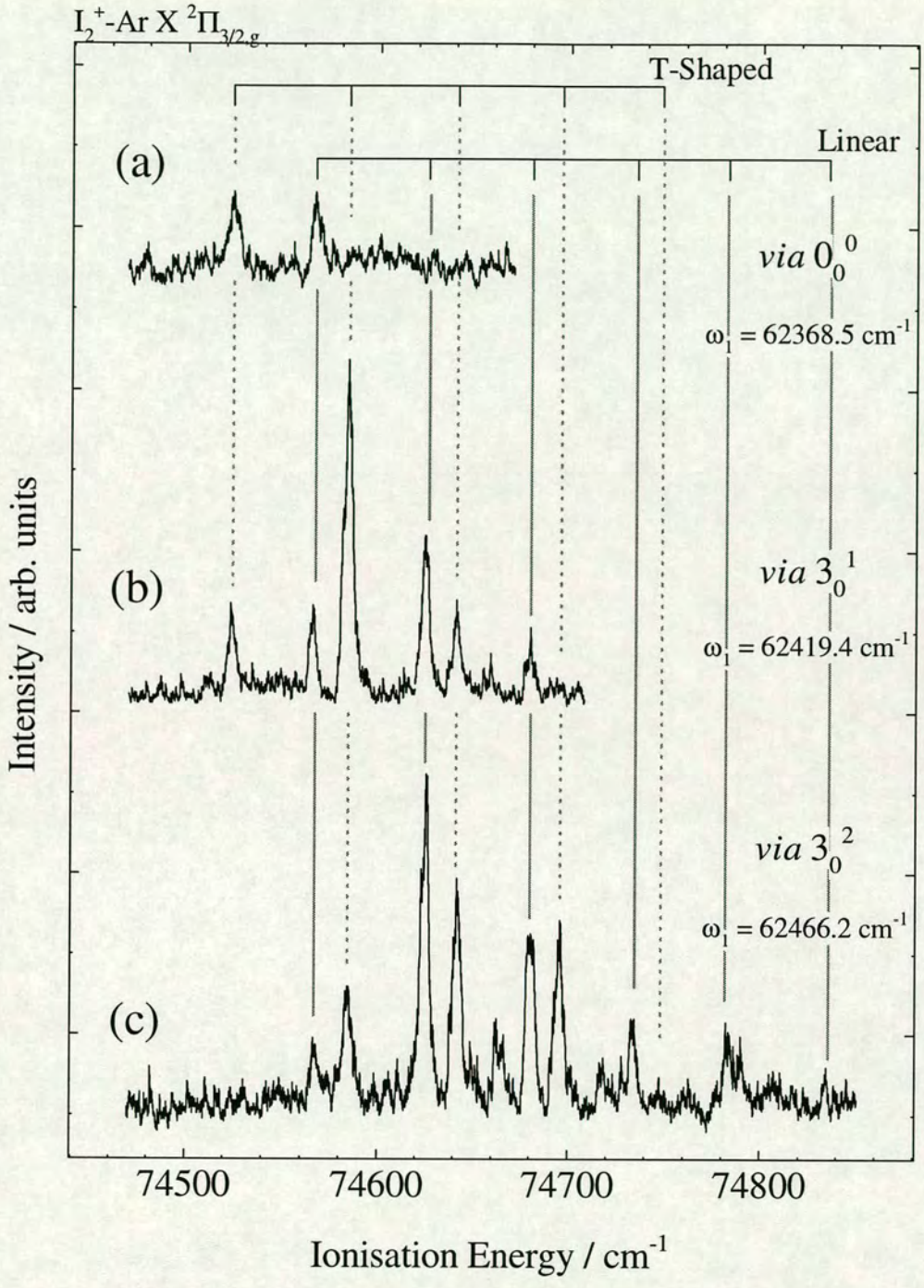

Figure 5-4 - The two-colour (2+1′) ZEKE-PFI spectra of I_2^+-Ar ionised (a) *via* the overlapping band origins (0_0^0) of the $[^2\Pi_{3/2}]_c$ 5d; 2_g Rydberg state, (b) *via* 3_0^1 and (c) *via* 3_0^2.

to the previously measured adiabatic ionisation energy of the T-shaped complex.[20] It follows that the total transition energy of 74566±2 cm^{-1} (corrected) measured for the higher energy band corresponds to the adiabatic ionisation energy of the linear isomer.

In the spectrum in figure 5-4(b) (*via* 3_0^1), the increased level of vibrational excitation in the intermediate state results in a corresponding increase in the vibrational activity in the ion. The spectrum is dominated by two vibrational progressions separated by 43 cm^{-1}, both of which exhibit typical Franck-Condon behaviour for the diagonal transition ($\Delta v = 0$). However, the higher energy progression exhibits slightly stronger intensity in the band origin compared with $v_3^+=1$ than is observed for the lower energy progression.

A further increase in vibrational excitation in the Rydberg state results in more extended progressions in the ZEKE-PFI spectrum. In the spectrum recorded *via* 3_0^2 in Figure 4.4(c) we see up to $v_3^+=5$ for the linear isomer and $v_3^+=4$ for the T-shaped complex. This time, however, while the lower energy progression shows a propensity for the $\Delta v = 0$ transition, the higher energy progression exhibits strong off-diagonal transition intensity with the $\Delta v = -1$ band dominating. The observation of vibrational intensity distributions that differ from those expected based solely on Franck-Condon factors is quite common in ZEKE-PFI spectroscopy. The origin of these intensity effects is discussed in Chapter 5 in relation to the ZEKE-PFI spectroscopy of Br_2 and IBr. One possibility here is that a Rydberg state converging on $v_3^+=2$ is resonant with the high *n* Rydberg states converging on $v_3^+=1$ and contributes to the intensity of the peak through the mechanism of forced vibrational autoionisation.

As a final aid to an assignment of the two overlapping progressions for the $[^2\Pi_{3/2}]_c$ 5d; 2_g Rydberg state, ZEKE-PFI spectra were recorded *via* the high energy wing of the 3_0^1 band and the higher energy component of the 3_0^2 band (see figure 5-5(a) and (b)). We see from figure 5-5(a) that the lower energy progression (attributed to the T-shaped isomer) has decreased in intensity relative to that of the higher energy progression. On this basis, we conclude that the linear isomer 3_0^1 band in the REMPI

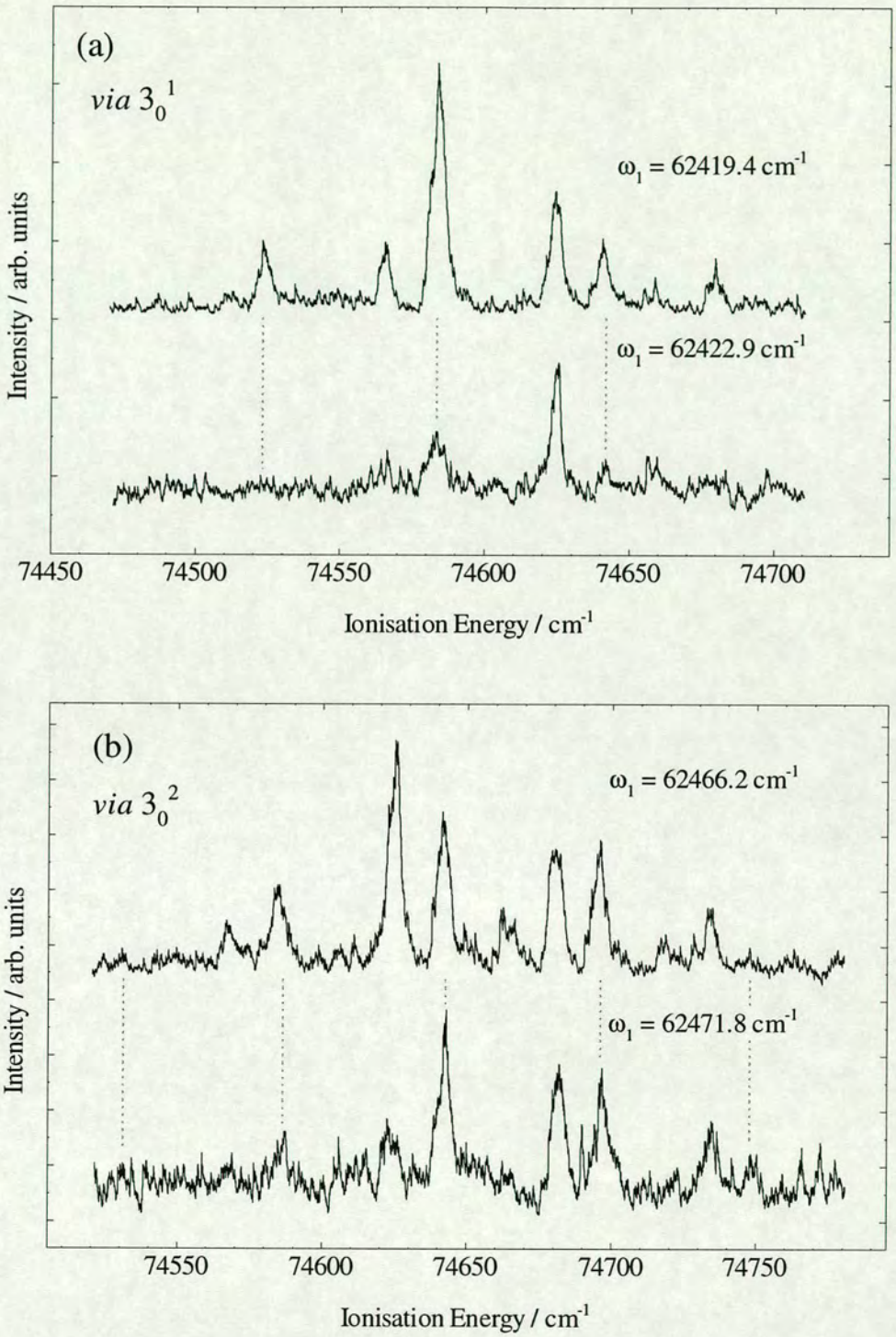

Figure 5-5 - A comparison of the ZEKE-PFI spectra recorded (a) *via* the high energy wing of the 3_0^1 band and (b) *via* the high energy component of the 3_0^2 band with the corresponding ZEKE-PFI spectra shown in **Figure 5-4** (b) and (c).

spectrum lies to slightly higher energy than that of the T-shaped isomer. In figure 5-5(b) recorded *via* the higher energy component of the 3_0^2 band, the higher energy progression has lost intensity relative to that of the lower energy progression (particularly so for the ν_3^+=1 band) and from this we conclude that the higher energy component of the 3_0^2 band is due to the T-shaped isomer and the lower energy component to the linear isomer. This assignment is entirely consistent with the assignment of the REMPI spectrum in Figure 4.2, in which the band positions for ν_1 = 2 of the $[^2\Pi_{3/2}]_c$ 5d; 2_g Rydberg state (which we assign as being due exclusively to the T-shaped isomer) are shown to overlap well with the higher energy components observed for the 3_0^2 bands for both ν_1 =0 and ν_1 =1, as well as the lower energy component of the respective 3_0^1 bands. The complete spectral assignments of both the REMPI and ZEKE-PFI spectra are presented in Table 5-1 and Table 5-2 while the band origins, ionisation energies, spectral redshifts and zero point dissociation energies are given in Table 5-3.

Table 5-1 Spectral peak positions and assignments of the $[^2\Pi_{3/2}]_c$ 5d;Ω_g (Ω=2,0) Rydberg states of I_2-Ar (T-shaped and linear isomers)

State	Transition energy (cm^{-1})	Vibrational spacing (cm^{-1})		Assignment [a]
T-shaped				
$[^2\Pi_{3/2}]_c$ 5d;2_g	62368	0		0_0^0
	62419	51		3_0^1
	62471	52		3_0^2
	62517	46		3_0^3
	62569	43		3_0^4
	62601	0	233	1_0^1
	62651	50		$3_0^1 1_0^1$
	62702	51		$3_0^2 1_0^1$
	62748	46		$3_0^3 1_0^1$
	62790	42		$3_0^4 1_0^1$
	62835	0	234	1_0^2
	62884	49		$3_0^1 1_0^2$
	62935	51		$3_0^2 1_0^2$
	62980	45		$3_0^3 1_0^2$
	63023	43		$3_0^4 1_0^2$
$[^2\Pi_{3/2}]_c$ 5d;0_g	63006	0	0	0_0^0
	63061	55		3_0^1
	63112	51		3_0^2
	63161	49		3_0^3
	63208	47		3_0^4
	63249	41		3_0^5
	63243	0	237	1_0^1
	63296	53		$3_0^1 1_0^1$
	63374	51		$3_0^2 1_0^1$
	63396	49		$3_0^3 1_0^1$
	63440	44		$3_0^4 1_0^1$
	63484	44		$3_0^5 1_0^1$
	63477	0	234	1_0^2
	63529	52		$3_0^1 1_0^2$
	63583	54		$3_0^2 1_0^2$
	63630	47		$3_0^3 1_0^2$
	63674	44		$3_0^4 1_0^2$
	63717	43		$3_0^5 1_0^2$
	63707	0	230	1_0^3
	63764	57		$3_0^1 1_0^3$
Linear				
$[^2\Pi_{3/2}]_c$ 5d;2_g	62372	0	0	0_0^0
	62422	50		3_0^1
	62466	44		3_0^2
	62510	44		3_0^3

Table 5-3 Spectroscopic data obtained for the two structural isomers of I_2-Ar (T-shaped and linear) from the REMPI and ZEKE spectra

State	Band origin (cm^{-1})	Spectral red shift (cm^{-1})	D_0 [a] (cm^{-1})	ϖ_e (cm^{-1})	$\varpi_e x_e$ (cm^{-1})
(a) T-shaped					
$[^2\Pi_{3/2}]_c$ 5d;2_g	62368±2	271±4	508±5	55±3	1.5±0.5
$[^2\Pi_{3/2}]_c$ 5d;0_g	63006±2	326±4	563±5	58±2	1.6±0.1
$\tilde{X}\,^2\Pi_{3/2,g}$	74523±2 [b]	546±4	783±5	63±2	1.4±0.1
(b) Linear					
$[^2\Pi_{3/2}]_c$ 5d;2_g	62372±2	267±4	504±5	51±3	1.1±0.5
$[^2\Pi_{3/2}]_c$ 5d;0_g [c]	63133±2	199±4	463±5	46±3	0.7±0.5
$\tilde{X}\,^2\Pi_{3/2,g}$	74566±2 [b]	503±4	740±5	61±2	1.4±0.1

[a] Zero point dissociation energy calculated from the observed spectral red shift and the known ground state dissociation energy for the T-shaped isomer. The accuracy of the values determined for the linear isomer should be taken in this light.

[b] Corrected to account for the field ionisation shift.

[c] Tentative assignment.

5.2.3 Discussion

The observation of two stable structural isomers in the $[^2\Pi_{3/2}]_c$ 5d; 2_g and $[^2\Pi_{3/2}]_c$ 5d; 0_g Rydberg states of I_2-Ar, as well as the $\tilde{X}\,^2\Pi_{3/2,g}$ state of I_2^+-Ar, answers and poses a few questions. The existence of a linear isomer explains the one atom cage effect in I_2-Ar where a linear isomer is needed to reproduce experimental results [28] in the theoretical calculations.[33] The question that is posed by these results is why we only see the linear isomer in these states and not in any of the other Rydberg states of I_2-Ar observed using REMPI spectroscopy.[19]

In the $[^2\Pi_{1/2}]_c$ 6s; 1_g Rydberg state the reason may lie in the radius of the Rydberg orbit. The radius of the 6s orbit (defined as the outer turning point of the classical motion of the Rydberg electron in a Coulomb potential) will be approximately 5.5 Å. This value puts the orbit of the Rydberg electron almost on top

of where a linearly orientated argon van der Waals partner would lie. The resulting electron-electron repulsion (between the Rydberg electron and argon) might destroy any potential minimum that might have existed for a linear complex. This would not be a problem for the T-shaped complex as the argon atom in this case would lie within the outer limits of the Rydberg orbit.[19]

In the case of the $[^2\Pi_{1/2}]_c$ 5d; 2_g, $[^2\Pi_{1/2}]_c$ 5d; 0_g, $[^2\Pi_{3/2}]_c$ 6d; 2_g, and $[^2\Pi_{3/2}]_c$ 6d; 0_g Rydberg states this explanation does not hold. Only in an *s* Rydberg state would the van der Waals partner be either enveloped or subject to such strong electron-electron repulsion with a Rydberg orbital. In a *d* Rydberg state of the I_2-Ar van der Waals complex, the Rydberg orbital (based on the I_2 core) would easily accomodate the prescence of the argon atom in a T-shaped or linear orientation relative to the I_2 bond. One possible explanation for the lack of structure attributable to a second isomer in the REMPI spectra of the *d* Rydberg states is electronic predissociation. One of the isomers of the I_2-Ar complex may be susceptible to strong electronic predissociation in these Rydberg states and as a result only one isomer is observed. However, no cases of isomer specific electronic predissociation have been reported in the literature.

In summary, we have presented the first direct spectroscopic evidence for the existence of two structural isomers of I_2-Ar. The mass-resolved REMPI spectrum of the $[^2\Pi_{3/2}]_c$ 5d; 2_g Rydberg state shows two overlapping vibrational progressions with near identical band origins which have been assigned to excitation of the T-shaped and linear isomers. The overlapping $[^2\Pi_{3/2}]_c$ 5d; 2_g Rydberg state band origins in the REMPI spectrum suggest that the change in the D_e between the ground and Rydberg states for the two geometries is nearly equal, although it appears that for the $[^2\Pi_{3/2}]_c$ 5d; 0_g Rydberg state, the change in binding energy for the linear isomer is 127 cm^{-1} smaller than that of the T-shaped isomer. In the two-colour ZEKE-PFI spectum of the ground ionic state of the ion recorded *via* a number of vibrational levels in the $[^2\Pi_{3/2}]_c$ 5d;2_g Rydberg state, two well separated vibrational progressions were observed. The measured difference in the ionisation energies of 43 cm^{-1} for the two isomers provides an indication of their relative stabilities in the ion, with the linear isomer being the more weakly bound.

5.3 The (2+1) REMPI and (2+1′) ZEKE-PFI spectra of I_2-Kr

5.3.1 Introduction

In contrast to the large body of work on the lighter iodine rare gas systems (I_2-X where X= He, Ne, Ar), very little work has been carried out on the heavier rare gas complexes. Goldstein *et al.* were first to detect the I_2-Kr and I_2-Xe complexes using intra-cavity laser spectroscopy.[42] The *B* - *X* transition in I_2-Kr was also looked for using LIF spectroscopy by Goldstein *et al.* but no fluorescence was observed from the *B* state of I_2. It is thought that the Kr atom induces strong electronic predissociation of the I_2 bond by coupling the *B* state with the repulsive $a\ ^3\Pi_{1g}$ state.[40,42] The strong coupling between the two states completely quenches the fluorescence signal from the *B* state of I_2. As a result none of the detailed spectroscopic information obtained for the lighter rare gas complexes[22] has been obtained for I_2-Kr. Electronic predissociation also occurs in the *B* state of I_2-Ar but only for the first twelve vibrational levels, after which the dominating decay channel is vibrational predissociation.[21,39]

Other work on the I_2-Kr complex include that by Wensink and van Voorst [43] who carried out calculations of elastic collisions of rare gases with I_2 in which they assumed that the I_2-Kr and I_2-Xe complexes are T-shaped based on the geometry of the three lighter rare gas complexes. More recently Schroder and Gabriel [44] carried out classical simulations of the cage effect in I_2-Kr_n as well as I_2-Ar_n and I_2-Xe_n ($n \leq 5$).

In this section we present the mass resolved (2+1) REMPI spectrum of the I_2-Kr van der Waals complex in the $[^2\Pi_{3/2}]_c$ 5d;Ω_g (Ω=0,2) Rydberg states as well as the (2+1′) ZEKE-PFI photoelectron spectrum of the I_2^+-Kr complex in the $\tilde{X}\ ^2\Pi_{3/2,g}$ ground ionic state. The results of this study are compared to the REMPI and ZEKE-PFI spectra of the analogous states of I_2-Ar.[19,20]

5.3.2 Results

5.3.2.1 Experimental Details

The pump dye laser used in the REMPI and ZEKE-PFI experiments was frequency doubled using KD*P crystals to produce ultraviolet light with wavelengths ranging from 323nm to 311nm (DCM and R640 dyes). Circular polarisation of the pump laser was achieved by passage of the laser output through a Soleil Babinet polariser. The probe dye laser in the ZEKE-PFI experiments used LDS821 dye (undoubled, ~816nm) to promote the Rydberg excited complex to the ionisation threshold. The I_2-Kr complex was produced by passing krypton in helium at various stagnation pressures (1 to 2.5 atmospheres) through a sample reservoir containing solid iodine (heated to produce a sufficient vapour pressure) located within the pulsed nozzle assembly. In the REMPI experiments a dc voltage of 3 kV was applied to the top plate with the lower plate held at earth. In the ZEKE-PFI experiments the voltage pulses were arranged as follows: a field ionisation pulse of 3.7 V/cm was applied to the top plate with a delay of 820 ns from laser excitation and a 0.4 V/cm discrimination pulse was applied to the lower plate between 300 and 630 ns after excitation.

5.3.2.2 The (2+1) REMPI spectra of the $[^2\Pi_{3/2}]_c$ 5d:Ω_g (Ω=0,2) Rydberg states of I_2-Kr

The mass resolved (2+1) REMPI spectrum of I_2-Kr recorded in the range 61900-63800 cm^{-1} (two-photon energy) is shown in figure 5-6. The upper trace in the figure was recorded using circularly polarised light which has the effect of enhancing transitions to the $[^2\Pi_{3/2}]_c$ 5d;2_g state and suppressing those to the $[^2\Pi_{3/2}]_c$ 5d;0_g state. The intensity variation with circularly polarised light agrees with the predictions of Bray and Hochstrasser[Error! Bookmark not defined.] for two-photon transitions in diatomic molecules. The assignment of the vibrational structure associated with each electronic state is given in Figure 4.6 and Table 5-4. Two vibrational progressions are observed for each state based on the I-I stretch (ν_1) and the $I_2\cdots Kr$ stretch (ν_3). The assignments are discussed in detail below.

The band origin of the first progression in the $[^2\Pi_{3/2}]_c$ 5d;2_g state is assigned to the peak at 62192±2 cm^{-1}. The progression appearing to lower energy, marked with an asterisk in figure 5-6 (a), is assigned to a hot band arising from transitions from $v''=1$ of the I-I stretch in the ground state (ν_1 mode) to $v'=0$ in the Rydberg state. The band origin of the bare I_2 $[^2\Pi_{3/2}]_c$ 5d;2_g state (previously assigned as the $[^2\Pi_{3/2}]_c$ 7s;2_g) was reported in an earlier publication [45] to be at 62639±2 cm^{-1}. The difference between the two band origins represents a spectral red-shift of 447±4 cm^{-1}. The large red-shift indicates significant strengthening of the van der Waals bond upon excitation to the Rydberg state. This observation corresponds well with the expected influence of charge-induced dipole forces that result from partial exposure of the krypton atom to the positively charged core of the iodine molecule. The start of the next main band appears 230±2 cm^{-1} higher in energy at 62422±2 cm^{-1}. This separation is almost identical to that between $v'=0$ and $v'=1$ of the bare I_2 $[^2\Pi_{3/2}]_c$ 5d;2_g Rydberg state (233 cm^{-1}) and consequently we can assign it to one quantum excited in the ν_1 mode. Two further bands can similarly be assigned to $v'=2$ and 3 in the I_2 stretch. An upper limit for the band origin of the $[^2\Pi_{3/2}]_c$ 5d;0_g state of the complex appears at 62853±2 cm^{-1} corresponding to a spectral red-shift of 479±4 cm^{-1} relative to the band origin of the bare I_2 molecule.[45] The next two bands of the $[^2\Pi_{3/2}]_c$ 5d;0_g state are assigned in the same manner as those of the $[^2\Pi_{3/2}]_c$ 5d;2_g state.

Each of the bands assigned are composed of an anharmonic progression in one of the van der Waals vibrational modes. The average vibrational spacing in these progressions (41 cm^{-1} for the $[^2\Pi_{3/2}]_c$ 5d;2_g and 43 cm^{-1} for the $[^2\Pi_{3/2}]_c$ 5d;0_g) is consistent with a single quantum excitation of the $I_2\cdots Kr$ stretching mode, ν_3. The peak positions of the first van der Waals vibrational progression of the $[^2\Pi_{3/2}]_c$ 5d;2_g state and $[^2\Pi_{3/2}]_c$ 5d;0_g state were fitted to the general expression for vibrational energy levels ($G_v = T_e + \tilde{\omega}_e(v+{}^1/_2) - \tilde{\omega}_e x_e(v+{}^1/_2)^2$) to yield values of the vibrational constants for the $I_2\cdots Kr$ van der Waals stretching mode. The constants are as follows,

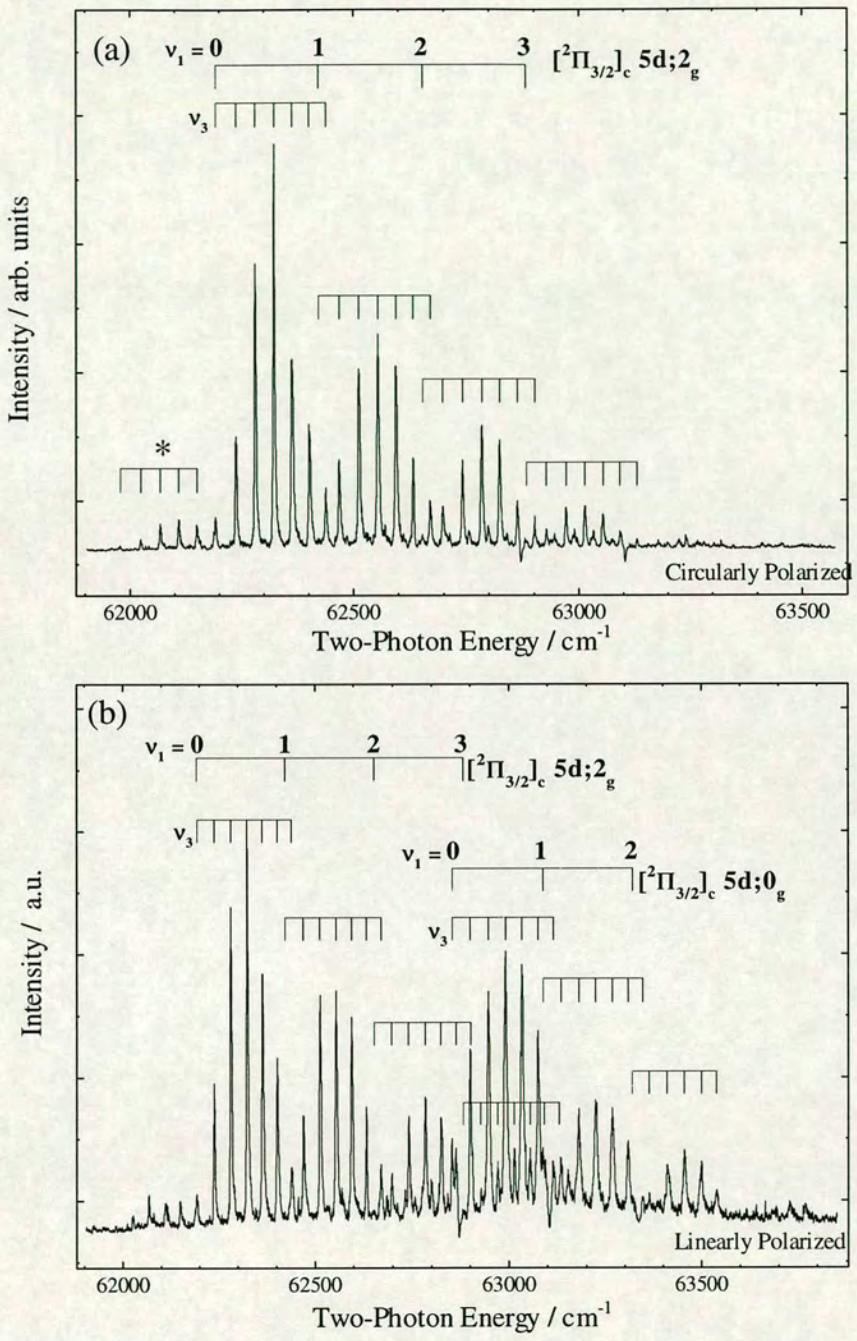

Figure 5-6 - The (2+1) mass-resolved REMPI excitation spectra of jet-cooled I_2-Kr recorded in the range 61900-63800 cm^{-1} monitoring the I_2^+-Kr mass channel. The upper spectrum, (a), was recorded with circularly polarised light, whilst that in the lower spectrum, (b), was recorded using linearly polarised light. The progression marked with an asterisk is due to a hot band.

$\tilde{\omega}_e$=47±2 cm^{-1} and $\tilde{\omega}_e x_e$=0.8±0.1 cm^{-1} for the $[^2\Pi_{3/2}]_c$ 5d;2_g state and $\tilde{\omega}_e$=49±2 cm^{-1} and $\tilde{\omega}_e x_e$=0.8±0.1 cm^{-1} for the $[^2\Pi_{3/2}]_c$ 5d;0_g state. The vibrational constants and the spectral red-shifts of the $[^2\Pi_{3/2}]_c$ 5d;2_g and $[^2\Pi_{3/2}]_c$ 5d;0_g Rydberg states are very similar. This similarity is a reflection of the fact that both Rydberg states are $d\pi$ states.[46] The unperturbed $d\pi$ states will interact in a very similar way with a van der Waals partner as the molecular orbitals have an almost identical shape.

From the extensive structure in the REMPI spectrum of the $[^2\Pi_{3/2}]_c$ 5d;2_g and $[^2\Pi_{3/2}]_c$ 5d;0_g states it is clear that the Franck-Condon overlap between these states and the ground state of the complex is fairly good, which indicates that the complex probably retains the same geometry upon excitation. If we assume that the I_2-Kr complex is T-shaped in the ground state [43] then we can tentatively assign a T-shaped geometry to the complex in both Rydberg states.

A Franck-Condon simulation of the first van der Waals vibrational progression of the two Rydberg states can be seen in figure 5-7. The simulation assumes that the potential curve along the I_2···Kr stretching coordinate can be adequately described by a Morse potential in the ground and $[^2\Pi_{3/2}]_c$ 5d Rydberg states. This approximation seemed reasonable given that only a small region around the minimum of the potential would be needed for the simulation. It was also shown to be a reasonable approximation in the simulation of the vibrational intensity distributions observed in the REMPI spectra of the *gerade* Rydberg states of I_2-Ar.[19]

The van der Waals potential for the ν_3 mode was approximated as a Morse potential. Experimental data for the ground state of I_2-Kr was not available so the appropriate parameters for the morse curves (D_e'', $\tilde{\omega}_e''$ and r_e'') were extrapolated from the values for I_2-He, Ne and Ar [22] using the method outlined by Wensink and van Voorst.[43] In this method known values of D_e'' and r_e'' for the O_2-X van der Waals complexes (where X is He, Ne, Ar, Kr and Xe) were fitted to a relationship based on atomic number of the rare gas atom. The relation was then used to give constants for I_2-Kr based on the data of I_2-He, Ne and Ar. This yields values of 294.1 cm^{-1} for D_e'', 4.79Å for r_e'' and a first approximation of 22.4 cm^{-1} for $\tilde{\omega}_e''$.

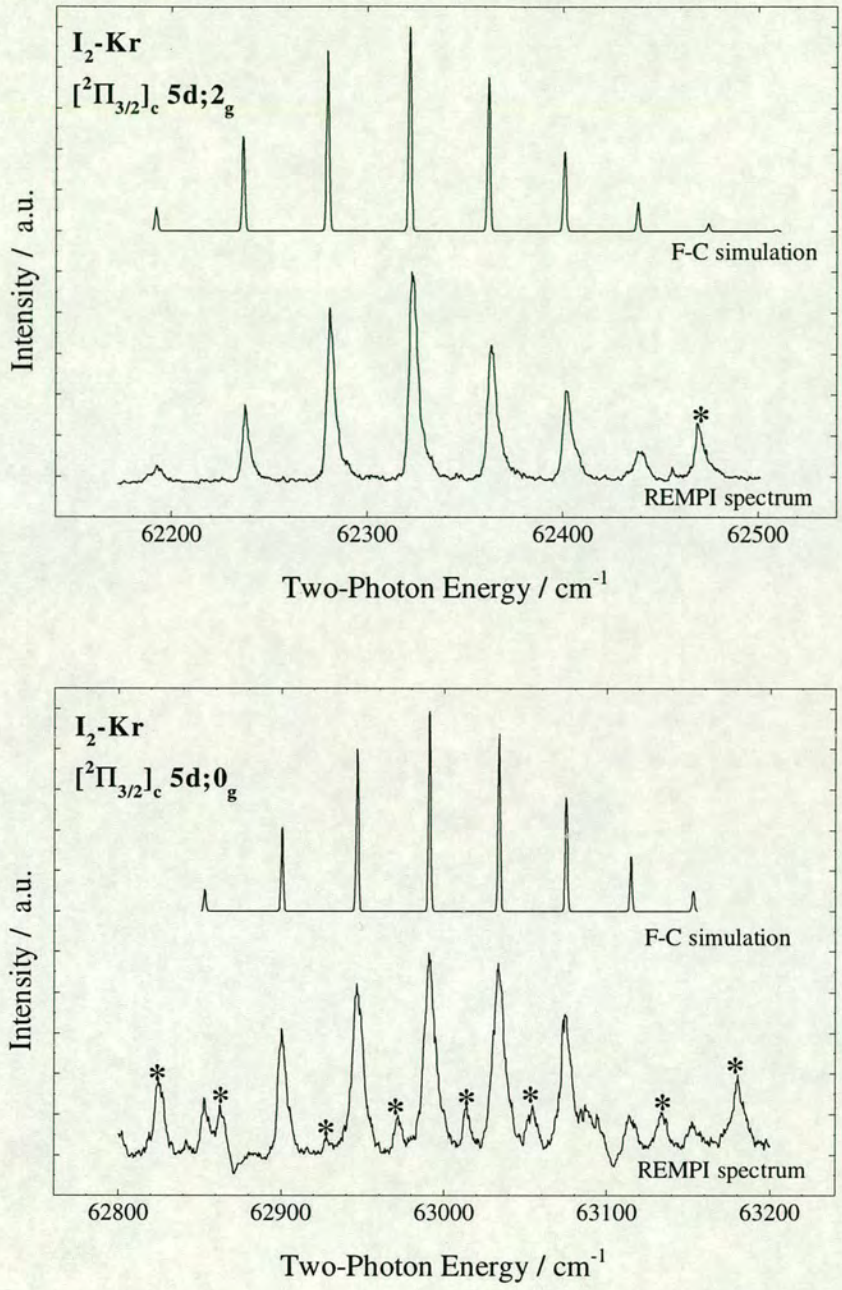

Figure 5-7 - (a) The observed spectra (bottom) and Franck-Condon simulation of the first combination band of the $[^2\Pi_{3/2}]_c$ 5d;2_g Rydberg state of I_2-Kr. (b) The observed (bottom) and Franck-Condon simulation of the first combination band of the $[^2\Pi_{3/2}]_c$ 5d;0_g Rydberg state of I_2-Kr. The asterisks in both (a) and (b) highlight peaks that do not belong to the progressions that are being simulated.

These values are for a T-shaped I_2-Kr van der Waals complex. The Franck-Condon simulation varied the values of r_e' and $\tilde{\omega}_e''$ in an attempt to reproduce the intensity pattern of the REMPI spectrum.

The large red shift in both Rydberg states together with the extended nature of the van der Waals progressions indicate that the bond length of the I_2-Kr complex is substantially reduced upon excitation. The simulation produced an r_e' value of 4.460Å for the $[^2\Pi_{3/2}]_c$ 5d;2_g state (Fig. 2(a)), representing a decrease of 0.330Å from the ground state, and a value of 24 cm^{-1} for $\tilde{\omega}_e''$. The $[^2\Pi_{3/2}]_c$ 5d;0_g simulation (figure 5-7 (b)) produced a value of 4.450Å for r_e' (0.345Å decrease) using $\tilde{\omega}_e'' = 24cm^{-1}$. The zero-point binding energy (D_0') of the Rydberg state complexes was then calculated by adding the D_0'' value ($D_0'' = D_e'' - \tilde{\omega}_e''/2$) to the red shift of each state yielding the following values; 729±4 cm^{-1} for the $[^2\Pi_{3/2}]_c$ 5d;2_g state and 761±4 cm^{-1} for the $[^2\Pi_{3/2}]_c$ 5d;0_g state.

5.3.2.3 The (2+1′) ZEKE-PFI Photoelectron Spectrum of the $\tilde{X}\,^2\Pi_{3/2,g}$ state of I_2-Kr

Figure 5-8 (a) shows the (2+1′) ZEKE-PFI spectrum of the I_2^+-Kr van der Waals complex in the lower spin-orbit component of the ground ionic state. The intermediate state used was the $[^2\Pi_{3/2}]_c$ 5d;2_g Rydberg state, excited using circularly polarized light. A summary of the data obtained from the REMPI and ZEKE-PFI spectra of I_2-Kr is given in Table 5-5.

Exciting the complex *via* the band origin of the $[^2\Pi_{3/2}]_c$ 5d;2_g state yields only one peak in the ZEKE spectrum (figure 5-8 (a)). Transitions from the $[^2\Pi_{3/2}]_c$ 5d;2_g Rydberg state to the corresponding ionic state ($\tilde{X}\,^2\Pi_{3/2,g}$) are expected to be highly diagonal ($\Delta v=0$) due to the similarity of the potential energy surfaces, allowing us to assign the peak as the origin band of the $\tilde{X}\,^2\Pi_{3/2,g}$ state of I_2^+-Kr. This gives a value for the adiabatic ionisation energy of 74248±3 cm^{-1} and a red-shift of 821±5 cm^{-1} when compared with the known adiabatic ionisation energy of I_2^+ (75069±2 cm^{-1} [47]).

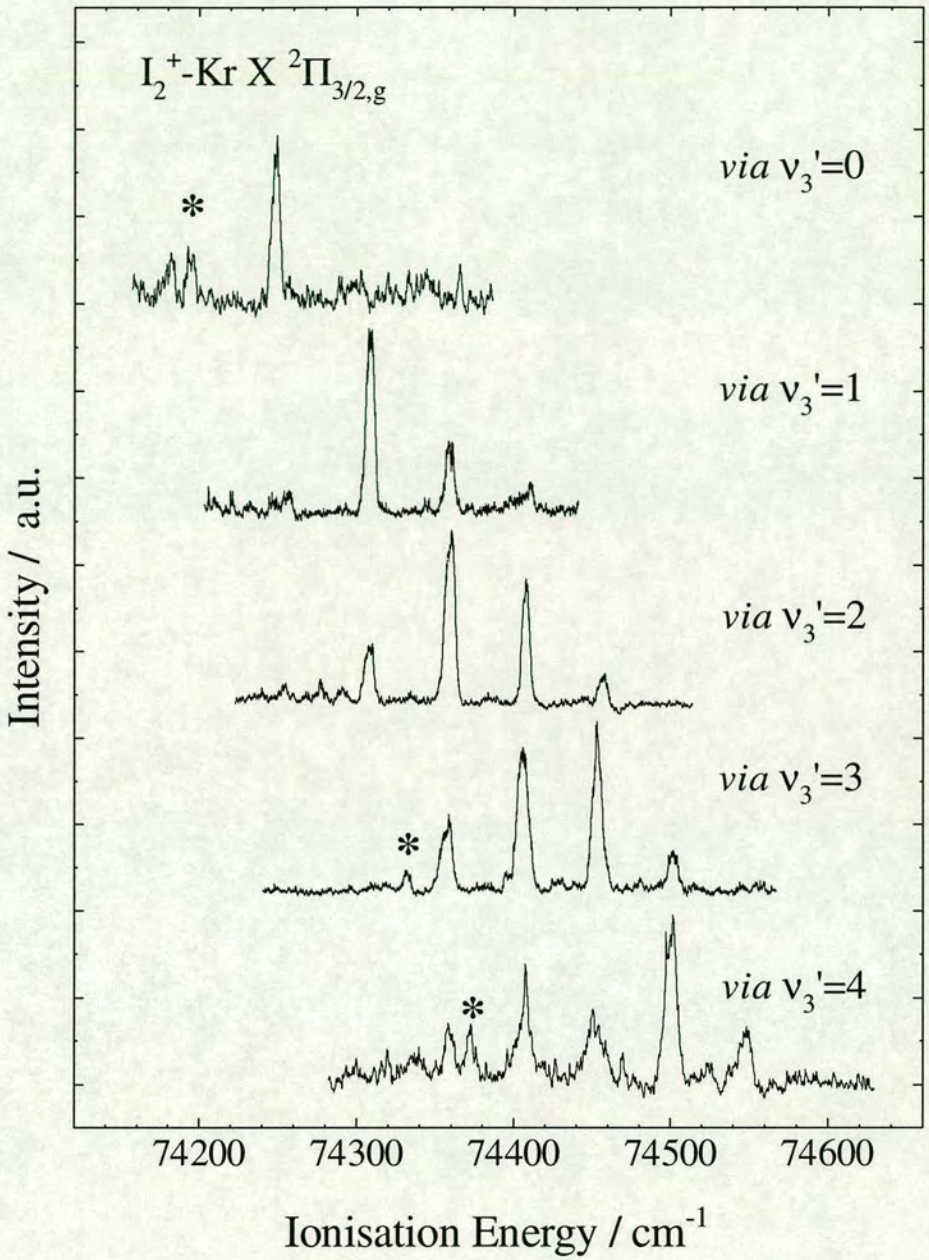

Figure 5-8 - (a) The (2+1′) ZEKE-PFI spectra of the $\tilde{X}\,^2\Pi_{3/2,g}$ state of I_2^+-Kr recorded *via* the band origin of the $[^2\Pi_{3/2}]_c$ 5d;2_g Rydberg state at 62192 cm^{-1} as well as *via* the first four vibrationally excited levels in the $I_2\cdots$Kr van der Waals stretching vibration, ν_3. The asterisks denote accidental A←X neutral state resonance in I_2. For **Figure 5-8 -** (b) see next page.

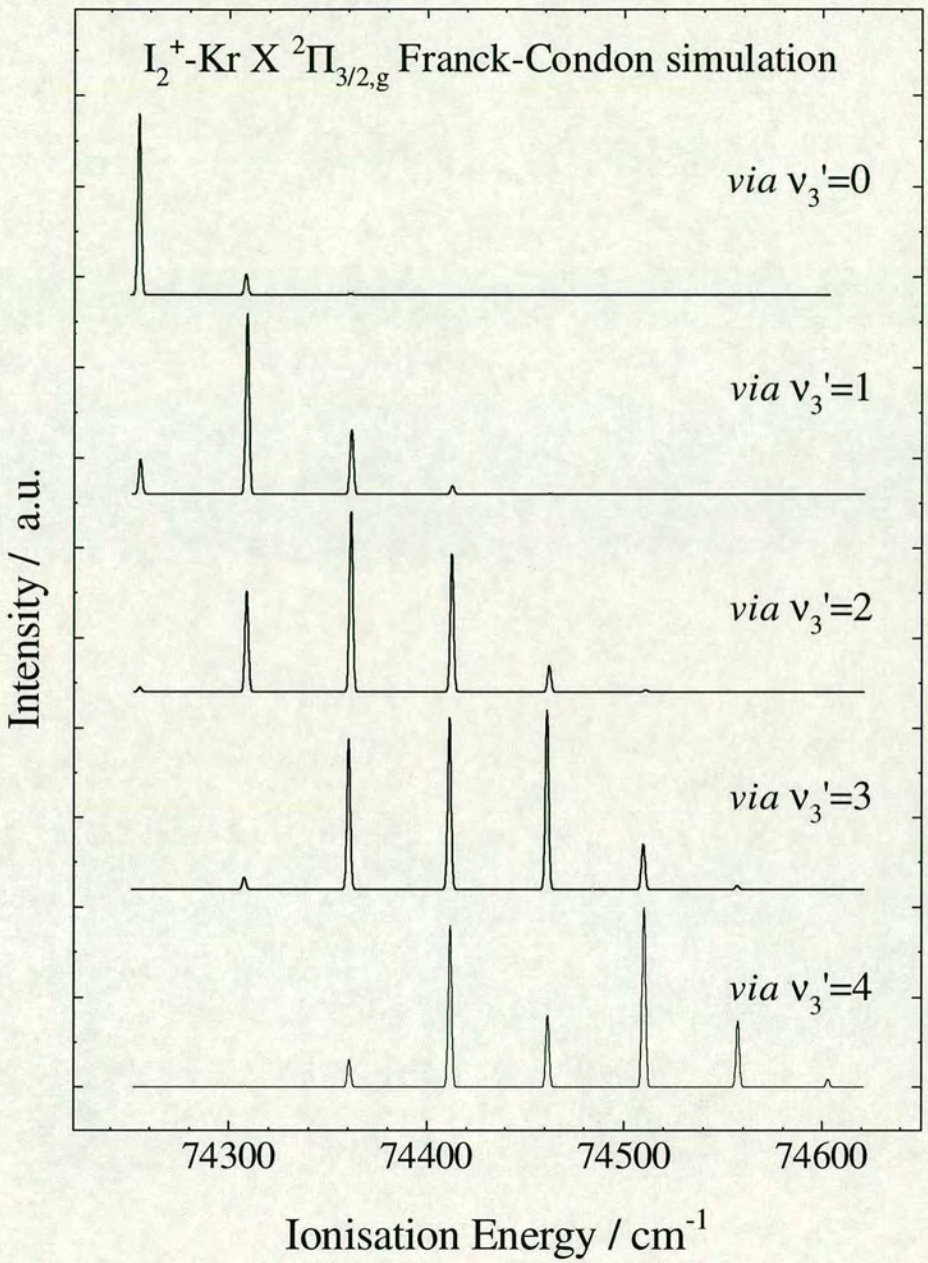

Figure 5-8 (b) - Franck-Condon simulations of the ZEKE spectra shown in **Figure 5-8** (a) for transitions from the $[^2\Pi_{3/2}]_c$ 5d;2_g Rydberg state into the $\tilde{X}\ ^2\Pi_{3/2,g}$ ionic state.

This gives us a lower limit for the dissociation energy of the ionic complex (D_0^+) of 1103±5 cm^{-1}. The large D_0^+ value, relative to the D_0' values of the $[^2\Pi_{3/2}]_c$ 5d;2_g and $[^2\Pi_{3/2}]_c$ 5d;0_g Rydberg states, illustrates the effect of completely unshielding the positively charged ionic core from the polarisable krypton atom.

It was necessary to record ZEKE-PFI spectra *via* four more vibrational levels of the ν_3 mode in the intermediate state in order to cover a reasonable portion of the ionic van der Waals potential. These scans, which can be seen in figure 5-8 (a), show clear anharmonic progressions in the $I_2^+\cdots$Kr van der Waals stretching mode, ν_3^+. The peak positions of the spectrum *via* $\nu_3' = 2$ were fitted to the expression for vibrational energy levels to yield values of 55±2 cm^{-1} for $\tilde{\omega}_e^+$ and 1.0±0.1 cm^{-1} for $\tilde{\omega}_e x_e^+$. The geometry of the complex ion can be tentatively assigned to be T-shaped based on the same arguments used in section 5.3.2.1 concerning the geometry of the complex in the two Rydberg states.

Franck-Condon simulations were carried out for the five ZEKE spectra, the results of which can be seen in figure 5-8(b). The intensity patterns of the ZEKE spectra have been reproduced quite well including the oscillatory pattern of the ZEKE spectrum recorded *via* ν_3=4. The reduction of the van der Waals bond length upon excitation was found to be between 0.053 and 0.047Å giving an average r_e^+ of 4.410Å, i.e. a total reduction of 0.380Å from the ground state bond length.

Table 5-4 Spectral peak positions and assignments of the $[^2\Pi_{3/2}]_c$ 5d;Ω_g (Ω=2,0) Rydberg states of I_2-Kr

State	Transition energy (cm^{-1})	Vibrational spacing (cm^{-1})		Assignment [a]
$[^2\Pi_{3/2}]_c$ 5d;2_g	62192	0	0	0_0^0
	62237	45		3_0^1
	62280	43		3_0^2
	62323	43		3_0^3
	62363	40		3_0^4
	62401	38		3_0^5
	62438	37		3_0^6
	62422	0	230	1_0^1
	62468	46		$3_0^1\ 1_0^1$
	62512	44		$3_0^2\ 1_0^1$
	62554	42		$3_0^3\ 1_0^1$
	62594	40		$3_0^4\ 1_0^1$
	62632	38		$3_0^5\ 1_0^1$
	62670	38		$3_0^6\ 1_0^1$
	62653	0	231	1_0^2
	62698	45		$3_0^1\ 1_0^2$
	62741	43		$3_0^2\ 1_0^2$
	62784	43		$3_0^3\ 1_0^2$
	62824	40		$3_0^4\ 1_0^2$
	62863	39		$3_0^5\ 1_0^2$
	62901	38		$3_0^6\ 1_0^2$
	62883	0	230	1_0^3
	62928	45		$3_0^1\ 1_0^3$
	62971	43		$3_0^2\ 1_0^3$
	63013	42		$3_0^3\ 1_0^3$
	63054	41		$3_0^4\ 1_0^3$
	63091	37		$3_0^5\ 1_0^3$
	63130	39		$3_0^6\ 1_0^3$
$[^2\Pi_{3/2}]_c$ 5d;0_g	62853	0	0	0_0^0
	62900	47		3_0^1
	62946	46		3_0^2
	62991	45		3_0^3
	63033	42		3_0^4
	63074	43		3_0^5
	63114	40		3_0^6
	63087	0	234	1_0^1
	63134	47		$3_0^1\ 1_0^1$
	63180	46		$3_0^2\ 1_0^1$
	63224	44		$3_0^3\ 1_0^1$
	63267	43		$3_0^4\ 1_0^1$
	63308	41		$3_0^5\ 1_0^1$
	63346	38		$3_0^6\ 1_0^1$

	63318	0	231	1_0^2
	63364	46		$3_0^1 1_0^2$
	63411	47		$3_0^2 1_0^2$
	63455	44		$3_0^3 1_0^2$
	63499	44		$3_0^4 1_0^2$
	63539	40		$3_0^5 1_0^2$

[a] In this notation $3_0^n\ 1_0^m$ refers to *m* quanta excited in the I_2 stretch, ν_1, and *n* quanta excited in the I_2···Kr van der Waals stretch, ν_3. The van der Waals stretch has been labelled ν_3 using the convention put forward by Mulliken.[41]

Table 5-5 Spectroscopic data obtained for the I_2-Kr van der Waals complex from the REMPI and ZEKE spectra

Complex /State	Band origin (cm^{-1})	Spectral red shift (cm^{-1})	D_0 (cm^{-1})	ϖ_e (cm^{-1})	$\varpi_e x_e$ (cm^{-1})
I_2-Kr $[^2\Pi_{3/2}]_c$ 5d;2_g	62192±2	447±4	729±4	47±2	0.8±0.1
I_2-Kr $[^2\Pi_{3/2}]_c$ 5d;0_g	62853±2	479±4	761±4	49±2	0.8±0.1
I_2^+-Kr $\tilde{X}\ ^2\Pi_{3/2,g}$	74248±3	821±5	1103±5	55±2	1.0±0.1

5.3.3 Discussion

One of the interesting features of this work is the differences between the REMPI spectrum of I_2-Kr and previous work on I_2-Ar (see section 5.2 and ref 19). The first obvious difference is that there is no evidence for more than one isomer. The peaks in the REMPI spectrum of the $[^2\Pi_{3/2}]_c$ 5d; 2_g Rydberg state of I_2-Kr (figure 5-6) have very sharp profiles with no sign of structure that could be attributed to a second isomer. There are also notable differences between the spectroscopic constants for I_2-Ar and I_2-Kr in the two Rydberg states. The values of the spectral red-shifts (and therefore the dissociation energies) for the $[^2\Pi_{3/2}]_c$ 5d Rydberg states of I_2-Kr are much larger than the corresponding red-shifts for I_2-Ar. The increased binding in both complexes is thought to be caused by exposure of the rare gas atom to the ionic core of the I_2 molecule through poor shielding by the non-penetrating 5d

Rydberg orbital. The relative increase in spectral red-shift for krypton compared to argon would be expected given that krypton is more polarisable ($\alpha(Kr) = 2.4844\times10^{-24}$ cm^3 and $\alpha(Ar) = 1.6411\times10^{-24}$ cm^3)[48] and as such will give rise to a larger charge-induced dipole interaction. This explanation also holds for the difference between the spectral red-shifts for the $\tilde{X}\ ^2\Pi_{3/2,g}$ states of I_2^+-Kr and I_2^+-Ar.

An attempt was made to record the (2+1) REMPI spectra of the $[^2\Pi_{1/2}]_g$ 6s;1_g, $[^2\Pi_{1/2}]_g$ 5d;Ω_g (Ω=2,0) and the $[^2\Pi_{3/2}]_g$ 6d;Ω_g (Ω=2,0) Rydberg states of I_2-Kr to compare with previous work on I_2-Ar. However, no significant parent ion (I_2^+-Kr) or fragment ion signal (I^+-Kr) was observed in the time-of-flight mass spectrum in the appropriate energy ranges. This result is surprising given that the I_2-Ar complex is observed in all seven Rydberg states mentioned above using the I_2^+-Ar mass channel (except for the $[^2\Pi_{1/2}]_g$ 6s;1_g Rydberg state in which I^+-Ar is the dominant product ion[19]). A similar situation has been observed in the Rydberg states of NO- rare gas van der Waals complexes in the REMPI spectra recorded by Miller *et al.*[10] The NO-Ar van der Waals complex is observed in both the $C\ ^2\Pi_{1/2}$ and the $D\ ^2\Sigma^+$ Rydberg states but the NO-Ne, NO-Kr and NO-Xe are only observed in the $C\ ^2\Pi_{1/2}$ Rydberg state. However, no explanation is given by Miller *et al.* for the absence of these Rydberg states.

A possible explanation for our failure to observe the above mentioned Rydberg states in I_2-Kr is that they are strongly predissociated, implying that the predissociation rates for Rydberg states of I_2-X complexes are sensitive to the identity of the van der Waals partner. This is certainly the case in the valence $B\ ^3\Pi_{0u}^+$ state of the I_2-rare gas complexes. The *B* state of the I_2-rare gas complexes is subject to electronic predissociation caused by a coupling to the repulsive $a\ ^3\Pi_{1g}$ state.[39] The I_2-He and I_2-Ne complexes undergo very little or no electronic predissociation whereas in the I_2-Ar complex electronic predissocition competes with vibrational predissociation as the main decay route. In I_2-Kr and I_2-Xe electronic predissociation becomes the main decay route resulting in no fluorescence being observed from the *B* state.[42]

We have also searched for Rydberg states of the I_2-Xe complex but with no success. As well as the possibility that I_2-Xe is strongly predissociated there are two other explanations that may explain the absence of the Rydberg states. One is that the xenon in the molecular beam preferentially forms Xe_2, which has been detected in large abundance.[49] The other explanation is that I_2 reacts with Xe to form the XeI* excimer. The threshold for this reaction is well known [50] and lies below the two-photon energy used to reach the Rydberg states of I_2.

In summary, we have observed and characterised, for the first time, the $[^2\Pi_{3/2}]_c$ 5d;2_g and $[^2\Pi_{3/2}]_c$ 5d;0_g Rydberg states of I_2-Kr. The $[^2\Pi_{3/2}]_c$ 5d;2_g Rydberg state has been used as an intermediate in a ZEKE-PFI photoelectron study to characterise the lower spin orbit component of the ground state I_2^+-Kr cation. The geometry of the complex in the $[^2\Pi_{3/2}]_c$ 5d;2_g and $[^2\Pi_{3/2}]_c$ 5d;0_g Rydberg states and the ground state of the cation are unchanged from that of the ground neutral state. The geometry of the complex in the ground neutral state is assumed to be T-shaped.

5.4 The (2+1) REMPI spectrum of I_2-N_2

5.4.1 Introduction

The I_2-N_2 van der Waals complex has seen even less study than the heavier rare gas - I_2 van der Waals complexes. The I_2-N_2 van der Waals complex was first observed in the laser-induced fluorescence emission and dispersed fluorescence spectra of Johnson and Levy,[51] in which they determined an estimate of the binding energy of the complex of in the ground (218-318 cm^{-1}) and *B* states (188-284 cm^{-1}).

The van der Waals interaction between I_2 and N_2 will have, as well as attractive dispersion and repulsive electron-electron interactions, a quadrupole-quadrupole interaction as both molecules have substantial quadrupoles. The change in binding upon excitation to a Rydberg state may be expected to be quite dramatic as there is the possibility of charge-quadrupole interactions between a partially shielded iodine molecular core and the nitrogen molecular quadrupole.

In this section we present the (2+1) REMPI spectrum of the I_2-N_2 van der Waals complex in the $[^2\Pi_{1/2}]_c$ 6s;Ω=1_g Rydberg state. This is the first observation of the I_2-N_2 complex in a Rydberg state. We also present an empirical potential of the ground state of the complex which has been used to investigate the geometry of the complex. The potential used is an isotropic atom-atom potential.[52] The spectroscopic information determined from this study is compared with the spectroscopic constants of the analogous Rydberg state in I_2-Ar.[19]

5.4.2 Results

5.4.2.1 Experimental Details

In the I_2-N_2 experiments the dye laser output was frequency mixed with the fundamental of the Nd:YAG laser (1064nm) using a KD*P crystal to produce light of wavelength 377nm to 366nm (R610 and R590 dyes). The frequency mixed output was separated from the dye fundamental and the Nd:YAG fundamental using coloured filters. The I_2-N_2 complex was produced by passing nitrogen in helium at

various stagnation pressures (600 to 700 Torr, 3:4 ratio of N_2 in He) through a sample reservoir containing solid iodine (heated to produce a sufficient vapour pressure) located within the pulsed nozzle assembly. A 2.5kV dc repelling voltage was applied to the top plate to drive the ions to the detector. The lower plate was set to earth.

5.4.2.2 REMPI spectrum of the $[^2\Pi_{1/2}]_c$ 6s;1_g Rydberg state of I_2-N_2

In figure 5-9 we present the (2+1) REMPI spectrum of the $[^2\Pi_{1/2}]_c$ 6s;1_g Rydberg state of the I_2-N_2 van der Waals complex recorded in the 53000-54800 cm^{-1} (two-photon) energy range. The spectrum was recorded by monitoring the I_2^+-N_2 mass channel. The assignment of the vibrational structure associated with the $[^2\Pi_{1/2}]_c$ 6s;1_g Rydberg state is given in figure 5-9 and Table 5-6. There are two vibrational progressions observed in the REMPI spectrum based on the I-I stretch (ν_1) and the I_2···N_2 stretch (ν_3). A summary of the spectroscopic data obtained for I_2-N_2 can be seen in Table 5-7.

The first peak in the spectrum appears at 53208±2 cm^{-1} and the lack of any obvious feature to lower energy allows us to assign it as the band origin of the $[^2\Pi_{1/2}]_c$ 6s;1_g Rydberg state of the complex. The band origin of the bare I_2 $[^2\Pi_{1/2}]_c$ 6s;1_g state [19] lies at 53582±2 cm^{-1} which yields a spectral red-shift of 374±4 cm^{-1} for the van der Waals complex, again indicating significant strengthening of the van der Waals bond with respect to the ground state. As with I_2-Ar and I_2-Kr this bond strengthening might be expected given the exposure of the N_2 molecule to the positively charged iodine core and the resultant charge-induced dipole force. However, given the relatively compact nature of the 6s Rydberg orbital, the increase could equally be due to larger dispersion forces caused by the more polarisable Rydberg orbital. The start of the next main band appears 242 cm^{-1} to higher energy at 53450 cm^{-1}, the separation is almost identical to that

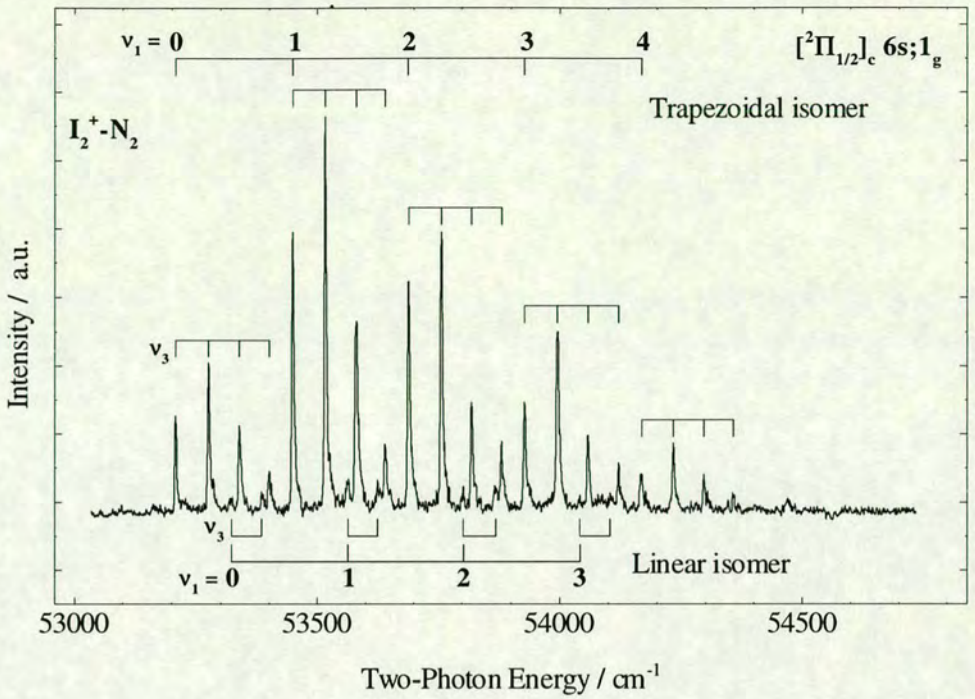

Figure 5-9 - The (2+1) mass-resolved REMPI excitation spectrum of jet-cooled I_2-N_2 recorded in the range 53000-54800 cm^{-1} monitoring the I_2^+-N_2 mass channel.

between v′=0 and v′=1 in the $[^2\Pi_{1/2}]_c$ 6s;1_g state of the bare I_2 molecule and consequently we can assign it to one quantum excited in the I_2 stretching mode. The next four bands can be assigned in exactly the same way. As in I_2-Kr each band is made up of an anharmonic progression in one of the van der Waals vibrational modes. The average vibrational spacings in these progressions is 64 cm^{-1} and is most likely due to a van der Waals stretching vibration. The peak positions of the first band were fitted to the vibrational energy level equation to yield values of 71±2 cm^{-1} for $\tilde{\omega}_e$ and 1.7±0.2 cm^{-1} for $\tilde{\omega}_e x_e$.

Apart from the main progression in the spectrum, weaker peaks can be seen to slightly lower energy of the third and fourth peak in each combination band. These weaker peaks, which form pairs, are unlikely to be hot bands as they are not far enough to the red for diagonal transitions of the I-I stretch. The possibility that they are Δv=1 and Δv=2 sequence bands of the van der Waals stretching mode can be excluded as the peaks are too far to the blue of the corresponding peaks in the main

progression. We have also considered that the peaks might be due to higher clusters (I_2-$(N_2)_n$ where n > 1). The REMPI spectrum was recorded by monitoring the I_2-N_2^+ mass channel but higher clusters might be detected in this channel through fragmentation of the parent complex. The simplicity of the spectrum suggests that this assignment is unlikely (see REMPI spectrum of I_2-Ar_2 [19]).

The explanation that seems most likely is that the extra structure is due to a second isomer of I_2-N_2, analagous to the second isomer seen I_2-Ar (see section 5.2). The spacing between the peaks in each pair is almost identical to those of the main van der Waals progression and the separation between the pairs of peaks is identical to the energy of the I-I stretch for this state. In the case of I_2-Ar the intermolecular stretch and the I-I stretch were found to be similar for both linear and T-shaped isomers.

An upper bound for the band origin of this possible second isomer in the $[^2\Pi_{1/2}]_c$ 6s;1_g state can be set at 53322±2 cm^{-1}. This represents a lower bound for the spectral red-shift of the second isomer of 260±4 cm^{-1} relative to the band origin of the $[^2\Pi_{1/2}]_c$ 6s;1_g state of the bare I_2 molecule.[19]

Table 5-6 Spectral peak positions and assignments of the $[^2\Pi_{1/2}]_c$ 6s;1_g Rydberg state of I_2-N_2

Isomer	Transition energy (cm^{-1})	Vibrational spacing (cm^{-1})	Assignment [a]
Trapezoidal isomer	53208	0 0	0_0^0
	53276	68	3_0^1
	53339	63	3_0^2
	53400	61	3_0^3
	53450	0 242	1_0^1
	53517	67	$3_0^1\ 1_0^1$
	53581	64	$3_0^2\ 1_0^1$
	53641	60	$3_0^3\ 1_0^1$
	53689	0 239	1_0^2
	53757	68	$3_0^1\ 1_0^2$
	53819	62	$3_0^2\ 1_0^2$
	53881	62	$3_0^3\ 1_0^2$
	53928	0 239	1_0^3
	53996	68	$3_0^1\ 1_0^3$
	54058	62	$3_0^2\ 1_0^3$
	54121	63	$3_0^3\ 1_0^3$
	54167	0 239	1_0^4
	54233	66	$3_0^1\ 1_0^4$
	54296	63	$3_0^2\ 1_0^4$
	54357	61	$3_0^3\ 1_0^4$
Linear Isomer	53322	0 0	0_0^0
	53385	63	3_0^1
	53565	0 243	1_0^1
	53625	60	$3_0^1\ 1_0^1$
	53803	0 238	1_0^2
	53869	66	$3_0^1\ 1_0^2$
	54042	0 239	1_0^3
	54104	62	$3_0^1\ 1_0^3$

[a] In this notation $3_0^n\ 1_0^m$ refers to *m* quanta excited in the I_2 stretch, ν_1, and *n* quanta excited in the I_2···N_2 van der Waals stretch, ν_3. The van der Waals stretch has been labelled ν_3 using the convention put forward by Mulliken.[41]

Table 5-7 Spectroscopic data obtained for the I_2-N_2 van der Waals complex from the REMPI spectrum

Complex /State	Band origin (cm^{-1})	Spectral red shift (cm^{-1})	D_0 (cm^{-1})	ϖ_e (cm^{-1})	$\varpi_e x_e$ (cm^{-1})
I_2-N_2 Trapezoidal $[^2\Pi_{1/2}]_c$ 6s;1_g	53208±2	374±4	-	71±2	1.7±0.2
I_2-N_2 Linear $[^2\Pi_{1/2}]_c$ 6s;1_g	53322±2	260±4	-	-	-

5.4.2.3 Empirical potential calculations of the ground state I_2-N_2 van der Waals complex.

The empirical potential used in this study was an isotropic atom-atom potential of the form (exp-6-1),[52]

$$V = \sum_{i=1}^{4}\sum_{j=1}^{4} A_{ij} \exp(-b_{ij} r_{ij}) - C_{ij} / r_{ij}^6 + q_i q_j / (4 \pi \varepsilon_0 r_{ij}) \qquad (5.1)$$

which includes a Born Mayer repulsive potential with coefficients A_{ij} and b_{ij}, a dispersion energy term with coefficient C_{ij} and a term to reproduce the quadrupole-quadrupole interaction between I_2 and N_2, using an arrangement of point charges on four sites for each molecule (two of which are the atom positions) to mimic the quadrupole moment of each diatomic molecule.

The subscripts i and j refer to the atoms of the molecules involved in the van der Waals interaction. The values of A_{ij}, b_{ij} and C_{ij} were calculated from the homonuclear A_{ii}, b_{ii} and C_{ii} terms of the I-I and N-N non-bonding potential interactions using equations 2-4,[53,54,55]

$$A_{ij} = (A_{ii}A_{jj})^{1/2} \qquad (5.2)$$

$$b_{ij} = (b_{ii}b_{jj})^{1/2} \qquad (5.3)$$

$$C_{ij} = (C_{ii}\,\alpha_i\,C_{jj}\,\alpha_j) / (C_{ii}\,\alpha_j^2 + C_{jj}\,\alpha_i^2) \qquad (5.4)$$

where α_i and α_j are the atomic polarisabilities.[56] The coefficients for the N-N non-bonding interaction were obtained from crystal structure calculations of azahydrocarbon crystals carried out by Williams and Cox.[57] The charge distribution of the N_2 quadrupole was also obtained from Williams and Cox.[57] The quadrupole moment of nitrogen was split into four equal point charges, with charges of $+0.377e$ placed on each nitrogen atom and charges of $-0.377e$ placed at two lone-pair sites extended 0.25Å from either end of the N-N bond. The magnitude of the point charges was calculated by using the distances of the charge sites and the known quadrupole moment of N_2 (-4.07×10^{-40} Cm^2).[56]

The dispersion coefficient for the non-bonding I-I interaction is calculated using the following expression,[54]

$$C_{ii} = {}^3/_2 \left((e\,h\,/\,m_e)/(4\pi\varepsilon_0)^2\right) \times \left(\alpha_i^2\,/\,2(\alpha_i/N_i^{eff})^{1/2}\right) \qquad (5.5)$$

where α_i is the atomic polarisability of iodine and N_i^{eff} is the effective number of electrons that can participate in the dispersion interaction (taken simply to be the total number of electrons minus the valence electrons). The Born-Mayer b_{ii} parameter for the non-bonding I-I interaction was calculated using the method of Xu and Marlow.[58] The A_{ii} Born Mayer potential parameter was then calculated using a simple rearrangement of an (exp-6) expression for the I-I non-bonding interaction and a non-bonding equilibrium separation of twice the van der Waals radius of an iodine atom.[59] The point charges for the quadrupole moment of molecular iodine (18.7×10^{-40} Cm^2)[56] were arranged by placing the positive charges on the iodine atoms and the corresponding negative charge sites midway between each atom and the centre of the I-I bond (a separation of 1.333Å between the negative point charges). This produced a magnitude of $0.438e$ for each charge site.

A Downhill Simplex method [60] was used to search across the potential surface for minima. The parameters used in the calculation are summarised in Table 5-8. It was found that the only stable I_2-N_2 complex adopts a trapezoidal structure of C_{2v} symmetry. The binding energy was calculated to be 208 cm^{-1} and $\tilde{\omega}_e''$ was estimated

to be 30 cm^{-1} with a separation of 4.34Å between the midpoints of the I-I and N-N bonds.

The values of binding energy and midpoint separation were found to be very sensitive to the arrangement of point charges for the iodine molecular quadrupole. On moving the negative point charges within the I-I bond closer to the centre of the bond the binding energy increases and the separation decreases. When the negative charge sites were moved to within 0.5Å of each other, a second bound minimum was found on the potential surface corresponding to a linear geometry of $C_{\infty v}$ symmetry. With this arrangement of point charges the trapezoidal geometry has a binding energy of 259cm^{-1} with a midpoint separation of 4.31Å. The linear geometry has a binding energy of 153cm^{-1} with a nearest atom separation of 4.29Å. It should be pointed out that the binding energies quoted here are the energies required to dissociate the complex along the coordinate of the van der Waals stretching mode (ν_3) and as such do not give any information on the barrier to internal rotation of the van der Waals molecule.

The empirical potential calculation and subsequent minimization allow us to conclude that the most stable geometry for the I_2-N_2 complex in its ground neutral state is probably trapezoidal with point group C_{2v}. Therefore we assign the most intense progression in the REMPI spectrum of the $[^2\Pi_{1/2}]_c$ 6s;1_g Rydberg to a trapezoidal complex. The appearance of a second bound minimum on the potential upon varying the point charges of the iodine quadrupole lends weight to the interpretation that the weaker structure in the REMPI spectrum of the $[^2\Pi_{1/2}]_c$ 6s;1_g Rydberg state of I_2-N_2 is due to the presence of a second, possibly linear, isomer.

Table 5-8 Potential parameters used in the (exp-6-1) atom-atom potential for the I_2-N_2 van der Waals complex

Potential Parameter [a,b]	
A_{ij} (i = 1,2 ; j = 1,2)	2.738×10^7 cm^{-1}
b_{ij} (i = 1,2 ; j = 1,2)	2.961 Å^{-1}
C_{ij} (i = 1,2 ; j = 1,2)	7.406×10^5 Å^6 cm^{-1}
q_i (i = 1...4)	0.438e
q_j (j = 1...4)	0.377e

[a] Subscript *i* refers to sites on the iodine molecule, subscript *j* refers to sites on the nitrogen molecule

[b] Atom sites are labelled 1 and 2 for each molecule, extra point charge sites are labelled 3 and 4

5.4.3 Discussion

The constants determined from the REMPI spectrum of the $[^2\Pi_{1/2}]_c$ 6s;1_g Rydberg state of I_2-N_2 allows us to compare the van der Waals interaction of I_2-N_2 with that of I_2-Ar in the same Rydberg state.[19] The spectral red-shifts for both trapezoidal and linear isomers of I_2-N_2 in this Rydberg state are substantially larger than that seen in I_2-Ar (I_2-N_2 (trap.) red shift = 374 cm^{-1}, I_2-N_2 (linear) red shift = 260 cm^{-1}, I_2-Ar (T) red shift = 152 cm^{-1}) . This increase could be partly caused by larger charge-induced dipole interactions as in I_2-Kr ($\overline{\alpha}$ (N_2) = 1.7403×10^{-24} cm^3)[48] but there is also the possibility of charge-quadrupole interactions between the partially shielded iodine ionic core and the nitrogen molecule, leading to a larger change in the binding energy of the I_2-N_2 complex relative to I_2-Ar.

As with I_2-Kr, an attempt was made to record the (2+1) REMPI spectra of the $[^2\Pi_{3/2}]_c$ 5d;Ω_g (Ω=2,0), $[^2\Pi_{1/2}]_c$ 5d;Ω_g (Ω=2,0) and $[^2\Pi_{3/2}]_c$ 6d;Ω_g (Ω=2,0) Rydberg states of the I_2-N_2 complex to compare with I_2-Ar. However, no parent ion (I_2^+-N_2) or fragment ion signal (I^+-N_2) was observed in the appropriate energy ranges. Predissociation provides a possible explanation for the inability to detect Rydberg states higher in energy than the $[^2\Pi_{1/2}]_c$ 6s;1_g state.

In summary, we have recorded the REMPI spectrum of the van der Waals dimer I_2-N_2 in its $[^2\Pi_{1/2}]_c$ 6s;1_g Rydberg state. The geometry of this complex in the ground neutral state is most probably trapezoidal. The most intense structure in the REMPI spectrum of the $[^2\Pi_{1/2}]_c$ 6s;1_g Rydberg state is assigned to a trapezoidal complex. This assignment is based on the results of empirical potential energy calculations. Also observed in the REMPI spectrum of the $[^2\Pi_{1/2}]_c$ 6s;1_g Rydberg state of I_2-N_2 is weaker structure that could indicate the existence of a second, linear, isomer.

5.5 Conclusions

In this chapter we have presented the results of a (2+1) REMPI and (2+1′) ZEKE-PFI spectroscopic study of the I_2-Ar, I_2-Kr and I_2-N_2 van der Waals complexes. The spectroscopic constants determined from this study are summarised in Table 5-9.

The $[^2\Pi_{3/2}]_c$ 5d; 2_g and $[^2\Pi_{3/2}]_c$ 5d; 0_g Rydberg states of I_2-Ar have been investigated using REMPI spectroscopy. Analysis of the REMPI spectra has shown that there are two isomers of I_2-Ar in these Rydberg states, T-shaped and linear. The $[^2\Pi_{3/2}]_c$ 5d; 2_g Rydberg state of I_2-Ar was used as an intermediate state in a (2+1′) ZEKE-PFI study of the $\tilde{X}\,^2\Pi_{3/2,g}$ state of I_2^+-Ar. The ZEKE-PFI spectra also showed structure which was assignable to two distinct structural isomers of the I_2-Ar van der Waals complex. This is the first direct evidence for the existance of two isomers of I_2-Ar. A linear isomer of I_2-Ar has been invoked in many studies of the one-atom cage effect to explain the degree of solvent caging observed for the complex.

An almost identical study to that performed for I_2-Ar has also been carried out for I_2-Kr. The $[^2\Pi_{3/2}]_c$ 5d; 2_g and $[^2\Pi_{3/2}]_c$ 5d; 0_g Rydberg states of I_2-Kr have been studied using REMPI spectroscopy and the $[^2\Pi_{3/2}]_c$ 5d; 2_g Rydberg state has been used as an intermediate in a ZEKE-PFI study of the $\tilde{X}\,^2\Pi_{3/2,g}$ state of I_2^+-Kr. The Rydberg states and the ionic state all show large red-shifts with respect to the bare I_2 states. This is an indication of a strengthening of the van der Waals interaction. The increased binding is due to charge-induced dipole attractive forces caused by exposure of the polarisable krypton atom to the ionic core of the I_2 molecule. The increase in binding of the I_2-Kr complex upon excitation to the Rydberg and the ionic states is larger than the increase in binding for the I_2-Ar complex. This simply reflects the fact that krypton is more polarisable than I_2-Ar. The biggest contrast between the I_2-Ar and I_2-Kr studies is that we only see one isomer for I_2-Kr in the two Rydberg states studied.

In the case of I_2-N_2 only a REMPI study was undertaken due to experimental restrictions. The REMPI spectrum of the $[^2\Pi_{1/2}]_c$ 6s;1_g Rydberg state shows evidence for the existence of two structural isomers of the van der Waals complex. The

binding energy of I_2-N_2 in the Rydberg state is larger than that in the ground state as evidenced by the significant red-shift of the Rydberg state band origin. The increase in binding upon excitation is much larger than for the same Rydberg state in I_2-Ar. The difference in the red-shifts for the two complexes can be explained by considering the possible charge-quadrupole interactions that can take place between the Rydberg excited iodine and nitrogen. An empirical potential calculation has shown that the most strongly bound isomer (the isomer responsible for the most intense structure in the REMPI spectrum) is most likely trapezoidal in structure and that the second isomer could be linear. The results for I_2-N_2 contrast with those of I_2-Ar in that the $[^2\Pi_{1/2}]_c$ 6s;1_g state of I_2-Ar shows no evidence of structural isomerism. The difference in binding energy for the I_2-N_2 complex compared to the I_2-Ar complex is probably due to the influence of charge-quadrupole interactions.

Table 5-9 Spectroscopic data obtained for the I_2-Ar, I_2-Kr and I_2-N_2 van der Waals complexes from REMPI and ZEKE-PFI spectra

Complex /State	Band origin (cm^1)	Spectral red shift (cm^{-1})	D_0 (cm^{-1})	ϖ_e (cm^{-1})	$\varpi_e x_e$ (cm^{-1})
I_2-Ar T-shaped					
$[^2\Pi_{1/2}]_c$ 6s;1_g [a]	53430±2	152±2	389±5	49±2	1.5±0.1
$[^2\Pi_{3/2}]_c$ 5d;2_g	62368±2	271±2	508±5	55±3	1.5±0.5
$[^2\Pi_{3/2}]_c$ 5d;0_g	63006±2	326±2	563±5	58±2	1.6±0.1
$\tilde{X}\ ^2\Pi_{3/2,g}$	74523±2	546±2	783±2	63±2	1.4±0.1
I_2-Ar linear					
$[^2\Pi_{3/2}]_c$ 5d;2_g	62372±2	267±2	504±5	51±3	1.1±0.5
$[^2\Pi_{3/2}]_c$ 5d;0_g	63133±2	199±2	436±5	46±3	0.7±0.1
$\tilde{X}\ ^2\Pi_{3/2,g}$	74566±2	503±2	740±2	61±2	1.4±0.1
I_2-Kr					
$[^2\Pi_{3/2}]_c$ 5d;2_g	62192±2	447±4	729±4	47±2	0.8±0.1
$[^2\Pi_{3/2}]_c$ 5d;0_g	62853±2	479±4	761±4	49±2	0.8±0.1
$\tilde{X}\ ^2\Pi_{3/2,g}$	74248±3	821±5	1103±5	55±2	1.0±0.1
I_2-N_2 Trapezoidal					
$[^2\Pi_{1/2}]_c$ 6s;1_g	53208±2	374±4	-	71±2	1.7±0.2
I_2-N_2 Linear					
$[^2\Pi_{1/2}]_c$ 6s;1_g	53322±2	260±4	-	-	-

[a] Constants taken from reference 19

5.6 References

[1] D. H. Levy, *Adv.Chem.Phys.* 1981 **47**, 323.

[2] J. B. Hopkins, D. E. Powers, R. E. Smalley, *J.Phys.Chem.* 1981, **85**, 3739.

[3] See Chapter 1 and Chapter 3 for a discussion on REMPI spectroscopy.

[4] K. Sato, Y. Achibo, K. Kimura, *J.Chem.Phys.* 1984, **81**, 57.

[5] K. H. Fung, W. E. Henke, T. R. Hays, H. L. Selzle, E. W. Schlag, *J.Phys.Chem.* 1981, **85**, 3560; L. A. Chewter, K. Muller-Dethlefs, E. W. Schlag, *Chem.Phys.Lett.* 1987, **135**, 219.

[6] J. L. Knee, P. M. Johnson, *J.Chem.Phys.* 1984, **80**, 13; X. Zhang, J. M. Smith, J. L. Knee, *J.Chem.Phys.* 1992, **97**, 2843.

[7] T. Troxler, S. Leutwyler, *J.Chem.Phys.* 1991, **95**, 4011.

[8] Q. Y. Shang, P. O. Moreno, S. Li, E. R. Bernstein, *J.Chem.Phys.* 1993, **98**, 1876; Q. Y. Shang, P. O. Moreno, E. R. Bernstein, *J.Am.Chem.Soc.* 1994, **116**, 302; Q. Y. Shang, E. R. Bernstein, *Chem.Rev.* 1994, **94**, 2015.

[9] J. A. Blazy, B. M. DeKoven, T. D. Russell, D. H. Levy, *J.Chem.Phys.* 1980, **72**, 2439.

[10] J. C. Miller, W. C. Cheng, *J.Phys.Chem.* 1985, **89**, 1647; J. C. Miller, *J.Chem.Phys.* 1987, **86**, 3166; J. C. Miller, NATO ASI Conference Proceedings, "Linking the Gaseous and Condensed Phases of Matter", 1993, Plenum.

[11] T. Suzuki, H. Katayanagi, M. C. Heaven, *J.Phys.Chem.A.* 1997, **101**, 6697

[12] P.R.R. Langridge-Smith, E. Carrasquillo M., D. H. Levy, *J.Chem.Phys.* 1981, **74**, 6513; J. C. Miller, *J.Chem.Phys.* 1989, **90**, 4031; K. Tsuji, K. Shibuya, K. Obi, *J.Chem.Phys.* 1994, **100**, 5441; M. J. McQuaid, G. W. Lemire, R. C. Sausa, *Chem.Phys.Lett.* 1994, **227**, 54.

[13] A. M. Bush, J. M. Dyke, P. Mack, D. M. Smith, T. G. Wright, *J.Chem.Phys.* 1996, **105**, 9804.

[14] K. Müller-Dethlefs, O. Dopfer, T. G. Wright, *Chem.Rev.* 1994, **94**, 1845.

[15] P. Johnson, L. Zhu, *J.Chem.Phys.* 1991, **94**, 5769; P. Johnson, L. Zhu, *Int.J.Mass.Spect.Ion.Proc.* 1994, **131**, 193.

[16] H. Krause, H. J. Neusser, *J.Chem.Phys.* 1992, **97**, 5923; *J.Chem.Phys.* 1993, **99**, 6278; T. L. Grebner, H. J. Neusser, *Int.J.Mass.Spect.Ion.Proc.* 1996, **159**, 137; Th. L. Grebner, P. v. Unold, H. J. Neusser, *J.Phys.Chem.* A. 1997, **101**, 158.

[17] R. P. Schmid, P. K. Chowdhury, J. Miyawaki, F. Ito, K. Sugawara, T. Nakanaga, H. Takeo, H. Jones, *Chem.Phys.* 1997, **218**, 291.

[18] A. Fujii, A. Iwasaki, K. Yoshida, T. Ebata, N. Mikami, *J.Phys.Chem.* A. 1997, **101**, 1798.

[19] M. C. R. Cockett, J. G. Goode, K. P. Lawley, R. J. Donovan, *Chem.Phys.Lett.* 1993, **214**, 27; M. C. R. Cockett, J. G. Goode, R. R. Maier, K. P. Lawley, R. J. Donovan, *J.Chem.Phys.* 1994, **101**, 126.

[20] J. G. Goode, M. C. R. Cockett, K. P. Lawley, R. J. Donovan, *Chem.Phys.Lett.* 1994, **231**, 521.

[21] G. Kubiak, P. S. H. Fitch, L. Wharton, D. H. Levy, *J.Chem.Phys.* 1978, **68**, 4477.

[22] J. A. Blazy, B. M. DeKoven, T. D. Russell, D. H. Levy, *J.Chem.Phys.* 1980, **72**, 2439.

[23] K. E. Johnson, W. Sharfin, D. H. Levy, *J.Chem.Phys.* 1981, **74**, 163; W. E. Sharfin, K. E. Johnson, L. Wharton, D. H. Levy, *J.Chem.Phys.* 1979, **71**, 1292; J. E. Kenny, K. E. Johnson, W. Sharfin, D. H. Levy, *J.Chem.Phys.* 1980, **72**, 1109; J. E. Kenny, T. D. Russell, D. H. Levy, *J.Chem.Phys.* 1980, **73**, 3607; M. S. Kim, R. E. Smalley, L. Wharton, D. H. Levy, *J.Chem.Phys.* 1976, **65**, 1216; K. W. Johnson, L. Wharton, D. H. Levy, *J.Chem.Phys.* 1978, **69**, 2719.

[24] J. A. Beswick, J. Jortner, *Adv.Chem.Phys.* 1981, **47**, p363

[25] J. T. Hynes, *Annu.Rev.Phys.Chem.* 1985, **36**, 573; A. L. Harris, J. K. Brown, C. B. Harris, *Annu.Rev.Phys.Chem.* 1988, **39**, 341; J. Schroeder, J. Troe, *Annu.Rev.Phys.Chem.* 1987, **38**, 163.

[26] K. L. Saenger, G. M. McClelland, D. R. Herschbach, *J.Phys.Chem.* 1981, **85**, 3333.

[27] J. J. Valentini, J. B. Cross, *J.Chem.Phys* 1982, **77**, 572.

[28] J. M. Phillipoz, R. Monot, H. van den Bergh, *Helv.Phys.Acta.* 1986, **58**, 1089; J. M. Phillipoz, H. van den Bergh, R. Monot, *J.Phys.Chem.* 1987, **91**, 2545; J. M. Phillipoz, P. Melinon, R. Monot, H van den Bergh, *Chem.Phys.Lett.* 1987, **138**, 579; J. M. Phillipoz, R. Monot, H. van den Bergh, *J.Chem.Phys.* 1990, **92**, 288; J. M. Phillipoz, R. Monot, H. van den Bergh, *J.Chem.Phys.* 1990, **93**, 8676.

[29] O. Roncero, N. Halberstadt, J. A. Beswick, "Reaction Dynamics in Clusters and Condensed Phases", J. Jortner *et al.* (Eds.), Kluwer, Dordecht, 1994, 73.

[30] J. A. Beswick, R. Monot, J. M. Phillippoz, H. van den Bergh, *J.Chem.Phys.* 1987, **86**, 3965.

[31] I. Noorbatcha, L. M. Raff, D. L. Thompson, *J.Chem.Phys.* 1984, **81**, 5658.

[32] M. P. Miranda, J. A. Beswick, N. Halberstadt, *Chem.Phys.* 1994, **187**, 185.

[33] J.-Y. Fang, C. C. Martens, *J.Chem.Phys.* 1996, **105**, 9072; A. J. Conley, J.-Y. Fang, C. C. Martens, *Chem.Phys.Lett.* 1997, **272**, 103.

[34] S. J. Harris, S. E. Novick, W. Klemperer, W. E. Falconer, *J.Chem.Phys.* 1974, **61**, 193; S. J. Harris, S. E. Novick, W. Klemperer, *J.Chem.Phys.* 1974, **60**, 3208; S. E. Novick, P. Davies, S. J. Harris, W. Klemperer, *J.Chem.Phys.* 1973, **59**, 2273.

[35] R. E. Smalley, L. Wharton, D. H. Levy, *J.Chem.Phys.* 1978, **68**, 671.

[36] F. Thommen, D. D. Evard, K. C. Janda, *J.Chem.Phys.* 1985, **82**, 5259.

[37] D. D. Evard, F. Thommen, K. C. Janda, *J.Chem.Phys.* 1986, **84**, 3630.

[38] D. D. Evard, J. I. Cline, K. C. Janda, *J.Chem.Phys.* 1988, **88**, 5433.

[39] M. L. Burke, W. Klemperer, *J.Chem.Phys.* 1993, **98**, 6642.

[40] M. L. Burke, W. Klemperer, *J.Chem.Phys.* 1993, **98**, 1797.

[41] R. S. Mulliken, *J.Chem.Phys.* 1955, **23**, 1997.

[42] N. Goldstein, T. L. Brack, G. H. Atkinson, *J.Chem.Phys.* 1986, **85**, 2684.

[43] W. A. Wensink, J. D. W. van Voorst, *Chem.Phys.* 1985, **99**, 155.

[44] H. Schroder, H. Gabriel, *J.Chem.Phys.* 1996, **104**, 587.

[45] R. J. Donovan, R. V. Flood, K. P. Lawley, A. J. Yencha and T. Ridley, *Chem.Phys.* 1992, **164**, 439

[46] R. J. Donovan, A. C. Flexen, K. P. Lawley, T. Ridley, *Chem.Phys.* (submitted for publication).

[47] M. C. R. Cockett, J. G. Goode, K. P. Lawley and R. J. Donovan, *J.Chem.Phys.* 1995, **102**, 5226.

[48] D. R. Lide (Ed.), *CRC Handbook of Chemistry and Physics*, 74th Edition, 1993-1994

[49] M. C. R. Cockett, *unpublished work.*

[50] B. V. O'Grady, R. J. Donovan, *Chem.Phys.Lett.* 1985, **122**, 503.

[51] K. E. Johnson, D. H. Levy, *J.Chem.Phys.* 1981, **74**, 1506.

[52] S. L. Price, *J.Chem.Soc.Farad.Trans.* 1996, **92**, 2997.

[53] M. Schauer, E. R. Bernstein, *J.Chem.Phys.* 1985, **82**, 726.

[54] M. Rigby, E. B. Smith, W. A. Wakeham, G. C. Maitland, *The Forces Between Molecules*, Clarendon Press, 1986, 186.

[55] A. D. Buckingham, P. W. Fowler, J. M. Hutson, *Chem.Rev.* 1988, **88** ,963.

[56] D. R. Lide (Ed.), *CRC Handbook of Chemistry and Physics*, 74th Edition, 1993-1994.

[57] D. E. Williams, S. R. Cox, *Acta.Cryst.B* 1984, **40**, 404.

[58] J. X. Lu, W. H. Marlow, *Phys.Rev.A.* 1995, **52**, 2141.

[59] A. Bondi, *J.Phys.Chem.* 1964, **68**, 441.

[60] W. H. Press, S. A. Teukolsky, W. T. Vetterling, B. P. Flannery, *Numerical Recipes in Fortran*, 2nd Ed. Cambridge University Press, 1992.

Appendix A - An Attempted ZEKE-PFI Study of Methyl Bromide

Methyl bromide (CH_3-Br) was identified as a possible candidate for investigation using ZEKE-PFI spectroscopy due to the ZEKE-PFI study carried out on methyl iodide by Strobel *et al.* [1] and the REMPI work on the Rydberg states of methyl bromide being carried out by Ridley *et al.*[2] in Edinburgh. Methyl bromide has been studied previously by conventional photoelectron spectroscopy [3] from which a value of 84930 cm^{-1} was determined for the adiabatic ionisation energy and 2560±30 cm^{-1} for the spin-orbit splitting of the ground ionic state. Rydberg extrapolations have also been used to determine the adiabatic ionisation energy yielding values between 85017±1 cm^{-1} and 85030±10 cm^{-1}.[2]

The long term goal of any ZEKE-PFI study of methyl bromide would be to use a two colour (1+1′) excitation scheme *via* a repulsive intermediate state to observe the same sort of extensive vibrational structure as seen in the ZEKE-PFI study of methyl iodide.[1] The need for a two-colour excitation scheme can be seen from the UV absorption spectra of methyl bromide [4] which shows that, unlike methyl iodide, the valence continua do not lie at the halfway energy to ionisation and cannot be accessed in a one-colour two-photon study of the ground ionic state. A two-colour (1+1′) excitation scheme of the type proposed has recently been used to probe the 6s Rydberg states of methyl iodide *via* the $^3Q_0$ valence continuum.[5]

The first stage in the study was to record a (2+1′) ZEKE-PFI spectrum of the ground ionic state, ^2E which is strongly spin-orbit split producing the $^2E_{3/2}$ and $^2E_{1/2}$ spin-orbit components. The Rydberg states chosen for this excitation route were the $[^2E_{3/2}]_c$ 5p and $[^2E_{1/2}]_c$ 5p which had already been characterised.[2,4] Figure A-1 shows the REMPI spectrum of the $[^2E_{3/2}]_c$ 5p Rydberg state of methyl bromide, recorded in the range 65700-67900 cm^{-1} using the CH_3^+ mass channel. The origin band is assigned to the peak at 66015 cm^{-1} on the basis of earlier work by Ridley *et al.*[2] The additional structure is easily assigned to vibrations involving the ν_2 mode (CH_3 umbrella mode) and the ν_3 mode (the CH_3···Br stretching mode). The spectrum consists of two scans using different dyes and no attempt has been made to power

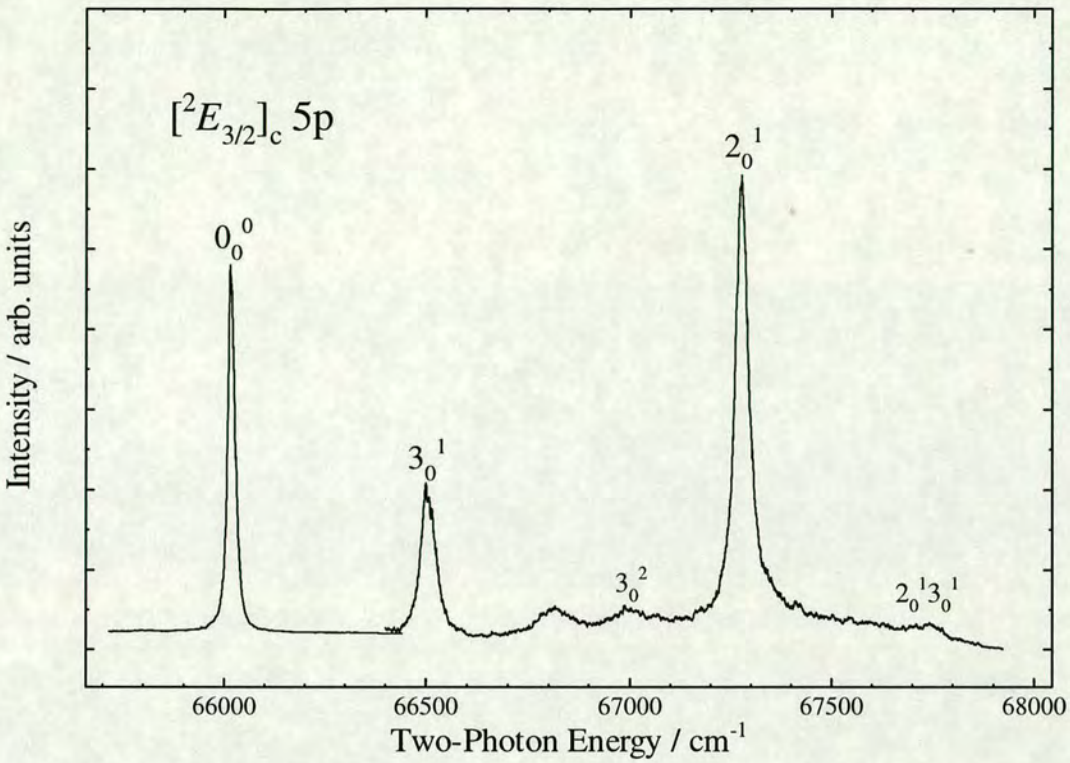

Figure A-1 - The (2+1) REMPI spectrum of methyl bromide recorded in the range 65700-67900 cm^{-1} using the CH_3^+ mass channel. The notation, 3_0^1, indicates the vibrational mode (ν_3) and the transition associated with that mode which, in the example given, is from $v'' = 0$ to $v' = 1$.

normalise the spectra. However, it should be noted that the origin band is in fact much stronger than any of the other vibrational bands.[2]

An attempt was made to record a ZEKE-PFI spectrum of the $^2E_{3/2}$ state of CH_3-Br^+ *via* the origin, 3_0^1 and 2_0^1 bands of the $[^2E_{3/2}]_c$ 5p Rydberg state. However, no ZEKE-PFI signal was observed. An attempt was also made to record a ZEKE-PFI spectrum *via* the band origins of two other Rydberg states, the $[^2E_{3/2}]_c$ 4d;2 and $[^2E_{3/2}]_c$ 4d;0 states at 72670 cm^{-1} and 72975 cm^{-1}.[2] Again, no ZEKE-PFI signal was observed. A possible explnantion for our failure to observe a signal using a (2+1′) excitation route is that the molecule continues to absorb pump photons after excitation to the Rydberg states and subsequently falls apart. This explanation is supported by the observation that only CH_3^+ and smaller molecular fragments were observed in the time-of-flight distribution when recording the REMPI spectra of these

states. The power of the pump laser was reduced using neutral density filters in an attempt to favour absorption of the probe laser photons. However, no molecular fragment or ZEKE-PFI signal was observed.

The next step was to try a single colour, coherent two-photon excitation route to take us directly to the ionic states without the use of an intermediate neutral state. As mentioned above, there are no valence continua in this region so the possibility of intermediate dissociation is negligible. Again, no ZEKE-PFI signal could be found around either of the spin-orbit compoments of the ground ionic state. As in the failed (2+1′) experiment only CH_3^+ and smaller molecular fragments were observed in the time-of-flight distribution when the ion signal was monitored. One possible explanation for these observations is that there is a very strong absorption to an ionic dissociative continuum. Molecules excited to the high *n*Rydberg states may be undergoing further excitation to a continuum state of the ion and dissociating before the application of a field ionisation pulse. Excitation *via* the high *n* Rydberg manifold can be a very strong process as evidenced by their use in PIRI (photoinduced Rydberg ionisation) spectroscopy as intermediates to probe electronically excited ionic states.[6] Absorption to an ionic dissociative continuum could also be the cause of the observation fragment ions as opposed to the molecular ion in REMPI studies (this work and Ridley *et al.*[2]).

Exactly the same experiments were attempted with deuterated methyl bromide and the same behaviour was seen in the REMPI spectra. No ZEKE-PFI signal was observed for deuterated methyl bromide.

References

---

[1] A. Strobel, A. Lochschmidt, I. Fischer, G. Niedner-Schatteburg, V. Bondybey, *J.Chem.Phys.* 1993, **99**, 733; A. Strobel, I. Fischer, A. Lochschmidt, K. Müller-Dethlefs, V. Bondybey, *J.Phys.Chem.* 1994, **98**, 2024.

[2] T. Ridley, J. Hennessy, R. J. Donovan, K. P. Lawley, (unpublished work)

[3] J. L. Ragle, I. A. Stenhouse, D. C. Frost, C. A. McDowell, *J.Chem.Phys.* 1970, **53**, 178.

[4] G. C. Causley, B. R. Russell, *J.Chem.Phys.* 1975, **62**, 848.

[5] Z. Min, T. Ridley, K. P. Lawley, R. J. Donovan, *J.Photochem.Photobiol.* A:Chemistry, 1996, **100**, 9.

[6] D. P. Taylor, J. G. Goode, J. E. LeClaire, P. M. Johnson, *J.Chem.Phys.* 1995, **103**, 6293.

Appendix B - Program Listing for I_2-N_2 Potential Surface Minimisation

This appendix contains a listing of the program used to evaluate the minimum geometry for the empirical potential surface of I_2-N_2 as detailed in section 5.3. The minimisation procedure is of a downhill simplex type as described in 'Numerical Recipes in Fortran', Cambridge University Press, Cambridge, 1992 by Press *et al.* The program is written in Fortran90 and is commented throughout.

```
module global_thingy
! This is the standard constants module for the
! programming that I will be doing. I will include all
! of the most common constants and conversion factors
! and the precision specification for all of my programs.
! pi is pi, h is planck's constant (Js) , hbar is h/2pi, me is the
! mass of an electron (kg), hc is the conversion factor for
! cm-1 --> Joules, ccm is the speed of light in centimeters
! cm is the speed of light in meters, u is the atomic mass unit(kg)
! fpi is 4*pi*e0, angs is one angstrom in meters,
! condr converts degrees to radians and conrd vice versa
! Modules are one of the very good points about Fortran90.
! It means I don't have to use common statements.
implicit none
save
integer, parameter :: i= selected_real_kind(P=14)
real(kind=i), parameter :: pi=3.141592654_i, h=6.626176E-34_i
real(kind=i), parameter :: hbar=1.054588664E-34_i
real(kind=i), parameter :: me=9.109534E-31_i,hc=1.98647759E-23_i
real(kind=i), parameter :: ccm=2.99792485E10_i,cm=2.99792485E8_i
real(kind=i), parameter :: u=1.6605655E-27_i
real(kind=i), parameter :: fpi=1.112650056E-10_i,angs=1.0E-10_i
real(kind=i), parameter :: condr=1.7453292E-2_i,conrd=57.29577951_i
integer, parameter :: NMAX=20,ITMAX=30000
end module global_thingy

program simplex1
```

```
use global_thingy
implicit none

! DATE - 08/10/96
! This program calculates local minima on an atom-atom potential
! surface using the downhill simplex method. The routine has
! been altered slightly in that it no longer acts smart. That is
! I have removed the part of the routine that extends the search for
! lower potential points. This applies for i2n2sim2.f90.
! This method is taken
! from Press et al. Numerical Recipes in Fortran. It is coded in
! Fortran77 but it should work. The minimization routine works
! in the standard coordinates (R(COM), theta, phi, beta). This
! requires that a coordinate transformation be carried out for every
! function evaluation. A lot of the stuff in this program has been
! cut and pasted from i2n2min3.f90 but this program is going to be
! much bigger.

! The program structure is as follows: The coordinate matrices are
! initialised (in the main program and using subroutine coord to get
! the atom-atom distance matrix from the jacobian coords). The value
! of the potential at each point of the simplex is calculated (using
! function funk) and then the simplex is manipulated using
! subroutines amoeba and amotry to evaluate the minimum.

! There will be quite a few subroutines, the two main ones being
! amoeba and coord. Within amoeba two there are two functions, ytry
! and funk. ytry is used by amoeba and funk is used by almost
! everything.

character(len=15) :: surface
! Here we have the arrays and vectors for the program
! r is the matrix for the atom-atom (or site-site) distances
! po is the starting point of the simplex
! lamd is a variable which estimtes the scale of the minimisation
! ptry is the new point after the modification of the simplex
! ftol is the tolerance of the procedure
```

```
! p is the matrix of the five points that make up the simplex
! e is a matrix containing unit vectors of the 4 coordinates
real(kind=i) :: r(1:4,1:4),po(1:4),lamd(1:4)
real(kind=i) :: p(1:5,1:4),y(1:5)
real(kind=i) :: ptry(1:4),ftol
real(kind=i) :: e(1:5,1:4)
real(kind=i), external :: funk,amotry
integer :: mp,np,ndim,iter,j,i2

mp=5
np=4
ndim=4
!ftol=0.01_i
ftol=1.0E-10_i
e(2,1)=1.0_i
e(3,2)=1.0_i
e(4,3)=1.0_i
e(5,4)=1.0_i

lamd(1)=0.05_i
lamd(2)=1.0_i
lamd(3)=1.0_i
lamd(4)=1.0_i

! Coordinates R(c.o.m), theta, phi, beta --> po(1) ..... po(4)
po(1)=8.0_i
po(2)=90.0_i
po(3)=90.0_i
po(4)=90.0_i

! Initialisation of the simplex matrix
do i2=1,5
 do j=1,4
  p(i2,j)=po(j)+e(i2,j)*lamd(j)
 enddo
enddo
```

```
! This was to test that the p matrix had the right values
!do j=1,4
!  write(unit=6, fmt=*) p(5,j)
!enddo

! Potential evaluation of the simplex data points
do i2=1,5
 do j=1,4
  ptry(j)=p(i2,j)
!   write(unit=6, fmt=*) i2
!   write(unit=6, fmt=*) ptry(j)
 enddo
 call coord(ptry,r)
 y(i2)=funk(r)
enddo

do i2=1,5
 write(unit=6, fmt=*) y(i2)
enddo

! All control now passes to subroutine amoeba until minimum is reached
call amoeba(p,y,mp,np,ndim,ftol,funk,iter,r)

! Output of potential minimum data to the screen
do j=1,4
  ptry(j)=p(1,j)
  write(unit=6, fmt=*) p(1,j)
enddo
call coord(ptry,r)
y(i2)=funk(r)
write(unit=6, fmt=*) y(i2)
write(unit=6, fmt=*) 'HUZZAH'



end program simplex1
```

```
! ------------------------------------------------------------
! ------------------------------------------------------------
! END OF MAIN PROGRAM - END OF MAIN PROGRAM
! ------------------------------------------------------------
! ------------------------------------------------------------



function funk(r)
! This is the function that calculates the value of the potential
! for any set of coordinates.  It uses the atom-atom distances.
! This is one of the few sub-units that does not use any other
! sub-unit (other than global_thingy of course)

use global_thingy
implicit none
real(kind=i) :: r(1:4,1:4),a(1:4,1:4),b(1:4,1:4),c(1:4,1:4)
real(kind=i) :: q(1:4,1:4),v1,v10,sumv,funk
integer :: n=4,m=4,i2,j

sumv=0.0_i
! the a, b, c and q matrices are the empirical potential parameters
! For details of their evaluation see chapter 5, section 3 or ask Dave : )
! a and b are the matrices for born mayer repulsive part of the potential
! c is the dispersion constant matrix
! q is the quadrupole interaction matrix.
a(1,1)=2.738046889E7_i
a(1,2)=2.738046889E7_i
a(2,1)=2.738046889E7_i
a(2,2)=2.738046889E7_i
b(1,1)=2.9609_i
b(1,2)=2.9609_i
b(2,1)=2.9609_i
b(2,2)=2.9609_i
c(1,1)=7.405860031E5_i
c(1,2)=7.405860031E5_i
c(2,1)=7.405860031E5_i
c(2,2)=7.405860031E5_i
```

```
q(1,1)=4.236865791E-39_i
q(1,2)=4.236865791E-39_i
q(1,3)=-4.236865791E-39_i
q(1,4)=-4.236865791E-39_i
q(2,1)=4.236865791E-39_i
q(2,2)=4.236865791E-39_i
q(2,3)=-4.236865791E-39_i
q(2,4)=-4.236865791E-39_i
q(3,1)=-4.236865791E-39_i
q(3,2)=-4.236865791E-39_i
q(3,3)=4.236865791E-39_i
q(3,4)=4.236865791E-39_i
q(4,1)=-4.236865791E-39_i
q(4,2)=-4.236865791E-39_i
q(4,3)=4.236865791E-39_i
q(4,4)=4.236865791E-39_i
!r(3,2)=12.0613953558709_i
!r(1,4)=12.1879212337461_i
!r(4,1)=12.0613953558709_i

!q(1,1)=3.293488048E-39_i
!q(1,2)=3.293488048E-39_i
!q(1,3)=-3.293488048E-39_i
!q(1,4)=-3.293488048E-39_i
!q(2,1)=3.293488048E-39_i
!q(2,2)=3.293488048E-39_i
!q(2,3)=-3.293488048E-39_i
!q(2,4)=-3.293488048E-39_i
!q(3,1)=-3.293488048E-39_i
!q(3,2)=-3.293488048E-39_i
!q(3,3)=3.293488048E-39_i
!q(3,4)=3.293488048E-39_i
!q(4,1)=-3.293488048E-39_i
!q(4,2)=-3.293488048E-39_i
!q(4,3)=3.293488048E-39_i
!q(4,4)=3.293488048E-39_i
```

```
!write(unit=6, fmt=*) r(1,1),r(1,2),r(1,3),r(1,4)
!write(unit=6, fmt=*) r(2,1),r(2,2),r(2,3),r(2,4)
!write(unit=6, fmt=*) r(3,1),r(3,2),r(3,3),r(3,4)
!write(unit=6, fmt=*) r(4,1),r(4,2),r(4,3),r(4,4)

! Evaluation of the potential energy for a given data point
do i2=1,m
 do j=1,n
 v1=a(i2,j)*exp(-b(i2,j)*r(i2,j))-(c(i2,j)/(r(i2,j)**6.0_i))
 v10=((q(i2,j)/(fpi*r(i2,j)*angs))/hc)
! write(unit=6, fmt=*) v1,v10
! stop
 sumv=sumv+v1+v10
! write(unit=6, fmt=*) sumv
 enddo
enddo
funk=sumv
!write(unit=6, fmt=*) funk,sumv
return
end function funk

! ------------------------------------------------------------
! ------------------------------------------------------------
! END OF FUNCTION FUNK - END OF FUNCTION FUNK
! ------------------------------------------------------------
! ------------------------------------------------------------


subroutine coord(ptry,r)
! This subroutine reads ptry which is just the values of
! r3 (rCOM), theta, phi and beta.  It then calculates the
! atom-atom distance matrix, r, and chucks it back.  This
! may sound trivial but as you will see when you look at the
! code it was a bloody nightmare :)
! If anyone comes up with a simpler method of transformation,
```

```
thet1=ptry(2)
phi1=ptry(3)
beta1=ptry(4)



chi1=180.0_i-thet1
eta1=180.0_i-phi1
iota1=90.0_i-beta1



if (iota1.lt.0.0_i) then
 iota1=iota1*(-1.0_i)
endif

! Conversion from degrees to radians
thet2=thet1*condr
phi2=phi1*condr
chi2=chi1*condr
eta2=eta1*condr
iota2=iota1*condr

!write(unit=6, fmt=*) r2_2,r2_34

r2_2xy=r2_2*cos(iota2)
r2_34xy=r2_34*cos(iota2)
r2_2z=r2_2*sin(iota2)
r2_34z=r2_34*sin(iota2)

!write(unit=6, fmt=*) r2_2xy,r2_34xy,r2_2z,r2_34z

ra=(r3**2.0_i+r2_2xy**2.0_i-2*r3*r2_2xy*cos(eta2))**0.5_i
rb=(r3**2.0_i+r2_2xy**2.0_i-2*r3*r2_2xy*cos(phi2))**0.5_i
rc=(r3**2.0_i+r2_34xy**2.0_i-2*r3*r2_34xy*cos(eta2))**0.5_i
rd=(r3**2.0_i+r2_34xy**2.0_i-2*r3*r2_34xy*cos(phi2))**0.5_i
re=(r3**2.0_i+r1_2**2.0_i-2*r3*r1_2*cos(thet2))**0.5_i
rf=(r3**2.0_i+r1_2**2.0_i-2*r3*r1_2*cos(chi2))**0.5_i
rg=(r3**2.0_i+r1_34**2.0_i-2*r3*r1_34*cos(thet2))**0.5_i
```

```
rh=(r3**2.0_i+r1_34**2.0_i-2*r3*r1_34*cos(chi2))**0.5_i

! ------------------------------------------------
! r_xy(1,1),(1,2),(2,1),(2,2) calculation
! ------------------------------------------------

!write(unit=6,fmt=*) ra,rb,rc,rd,re,rf,rg,rh

thetx2=acos((r2_2xy**2.0_i-r3**2.0_i-ra**2.0_i)/(tj*r3*ra))
!write(unit=6, fmt=*) thetx2
thetx1=thetx2*conrd
thety1=thet1-thetx1
thety2=thety1*condr
r_xy(2,2)=(ra**2.0_i+r1_2**2.0_i-2.0_i*ra*r1_2*cos(thety2))**0.5_i
chix2=acos((r2_2xy**2.0_i-r3**2.0_i-rb**2.0_i)/(tj*r3*rb))
!write(unit=6, fmt=*) chix2
chix1=chix2*conrd
chiy1=chi1-chix1
chiy2=chiy1*condr
r_xy(1,1)=(rb**2.0_i+r1_2**2.0_i-2.0_i*rb*r1_2*cos(chiy2))**0.5_i
sigx2=acos((r3**ti-r1_2**ti-re**ti)/(tj*r1_2*re))
!write(unit=6, fmt=*) sigx2
sigy2=acos((r2_2xy**ti-r_xy(2,2)**ti-re**ti)/(tj*r_xy(2,2)*re))
!write(unit=6, fmt=*) sigy2
sigx1=sigx2*conrd
sigy1=sigy2*conrd
sig1=sigx1+sigy1
sig2=sig1*condr
r_xy(1,2)=(r1**ti+r_xy(2,2)**ti-ti*r1*r_xy(2,2)*cos(sig2))**0.5_i
gamx2=acos((r3**ti-r1_2**ti-rf**ti)/(tj*r1_2*rf))
!write(unit=6, fmt=*) r2_2xy,r_xy(1,1),rf,ti
gamy2=acos((r2_2xy**ti-r_xy(1,1)**ti-rf**ti)/(tj*r_xy(1,1)*rf))
!write(unit=6, fmt=*) gamy2
gamx1=gamx2*conrd
gamy1=gamy2*conrd
gam1=gamx1+gamy1
gam2=gam1*condr
```

```
r_xy(2,1)=(r1**ti+r_xy(1,1)**ti-ti*r1*r_xy(1,1)*cos(gam2))**0.5_i

!write(unit=6,fmt=*) 'hello'
! -----------------------------------------------------
! r_xy(1,3),(1,4),(2,3),(2,4) calculation
! -----------------------------------------------------

thetx2=acos((r2_34xy**ti-r3**ti-rc**ti)/(tj*r3*rc))
thetx1=thetx2*conrd
thety1=thet1-thetx1
thety2=thety1*condr
r_xy(2,4)=(rc**ti+r1_2**ti-ti*rc*r1_2*cos(thety2))**0.5_i
chix2=acos((r2_34xy**ti-r3**ti-rd**ti)/(tj*r3*rd))
chix1=chix2*conrd
chiy1=chi1-chix1
chiy2=chiy1*condr
r_xy(1,3)=(rd**ti+r1_2**ti-ti*rd*r1_2*cos(chiy2))**0.5_i
lamx2=acos((r3**ti-r1_2**ti-re**ti)/(tj*r1_2*re))
lamy2=acos((r2_34xy**ti-r_xy(2,4)**ti-re**ti)/(tj*r_xy(2,4)*re))
lamx1=lamx2*conrd
lamy1=lamy2*conrd
lam1=lamx1+lamy1
lam2=lam1*condr
r_xy(1,4)=(r1**ti+r_xy(2,4)**ti-ti*r1*r_xy(2,4)*cos(lam2))**0.5_i
nux2=acos((r3**ti-r1_2**ti-rf**ti)/(tj*r1_2*rf))
nuy2=acos((r2_34xy**ti-r_xy(1,3)**ti-rf**ti)/(tj*r_xy(1,3)*rf))
nux1=nux2*conrd
nuy1=nuy2*conrd
nu1=nux1+nuy1
nu2=nu1*condr
r_xy(2,3)=(r1**ti+r_xy(1,3)**ti-ti*r1*r_xy(1,3)*cos(nu2))**0.5_i

! -----------------------------------------------------
! r_xy(3,3),(3,4),(4,3),(4,4) calculation
! -----------------------------------------------------

thetx2=acos((r2_34xy**ti-r3**ti-rc**ti)/(tj*r3*rc))
```

```
thetx1=thetx2*conrd
thety1=thet1-thetx1
thety2=thety1*condr
r_xy(4,4)=(rc**ti+r1_34**ti-ti*rc*r1_34*cos(thety2))**0.5_i
chix2=acos((r2_34xy**ti-r3**ti-rd**ti)/(tj*r3*rd))
chix1=chix2*conrd
chiy1=chi1-chix1
chiy2=chiy1*condr
r_xy(3,3)=(rd**ti+r1_34**ti-ti*rd*r1_34*cos(chiy2))**0.5_i
kapx2=acos((r3**ti-r1_34**ti-rg**ti)/(tj*r1_34*rg))
kapy2=acos((r2_34xy**ti-r_xy(4,4)**ti-rg**ti)/(tj*r_xy(4,4)*rg))
kapx1=kapx2*conrd
kapy1=kapy2*conrd
kap1=kapx1+kapy1
kap2=kap1*condr
r_xy(3,4)=(r34**ti+r_xy(4,4)**ti-ti*r34*r_xy(4,4)*cos(kap2))**0.5_i
zetax2=acos((r3**ti-r1_34**ti-rh**ti)/(tj*r1_34*rh))
zetay2=acos((r2_34xy**ti-r_xy(3,3)**ti-rh**ti)/(tj*r_xy(3,3)*rh))
zetax1=zetax2*conrd
zetay1=zetay2*conrd
zeta1=zetax1+zetay1
zeta2=zeta1*condr
r_xy(4,3)=(r34**ti+r_xy(3,3)**ti-ti*r34*r_xy(3,3)*cos(zeta2))**0.5_i

! ------------------------------------------------------
! r_xy(3,1),(3,2),(4,1),(4,2) calculation
! ------------------------------------------------------

thetx2=acos((r2_2xy**ti-r3**ti-ra**ti)/(tj*r3*ra))
thetx1=thetx2*conrd
thety1=thet1-thetx1
thety2=thety1*condr
r_xy(4,2)=(ra**ti+r1_34**ti-ti*ra*r1_34*cos(thety2))**0.5_i
chix2=acos((r2_2xy**ti-r3**ti-rb**ti)/(tj*r3*rb))
chix1=chix2*conrd
chiy1=chi1-chix1
chiy2=chiy1*condr
```

```
r_xy(3,1)=(rb**ti+r1_34**ti-ti*rb*r1_34*cos(chiy2))**0.5_i
mux2=acos((r3**ti-r1_34**ti-rg**ti)/(tj*r1_34*rg))
muy2=acos((r2_2xy**ti-r_xy(4,2)**ti-rg**ti)/(tj*r_xy(4,2)*rg))
mux1=mux2*conrd
muy1=muy2*conrd
mu1=mux1+muy1
mu2=mu1*condr
r_xy(3,2)=(r34**ti+r_xy(4,2)**ti-ti*r34*r_xy(4,2)*cos(mu2))**0.5_i
epsx2=acos((r3**ti-r1_34**ti-rh**ti)/(tj*r1_34*rh))
epsy2=acos((r2_2xy**ti-r_xy(3,1)**ti-rh**ti)/(tj*r_xy(3,1)*rh))
epsx1=epsx2*conrd
epsy1=epsy2*conrd
eps1=epsx1+epsy1
eps2=eps1*condr
r_xy(4,1)=(r34**ti+r_xy(3,1)**ti-ti*r34*r_xy(3,1)*cos(eps2))**0.5_i

! ------------------------------------------------------------
! r(i,j) calculation
! ------------------------------------------------------------

r(1,1)=(r2_2z**ti + r_xy(1,1)**ti)**0.5_i
r(1,2)=(r2_2z**ti + r_xy(1,2)**ti)**0.5_i
r(1,3)=(r2_34z**ti + r_xy(1,3)**ti)**0.5_i
r(1,4)=(r2_34z**ti + r_xy(1,4)**ti)**0.5_i
r(2,1)=(r2_2z**ti + r_xy(2,1)**ti)**0.5_i
r(2,2)=(r2_2z**ti + r_xy(2,2)**ti)**0.5_i
r(2,3)=(r2_34z**ti + r_xy(2,3)**ti)**0.5_i
r(2,4)=(r2_34z**ti + r_xy(2,4)**ti)**0.5_i
r(3,1)=(r2_2z**ti + r_xy(3,1)**ti)**0.5_i
r(3,2)=(r2_2z**ti + r_xy(3,2)**ti)**0.5_i
r(3,3)=(r2_34z**ti + r_xy(3,3)**ti)**0.5_i
r(3,4)=(r2_34z**ti + r_xy(3,4)**ti)**0.5_i
r(4,1)=(r2_2z**ti + r_xy(4,1)**ti)**0.5_i
r(4,2)=(r2_2z**ti + r_xy(4,2)**ti)**0.5_i
r(4,3)=(r2_34z**ti + r_xy(4,3)**ti)**0.5_i
r(4,4)=(r2_34z**ti + r_xy(4,4)**ti)**0.5_i
!write(unit=6, fmt=*) r(1,1),r(1,2),r(1,3),r(1,4)
```

```
!write(unit=6, fmt=*) r(2,1),r(2,2),r(2,3),r(2,4)
!write(unit=6, fmt=*) r(3,1),r(3,2),r(3,3),r(3,4)
!write(unit=6, fmt=*) r(4,1),r(4,2),r(4,3),r(4,4)
!write(unit=6, fmt=*) r_xy(1,4),r(1,4)
!write(unit=6, fmt=*) r_xy(4,1),r(4,1)
!write(unit=6, fmt=*) r_xy(3,2),r(3,2)

return
end subroutine coord

! ------------------------------------------------------------
! ------------------------------------------------------------
! END OF SUBROUTINE COORD - END OF SUBROUTINE COORD
! ------------------------------------------------------------
! ------------------------------------------------------------



subroutine amoeba(p,y,mp,np,ndim,ftol,funk,iter,r)

! This is the subroutine from Numerical Recipes. It is a
! multidimensional minimization of the function funk(r) where
! r is the matrix of atom atom distance for the I2-N2 system.
! The minimization uses the downhillsimplex method of Nelder
! and Mead.  The matrix p(1:ndim+1,1:ndim) is input.

use global_thingy
implicit none
real(kind=i) :: p(1:5,1:4),y(1:5),ftol,r(1:4,1:4),shit
integer :: mp,np,iter,ndim
real(kind=i), external :: funk,amotry
integer :: i2,ihi,ilo,inhi,j,m,n
real(kind=i) :: rtol,sum,swap,ysave,ytry,psum(1:4),ptry(1:4)

!do i2=1,5
! do j=1,4
!  write(unit=6, fmt=*) p(i2,j)
! enddo
```

```
!enddo

!do i2=1,5
! write(unit=6, fmt=*) y(i2)
!enddo

!write(unit=6, fmt=*) ftol,mp,np,ndim
!stop

iter=0

1  do n=1,4
     sum=0.0_i
     do m=1,5
       sum=sum+p(m,n)
     enddo
     psum(n)=sum
   enddo
2  ilo=1
   if (y(1).gt.y(2)) then
     ihi=1
     inhi=2
   else
     ihi=2
     inhi=1
   endif
   do i2=1,5
     if (y(i2).le.y(ilo)) ilo=i2
     if (y(i2).gt.y(ihi)) then
       inhi=ihi
       ihi=i2
     elseif (y(i2).gt.y(inhi)) then
       if (i2.ne.ihi) inhi=i2
     endif
   enddo
!  write(unit=6, fmt=*) ilo
!  write(unit=6, fmt=*) y(ilo)
```

```
      rtol=2.0_i*abs(y(ihi)-y(ilo))/(abs(y(ihi))+abs(y(ilo)))
!     write(unit=6, fmt=*) rtol
      shit=abs(y(ihi))
!     write(unit=6, fmt=*) shit
!     stop
      if (rtol.lt.ftol) then
        swap=y(1)
        y(1)=y(ilo)
        y(ilo)=swap
        do n=1,4
          swap=p(1,n)
          p(1,n)=p(ilo,n)
          p(ilo,n)=swap
        enddo
        return
      endif
!     do i2=1,5
!       do j=1,4
!         write(unit=6, fmt=*) p(i2,j)
!       enddo
!     enddo
      if (iter.ge.ITMAX) then
        do j=1,4
!         write(unit=6, fmt=*) psum(j)
        enddo
        write(unit=6, fmt=*) 'ITMAX exceeded in amoeba'
!       write(unit=6, fmt=*) iter
!       write(unit=6, fmt=*) ytry
        do i2=1,5
          do j=1,4
!           write(unit=6, fmt=*) p(i2,j)
            ptry(j)=p(i2,j)
          enddo
          call coord(ptry,r)
          ytry=funk(r)
!         write(unit=6, fmt=*) ytry
        enddo
```

```
      stop
     endif
     iter=iter+2
     ytry=amotry(p,y,psum,mp,np,ndim,funk,r,ihi,-1.0_i)
!    write(unit=6, fmt=*) ytry
!    stop
!    if (iter.ge.39950) then
!     write(unit=6, fmt=*) ytry
!    endif

! the next three lines should be in the code but I commented
! them out to reduce the chance of huge changes
!    if (ytry.le.y(ilo)) then
!      ytry=amotry(p,y,psum,mp,np,ndim,funk,r,ihi,2.0_i)
!    elseif (ytry.ge.y(inhi)) then
     if (ytry.ge.y(inhi)) then
      ysave=y(ihi)
      ytry=amotry(p,y,psum,mp,np,ndim,funk,r,ihi,0.5_i)
!      write(unit=6, fmt=*) ytry
!      stop
      if (ytry.ge.ysave) then
       do i2=1,5
        if (i2.ne.ilo) then
         do j=1,4
          psum(j)=0.5_i*(p(i2,j)+p(ilo,j))
          p(i2,j)=psum(j)
         enddo
         ptry=psum
         call coord(ptry,r)
         y(i2)=funk(r)
        endif
       enddo
       iter=iter+ndim
       goto1
      endif
     else
      iter=iter-1
```

```
  endif
  goto2

end subroutine amoeba

! ------------------------------------------------------
! ------------------------------------------------------
! END OF SUBROUTINE AMOEBA
! ------------------------------------------------------
! ------------------------------------------------------


function amotry(p,y,psum,mp,np,ndim,funk,r,ihi,fac)
use global_thingy
implicit none
real(kind=i) :: amotry,fac,p(1:5,1:4),psum(1:4),y(1:5)
integer :: ihi,mp,np,ndim,j,i2
real(kind=i), external :: funk
real(kind=i) :: fac1,fac2,ytry,ptry(1:4),r(1:4,1:4)
fac1=(1.0_i-fac)/4.0_i
fac2=fac1-fac
!write(unit=6, fmt=*) fac1,fac2
do j=1,4
  ptry(j)=psum(j)*fac1-p(ihi,j)*fac2
!  write(unit=6, fmt=*) psum(j)
enddo
!do i2=1,4
! write(unit=6, fmt=*) psum(i2)
!enddo
call coord(ptry,r)
ytry=funk(r)
!write(unit=6, fmt=*) ytry
if (ytry.lt.y(ihi)) then
  y(ihi)=ytry
  do j=1,4
    psum(j)=psum(j)-p(ihi,j)+ptry(j)
    p(ihi,j)=ptry(j)
```

```
!    write(unit=6, fmt=*) p(ihi,j)
  enddo
!  write(unit=6, fmt=*) ytry
endif
amotry=ytry
!write(unit=6, fmt=*) ytry
!do i2=1,3
! write(unit=6, fmt=*) y(i2)
!enddo
!do i2=1,3
! do j=1,2
!  write(unit=6, fmt=*) p(i2,j)
! enddo
!enddo
!do j=1,2
! write(unit=6, fmt=*) ptry(j)
!enddo
!stop

return
end function amotry

! ------------------------------------------------------
! ------------------------------------------------------
! END OF FUNCTION AMOTRY
! ------------------------------------------------------
! ------------------------------------------------------
```

University Regulations

There follows a list of the lecture courses I attended during the time that I was carrying out research in the Department of Chemistry. Also given is a list of the conferences I attended and those at which I presented the results of my research.

List of courses:

1. *Introduction to Fortran 90*, 5 day course, University of Edinburgh Computer Service.
2. *IR Spectroscopy: Practice and Theory*, 6 lectures, Prof. D. C. McKean and Dr. C. R. Pulham, The University of Edinburgh.
3. *Numerical Data Handling*, 5 lectures, Prof. Jim Scrivens, ICI Wilton Research Centre.
4. *MaxEnt: An Introduction to Probabilistic Data Handling*, 3 lectures,
5. *Surface Imaging and Analysis*, 4 lectures, Dr. D. McComb, Dr. J. Fryer, Dr. E. E. Lachowski, Dr. G. McPherson.
6. *Physical Section Colloquia*, 1994-95, 1995-96, 1996-97 academic years.

List of conferences attended:

1. RSC Faraday Division, One Day Symposium on 'Dynamics of Electronically Excited States', Univeristy of Manchester, 29 March 1995
2. RSC Annual Chemical Congress, Heriot Watt University, 10-13 April 1995.
3. 'ECAMP 5 (European Conference on Atomic and Molecular Physics)', University of Edinburgh, 3-7 April 1995.
4. 'International Workshop on Photoionisation Dynamics, Rydberg States and Large Amplitude Motion', University of York, 3-5 November 1996.

List of contributions to conferences:

1. 'Very High Resolution Spectroscopy with Photoelectrons', Lenggries, Germany, 23-28 September 1995. Poster contribution: 'A Study of Structural Isomerism in the I_2-Ar van der Waals complex using REMPI and ZEKE Photoelectron Spectroscopy'.
2. 'ATMOP 23 (Atomic Molecular and Optical Physics Division, IOP)', Keble College, Oxford University, 1-4 April 1996. Poster contribution: 'The (2+1′) ZEKE-PFI Phototelectron Spectrum of IBr: Evidence for Vibrational Autoionisation'.
3. 'ANUMOCP 6 (6^{th} Annual Northern Universities' Meeting on Chemical Physics)', University of Northumbria at Newcastle, 4 July 1996. Poster contribution: 'The (2+1′) ZEKE-PFI Photoelectron Spectroscopy and Rydberg State Spectroscopy of Bromine'.
4. Annual Meeting of the Physical Section of the Department of Chemistry, University of Edinburgh, Firbush Point Field Centre, June 1995, 1996, 1997.
5. Fifteenth Colloquium on High Resolution Molecular Spectroscopy, Strathclyde University, Glasgow, 7-11 September 1997. Poster contribution: 'The (2+1) REMPI Spectra of the I_2-Kr and I_2-N_2 van der Waals complexes and the (2+1′) ZEKE-PFI Photoelectron Spectrum of I_2^+-Kr'.

List of Publications

1. 'Structural isomerism in the I_2-Ar van der Waals complex studied by ZEKE-PFI spectroscopy: evidence for both linear and T-shaped isomers', M. C. R. Cockett, D. A. Beattie, R. J. Donovan, K. P. Lawley, *Chem.Phys.Lett.* 1996, **259**, 554.
2. 'The (2+1) REMPI spectra of the I_2-Kr and I_2-N_2 van der Waals complexes and the (2+1′) ZEKE-PFI photoelectron spectrum of I_2^+-Kr', D. A. Beattie, M. C. R. Cockett, K. P. Lawley, R. J. Donovan, *J.Chem.Soc.Farad.Trans.* 1997, **93**, 4245.

List of Figures

List of Tables